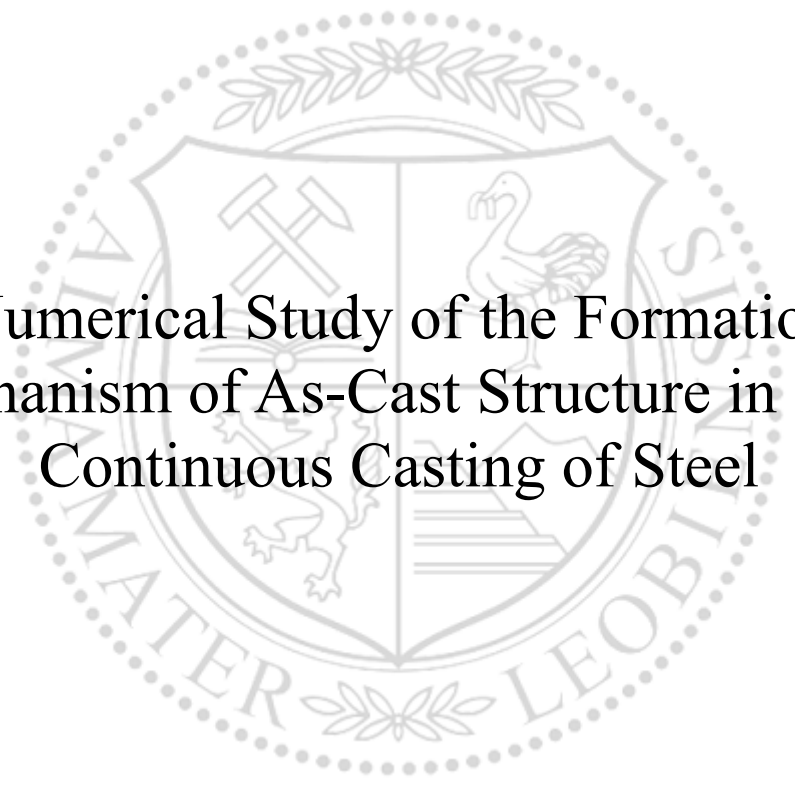




Chair of Simulation and Modelling of Metallurgical Processes

Doctoral Thesis



Numerical Study of the Formation  
Mechanism of As-Cast Structure in Semi  
Continuous Casting of Steel

Zhao Zhang

February 2023





**MONTANUNIVERSITÄT LEOBEN**

www.unileoben.ac.at

**AFFIDAVIT**

I declare on oath that I wrote this thesis independently, did not use other than the specified sources and aids, and did not otherwise use any unauthorized aids.

I declare that I have read, understood, and complied with the guidelines of the senate of the Montanuniversität Leoben for "Good Scientific Practice".

Furthermore, I declare that the electronic and printed version of the submitted thesis are identical, both, formally and with regard to content.

Date 22.02.2023

*Zhao Zhang*

Signature Author  
Zhao Zhang



## Acknowledgements

First and foremost, I would like to express my deepest gratitude to my supervisor, Prof. Menghuai Wu, for his continuous support, invaluable patience, and great encouragement. His immense knowledge and plentiful experience have encouraged and inspired me all the time during my academic research. Studying and working with Prof. Wu for the past four years has been extremely helpful to me. This work would not have been possible without his generous assistance.

I would like to extend my sincere thanks to Prof. Andreas Ludwig for giving me the opportunity to work at the chair of Simulation and Modelling of Metallurgical Processes (SMMP) of the University of Leoben. It is such a good pleasure to work with so many talented researchers in this chair. I am also grateful to Prof. Abdellah Kharicha for his generous help in studying the electromagnetic field during this scientific work.

Great thanks should also go to my mentor Prof. Christian Bernhard for his help in the lecture about the continuous casting process. It is really an enjoyable experience to discuss with him.

Many thanks to Prof. Ri Li at the Hebei University of Technology. Without his kind help and recommendation, it would not have been possible for me to come to the University of Leoben and finish this Ph.D thesis here.

I would like to acknowledge the financial support from the Austria Research Promotion Agency (FFG) through the Bridge 1 project (No. 868070) as well as the technical support of the industrial partner Primetals Technologies Austria GmbH. I would like to express my thanks to those industrial experts, Susanne Hahn, Franz Wimmer, Denijel Burzic, Reisenberger Eward, Guoxin Shan, Felix Lindlbauer, Philipp Wieser, Michael Riedler, for their generous advice and comments.

Great thanks also to my colleagues in SMMP: Haijie Zhang, Christian Gomes Rodrigues, Ebrahim Karimi-Sibaki, Alexander Vakhrushev, Mehran Abdi, Golshan Siyahatshayesteh, Mohamad Al Nasser, Hadi Barati, Johann Mogeritsch, Michaela Stefan-Kharicha, Jan Bohacek, Ibrahim Sari, Anastasiia Kadylnykova, Klaus-Jürgen Otto, Claudia Heinzl, Sabine Strassegger for their help in the academic work and daily life. It is such a joyful experience to work with them.

Finally, many thanks to my parents for their love, support, and encouragement during this academic career. Special thanks to my wife, Yanxia Kang. She takes care of the family during much of my Ph.D study. Without her support and unfailing love, it would not have been possible for me to concentrate on this thesis. Along with her, I would like to express my thanks to my daughter, Xinxuan Zhang. So many joys come from her laughter. This work is dedicated to them.

## Kurzfassung

Ein grundlegendes Verständnis des Erstarrungsprozesses von großen Gussteilen hinsichtlich der Ausbildung der Gussgefüge und der Makroseigerung ist von entscheidender Bedeutung, insbesondere um den hohen Qualitätsansprüchen mit einer steigenden Nachfrage an hochwertigen Gusskomponenten in der Schwerindustrie gerecht zu werden. Die bestehenden Gießtechnologien können die hohen Anforderungen an diese Gusskomponenten nur teilweise erfüllen. Der herkömmliche Blockguss (IC) ist durch die Höhe des Blocks begrenzt und hat eine geringere Ausbringung, was zu höheren Produktionskosten führt. Der Strangguss (CC) ist durch den begrenzten Querschnitt des Strangs eingeschränkt. Daher wurde kürzlich ein neues Gießkonzept, das sogenannte semi-continuous casting (SCC), vorgeschlagen. SCC versucht, die Vorteile von IC und CC zu kombinieren. Obwohl ein ähnliches Gießverfahren (DC casting) bei der Herstellung von Nichteisenlegierungen etabliert ist, stellt das SCC-Verfahren für Stahl, aufgrund seiner geringen Wärmeleitfähigkeit und hohen Gießtemperatur, eine Herausforderung dar. In dieser Arbeit wurde ein dreiphasiges „mixed columnar-equiaxed“ Erstarrungsmodell, das von Wu und Ludwig vorgeschlagen wurde, erweitert und verwendet, um die Bildung des Gussgefüges und der Makroseigerung während des SCC-Prozesses von Stahl zu untersuchen.

Zunächst wurde das dreiphasige Erstarrungsmodell erweitert: 1) Die Kristall-Fragmentation, die als Hauptquelle der äquiaxialen Kristalle dient, wird berücksichtigt; 2) ein Kopplungsschema zwischen der Strömung und dem elektromagnetischen Feld wird eingerichtet; 3) Phänomene des Umschmelzens und der Zerstörung der äquiaxialen Kristalle werden berücksichtigt.

Das neu entwickelte Modell wurde validiert, indem die Simulationsergebnisse mit Benchmark-Experimenten im Labormaßstab und dem Strangguss im industriellen Maßstab verglichen wurden. 1) Die Bildung des Gussgefüges und der Makroseigerung einer SnPb-Legierung unter dem Einfluss verschiedener Arten erzwungener Konvektion, die durch ein magnetisches Feld (TMF) angetrieben wird, wurde von Hachani et al. 2015 am SIMAP-Labor in Grenoble, Frankreich, systematisch untersucht. Vier Experimente wurden durchgeführt: i) ohne TMF; ii) TMF in der gleichen Richtung wie natürliche Konvektion; iii) TMF in entgegengesetzter Richtung wie natürliche Konvektion; iv) TMF in Bezug auf natürliche

Konvektion periodisch umgekehrt. Es wurde festgestellt, dass das TMF eine wichtige Rolle bei der Homogenisierung der Temperatur und der Erhöhung der Makrosegregationsintensität spielt. Es wurde eine gute Simulation-Experiment-Übereinstimmung hinsichtlich Temperaturfeld, Gussgefüge und Makroseigerung erzielt. 2) Der Einfluss des elektromagnetischen Rührens (M-EMS) auf die Bildung des Gussgefüges und der Makroseigerung eines Billet-Stranggusses (195 mm × 195 mm) wurde untersucht. Das M-EMS neigt dazu, die Dissipation der Überhitzung der Stahlschmelze im Formbereich zu beschleunigen, wodurch die Schmelze aus dem Formbereich weitgehend unterkühlt bleibt. Außerdem ist die Rate der Kristall-Fragmentation von der M-EMS-Intensität abhängig. Das rechnerisch vorhergesagte Gussgefüge zeigte auch eine gute Übereinstimmung mit dem Experiment.

Abschließend wurde das erweiterte und validierte dreiphasige Erstarrungsmodell verwendet, um den Erstarrungsprozess von SCC mit der Wirkung von EMS zu simulieren. Das Erstarrungsprinzip während des SCC-Prozesses wurde eingehend untersucht. In Zukunft kann das Modell verwendet werden, um systematische Parameterstudien anstelle von kostspieligen Pilot-/Gießversuchen im Feld zur Optimierung des SCC-Prozesses durchzuführen. Die Rechnerkapazität (Hardware) ist dabei immer noch ein begrenzender Faktor.



## Abstract

The surging demand for high-quality rotor shafts or similar components with large format in heavy industries poses new challenges to steelmakers. Due to the inherent shortcomings and limitations of the existing technologies, they do not work properly for these components. For example, the conventional ingot casting (IC) technology is limited by the ingot height and has lower yield and higher operational costs; the developed continuous casting (CC) technology is restricted by the cross-section of the strand. Therefore, a new casting concept, semi-continuous casting (SCC), which attempts to combine the advantages of IC and CC, is recently proposed for steel production. Although a similar casting process, i.e., direct-chill casting, is mature in producing non-ferrous alloys, the application of the SCC in the production of quality steel requires addressing certain challenges due to the low thermal conductivity and high pouring temperature of steel. Additionally, the understanding of the solidification process regarding the formation of the as-cast structure and macrosegregation during the SCC process is still unknown. In this thesis, a three-phase columnar-equiaxed solidification model, which was previously proposed by Wu and Ludwig, was extended and used to investigate the formation of the as-cast structure and macrosegregation during the SCC process of steel.

Firstly, the three-phase multiphase solidification model was extended: 1) the fragmentation of columnar equiaxed, which serves as a main source of the equiaxed grains, is considered; 2) a coupling scheme between the flow field and electromagnetic field is established; 3) phenomena of remelting and destruction of the equiaxed grains are considered when the grains are exposed to the superheated region.

Secondly, the well-established model was validated by comparing the simulation results with the benchmark experiments at the laboratory scale and the continuous casting of steel billet at the industrial scale. 1) The evolutions of the as-cast structure and macrosegregation of Sn-10wt.% Pb alloy under the effect of different types of forced convection, which is powered by a travelling magnetic field (TMF), were systematically studied by Hachani et al., in 2015 at the SIMAP Laboratory in Grenoble, France. Four different experiments were investigated: (i) without TMF; (ii) TMF in the same direction as natural convection; (iii) TMF in the opposite direction as natural convection; (iv) TMF periodically reversed with respect to natural convection. The TMF is found to play an important role in homogenizing

the temperature and increasing the macrosegregation intensity. Good simulation-experiment agreements in terms of temperature field, as-cast structure and macrosegregation were obtained. 2) The effect of the mold electromagnetic stirring (M-EMS) on the formation of as-cast structure and macrosegregation of a steel billet (195 mm × 195 mm) was investigated. The M-EMS tends to accelerate the superheat dissipation in the mold region, leaving the liquid core out of the mold region largely undercooled. Additionally, the fragmentation rate is sensitive to the M-EMS implementation. The calculated macrostructure showed a satisfactory agreement with the as-cast structure.

Finally, the extended three-phase model was used to simulate the solidification process of the SCC under the effect of EMS. The solidification principle during the SCC process was deeply investigated. As an outlook, the model can be used to perform systematic parameter studies, instead of costly pilot/field-casting trials, towards the optimization of the SCC process. The computational capacity (hardware) is still a limiting factor for this purpose.

## **Thesis structure**

This thesis consists of two main parts. Part I is the executive summary, which includes the background and motivation of this work, state of the art, executive summary and main conclusions of the Ph.D work. Part II contains the collection of the 5 peer reviewed journal articles of the candidate, among which 3 have been published, 1 has been accepted for publication, and 1 is under review.



# Contents

Acknowledgements .....	I
Kurzfassung .....	III
Abstract.....	V
Thesis structure.....	VII
Nomenclature.....	XI
Part I: Executive summary .....	1
1. Introduction .....	3
1.1 Background.....	3
1.2 Objectives .....	4
2. State of the art.....	5
2.1 Conventional steel casting technologies .....	5
2.1.1 Ingot casting (IC).....	5
2.1.2 Continuous casting (CC) .....	9
2.2 Large vertical steel casting .....	19
2.2.1 Vertical continuous casting (VCC) .....	19
2.2.2 Large ingot casting caster (LICC) .....	20
2.2.3 Segment casting (SC) .....	22
2.2.4 Semi-continuous casting (SCC) .....	23
2.3 Modelling.....	25
2.3.1 Multiphase solidification model .....	25
2.3.2 Computational magnetohydrodynamic methods .....	30
3. Summary of the Ph.D works.....	37

3.1 Modeling mixed columnar-equiaxed solidification of Sn-10wt.% Pb alloy under different types of forced convection .....	37
3.2 Numerical study of the as-cast structure and macrosegregation in the continuous casting of a steel billet .....	41
3.3 Evaluation of the coupling schemes between the flow field and electromagnetic field	45
3.4 Solidification principle of the SCC .....	49
4. Main conclusions of the Ph.D works .....	53
5. Reference .....	55
Part II: Publications.....	65
Paper 1 .....	69
Paper 2.....	87
Paper 3.....	103
Paper 4.....	139
Paper 5.....	167

## Nomenclature

$A_k$	the total k-j interface area enclosed in the volume element	$m^2$
$\bar{B}, \bar{B}_0, \bar{b}$	combined, external, and induced magnetic field	T
$\bar{B}^*$	conjugate magnetic field	T
$c_\ell, c_e, c_c$	species concentration	wt.%
$c_0, c^{\text{ref}}$	initial and reference concentration of the alloy	wt.%
$c_\ell^*, c_e^*, c_c^*$	equilibrium concentration	wt.%
$C_{\ell e}, C_{\ell c}, C_{ce}$	species exchange between phases	$kg\ m^{-3}\ s^{-1}$
$c_p^\ell, c_p^e, c_p^c$	specific heat	$J\ kg^{-1}\ K^{-1}$
$d_e, d_c$	grain diameter	m
$d_{e,\text{frag}}^0$	initial fragment size in diameter	m
$\hat{d}_e$	geometric mean of the equiaxed grains size	m
$D_\ell, D_e, D_c$	diffusion coefficient	$m^2\ s^{-1}$
$\bar{e}$	unit vector	-
$\bar{E}$	electric field	$V\ m^{-1}$
$f_\ell, f_e, f_c$	volume fraction for different phases	-
$f_k, f_j$	volume fraction for phase-k and phase-j	-
$f_e^{\text{env}}$	volume fraction of equiaxed grain envelop	-
$f_{\text{si}}$	fraction solid in equiaxed grain envelop	-
$f, f_{\text{eff}}$	original and effective magnetic field frequency	Hz
$\bar{F}, \bar{F}_L, \bar{F}'_L$	Lorentz force, original and modified time-averaged Lorentz force	$N\ m^{-3}$
$\bar{F}_r, \bar{F}_\theta$	Lorentz forces in the radius and azimuthal directions	$N\ m^{-3}$
$\bar{g}, \bar{g}'_\ell$	gravity and deduced gravity	$m\ s^{-2}$
$h_\ell, h_e, h_c$	enthalpy	$J\ kg^{-1}$
$h_\ell^{\text{ref}}, h_e^{\text{ref}}, h_c^{\text{ref}}$	reference enthalpy	$J\ kg^{-1}$
$H^*$	volume heat transfer coefficient between phases	$W\ m^{-3}\ K^{-1}$
$\bar{J}$	electric current density	$A\ m^{-2}$
$k$	solute partitioning coefficient at the solid/liquid interface	-
$k_\ell, k_e, k_c$	thermal conductivity	$W\ m^{-1}\ K^{-1}$
$K$	permeability of liquid in porous medium	$m^2$

$K_{\ell e}, K_{\ell c}, K_{ce}$	drag coefficient between phases	$\text{kg m}^{-3} \text{s}^{-1}$
$l$	actual columnar length in tip cell	m
$m$	slope of liquidus in phase diagram	K
$M_{\ell e}, M_{\ell c}, M_{ce}$	net mass transfer rate between phases	$\text{kg m}^{-3} \text{s}^{-1}$
$n_e, n_c, n_{in}$	number density (equiaxed, columnar, inoculant)	$\text{m}^{-3}$
$N_{des}$	destruction rate of the equiaxed grains	$\text{m}^{-3} \text{s}^{-1}$
$N_{frag}$	fragmentation rate	$\text{m}^{-3} \text{s}^{-1}$
$N_{nu}$	heterogeneous nucleation rate	$\text{m}^{-3} \text{s}^{-1}$
$p$	pressure	$\text{N m}^{-2}$
$q$	electric charge density	$\text{C m}^{-3}$
$Q_{\ell e}^M, Q_{\ell c}^M$	energy exchange due to phase change	$\text{J m}^{-3} \text{s}^{-1}$
$Q_{\ell e}^D, Q_{\ell c}^D, Q_{ce}^D$	energy transfer between phases	$\text{J m}^{-3} \text{s}^{-1}$
$r$	radial coordinate	m
$R$	radius of the sample (Cu, Al, and AlSi7)	m
$R_{eq}, R_c$	grain radius (equiaxed, columnar)	m
$R_{fe}, R_{fc}$	maximal radius of the grain	m
$R_{tip}$	tip radius of columnar primary dendrite	m
$R_e$	real part of a complex number	-
Re	Reynolds number	-
Sc	Schmidt number	-
$t$	time	s
$T_\ell, T_e, T_c$	temperature	K
$T^{ref}$	reference temperature	K
$\Delta T$	constitutional undercooling	K
$\Delta T_N$	undercooling for maximum grain production rate	K
$\Delta T_\sigma$	Gaussian distribution width of nucleation law	K
$\vec{u}_\ell, \vec{u}_e, \vec{u}_c$	velocity for different phases	$\text{m s}^{-1}$
$u_\theta$	azimuthal velocity magnitude	$\text{m s}^{-1}$
$\vec{u}_k^{int} (= \vec{u}_k + \vec{v}_k^{int})$	velocity of the k-j interface	$\text{m s}^{-1}$
$\vec{u}_k, \vec{v}_k^{int}$	moving velocity and growth velocity of the k-j interface	$\text{m s}^{-1}$
$\vec{U}_{\ell e}, \vec{U}_{\ell c}, \vec{U}_{ce}$	total momentum exchange rate between phases	$\text{kg m}^{-2} \text{s}^{-2}$
$v_{Req}, v_{Rc}$	growth speed in radius direction (equiaxed, columnar)	$\text{m s}^{-1}$



$v_{\text{tip}}$	grain growth speed in tip direction	$\text{m s}^{-1}$
$V_0$	volume of the representative volume element	$\text{m}^3$
$V_k, V_j$	volumes of phase-k and phase-j in $V_0$	$\text{m}^3$
$x$	equiaxed grains diameter of different size classes	$\text{m}$
$\omega_B$	angular speed of the magnetic field	$\text{Rad s}^{-1}$
$\bar{\omega}_l$	average fluid angular speed	$\text{Rad s}^{-1}$
$\beta_T$	thermal expansion coefficient	$\text{K}^{-1}$
$\beta_C$	solubility expansion coefficient	$\text{wt.\%}^{-1}$
$\rho_l, \rho_e, \rho_c$	density for different phase	$\text{kg m}^{-3}$
$\rho_l^{\text{ref}}$	reference density	$\text{kg m}^{-3}$
$\rho_l^b$	density for buoyancy force	$\text{kg m}^{-3}$
$\tau$	torque	$\text{N m}$
$\tau_l, \tau_e$	stress-strain tensors	$\text{kg m}^{-1} \text{s}^{-1}$
$\mu, \mu_0, \mu_r$	combined, vacuum, and relative magnetic permeability	$\text{H m}^{-1}$
$\mu_l, \mu_e$	viscosity	$\text{kg m}^{-1} \text{s}^{-1}$
$\lambda_1, \lambda_2$	primary and secondary dendrite arm spacing	$\text{m}$
$\gamma$	fragmentation coefficient	-
$\Phi_{\text{imp}}^e, \Phi_{\text{imp}}^c$	growth impingement factor	-
$\sigma$	electromagnetic conductivity of the conductive material	$\text{S m}^{-1}$
$\sigma_g$	geometric standard deviation of the lognormal distribution	-
$\epsilon_0$	vacuum permittivity	$\text{F m}^{-1}$

\* Subscripts  $l, e, c$ , indicate the liquid melt, equiaxed grain, and columnar dendrite.

### Auxiliary equations:

$$\text{Mixture concentration: } c_{\text{mix}} = \frac{f_l \rho_l c_l + f_e \rho_e c_e + f_c \rho_c c_c}{f_l \rho_l + f_e \rho_e + f_c \rho_c}.$$

$$\text{Macrosegregation index: } c_{\text{mix}}^{\text{index}} = \frac{c_{\text{mix}} - c_0}{c_0} \times 100\%.$$

$$\text{Global macrosegregation index: } \text{GMI} = \iiint_{\text{vol}} |c_{\text{mix}}^{\text{index}}| dv.$$



# **Part I: Executive summary**



# 1. Introduction

## 1.1 Background

A rising demand for the high-quality rotor shafts or similar components with large format in heavy industries poses new challenges to steelmakers. The initial form of these components is usually made by casting, but the solidification of steel (inherently low thermal conductivity) takes an extremely long time, especially with the increased product section. It consequently leads to internal quality problems such as macrosegregation and centerline shrinkage porosity [1–2]. The existing casting technologies do not work properly for these components. For example, the conventional ingot casting (IC) technology can produce components of large section, but it is limited by the ingot height and has lower yield and higher operational costs. The developed continuous casting (CC) technology has higher productivity and lower operational costs, however, the cross section of the strand is limited. Therefore, a concept of semi-continuous casting (SCC), attempting to combine certain advantages of CC and IC and eliminate their corresponding limitations, is proposed as an alternative technique to produce steel with large format, especially rounds from  $\phi$  300 mm up to  $\phi$  1500 mm at a length of up to 12 m [3].

Principally, the SCC process consists of two main procedures, casting, and solidification. Following the CC technology, the casting procedure is conducted at CC machines. The casting process can be well controlled by the implementation of a submerged entry nozzle (SEN) for mold filling, water-cooled mold with oscillating technology, and secondary cooling system for self-carrying strand shell formation, and mold electromagnetic stirring (M-EMS) for flow control and superheat dissipation. Following the IC technology, when the as-filled and partially solidified casting is put aside for the remaining solidification, further additional measures can be applied, i.e., the hot-topping and static or dynamic shielding for the controlled cooling. This keeps the inner melt for a long time in the strand, which is similar to IC. The strand electromagnetic stirring (S-EMS) can even be performed to promote the formation of equiaxed grains, hence, improving the inner quality of the strand.

Owing to the harsh environment and high costs, it is impossible to observe and analyze the solidification phenomena during the casting processes with field experiments. The

numerical modelling, which are of obvious advantage for their high flexibility and low costs, has become an alternative and effective tool for this purpose. Numerous numerical methods, e.g., mixture continuum model [4–10], cellular automata finite elements (CAFE) method [11–15], cellular automata – finite volume method (CA-FVM) [16] and volume averaged (VA) method [17–24], have been used to simulate the solidification process and try to give a better understanding for the accompanying phenomena. The VA method stands out among these methods due to its compatibility to consider most of the key features occurred during the solidification process, i.e., growth of the columnar dendrites with the explicit tracking of the dendritic tip, nucleation and growth of the equiaxed grains, interdendritic flow and grain sedimentation, interaction between the columnar dendrites and equiaxed grains (CET & ECT). Additionally, the macroscopic transport phenomena (i.e., the transport of mass, momentum, enthalpy, and species) and the microscopic physical phenomena occurring at the interfacial scale (i.e., the mass transfer due to solidification, solute partitioning at the interface, release of latent heat, momentum exchange between phases) can be coupled [25]. Nevertheless, to make the model be applicable for the SCC process, some modifications and extensions to the model are also needed.

## 1.2 Objectives

The target of this thesis is to simulate and analyze the formation mechanism of as-cast structure and the accompanying macrosegregation in SCC of steel. A three-phase mixed columnar-equiaxed solidification model was used for this purpose. To allow the model to capture some important/key features of the SCC process, extensions and validations of the model are necessary.

- (1) Firstly, the multiphase model is extended to consider the following features: (a) fragmentation of the columnar dendrites, which served as one of the origins of the equiaxed grains; (b) remelting and destruction of the equiaxed grains; (c) coupling between the flow field and electromagnetic field.
- (2) Secondly, the extended model is validated by making the comparisons with the Sn-Pb experiments at the laboratory scale and the CC of billet strand at the industrial scale.
- (3) Finally, the well-developed numerical model is used to simulate the SCC of steel. Parameter studies are performed toward the optimization of the SCC process.

## 2. State of the art

### 2.1 Conventional steel casting technologies

#### 2.1.1 Ingot casting (IC)

The ingot casting (IC) route dominated the entire steel production until 1970s. The schematic of the typical IC process at Ovako Steel [26–27] is shown in Figure 2.1. The scrap is charged and melted in an electric arc furnace (EAF). The slag is then skimmed, and the produced melt is tapped into a ladle. After the procedures of deoxidation and alloying, the melt is poured into the vacuum degasser. After a time of heating and stirring, the steel is cast using uphill teeming. Actually, two ways of pouring methods can be performed in the mold filling, i.e., top pouring and bottom pouring (uphill teeming). However, the melt splash to the mold walls and produces surface defects on the ingot skin during the top pouring process, and the reoxidation products and mold power can be entrapped into the bulk. It makes the top pouring method unable to reach the requirements of high-quality steel production. Hence, the bottom pouring method, which can reduce the exposure of melt to air and entrapment of mold power, is preferred [28].

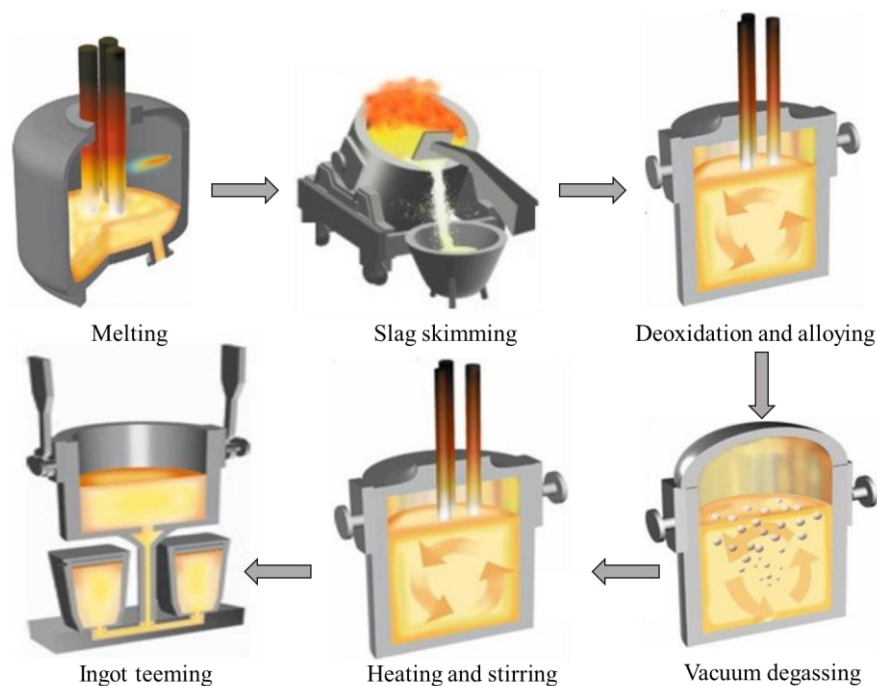
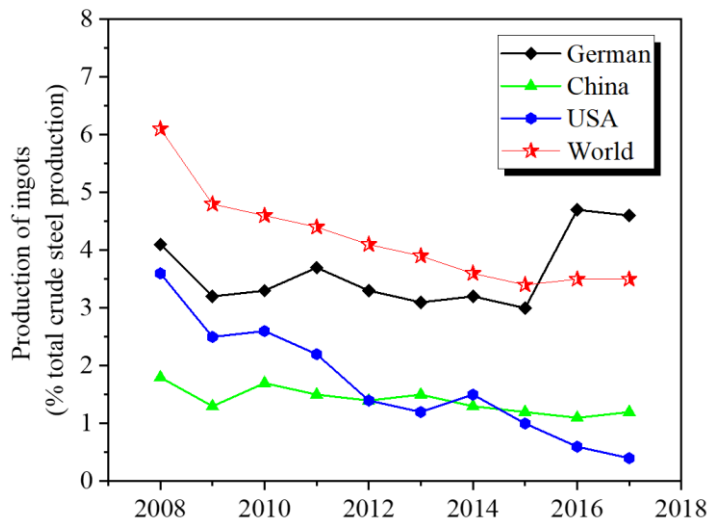


Figure 2.1. Schematic of the steelmaking process through IC route [26–27].

Since the CC method was proposed and fully developed in 1940s, the share of the steel production in the world through IC route has decreased to only 3.5 % in 2017 (Figure 2.2). The production of steel ingots was about 2.0 million metric tonnes in German, 10.0 million metric tonnes in China, 0.3 million metric tonnes in United States, and 59.0 million metric tonnes in the world [29]. However, for some low-alloy steel grade and steel for special applications with large format, i.e., shafts for engines and drives, turbine blades, bearing steel and heavy forging [30–31], they can currently just be produced via IC route.



**Figure 2.2.** Production of steel ingots (in percentage) in German, China, USA, and in the world [29] from 2008 to 2017.

When the hot melt is poured into the casting mold, the chilling effect of the mold produces a solidified shell (chill zone) with the refined grains. The mold temperature is increased during the pouring process, which will decrease the cooling effect consequently. The orientation of the temperature gradient causes the grains to grow perpendicularly to the mold wall. The columnar zone is then formed. Under the effect of the interdendritic flow, fragmentation could be generated and grow to the equiaxed grains in the mushy zone. On the other hand, the inoculants entrapped in the bulk provide the nucleation site for the equiaxed grains. Once the undercooled condition is reached, the inoculants will be activated as nuclei of the equiaxed grains. Due to the density difference between the equiaxed grains and melt, the grains tend to sediment to the ingot bottom. The appearance of the columnar-to-equiaxed transient (CET) could happen under two different mechanisms: 1) hard blocking [32], i.e., the volume fraction of the equiaxed grains ahead of the columnar dendrites is large enough to inhibit the growth of the columnar dendrites; 2) soft blocking [33], i.e., the solute rejected



during the solidification of equiaxed grains is sufficiently enriched to stop the growth of the columnar tip front. The schematic pattern of the as-cast structure of a 65-ton ingot [34] is shown in Figure 2.3(a). The columnar dendrites distribute in the outer side near the surface, and globular equiaxed grains accumulate in the center from the bottom up to 75% of the ingot height. On the top of the ingot, the equiaxed grains revealed in the form of dendrite. Different types of macrosegregation in the ingot are displayed in Figure 2.3(a). In the columnar zone, the distribution of the composition is relatively uniform (nearly equal to nominal concentration). The negative segregation is observed in the lower part of the ingot due to the accumulation of the equiaxed grains, and serious positive segregation is found in the upper dendritic equiaxed zone. Additionally, two types of channel segregations (A-segregation and V-segregation) are also found in the ingot and will impair the quality of the products (Figure 2.3(b)).

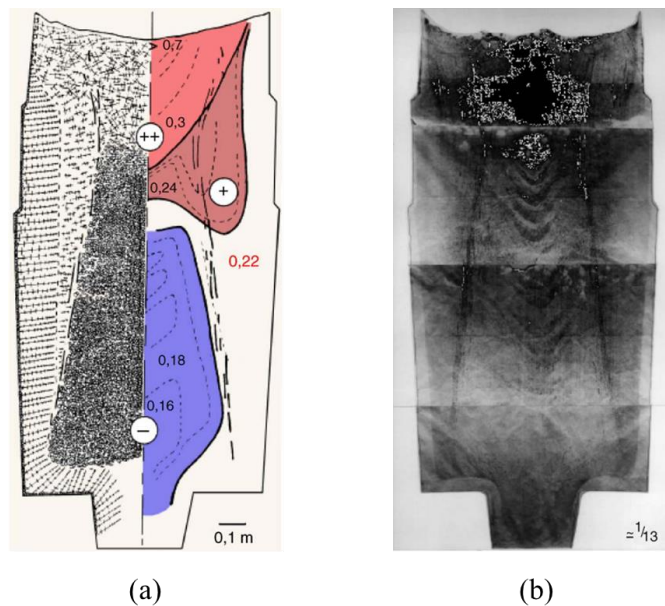


**Figure 2.3.** Structural and compositional analysis on the longitudinal section of a 65-ton steel ingot: (a) various type of the macrostructure as well as the carbon macrosegregation; (b) sulphur print [34].

In addition to the macrosegregation, the shrinkage defects also impair the ingot quality. Two main shrinkage defects are confirmed, i.e., macroscopic shrinkage cavity, and micro porosity [35]. The former one is mainly formed in the top ingot region during the late stage of the solidification. Due to the increase of the melt density with the decrease of the temperature, the accumulated volume solidification shrinkage and the shrinkage causes the sink of the melt level, which causes the macroscopic shrinkage cavity. The micro porosity is usually

observed in the center of the ingot, the insufficient feeding flow together with the so-called “bridging” phenomenon will create the micro porosity. The thermal-field based criterion, i.e., Niyama criterion [36], is a well-known effective method to predict such micro porosity. Based on this criterion and its extensions, two common commercial software, i.e., ProCAST [37–42] and MAGMASOFT [43–45], are widely used to predict the appearance of the porosity. With the extension of this criterion by considering the morphology of the mush zone and its permeability, the Carlson-Beckermann-Niyama (CBN) criterion [46] is used to qualitatively evaluate the micro shrinkage porosity. The main limitation of the method is that it can only predict the occurrence possibility of the porosity in the columnar zone, and might not apply for those in the equiaxed zone.

To reduce or eliminate the porosity defect of the ingot, the liquid melt in the top region should maintain a good fluidity to feed the shrinkage during the solidification process. It can be realized by using the insulation powder covering and/or hot top. Specially, the hot top should be reasonably designed. The height and shape of the hot top impact the solidification characteristics significantly [47–50]. One example of a 100-ton 30Cr2Ni4MoV forging ingot [47–48] is displayed in Figure 2.4. The shrinkage porosities can be greatly reduced after improving the ingot design.

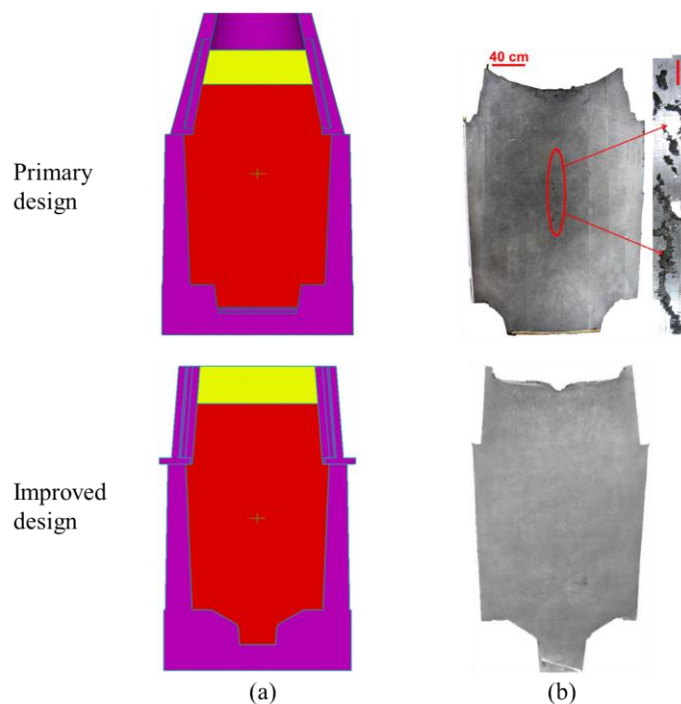


**Figure 2.4.** Comparisons of the quality of a 30Cr2Ni4MoV forging ingot between two different designs [47–48]. (a) Primary and improved designs; (b) metallographic analyses.

## 2.1.2 Continuous casting (CC)

The idea of the CC of lead and other soft metals can date back to 1843. Laing [51] invented an apparatus that can continuously produce lead pipe. Then, the trial manufacture of iron sheets was proposed by Bessemer [52] in 1846. But until the 1930s, the CC just became a common method for the production of nonferrous metals. Since the relatively lower thermal conductivity and higher casting (pouring) temperature of the steel, many accompanying problems needed to be solved during the CC of steel. It was not until the 1960s that the CC method rapidly developed in the process of steel production [53–54]. From the 1970s, the CC has obtained undisputed dominance over the IC and became the most popular casting method. It has the advantage of high productivity and strand quality. In 2017, about 96.2 % of the total crude steel in the world (Figure 2.2) is made through the CC route [29].

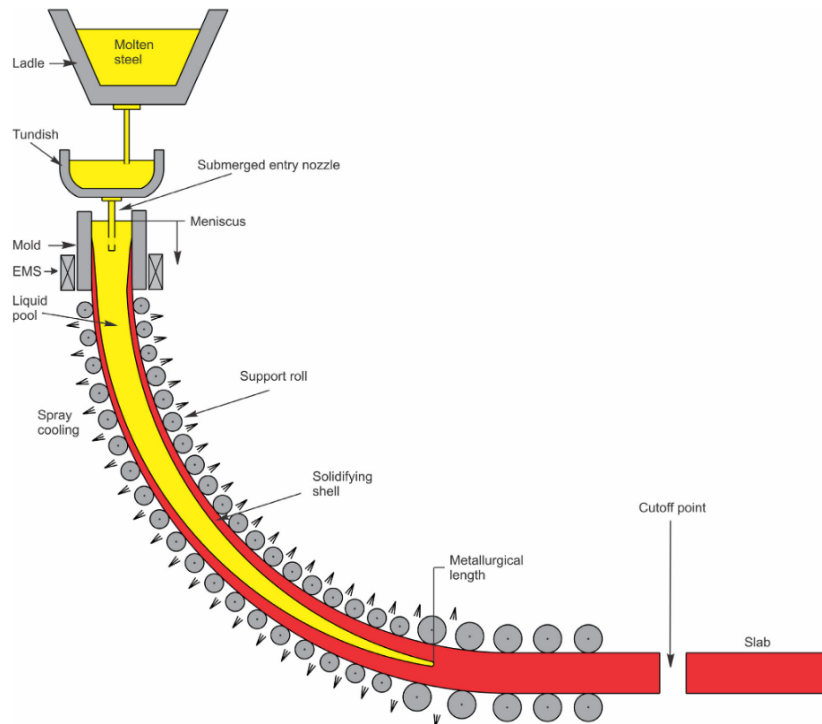


**Figure 2.5.** Schematic of the continuous casting process [55].

Schematic of the CC process is shown in Figure 2.5 [55]. After the primary and secondary steelmaking processes, a ladle which contains the steel melt is transferred to the CC machine. When the operation starts, the melt flows to the tundish from bottom of the ladle. The impurities and slag are filtered in the tundish before they flow into the mold. Through the submerged entry nozzle, the melt is poured into one mold or several molds. The

mold is usually made of the copper (high heat conductivity) and accompanied by the water-cooled and oscillating systems. Under the intensive cooling effect of mold, a solidified shell first forms in the melt and mold interface and progressively develops during the later withdrawing process. To avoid the breakout, the solidified shell at the mold exit must be strong/thick enough to hold the liquid melt (ferrostatic pressure). Below the mold, the strand is continuously cooled by the spray water (secondary cooling) and spray air [56–57]. Additionally, the semi-solid strand is supported by many rolls to reduce the bulging effect of the shell. At the end of the machine, the strand is cut off by the oxyacetylene torch.

### 2.1.2.1 Types of continuous casting

According to the types of casters, the CC machine is normally divided into the following four different casters (Figure 2.6): 1) vertical caster; 2) vertical-bending caster; 3) bow-type caster and 4) horizontal caster. The first industrial CC caster for the production of steel was a simply vertical type. A relatively symmetric macrostructure and good surface quality could be obtained through this method. However, the productivity or yield is severely limited by the machine height. Additionally, the risk of bulging increases as the machine height increases. Thus, the vertical-bending caster and bow-type caster were proposed to reduce the investment cost. The objective of these two casters is to conduct the CC machine with a less space. The casting speed could also be increased correspondingly. However, the non-metallic inclusions are easily entrapped into the inner arc of the solidified shell when they are floating up. In addition, it is also possible to cause inner and surface cracks during the bending and straightening processes. The horizontal caster has a lower investment cost because all the machines are on the same level, and they have good conjunction with some other manufacturing processes. But this type of caster is mainly used to produce the nonferrous alloy, and it is not widely used for steel. Although the bow-type caster with curved mold is the most widely used machine today, the strands with large format, especially the slabs, are normally produced via vertical-bending caster due to the growing need for the cleanness [54].

According to the cross-section format of the products, the CC strand is divided to billet, bloom and slab. The product which has a smaller dimension ( $< 200 \times 200 \text{ mm}^2$ ) is normally called billet, and the product which has a big rectangular section (width 1000–2000 mm, thickness 100–200 mm) is called slab. The product between them is named as bloom.

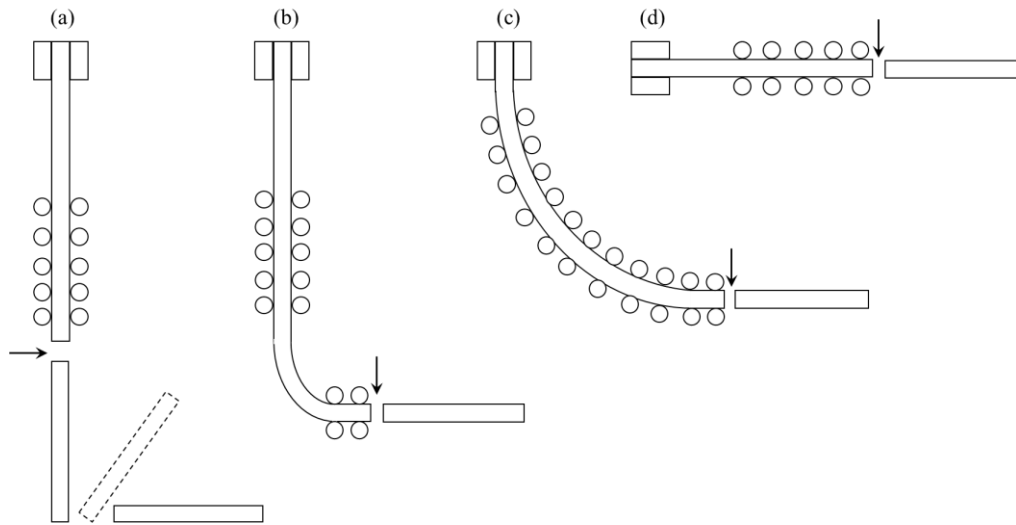


**Figure 2.6.** Schematic of the four different casters. (a) Vertical caster; (b) vertical-bending caster; (c) bow-type caster; (d) horizontal caster.

### 2.1.2.2 Electromagnetic stirring for CC

It is acknowledged that the fluid flow and movement of the solid grains play an important role in the formation of the as-cast structure and macrosegregation. A well-controlled flow field is confirmed to greatly improve the strand quality of the continuous casting. Electromagnetic stirring (EMS) serves as a nonintrusive stirring manner, and it has been widely used to control the fluid flow, impede the growth of the columnar dendrites, promote the formation of equiaxed grains, improve the surface and subsurface quality, and reduce or even eliminate the centerline segregation and porosity [58-70].

The principle of the EMS is simple, when an alternating magnetic field ( $\vec{B}$ ) is applied to a conductive material, an electric current ( $\vec{J}$ ) is induced in the conductor. The interaction of the magnetic field and induced electric current produces the Lorentz force ( $\vec{F}$ ) in the conductor, and if the conductor is a fluid, it will be forced to move in response to the Lorentz force imposed in its body [71].

According to the manner of the Lorentz force, the EMS can be categorized as the rotational stirrer and linear stirrer (Figure 2.7), the former one (Figure 2.7(a)) applies mostly to the billet and bloom strand [58–59, 62, 64, 72], while the later one (Figure 2.7(b)) is normally implemented in the slab [60, 73]. The rotational stirrer is more likely to be the stator of an electric motor, while the liquid pool inside of the solidified shell is similar to the rotor

of the motor [74]. It is usually powered by a three-phase or sometimes a two-phase alternating current. The generated alternating magnetic field rotates around the strand with a specific frequency ( $f$ ). The melt inside of the solidified shell rotates consequently and the main component of the liquid velocity locates in the azimuthal direction. A so-called primary flow is formed. The maximal liquid velocity appears at the center of the stirrer due to the biggest Lorentz force being applied there. A vertical pressure gradient is then formed, and the melt will be forced to flow upward (and downward) along the solidification front and returns to the stirrer along the center of the strand. A so-called secondary flow is formed, and it plays an important role in the heat and mass transfer processes.

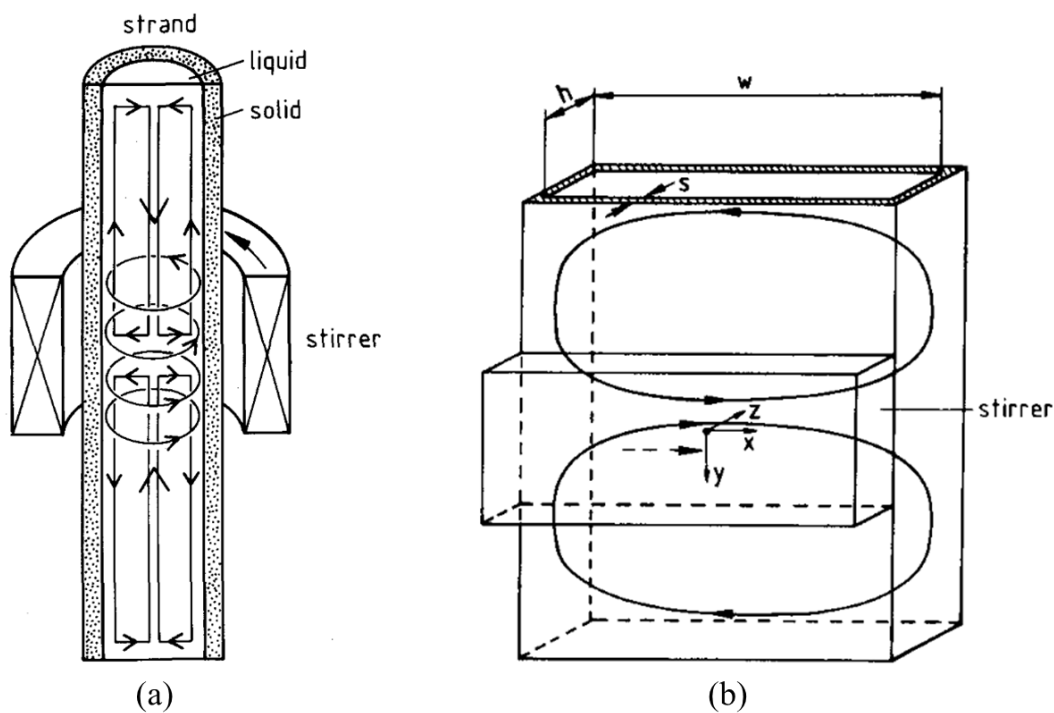


**Figure 2.7.** Types of EMS based on the manner of Lorentz force. (a) Rotational stirrer [64]; (b) linear stirrer [73].

The linear stirrer is principally similar to the linear motor, and it is always placed in the wide wall of the strand or mold [75–80]. According to the arrangement direction of the current coils, the stirrer can create the Lorentz force in the horizontal or vertical direction. A so-called “butterfly” flow pattern is formed in the melt when the horizontal Lorentz force is applied [75], and the extension of this flow is mainly limited by the strand width. Thus, to increase the extension of this type of flow, multi-stage EMS is normally used.

Specifically, three different moving fields can be generated in the mold region by a couple of linear stirrers [79]. As shown in Figure 2.8, four stirrers are installed in the mold region with two on each wide face (Figure 2.8(a)). When the magnetic field travels in the same direction as the jet flow (Figure 2.8(b)), the flow velocity will be accelerated, and this type of magnetic mode is referred to as Electromagnetic Level Accelerator (EMLA). When the magnetic field travels in the opposite direction as the jet flow (Figure 2.8(c)), the flow velocity will be slowed, and this type of magnetic mode is referred to as Electromagnetic Level Stabilizer (EMLS). For the last one (Figure 2.8(d)), the magnetic field travels in the same direction over one wide face but in opposite direction on the other wide face. The melt then rotates in the horizontal section under the effect of Electromagnetic Rotating Stirrer (EMRS). Although the flow pattern in the melt is similar to the primary flow generated by the rotational stirrer (Figure 2.7(a)), the extension of this flow is limited and mainly distributed in the stirrer region [75].

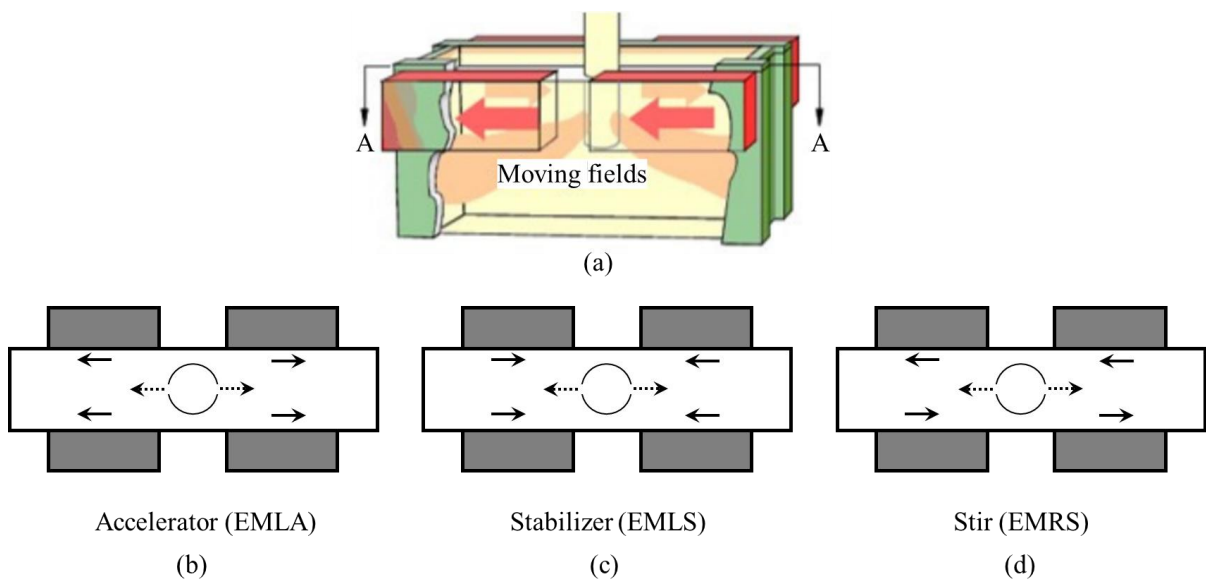


**Figure 2.8.** Types of moving magnetic fields with linear stirrer [79]. (a) Schematic of the installation of the magnetic field generator. (b) Electromagnetic Level Accelerator (EMLA); (c) Electromagnetic Level Stabilizer (EMLS); (d) Electromagnetic Rotating Stirrer (EMRS).

According to the installation position of the stirrer (Figure 2.9), the EMS is categorized as the mold-EMS (M-EMS), strand-EMS (S-EMS) and final-EMS (F-EMS). As its name implies, M-EMS is normally installed in the mold region, S-EMS is implemented in the secondary cooling zone, and F-EMS is applied in the final solidification region of the strand [62].

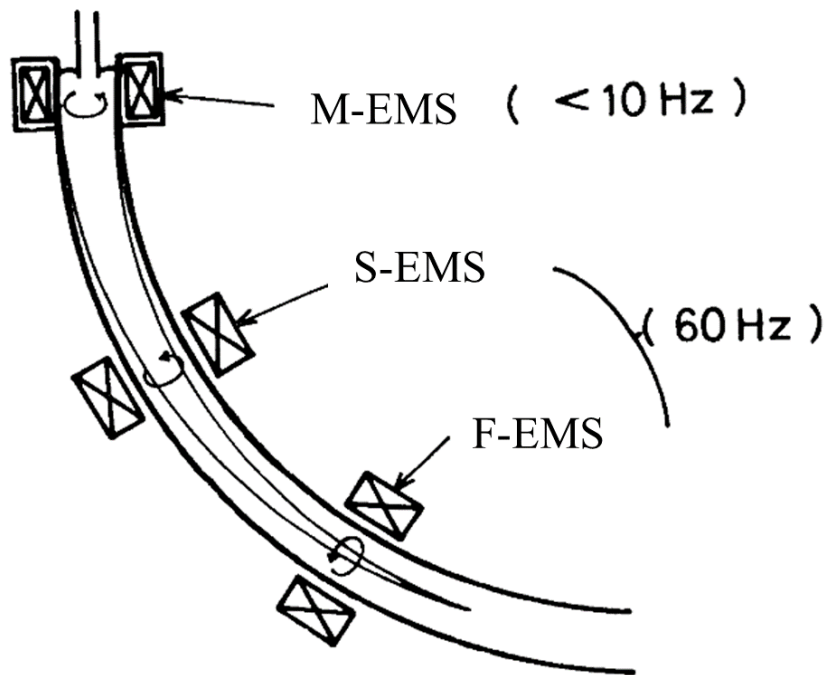
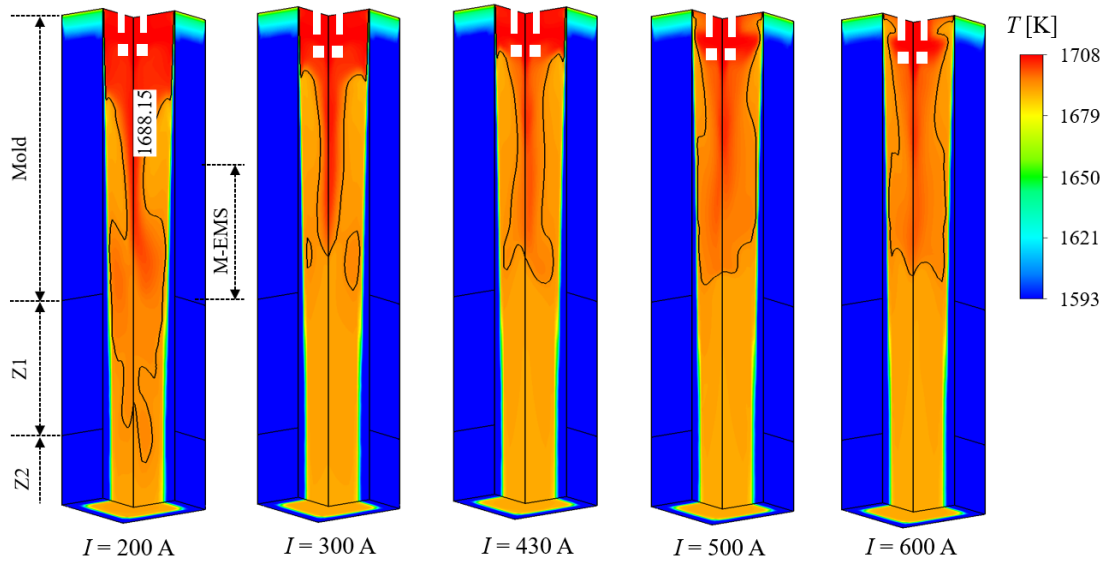


Figure 2.9. Types of the EMS based on the installation position [62].

Although the invention and implementation of the M-EMS is later than the S-EMS, the high efficiency of this technique in improving the surface and inner quality, and promoting the formation of equiaxed grains attracted more attentions on itself. It is acknowledged that the M-EMS plays an important role in promoting the superheat dissipation in the strand [62, 67, 81–86] through the M-EMS-induced primary and secondary flows. As shown in Figure 2.10, the superheated zone coming from the SEN is shifted upward significantly as increasing the current intensity of the M-EMS [18]. In addition to being a cooler, another important role of M-EMS is to promote the formation of equiaxed grains through the fragmentation mechanism [87]. The fragments tend to grow and convert to the equiaxed grains in the undercooled melt. Thus, the central equiaxed grain zone can be increased evidently with the application of M-EMS [62, 88–92]. As shown in Figure 2.11, the developed equiaxed grains in the center of the strand is beneficial to decrease or eliminate the central porosity and reduce the center segregation [66, 81, 90–91, 93–94]. However, it was also reported that the M-EMS alone cannot efficiently reduce the mean value of the center segregation [62], especially for the low and high carbon steel, thus, a combined stirring mode, i.e., M+F-EMS or M+S+F-EMS, is preferred.





**Figure 2.10.** Influence of the M-EMS current intensity on the temperature distribution of a steel billet (195 mm × 195 mm). The liquidus isoline (1688.15 K) is overlaid with the temperature contour on the vertical symmetry planes [18].

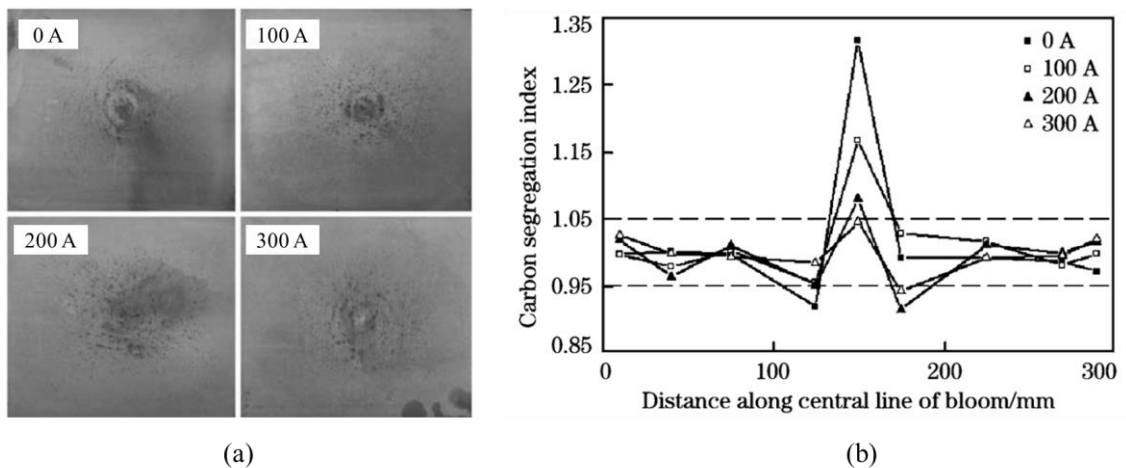


**Figure 2.11.** Effect of current intensity of M-EMS on the as-cast structure (a), and center segregation (b) of the steel bloom (260 mm × 300 mm) [82].

A primary magnetic field is generated in the space by activating the alternating current (AC) in the stirrer. When the alternating primary magnetic field penetrates into the copper mold, the eddy current is generated, and it mostly distributes in the outer side of the electrically conductive material (“skin effect”). A secondary magnetic field is then created by the eddy current and has the opposite direction with the changing direction of the primary magnetic field (Figure 2.12(a)). The efficiency of the M-EMS in rotating the melt is then reduced somehow. To weaken the shielding effect of the copper mold, the frequency of the AC should be determined reasonably. There is an optimum frequency to get the maximal

torque or force ( $F \propto B^2 f$ ), and it has a correlation with the copper mold thickness and the strand section size. As shown in Figure 2.12(b), the optimum frequency is decreased as increasing the mold thickness and the section size of the strand [75]. Recently, a new method to reduce the shielding effect of the copper mold of the steel bloom was proposed by placing the insulating layers in the mold [95]. It was reported that the combined (vertical and dual transverse) insulating layers can effectively weaken the shielding effect of copper mold.

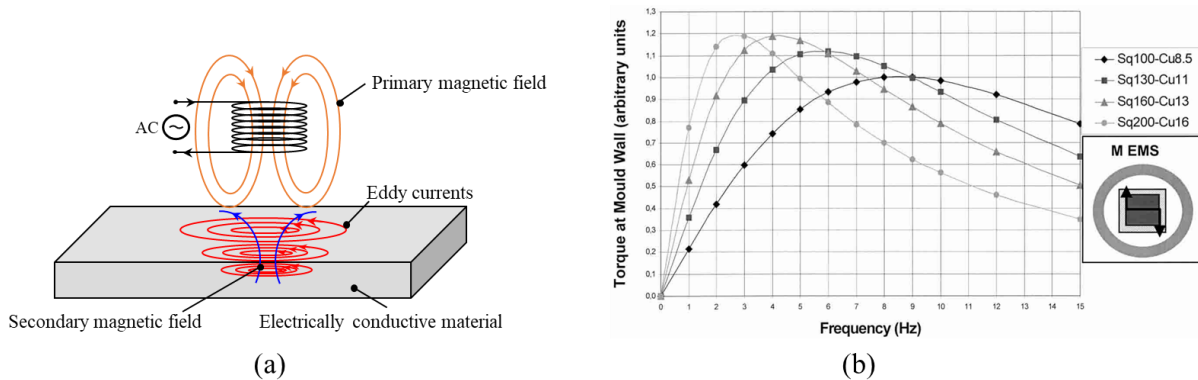


**Figure 2.12.** Shielding effect of copper mold. (a) Schematic of the skin effect generated in the electrically conductive material (copper mold); (b) relation of the torque at mold inner wall with the billet section and mold thickness [75].

S-EMS was initially invented to improve the as-cast structure of the strand by inhibiting the growth of columnar dendrites and promoting the formation of equiaxed grains [62, 96–97]. However, the negative segregation (“white band”) formed in the S-EMS operating area [59, 97–98] inhibits the further development of this technique. As shown in Figure 2.13, the effect of S-EMS on the formation of the “white band” of a steel billet (127 mm × 127 mm) under different shell thickness at the stirrer position are experimentally studied [98]. Compared to the casting without S-EMS, the “white band” defects are obviously observed on the cross-section of the strand once the stirrer is applied, and the position of the “white band” is closely depended on the shell thickness at the stirrer position. Additionally, the efficiency in promoting the generation of equiaxed grains and decreasing the center porosity of S-EMS is far behind M-EMS (Figure 2.14) [62]. Thus, the S-EMS is normally used as combined stirring mode.

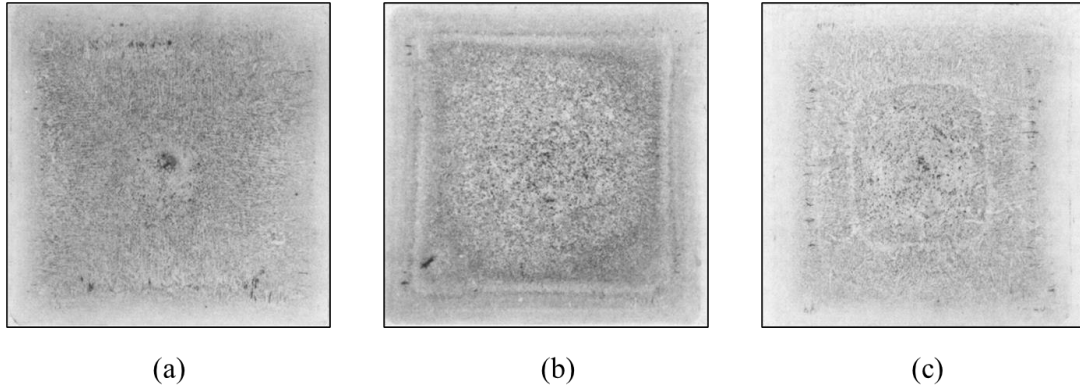


**Figure 2.13.** Sulfur prints showing the effect of S-EMS on the formation of the “white band” of a steel billet (127 mm × 127 mm) under different shell thickness at the stirrer [98]. (a) Without stirrer; (b) stirrer at the position when the shell thickness is 18 mm; (c) stirrer at the position when the shell thickness is 36 mm.

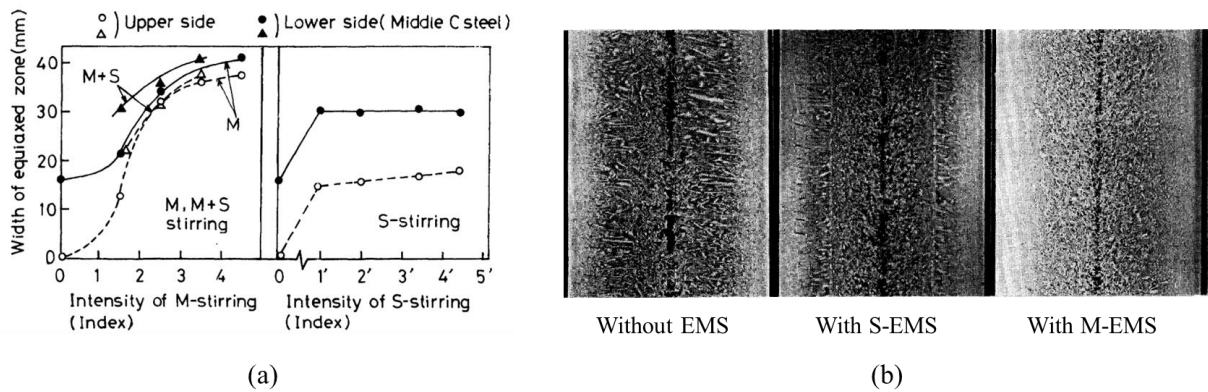


**Figure 2.14.** Comparisons of the efficiencies of creating the equiaxed zone and decreasing the central porosity between M-EMS and S-EMS of a steel billet (125 mm × 125 mm) [62].

F-EMS is usually placed at the final solidification area of the strand to eliminate the center porosity problem and reduce the ratio of the center carbon segregation [99–101]. Due to the well-developed solid shell and its self-shielding effect on the magnetic field, the current intensity and frequency of F-EMS is generally larger than that of M-EMS. However, the equiaxed zone is found to be less sensitive to the F-EMS intensity. As displayed in Figure 2.15, the effects of F-EMS intensity on equiaxed zone and central porosity of a steel bloom (510 mm × 390 mm) were experimentally investigated. The equiaxed zone ratio just stays in the range of 25.3% – 25.8% with different current intensity. Nevertheless, the central porosity defect could be significantly reduced by the F-EMS, i.e., the large central porosities are replaced by numerous of fined spots [91].

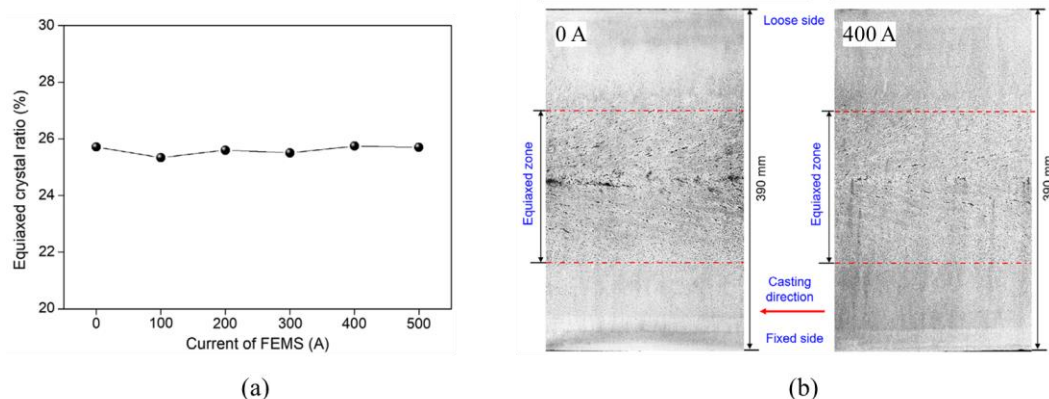


**Figure 2.15.** Effect of F-EMS intensity on the equiaxed zone (a), and central porosity (b) of a steel bloom (510 mm × 390 mm) [91].

As shown in Table 1, the effect of EMS systems on the quality of continuous casting billets are compared in terms of surface cracks, center porosity, center segregation and so on. The full combined mode, M+S+F-EMS, is found to be most powerful to improve the quality of the billets [102].

**Table 1.** Summary of the effect of EMS systems on the surface and macrostructure quality of steel billet [102].

EMS installation site	Effect of EMS systems on the surface and macrostructure quality of CCB								
	pin and skin holes	surface and subsurface cracks	point imperfection	reduced number of breakouts	crystalline structure and internal cracks	center porosity	center segregation	pipe segregation	V-shaped segregation
M-EMS	+++	+++	++	++	++	++	++	++	+
M+F-EMS	+++	+++	++	++	++	+++	+++	+++	+++
M+S+F-EMS	+++	+++	+++	++	+++	+++	+++	+++	+++
M+S-EMS	+++	+++	+++	++	++	++	++	++	++
S+F-EMS	-	-	++	-	+	++	+++	++	++
S-EMS	-	-	++	-	+	++	++	+	+
F-EMS	-	-	-	-	-	+	+	+	++

\* CCB: continuous casting billets.

Effect of EMS on billet quality: “-”, no effect; “+”, weak effect; “++”, moderate effect; “+++”, strong effect.

**Summary:** The two conventional technologies (IC and CC) are mature in producing steel. However, they still don’t work properly for high-quality rotor shafts or similar components of large formats because of their own limitations. New ideas or concepts are still demanded for producing high-quality steel components of large format.

## 2.2 Large vertical steel casting

Several new process concepts have been proposed to produce the steel components with large format, including vertical continuous casting (VCC), large ingot casting caster (LICC), segment casting (SC) and semi-continuous casting (SCC).

### 2.2.1 Vertical continuous casting (VCC)

Since the vertical continuous casting (VCC) is free from bending and straightening procedures, a relatively symmetric macrostructure and good surface quality could be obtained through this method. A VCC machine was built by Zhong Yuan Special Steel in 2015 to produce the steel strands with large format [11, 103]. As shown in Figure 2.16, the machine is constructed of concrete, the total height is 52 m with ground height 25 m and underground height 27 m. It is used to produce the heavy round blooms with diameters of 400 mm, 600 mm and even 800 mm. The height of the products ranges from 2.5 m to 6.0 m. The maximum casting speed is set as 0.4 m/min for the small bloom, and 0.1m/s for the large bloom, respectively. Multi-stage stirring (M-EMS, S-EMS, F-EMS) can be implemented along the strand to improve the inner and surface quality of the products [104–108].

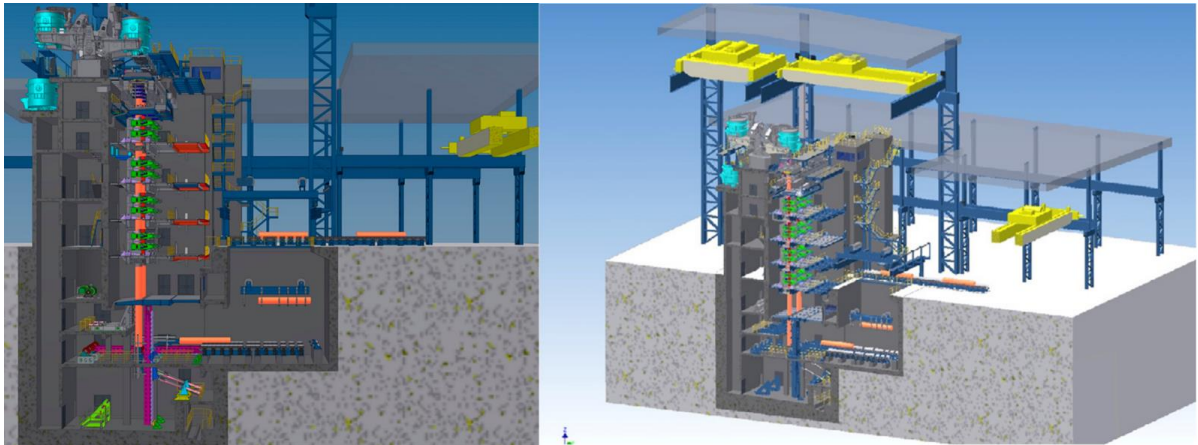
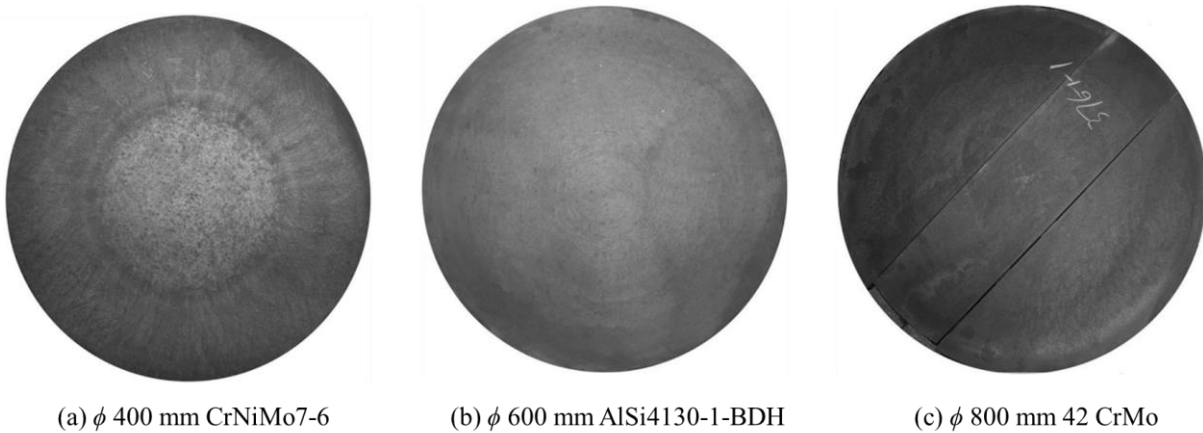


Figure 2.16. Schematic of the large vertical continuous casting [11, 103].

Typical as-cast structure of the steel for different formats and alloys through the procedure of VCC are shown in Figure 2.17. A good inner structure was obtained for the small-section low-alloy steel (Figure 2.17(a)), but the central porosity is still an annoying problem that needs to be solved. The grain structures have been improved for large sections and higher alloy steel (Figure 2.17(b)–(c)). However, some parameter studies need to be

further conducted to reduce the surface cracks, central segregation and central cracks for the medium-high-alloy steel.



**Figure 2.17.** Typical as-cast structure of the steel for different sections and alloys through the procedure of vertical continuous casting [11].

### 2.2.2 Large ingot casting caster (LICC)

To obtain higher yield/productivity and improve the quality of extra-large sections and high alloy steel strand, a concept of large ingot casting caster (LICC) was proposed by POSCO in 2007 [109–110]. Schematic views of the LICC pilot caster and casting process are shown in Figure 2.18. The LICC process is divided into three stages, i.e., casting, solidification and finishing. The first stage is similar to that of CC, the casting is withdrawn vertically from the water-cooled copper mold. The solid shell is formed, and the semi-solid strand is run out of the mold along with the dummy bar. Then, at the end of the withdrawing process (the target height of the strand is achieved), no more fresh melt is poured into the mold through the SEN, and the strand moves downwards and stops at a certain distance below the mold. It then stands vertically till the end of the solidification. The top heating and stirrer techniques could be applied during this period to improve the quality of the strand. When the strand is fully solidified, it is then placed horizontally to the tilter for the later procedures. Since the procedure of the LICC is actually semi-continuous, the yield of the strand is relatively lower than that of the CC, which should be improved consequently.

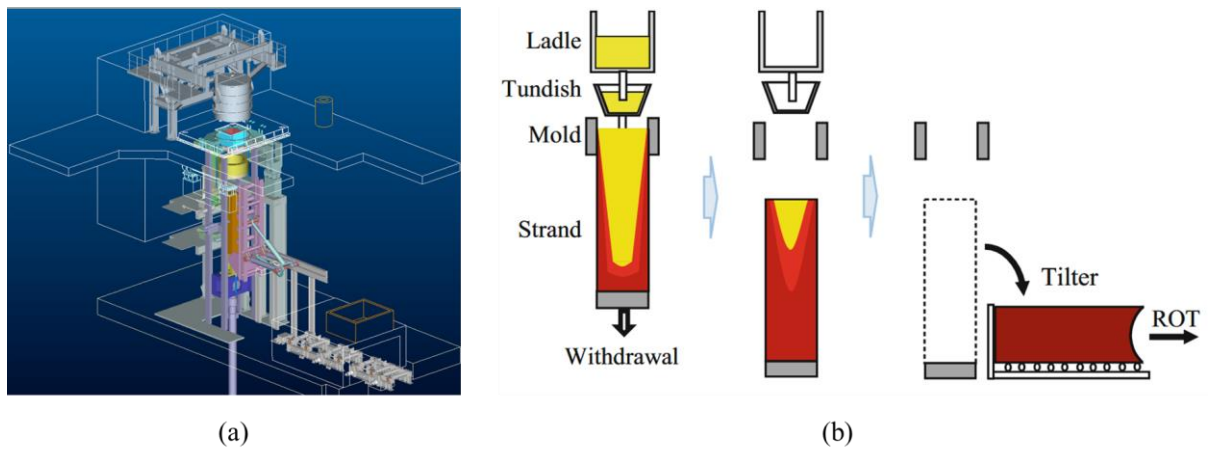


**Figure 2.18.** Schematic of the LICC pilot caster (a) [109] and casting process (b) [110].

Compared to the ingot casting, the strand produced through the LICC process have a better inner as-cast structure. As shown in Figure 2.19(a), the refined global equiaxed grains is observed in the inner part of the LICC bloom [109]. Additionally, the equiaxed zone is enlarged compared to that of the IC. During the casting process, M-EMS is applied to promote the formation of equiaxed grains and accelerate the superheat dissipation. Near the end of the casting process, the M-EMS moves with the strand and keeps its position at the upper part of the strand till the end of the solidification. Together with the top heating technique, the shrinkage pipe at the top of the strand is effectively reduced (Figure 2.19(b)), i.e., the length of the pipe is decreased by 77%.

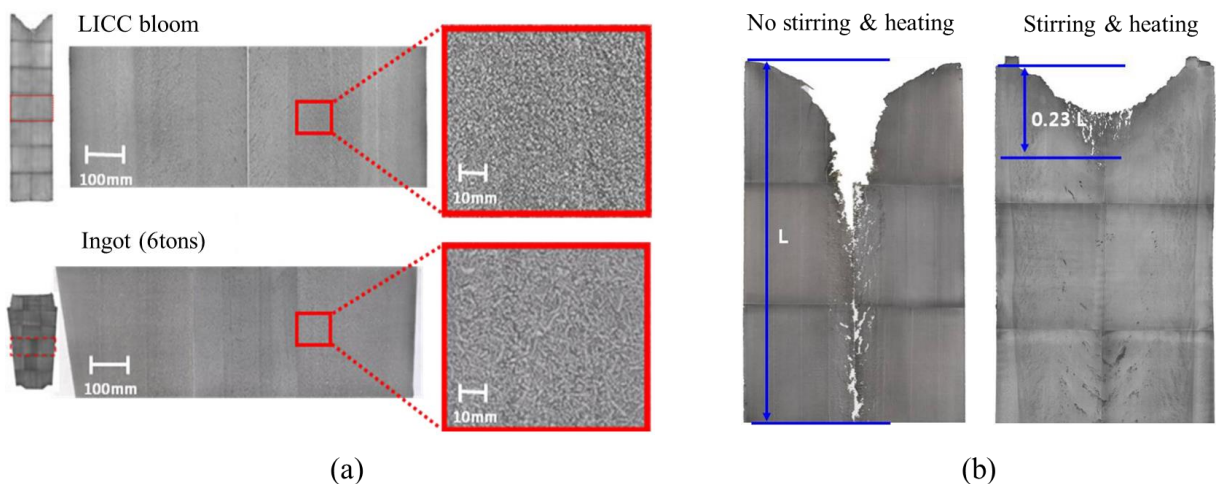


**Figure 2.19.** (a) Comparison of the as-cast structure between the LICC bloom (700 mm × 700 mm) and ingot (6-ton). (b) Effect of the EMS and top heating techniques on the formation of the shrinkage pipe at the top region of the LICC strand [109].

The central porosity, central segregation and channel segregations (A-segregation and V-segregation) are the defects which is harmful to the strand quality. It is found that the EMS in one direction tends to deteriorate the internal soundness of the LICC strand. Thus, a periodically alternating stirring is proposed. As shown in Figure 2.20, this type of the stirring mode is proved to significantly reduce the central porosity (or mini-ingots) and the macrosegregation.

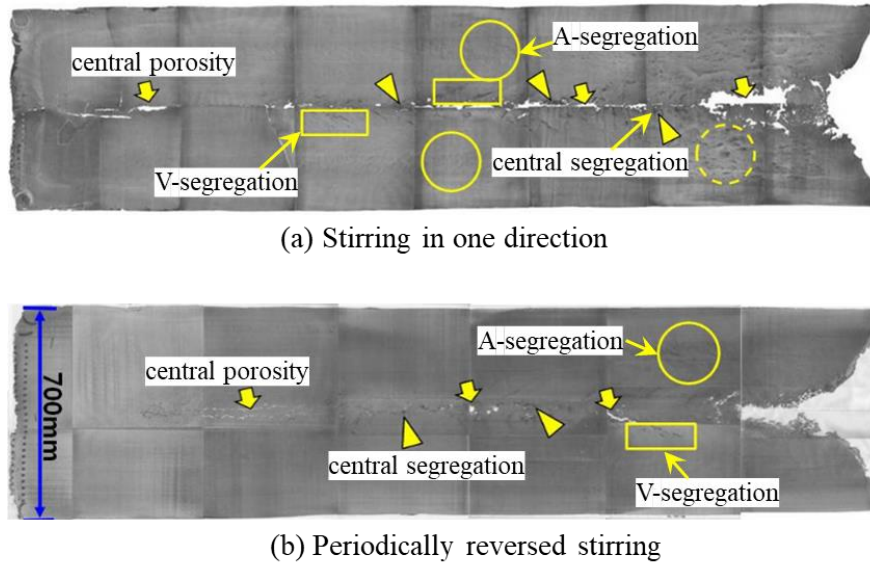


**Figure 2.20.** Effect of the stirring manner on the formation of the macrosegregation and central porosity of the LICC strand [109].

### 2.2.3 Segment casting (SC)

A concept of segment casting (SC) was proposed by INTECO Melting and Casting Technologies GmbH [2, 111] to produce the medium and high-alloyed steel grades with large formats. Schematic views of the caster layout and casting process are displayed in Figure 2.21. The whole process is divided into two phases, casting and solidification. The casting process is similar to the standard continuous casting process, and the strand is withdrawn in a fully vertical manner. M-EMS is applied to promote the formation of equiaxed grains and reduce the central porosity/segregation. When the strand is withdrawn to the target length (7 ~ 14 m), the casting phase is terminated, which marks the start of the solidification phase. During this period, the strand will not be moved any further, and M-EMS and S-EMS are applied. Additionally, the hot-topping powered by a patented induction heating technology is



arranged at the top region of the strand to reduce shrinkage pipe. The format of the strand can reach 1500 mm in diameter and 14 m in height.

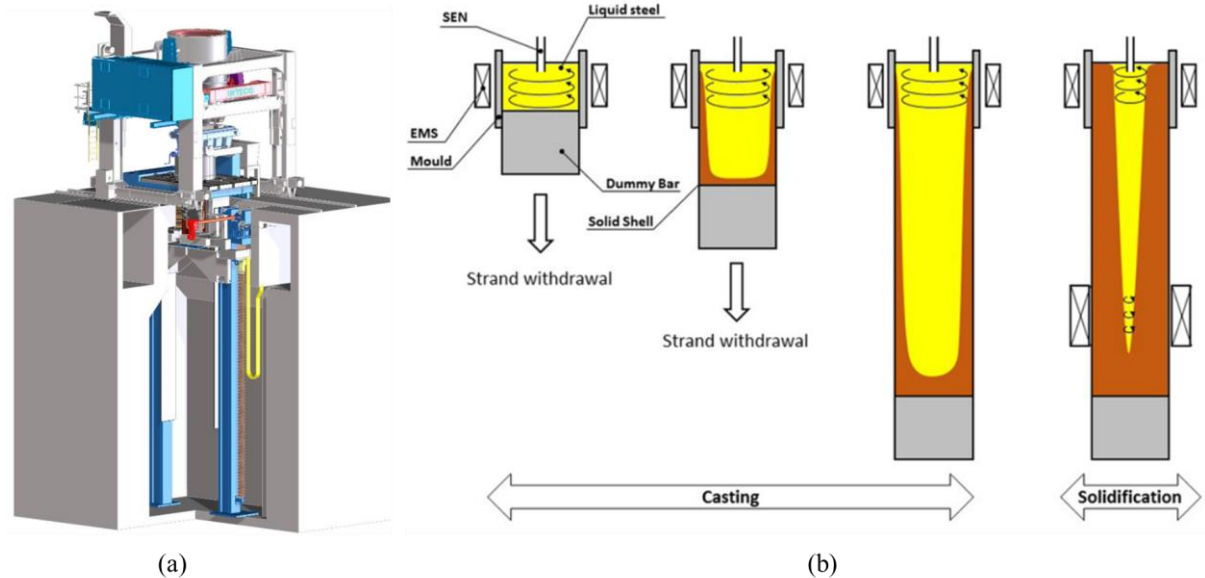


**Figure 2.21.** Schematic views of the segment casting (SC) caster layout (a) [111] and casting process (b) [2].

Compared to the IC, the SC is also a more promising technique in producing the electrode for the electroslag remelting (ESR) process. As shown in Table 2, the ingot length, quality, and yield are greatly improved by the SC procedure. Beneficial from the lower cost and shorter mould, the investment in the SC process could also be reduced remarkably.

**Table 2.** Comparison between conventional IC and SC for electroslag remelting (ESR) electrode production [111].

	Conventional ingot casting	Segment Casting
Process type	Batch	Batch
Investment	Low	Moderate
Possible ingot length	~5 m	~14 m and more
Ingot quality	Good	Better
Yield (liquid in ladle to useable material)	Up to ~87%	Up to ~95%
<i>For use as ESR-electrode:</i>		
Number of electrode changes per ingot	Up to 6	0–1 possible
Costs for electrode preparation	High (up to 7 stub weldings)	Low (1–2 stub weldings)

## 2.2.4 Semi-continuous casting (SCC)

Semi-continuous casting (SCC), which intend to combine the advantages of IC and CC, has been widely used to produce the non-ferrous alloys (e.g., copper and aluminum) [112–120]. However, due to the low thermal conductivity and high pouring temperature of the steel,

it is still challenging to apply this technology to produce the steel strand. Recently, a new SCC technology was proposed by Primetals Technologies Austria GmbH [1, 3] to produce the steel strand with large section. Schematic views of the caster and SCC process are shown in Figure 2.22. Two steps are included in the process, i.e., casting and final cooling. First, the casting is withdrawn downwards, and the solid shell, which is sufficient to withstand the inner ferrostatic pressure, is quickly formed in the water-cooled copper mold and secondary cooling zone. Below the secondary cooling zone, a static or dynamic shielding system is arranged to slow down the solidification speed of the inner strand. When the casting is withdrawn to an expected length, the stand, together with the shielding system, is moved aside for the final solidification, and the mold is ready for producing the next bloom, which guarantee the high yield. Hot-topping is then arranged at the top of the strand to reduce the defect of shrinkage porosity. In addition, the S-EMS could be also applied to promote the formation of the equiaxed grains and reduce the central segregation. This new technology can be used to produce the single blooms, especially rounds from  $\phi$  300 mm to  $\phi$  1500 mm at a length up to 12 m [1].

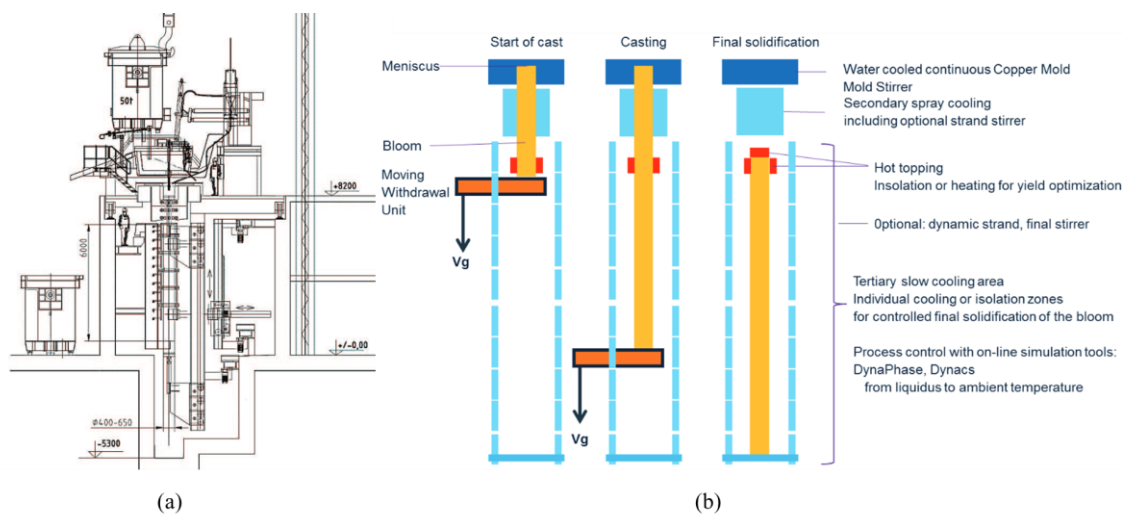


**Figure 2.22.** Design of a SCC caster (a) and schematic of the SCC process (b) [1].

**Summary:** Due to the critical process parameters are yet determined, none of the proposed new processes for large vertical steel casting (VCC, LICC, SC and SCC) are optimally put in operation. They are still in their trial period. Thus, it is particularly necessary to optimize the process parameters with the aid of numerical models.

## 2.3 Modelling

### 2.3.1 Multiphase solidification model

Due to the harsh environment of the field trials, it is difficult to observe the solidification process and get a better understanding of the fundamental behaviours during the casting process. Therefore, the numerical modelling, which has been significantly developed in recent years, could be treated as an alternative and effective tool for this purpose owing to their obvious advantages of high flexibility and low costs. Numerous numerical models were proposed and utilized to investigate the solidification phenomena during the casting process, i.e., mixture continuum model [4–10], cellular automata finite elements (CAFE) method [11–15], cellular automata – finite volume method (CA-FVM) [16] etc. However, one must be conscious of the inherently multiphase and multiscale nature of the solidification phenomena. Most such models are limited by the computational capacity (hardware), so that they can only be applied to investigate the solidification process of the limited length scale. The volume-averaged (VA) method, which is based on the Euler-Euler approach, has been proposed [121–123] and been greatly developed [124–140]. It is now becoming one of the most promising models for simulation of the solidification process of the engineering scale.

Principally, the macroscopic conservation equations of each phase (melt, equiaxed grains, columnar dendrites, gas, etc.) can be derived by averaging the microscopic equations over a specific volume  $V_0$ . This volume must be smaller than the system domain and larger than the characteristic size of the interfacial structures [121]. A representative volume including two phases (k and j) is shown in Figure 2.23. The volumes of both phases are  $V_k$  and  $V_j$ , and their volume fractions are  $f_k$  and  $f_j$ , with  $f_k + f_j = 1.0$ . It is assumed that the solid phase (k) is treated as a pseudo-fluid. The velocities of both phases are  $\bar{u}_k$  and  $\bar{u}_j$ . Specially, the velocity of k-j interface ( $\bar{u}_k^{\text{int}}$ ) is a sum of two parts, i.e.,  $\bar{u}_k^{\text{int}} = \bar{v}_k^{\text{int}} + \bar{u}_k$ , where  $\bar{v}_k^{\text{int}}$  is the growth velocity of the k-j interface due to solidification or remelting, and  $\bar{u}_k$  is the moving velocity of the k-interface [131].

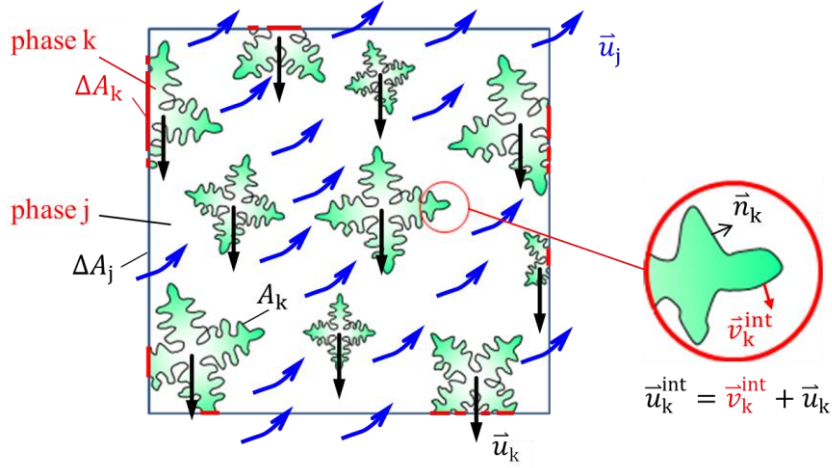


**Figure 2.23.** A representative volume  $V_0$ , which includes two phases, k and j. The velocity of each phase is  $\bar{u}_k$  and  $\bar{u}_j$ , respectively. The volumes of both phases are  $V_k$  and  $V_j$ , and their volume fractions are  $f_k$  and  $f_j$ , with  $f_k + f_j = 1.0$ . The total k-j interface area being enclosed in the volume element is  $A_k$ , while the k-phase border area being enveloped by the volume element (red) is  $\Delta A_k$  [131].

The transport equations for mass, momentum, energy, species, etc., at the microscopic scale can be expressed by a general form

$$\frac{\partial \psi}{\partial t} + \nabla \cdot (\psi \bar{u}) = -\nabla \cdot (\bar{\Phi}) + \psi \dot{\psi}, \quad (1)$$

where  $\psi$  is the volume-weighted quality,  $\bar{u}$  is the velocity,  $\bar{\Phi}$  is the diffusive flux terms,  $\psi \dot{\psi}$  is the source term. By making the volume averaging operation  $\langle \cdot \rangle^{V_0}$  of Equation (1) over the representation volume  $V_0$ , the transport equations at the macroscopic scale can be derived as

$$\left\langle \frac{\partial \psi}{\partial t} \right\rangle^{V_0} + \langle \nabla \cdot (\psi \bar{u}) \rangle^{V_0} = -\langle \nabla \cdot (\bar{\Phi}) \rangle^{V_0} + \langle \psi \dot{\psi} \rangle^{V_0}. \quad (2)$$

It is noted that the volume average of a variable  $\psi_k$  of the phase k over the volume  $V_0$  is

$\langle \psi_k \rangle^{V_0} = \frac{1}{V_0} \int_{V_k} \psi_k dV$ , and the intrinsic volume average of the variable  $\psi_k$  of the phase k is

written by  $\langle \psi_k \rangle^{V_k} = \frac{1}{V_k} \int_{V_k} \psi_k dV$ .

The relation between these two quantities is  $\langle \psi_k \rangle^{V_0} = f_k \cdot \langle \psi_k \rangle^{V_k}$ . Thus, the macroscopic transport equation of the phase k can be written as

$$\frac{\partial}{\partial t} \left( f_k \langle \psi_k \rangle^{V_k} \right) + \nabla \cdot \left( f_k \langle \psi_k \rangle^{V_k} \langle \bar{u}_k \rangle^{V_k} \right) = -\nabla \cdot \left( f_k \langle \bar{\Phi}_k \rangle^{V_k} + f_k \langle \bar{\Phi}_k^d \rangle^{V_k} \right) + \psi_k^M + \psi_k^D + f_k \langle \dot{\psi} \rangle^{V_k}, \quad (3)$$

where  $\langle \bar{\Phi}_k^d \rangle^{V_k}$  is the dispersive flux term,  $\psi_k^M$  is the exchange term due to the phase transition, and  $\psi_k^D$  is the exchange term due to the diffusive/viscous stress transfer.

Specially, the physical quantities ( $\xi$ ) are normally defined as mass-weighted ones, i.e.,  $\psi = \rho \xi$ . Therefore, the Equation (3) can be simplified and written as

$$\frac{\partial}{\partial t} (f_k \rho_k \xi_k) + \nabla \cdot (f_k \rho_k \xi_k \bar{u}_k) = -\nabla \cdot \left( f_k (\bar{\Phi}_k + \bar{\Phi}_k^d) \right) + \psi_k^M + \psi_k^D + f_k \dot{\psi}_k \quad (4)$$

As a reference, a three-phase volume-average solidification model, which was proposed by Wu et al. [126–127], are presented here. Some necessary extensions are considered. Three phases are included: liquid melt ( $\ell$ ), equiaxed grains ( $e$ ) and columnar dendrites ( $c$ ). Both the liquid melt and equiaxed grains are treated as moving phases, for which the macroscopic transport equations are solved to obtain the liquid velocity ( $\bar{u}_\ell$ ) and equiaxed velocity ( $\bar{u}_e$ ). Simple morphologies are assumed for the two solid phases: stepwise cylinders for columnar trunks and spheres for equiaxed grains. To address the drag force and other hydrodynamic interactions between phases, an equiaxed grain envelop ( $f_e^{\text{env}}$ ) is considered for equiaxed grains. The volume ratio of the solid “dendrite” to the dendritic envelop is defined as  $f_{si}$  ( $= f_e / f_e^{\text{env}}$ ). The solidification of both solid phases is based on a diffusion-governed growth kinetic. A so-called effective equiaxed viscosity ( $\mu_e$ ), is used to treat the interaction between the equiaxed grains [124]. The heterogeneous nucleation [124, 141] and fragmentation [142–143] are considered as the origin of the equiaxed grains. When the grains are exposed into the superheated region, they will be remelted and further destroyed [144]. The position of the columnar tip front is traced dynamically based on the Lipton-Glicksman-Kurz (LGK) model [145]. The macroscopic conservation equations about the transport of the mass, momentum, heat, and species can be seen in Table 3. The corresponding source terms of the interphase transfer are listed in Table 4.

**Table 3.** Macroscopic transport equations of the three-phase solidification model.

1. Mass conservations:

$$\frac{\partial}{\partial t}(f_\ell \rho_\ell) + \nabla \cdot (f_\ell \rho_\ell \bar{u}_\ell) = -M_{\ell c} - M_{\ell e} \quad (5)$$

$$\frac{\partial}{\partial t}(f_c \rho_c) + \nabla \cdot (f_c \rho_c \bar{u}_c) = M_{\ell c} + M_{ce} \quad (6)$$

$$\frac{\partial}{\partial t}(f_c \rho_c) = M_{\ell c} - M_{ce} \quad (7)$$

2. Momentum conservations:

$$\frac{\partial}{\partial t}(f_\ell \rho_\ell \bar{u}_\ell) + \nabla \cdot (f_\ell \rho_\ell \bar{u}_\ell \otimes \bar{u}_\ell) = -f_\ell \nabla p + \nabla \cdot \bar{\tau}_\ell + f_\ell \rho_\ell \bar{g}'_\ell + f_\ell \bar{F}'_\ell - \bar{U}_{\ell c} - \bar{U}_{\ell e} \quad (8)$$

with  $\bar{\tau}_\ell = \mu_\ell f_\ell (\nabla \otimes u_\ell + (\nabla \otimes u_\ell)^T)$ ,  $\bar{g}'_\ell = \frac{\rho_\ell^b(T_\ell, c_\ell) - \rho_\ell^{\text{ref}}}{\rho_\ell^{\text{ref}}} \bar{g}$ ,  $\rho_\ell^b(T_\ell, c_\ell) = \rho_\ell^{\text{ref}} (1 + \beta_T \cdot (T^{\text{ref}} - T_\ell) + \beta_C \cdot (c^{\text{ref}} - c_\ell))$

$$\frac{\partial}{\partial t}(f_c \rho_c \bar{u}_c) + \nabla \cdot (f_c \rho_c \bar{u}_c \otimes \bar{u}_c) = -f_c \nabla p + \nabla \cdot \bar{\tau}_c + f_c \rho_c \bar{g} + f_c \bar{F}'_c + \bar{U}_{\ell c} + \bar{U}_{ce} \quad (9)$$

with  $\bar{\tau}_c = \mu_c f_c (\nabla \otimes u_c + (\nabla \otimes u_c)^T)$

3. Enthalpy conservations:

$$\frac{\partial}{\partial t}(f_\ell \rho_\ell h_\ell) + \nabla \cdot (f_\ell \rho_\ell \bar{u}_\ell h_\ell) = \nabla \cdot (f_\ell k_\ell \nabla \cdot T_\ell) + f_\ell (Q_{\ell c}^M + Q_{\ell e}^M) - Q_{\ell c}^D - Q_{\ell e}^D \quad (10)$$

$$\frac{\partial}{\partial t}(f_c \rho_c h_c) + \nabla \cdot (f_c \rho_c \bar{u}_c h_c) = \nabla \cdot (f_c k_c \nabla \cdot T_c) + f_c (Q_{\ell c}^M + Q_{\ell e}^M) + Q_{\ell c}^D + Q_{ce}^D \quad (11)$$

$$\frac{\partial}{\partial t}(f_c \rho_c h_c) = \nabla \cdot (f_c k_c \nabla \cdot T_c) + f_c (Q_{\ell c}^M + Q_{\ell e}^M) + Q_{\ell c}^D - Q_{ce}^D \quad (12)$$

4. Species conservations:

$$\frac{\partial}{\partial t}(f_\ell \rho_\ell c_\ell) + \nabla \cdot (f_\ell \rho_\ell \bar{u}_\ell c_\ell) = \nabla \cdot (f_\ell \rho_\ell D_\ell \nabla c_\ell) - C_{\ell e} - C_{\ell c} \quad (13)$$

$$\frac{\partial}{\partial t}(f_c \rho_c c_c) + \nabla \cdot (f_c \rho_c \bar{u}_c c_c) = \nabla \cdot (f_c \rho_c D_c \nabla c_c) + C_{\ell e} + C_{ce} \quad (14)$$

$$\frac{\partial}{\partial t}(f_c \rho_c c_c) = \nabla \cdot (f_c \rho_c D_c \nabla c_c) + C_{\ell c} - C_{ce} \quad (15)$$

5. Equiaxed grains and inoculant

$$\frac{\partial}{\partial t} n_e + \nabla \cdot (\bar{u}_e n_e) = N_{\text{nu}} + N_{\text{frag}} + N_{\text{des}} \quad (16)$$

$$\frac{\partial}{\partial t} n_{\text{in}} + \nabla \cdot (\bar{u}_\ell n_{\text{in}}) = -N_{\text{nu}} - N_{\text{des}} \quad (17)$$

**Table 4.** Interphase transfer terms and source terms of the macroscopic transport equations.

1. Mass transfer

$$M_{\ell c} = v_{\text{Req}} \cdot (n_c \cdot \pi d_c^2) \cdot \rho_c \cdot \Phi_{\text{imp}}^c \quad (18)$$

$$\text{with } \begin{cases} v_{\text{Req}} = \frac{D_\ell}{R_{\text{eq}}(1 - R_{\text{eq}}/R_{\ell c})} \cdot \frac{(c_\ell^* - c_\ell)}{(c_\ell^* - c_c^*)} + \frac{2D_c}{R_{\text{eq}}} \cdot \frac{c_c^* - c_c}{c_\ell^* - c_c^*}, \Phi_{\text{imp}}^c = f_\ell & \text{for solidification} \\ v_{\text{Req}} = \frac{D_\ell}{R_{\text{eq}}/(1 + 0.6 \cdot \text{Sc}^{1/3} \cdot \text{Re}^{1/2})} \cdot \frac{(c_\ell^* - c_\ell)}{(c_\ell^* - c_c)} , \text{Sc} = \mu_\ell / \rho_\ell D_\ell, \text{Re} = d_c \rho_\ell |\bar{u}_\ell - \bar{u}_c| / \mu_\ell, \Phi_{\text{imp}}^c = 1 & \text{for re-melting} \end{cases}$$

$$M_{\ell c} = \begin{cases} v_{\text{Rc}} \cdot (\pi d_c / \lambda_1^2) \cdot \rho_c \cdot \Phi_{\text{imp}}^c & \text{for columnar trunk without primary tips} \\ [v_{\text{Rc}} \cdot (\pi d_c \cdot l) + v_{\text{tip}} \cdot (\pi R_{\text{tip}}^2)] \cdot n_c \cdot \rho_c \cdot \Phi_{\text{imp}}^c & \text{for columnar trunk with primary tips} \end{cases} \quad (19)$$

$$\text{with } v_{\text{Rc}} = \frac{D_\ell}{R_c} \cdot \frac{c_\ell^* - c_\ell}{c_\ell^* - c_c^*} \cdot \ln^{-1} \left( \frac{R_{\ell c}}{R_c} \right) + \frac{2D_c}{R_c} \cdot \frac{c_c^* - c_c}{c_\ell^* - c_c^*}, \Phi_{\text{imp}}^c = \begin{cases} 1 & d_c \leq \lambda_1 \\ 4f_\ell / (4 - \pi) & d_c > \lambda_1 \end{cases}$$

$$M_{\text{cc}} = -\gamma \cdot (\bar{u}_\ell - \bar{u}_c) \cdot \nabla c_\ell \cdot \rho_c \quad \text{fragmentation} \quad (20)$$

2. Momentum transfer

$$\bar{U}_{\ell c} = \begin{cases} \bar{u}_\ell \cdot M_{\ell c} + K_{\ell c} (\bar{u}_\ell - \bar{u}_c) & \text{for solidification} \\ \bar{u}_c \cdot M_{\ell c} + K_{\ell c} (\bar{u}_\ell - \bar{u}_c) & \text{for re-melting} \end{cases} \quad (21)$$

$$\text{with } K_{\ell c} = \begin{cases} 180 \mu_\ell \frac{f_c^2}{f_\ell d_c^2} & (f_c \leq 0.637) \\ \mu_\ell \frac{f_\ell^2}{K}, K = \frac{d_c^2}{180} \cdot \frac{f_\ell^3}{f_c^2} & (f_c > 0.637) \end{cases}$$

$$\bar{U}_{\ell c} = \begin{cases} \bar{u}_\ell \cdot M_{\ell c} + K_{\ell c} (\bar{u}_\ell - \bar{u}_c) & \text{for solidification} \\ \bar{u}_c \cdot M_{\ell c} + K_{\ell c} (\bar{u}_\ell - \bar{u}_c) & \text{for re-melting} \end{cases} \quad (22)$$

$$\text{with } K_{\ell c} = 6 \times 10^{-4} \lambda_1^2 \frac{f_\ell^3}{(1 - f_\ell)^2}$$

$$\bar{U}_{\text{cc}} = \bar{u}_c \cdot M_{\text{cc}} + K_{\text{cc}} (\bar{u}_c - \bar{u}_\ell) \quad \text{fragmentation} \quad (23)$$

$$\text{with } K_{\text{cc}} = \begin{cases} \infty & (f_c \geq 0.2) \\ 0 & (f_c < 0.2) \end{cases}$$

3. Energy transfer

$$Q_{\ell c}^{\text{M}} = (h_\ell - h_c) \cdot M_{\ell c} \quad (24)$$

$$Q_{\ell c}^{\text{D}} = H^* (T_\ell - T_c) \quad (25)$$

$$Q_{\ell c}^{\text{M}} = (h_\ell - h_c) \cdot M_{\ell c} \quad (26)$$

$$Q_{\ell c}^{\text{D}} = H^* (T_\ell - T_c) \quad (27)$$

$$Q_{\text{cc}}^{\text{D}} = H^* (T_c - T_\ell) \quad (28)$$

---


$$\text{with } h_\ell = \int_{T_{\text{ref}}}^{T_\ell} c_p^\ell dT + h_\ell^{\text{ref}}, \quad h_e = \int_{T_{\text{ref}}}^{T_e} c_p^e dT + h_e^{\text{ref}}, \quad h_c = \int_{T_{\text{ref}}}^{T_c} c_p^c dT + h_c^{\text{ref}}, \quad H^* = 10^9 \text{ W} \cdot \text{m}^{-3} \cdot \text{K}^{-1}.$$


---

#### 4. Species transfer

$$C_{\ell e} = \begin{cases} k \cdot c_\ell^* \cdot M_{\ell e} & \text{solidification} \\ c_e \cdot M_{\ell e} & \text{re-melting} \end{cases} \quad (29)$$

$$C_{\ell c} = \begin{cases} k \cdot c_\ell^* \cdot M_{\ell c} & \text{solidification} \\ c_c \cdot M_{\ell c} & \text{re-melting} \end{cases} \quad (30)$$

$$C_{ce} = c_c \cdot M_{ce} \quad \text{fragmentation} \quad (31)$$


---

#### 5. Source and sink terms for equiaxed grains and inoculants

$$N_{\text{nu}} = \frac{D(\Delta T)}{Dt} \cdot \frac{dn_e}{d(\Delta T)} \quad (32)$$

$$\text{with } \frac{D(\Delta T)}{Dt} = \frac{\partial(\Delta T)}{\partial t} + m \cdot \vec{u}_\ell \cdot \nabla c_\ell - \vec{u}_\ell \cdot \nabla T_\ell, \quad \frac{dn_e}{d(\Delta T)} = \frac{n_{\text{in}}}{\sqrt{2\pi} \cdot \Delta T_\sigma} \cdot e^{-\frac{1}{2} \left( \frac{\Delta T - \Delta T_k}{\Delta T_\sigma} \right)^2}.$$

$$N_{\text{frag}} = \frac{M_{ce}}{\rho_c \cdot \frac{\pi}{6} (d_{e,\text{frag}}^0)^3} \quad (33)$$

$$\text{with } d_{e,\text{frag}}^0 = \lambda_2 \cdot f_c.$$

$$N_{\text{des}} = v_{\text{Req}} \cdot \left. \frac{d(n_e)}{d(x)} \right|_{x=d_{e,\text{critical}}} \quad (34)$$

$$\text{with } \frac{d(n_e)}{d(x)} = \frac{n_e}{\sqrt{2\pi} \cdot \sigma \cdot x} \cdot e^{-\frac{1}{2} \left( \frac{\ln(x) - \ln(d_e)}{\sigma} \right)^2}.$$


---

### 2.3.2 Computational magnetohydrodynamic methods

In order to study and understand the effect of the electromagnetic field during solidification, many computational magnetohydrodynamic (MHD) methods were proposed. Three different methods are described in this section and the characteristics of each method are discussed.

#### 2.3.2.1 Analytical (theoretical) approach

With the assumptions that: 1) the electromagnetic field is in its steady state, and 2) the solid shell thickness is negligible. The electromagnetic force (Lorentz force) in the radius direction ( $\vec{F}_r$ ) is expressed as [64, 146–149]



$$\bar{F}_r = -\frac{1}{8} \sigma^2 r^3 B_0^2 \omega_B^2 \mu_0 \left(1 - \frac{u_0}{\omega_B r}\right)^2 \bar{e} \quad , \quad (35)$$

where  $\sigma$  is the electromagnetic conductivity of the melt,  $r$  is the radial coordinate,  $B_0$  is the external magnetic field intensity,  $\omega_B$  is the angular speed of the magnetic field,  $\mu_0$  is the vacuum magnetic permeability,  $u_0$  is the azimuthal velocity magnitude of the melt, and  $\bar{e}$  is the unit vector.

The Lorentz force in the azimuthal direction is written as

$$\bar{F}_\theta = \frac{1}{2} \sigma r B_0^2 \omega_B \left(1 - \frac{u_0}{\omega_B r}\right) \bar{e} \quad . \quad (36)$$

In this method, the  $B_0$  and  $\omega_B$  must be known in advance, and the relative motion between the magnetic field and liquid melt is considered by using a factor of  $\left(1 - \frac{u_0}{\omega_B r}\right)$ .

However, due to the ignorance of the eddy effect of this simplified approach, it is not adapted to the situation of high frequency magnetic fields. Additionally, this method can only be used for axis symmetrical system.

### 2.3.2.2 CFD (Computational fluid dynamic)-MHD coupled method

Rigorously, the electromagnetic field and fluid field should be well coupled to precisely calculate the solidification process. ANSYS Fluent commercial software provides an add-on MHD module [150–152] to consider the interaction between the magnetic field and flow field. The coupling scheme is on the basis of two fundamental effects: a) the induction of electric current due to the movement of the magnetic field in the conducting materials; 2) the effect of the Lorentz force caused by the interaction of the induced current and the magnetic field. Generally, the Maxwell's equations can be written as

$$\nabla \cdot \bar{E} = \frac{q}{\epsilon_0} \quad , \quad (37)$$

$$\nabla \cdot \bar{B} = 0 \quad , \quad (38)$$

$$\nabla \times \vec{E} = -\frac{\partial \vec{B}}{\partial t}, \quad (39)$$

$$\nabla \times \vec{B} = \mu \left( \vec{J} + \varepsilon_0 \frac{\partial \vec{E}}{\partial t} \right), \quad (40)$$

where  $\vec{E}$  is the electric field,  $q$  is the electric charge density,  $\varepsilon_0$  is the vacuum permittivity,  $\vec{B}$  is the magnetic field,  $t$  is the time,  $\mu$  ( $=\mu_0\mu_r$ ) is the magnetic permeability,  $\mu_r$  is the relative magnetic permeability,  $\vec{J}$  is the current density. For some sufficiently conducting materials (i.e., metals), the  $q$  and the displacement current  $\varepsilon_0 \frac{\partial \vec{E}}{\partial t}$  can be neglected. Based on the Ohm's law, the  $\vec{J}$  is a function of

$$\vec{J} = \sigma \vec{E}. \quad (41)$$

If the materials (melt) flow in a velocity of  $\vec{u}$ , the Equation (41) can be adapted as

$$\vec{J} = \sigma(\vec{E} + \vec{u} \times \vec{B}) \quad (42)$$

By converging the Equation (40) and Equation (42) for the sufficiently conducting materials, the induction equation can be written as

$$\frac{\partial \vec{B}}{\partial t} = \frac{1}{\mu\sigma} \nabla^2 \vec{B} + \nabla \times (\vec{u} \times \vec{B}), \quad (43)$$

or in the form of

$$\frac{\partial \vec{B}}{\partial t} + (\vec{u} \cdot \nabla) \vec{B} = \frac{1}{\mu\sigma} \nabla^2 \vec{B} + (\vec{B} \cdot \nabla) \vec{u}. \quad (44)$$

It is noted that the  $\vec{B}$  is composed of two terms,  $\vec{B} = \vec{B}_0 + \vec{b}$ . Similar to the analytical method, the external magnetic field  $\vec{B}_0$  should be given through the measurement data or by some other electromagnetic solver, e.g., ANSYS Maxwell. While the induced magnetic field  $\vec{b}$  can be calculated by solving User-Defined-Scalar (UDS) equations. Thus, the induction equation is adapted as

$$\frac{\partial \bar{b}}{\partial t} + (\bar{u} \cdot \nabla) \bar{b} = \frac{1}{\mu \sigma} \nabla^2 \bar{b} + ((\bar{B}_0 + \bar{b}) \cdot \nabla) \bar{u} - (\bar{u} \cdot \nabla) \bar{B}_0, \quad (45)$$

The current density  $\bar{J}$  is given by

$$\bar{J} = \frac{1}{\mu} \nabla \times (\bar{B}_0 + \bar{b}) \quad (46)$$

Finally, the Lorentz force is calculated by

$$\bar{F} = \bar{J} \times \bar{B} \quad (47)$$

Together with the generated Joule heat ( $Q = \frac{1}{\sigma} \int_{vol} \bar{J}^2 dV$ ), these two terms served as one

of the source terms in the momentum and energy conservation equations, respectively. The liquid melt will be driven to flow under the effect of Lorentz force. In turn, the  $\bar{b}$  is updated by the flow field ( $\bar{u}$ ). The coupling between  $\bar{B}$ ,  $\bar{u}$  and the temperature ( $T$ ) is automatically solved in the MHD solver. Therefore, a full coupling scheme between the magnetic field and flow field is achieved. However, due to the calculation is transient, thus, the time step must be small enough to resolve the rotation of the magnetic field. Additionally, this method is incompatible with the Euler-Euler multiphase approach. Therefore, the usage of this method is limited to single-phase flow.

### 2.3.2.3 Electromagnetic field – computational fluid dynamic (EM–CFD) iteration scheme

Instead of obtaining the Lorentz force by analytical solutions or by CFD solvers, some EM solvers (i.e., ANSYS Maxwell) is more capable and specially used for the calculation of the electromagnetic field. The time-averaged Lorentz force  $\bar{F}_L$  is written as

$$\bar{F}_L = \frac{1}{2} R_e (\bar{J} \times \bar{B}^*) \quad (48)$$

where  $R_e$  means the real part of a complex number,  $\bar{B}^*$  is the conjugate magnetic field. The  $\bar{F}_L$  is exported from the EM solves and then interpolate into the CFD solvers (i.e., ANSYS Fluent) for the later solidification calculations. Three different strategies are normally used for EM-CFD iteration scheme.

#### *a. EM-CFD coupling scheme without any modification and iteration*

Without any treatment of the time averaged Lorentz force, the  $\bar{F}_L$  is then directly added as a source term to the momentum conservation equation. The effect of flow field on the  $\bar{F}_L$  is ignored. Most recent studies on the continuous casting process adopted this method [153–159]. However, one must be aware of the  $\bar{F}_L$  decreases with the induced flow field, and the ignorance of this effect is only valid when the fluid angular speed ( $\omega_f$ ) is much smaller than the angular speed of the magnetic field ( $\omega_B$ ). Otherwise, it would lead to an overestimation of the flow field.

*b. One-way EM-CFD coupling scheme with modification*

Different from the first method, to consider the relative motion between the magnetic field and fluid flow, a modification of  $\bar{F}_L$  is made by considering a factor of  $(1 - \frac{u_\theta}{\omega_B r})$ , the modified Lorentz force ( $\bar{F}_L'$ ) is written as

$$\bar{F}_L' = \bar{F}_L \left( 1 - \frac{u_\theta}{\omega_B r} \right) \quad (49)$$

The  $\bar{F}_L'$  is then weighted by the corresponding phase volume fraction ( $f_l, f_e$ ) and then added as a source term to the momentum conservation equation for each phase (Equation (8), Equation (9)). Although the effect of flow field on the  $\bar{F}_L$  is considered, the full coupled scheme between the EM field and flow field is not realized. Thus, it is still treated as a decoupled method.

*c. EM-CFD iteration scheme*

To realize the full-coupling scheme, an iteration method is proposed to consider the flow-electromagnetic interaction. On the basis of method (b), after the fluid is induced to rotate under the effect of  $\bar{F}_L'$ , the averaged fluid rotating angular speed ( $\bar{\omega}_f$ ) is calculated

$$\bar{\omega}_f = \left( \int_0^R |\bar{u}_\theta| dr \right) / R^2, \quad (50)$$

where  $R$  is the radius of the sample. The effective frequency of the magnetic field ( $f_{\text{eff}}$ ) is derived as

$$f_{\text{eff}} = (\omega_B - \bar{\omega}_\ell) / 2\pi f, \quad (51)$$

where  $f$  is the original magnetic field frequency. The  $\bar{F}_L$  is then updated based on the  $f_{\text{eff}}$  in the next EM-CFD iteration procedure. The numbers of the iterations can be adjusted based on the accuracy requirements. However, the iteration procedure must be performed manually, and the fluid rotating angular speed ( $\omega_\ell$ ) is normally not uniform along the axis direction of the SCC strand. Thus, this EM-CFD iteration procedure cannot be fully applied in the SCC process.

**Summary:** The solidification model proposed by Wu et al. [126–127] is efficient in simulating the growth of the columnar dendrite, nucleation and growth of the equiaxed grains, movement of the equiaxed grains and their interaction with the columnar dendrites, etc. However, some further extensions, i.e., fragmentation, remelting/destruction of the equiaxed grains, CFD-MHD coupling, are still necessary to allow the model to capture some important/key features of the SCC process.



### 3. Summary of the Ph.D works

#### 3.1 Modeling mixed columnar-equiaxed solidification of Sn-10wt.% Pb alloy under different types of forced convection

To validate the three-phase solidification model [126–127], one benchmark experiment of Sn-10wt.% Pb alloy at the laboratory scale is selected. Based on the previously proposed solidification model, further extensions with improved approaches for fragmentation [142] and remelting/destruction [144] of equiaxed grains, were considered in this study. Detailed information refers to Paper 3 of Part II.

Followed by the experiments conducted by Hebditch [160], serious of experiments [161] on laboratory scale have been performed to investigate the formation of the as-cast structure and macrosegregation under different types of forced convection at the SIMAP Laboratory in Grenoble France. Schematic view of the experimental facility is shown in Figure 3.1(a), the experiment consists in solidifying a rectangular ingot (100 mm × 60 mm × 10 mm) of Sn-10 wt.% Pb alloy by using two lateral heat exchangers. The heating and cooling history of the two exchangers is demonstrated in Figure 3.1(b). A linear motor used to generate the travelling magnetic force (TMF) is placed 5 mm beneath the bottom wall of the sample. The current intensity of the three-phase alternative current (AC) is 8.5 A with a frequency of 50 Hz. Four different cases were conducted (Figure 3.1 (c)): without TMF (Case I); TMF in the same direction as natural convection (Case II); TMF in the opposite direction as natural convection (Case III); and TMF periodically reversed with respect to natural convection (Case IV).

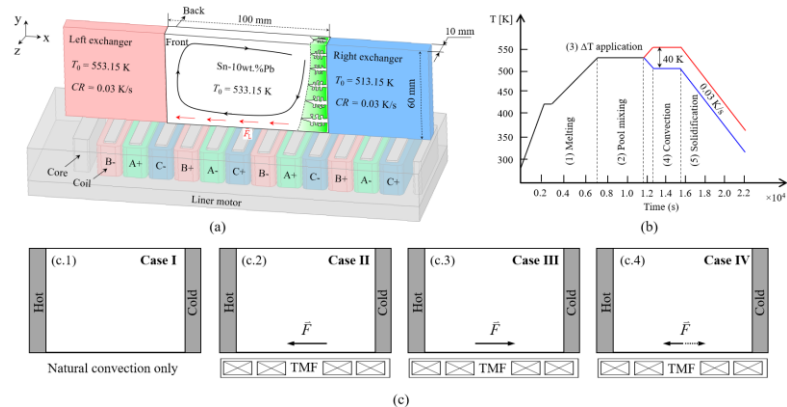


**Figure 3.1** (a) Schematic view of the experimental facility; (b) heating and cooling history of the two exchangers; (c) four different stirring modes.

The as-solidified sample was analyzed metallurgically and the as-cast structure of the four cases are displayed in Figures 3.2(a.x). The calculated distributions of  $f_c$  and  $f_e$  are shown in Figures 3.2(b.x) and Figures 3.2(c.x), respectively. Satisfactory simulation-experiment agreements are obtained for Case I, II, and IV, but not for Case III. The mismatch for Case III will be discussed later. For Case I, the upwind tilting of the columnar dendrites dominates the as-cast structure, and the equiaxed grains are mainly distributed in the left-top part of the sample. The enhanced flow convection (Case II) promotes the formation of the equiaxed grains (Figure 3.2(c.2)), and the growth of the columnar dendrites is inhibited (Figure 3.2(b.2)). For Case IV, the periodically reversed flow pattern further extends the equiaxed zone (Figure 3.2(c.4)), and the columnar dendrites are facilitated in the two right-hand corners (Figure 3.2(b.4)).

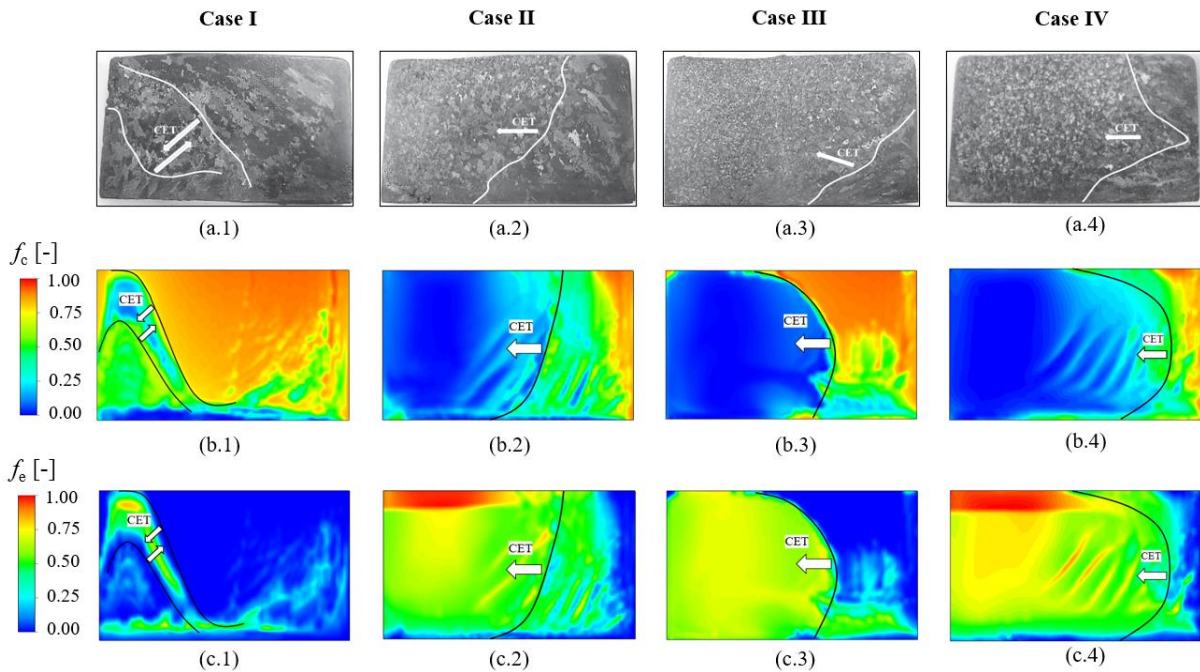


**Figure 3.2.** Comparison of the as-cast structure for the four cases (I - IV) based on metallographic analysis (a.x) in laboratory experiments [161] and the simulated volume fraction of columnar dendrites (b.x) and equiaxed grains (c.x).

The experimentally measured macrosegregation profiles obtained by X-radiography and digital processing methods are shown in Figures 3.3(a.x) and Figures 3.3(b.x), respectively. The calculated segregation profiles obtained by averaging the Pb concentrations for ten cross-section planes along the thickness direction are presented in Figure 3.3(c.x). Good agreements are achieved between the simulation results and experimental measurements except for Case III. Under the effect of natural convection (Case I), the positive segregation is formed in the



left-bottom region, and the negative segregation is mainly observed in the upper-right region (Figure 3.3(a.1) – (c.1)). Additionally, several channel segregations are found in the right part of the sample. The enhanced flow convection (Case II) pushes the serious positive segregation to the left-bottom corner (Figure 3.3(a.2) – (c.2)), while the periodically reversed convection (Case IV) is observed to shift this positive segregation to the central-bottom area (Figures 3.3(a.4) – (c.4)). On the other hand, the numbers of the channel segregation are increased under TMF. By integrating the macrosegregation index in the calculation domain, the global macrosegregation index ( $GMI = \iiint_{vol} |c_{mix}^{index}| dv$ ) is determined to be 38.17% for Case I. By applying the TMF, the GMI is increased to 39.45% for Case II and 39.77% for Case IV. It is found that macrosegregation is generally intensified by the TMF.

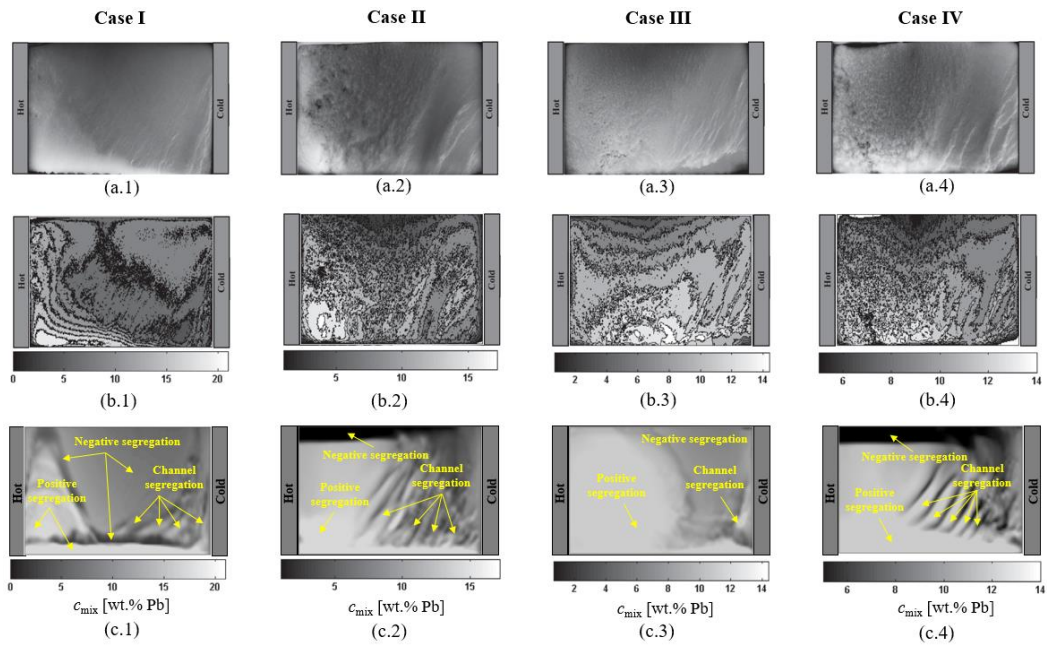


**Figure 3.3.** Macro-segregation maps obtained for the sample under the effect of different electromagnetic stirring modes: (a.x) X-radiography of the as-solidified ingot [161]; (b.x) Pb concentration map digitally processed from (a.x) [161]; (c.x) simulated mean Pb concentration through the thickness direction.

For Case III, one reason for the simulation-experiment mismatch could be the avalanche phenomenon [162], which probably occurs when the columnar dendrites solidify from the upper-right corner of the ingot in the early stage of solidification. The evolution of the columnar structure, which is represented by the isosurface of  $f_c = 0.05$ , is shown in Figure 3.4(a) – (b). The temperature field overlaid with the liquid velocity in vector is displayed on

the central vertical plane. As shown in Figure 3.4(a), at 50 s, the lowest temperature ( $T_{\text{low}} = 490.49$  K) of the melt appears at the upper-right corner of the sample, and the associated solidification of the columnar structure should also start from this area. At 100 s (Figure 3.4(b)), the columnar tip front continually grows and extends downwards along the cold wall. A zoomed view of the distribution of  $\bar{u}_\ell \cdot \nabla c_\ell$  near the upper-right corner (Zone A marked in Figure 3.4(b)) on the central vertical plane is shown in Figure 3.4(c). The interdendritic flow ( $\bar{u}_\ell$ ) in the direction opposite to the liquid concentration gradient ( $\nabla c_\ell$ ) leads to local remelting. The ‘blue’ region with a negative value of  $\bar{u}_\ell \cdot \nabla c_\ell$ , where the angle between  $\bar{u}_\ell$  and  $\nabla c_\ell$  is larger than  $90^\circ$ , is observed near the right wall. If the remelting of columnar dendrite roots causes massive dendrites to fall off from the right wall, as schematically shown in Figure 3.4(d), the avalanche phenomenon is likely to occur. However, this phenomenon is still far more complex for the recent model. According to the current model, the growth of the columnar dendrites in the upper-right part is further promoted during the later solidification stage. Finally, the as-solidified columnar dendrites capture the upper-right part of the sample in Case III (Figure 3.2(b.3)), leading to a mismatch to the measurement result (Figure 3.2(a.3)).

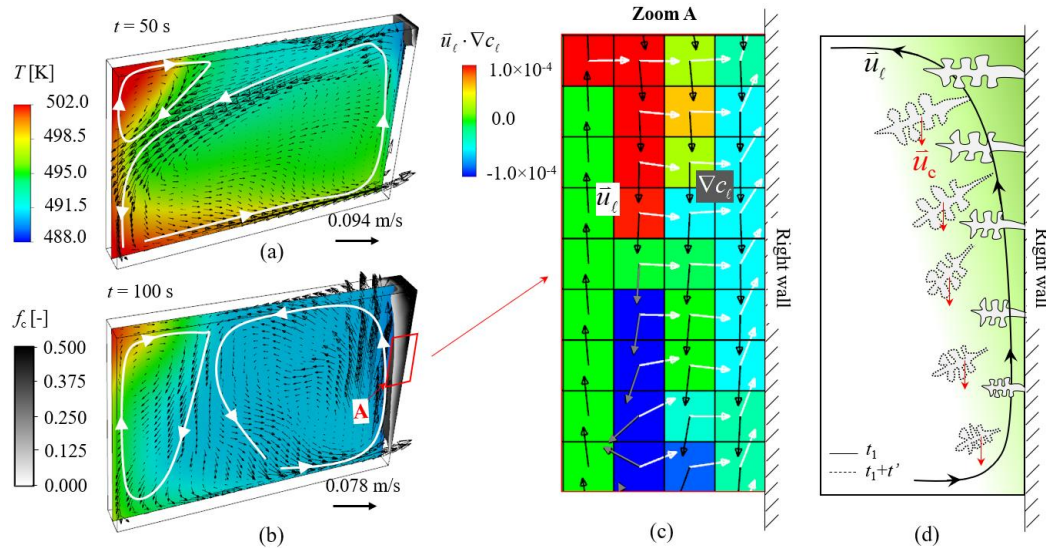


**Figure 3.4.** Solidification sequence of the columnar dendrites (iso-surface of  $f_c = 0.05$ ) for Case III: (a)  $t = 50$  s; (b)  $t = 100$  s; (c) zoom view of the  $\bar{u}_\ell \cdot \nabla c_\ell$  distribution in Zone A shown in (b). Temperature field overlaid with liquid velocity vector is shown on the central vertical plane; (d) schematic view of the avalanche phenomenon.

### 3.2 Numerical study of the as-cast structure and macrosegregation in the continuous casting of a steel billet

The main purpose of this study is to further validate the numerical model and prove its capability in simulating the casting process at the industrial scale. The proposed model is extended, i.e., in addition to the fragmentation mechanism, the heterogeneous nucleation is considered as another source of the equiaxed grains. Detailed information refers to Paper 1-2 of Part II.

Schematic of the continuous casting of a steel billet under the effect of M-EMS is shown in Figure 3.5. The composition of the steel billet is simplified as a binary alloy, i.e., Fe-0.53wt.%C, and the casting geometry (195 mm × 195mm) corresponded to that of an industrial process. The simulation was performed from the start stage (Figure 3.5(a)) till the quasi-steady stage of the casting (Figure 3.5(b)). The calculation domain is limited to only 12 m from the meniscus, which covers the mold region and three subsequent secondary cooling zones (Z1 - Z3). The flow field, temperature field, concentration field and solidification phenomena are analyzed in the upper quasi-steady state region, and the as-cast structure and macrosegregation are analyzed in the lower as-solidified region.

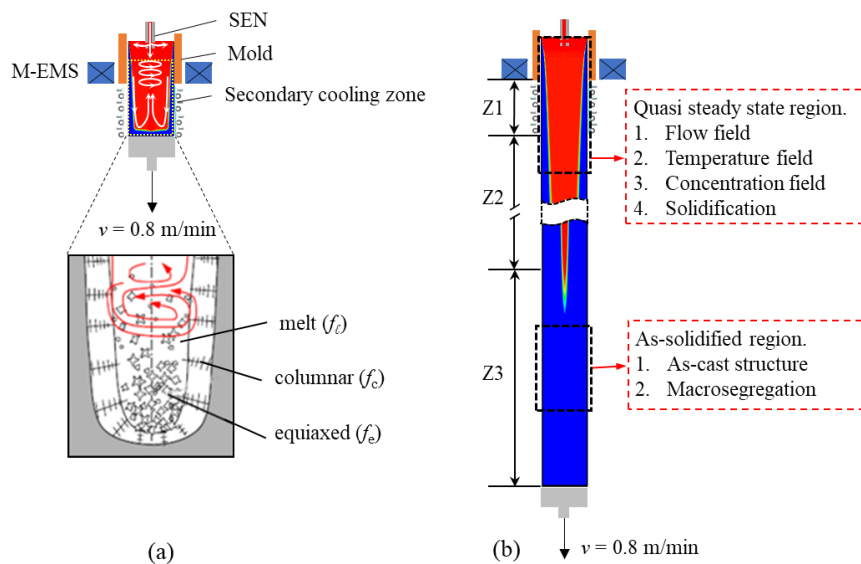


**Figure 3.5.** Schematic of continuous casting process under the effect of M-EMS. (a) Start stage of the casting with the zoom-in view of mixed columnar-equiaxed solidifications; (b) quasi-steady stage of the casting.

The transient solidification process together with the temperature/velocity fields for the case with M-EMS are shown in Figure 3.6(a) – (c). For comparison, the temperature field for

the case without M-EMS is depicted in Figure 3.6(d). As shown in Figure 3.6(a), one important role of the M-EMS is to confine the superheat area to the mold region, leaving the liquid core out of the mold region undercooled. In contrast to the case with M-EMS, the superheated region in the case without M-EMS can extend through the liquid core of the strand far below the mold region (Figure 3.6(d)).

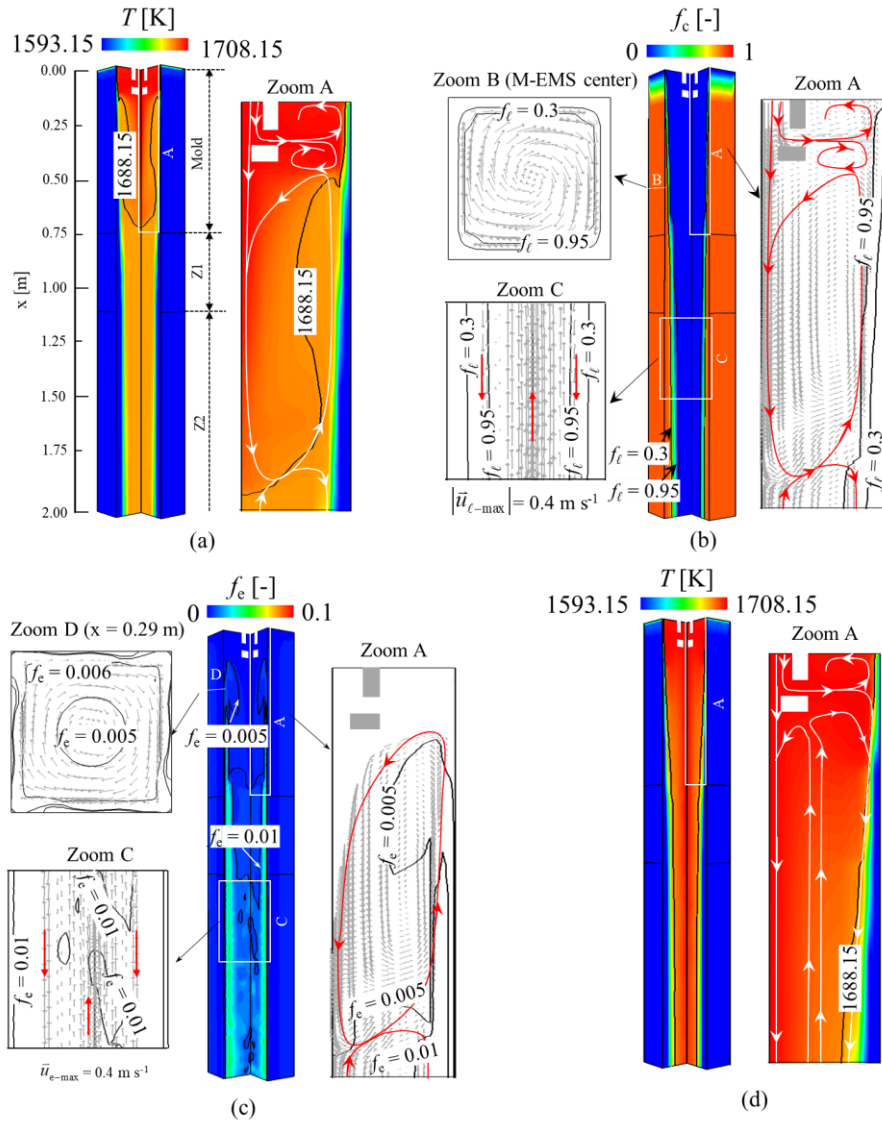


**Figure 3.6.** Solidification process in the upper part of the strand with M-EMS. (a) Temperature field overlaid with the liquidus isotherm (1688.15 K), indicating the superheated zone; (b) volume fraction of the columnar phase ( $f_c$ ) overlaid with  $\bar{u}_l$  vectors (grey) and streamlines (red) schematically highlighting the flow direction; (c) volume fraction of the equiaxed phase ( $f_e$ ) overlaid with  $\bar{u}_e$  vectors (grey) and streamlines (red) schematically highlighting the direction of motion of the equiaxed phase; (d) for comparison, the temperature field for the case without M-EMS is shown.

Contour of the volume fraction of columnar dendrites ( $f_c$ ) overlaid with the liquid velocity ( $\bar{u}_c$ ) is shown in Figure 3.6(b), and contour of the volume fraction of equiaxed grains ( $f_e$ ) overlaid with the equiaxed velocity ( $\bar{u}_e$ ) is shown in Figure 3.6(c). Two iso-lines are used in Figure 3.6(b) to define the solid shell ( $f_l = 0.3$ ) and the position of the columnar tip front ( $f_l = 0.95$ ). Near the middle height of the stirrer (Zone B), the M-EMS-induced swirling flow is confined by the solidified shell. In the mold region (Zone A), the downward jet flow coming from the bottom exit of the submerged entry nozzle (SEN) is brought back to the upper part of the mold region along the solidification front by the M-EMS-induced secondary flow Figure 3.6(b). A small portion of equiaxed grains could also be carried to the upper mold region by this secondary flow and partially remelts in the superheated zone (Figure 3.6(c)). In the secondary cooling zone, most equiaxed grains settle down and continue to grow during settling (Zone C in Figure 3.6(c)).

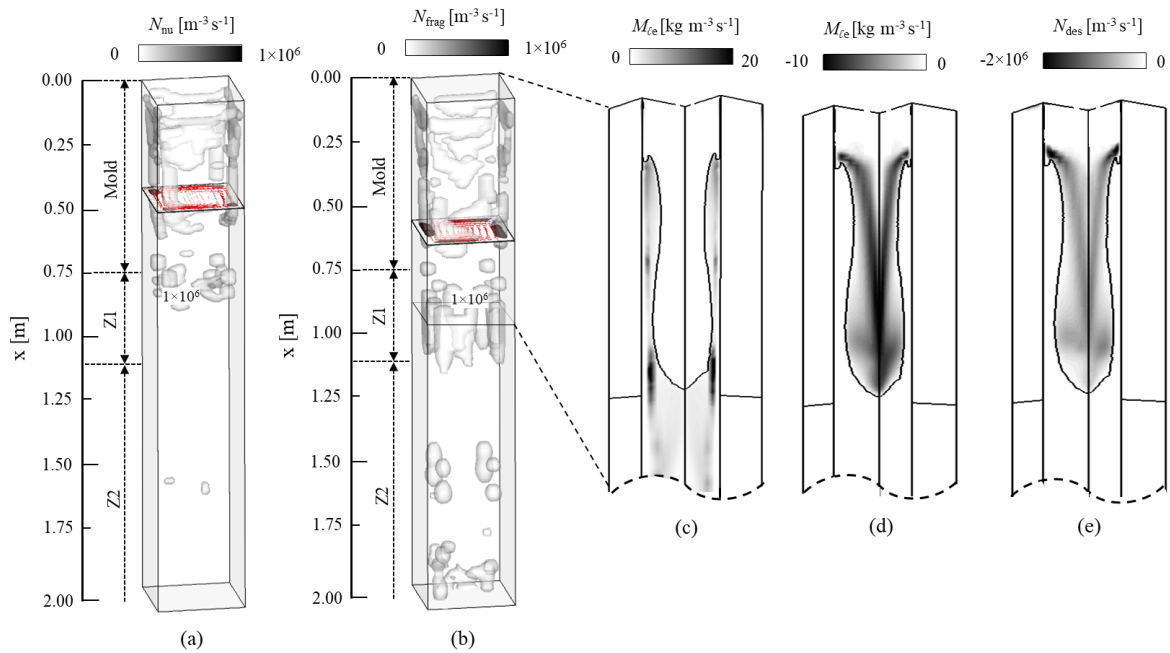


**Figure 3.7.** Evolution of the equiaxed grains in the upper part of the strand. (a) Heterogeneous nucleation rate  $N_{nu}$ ; (b) crystal fragmentation rate  $N_{frag}$ ; (c) – (d) net mass transfer rate ( $M_{te}$ ) between the melt and equiaxed grains for solidification (c) and remelting (d); (e) destruction rate of the equiaxed grains  $N_{des}$ .

The evolution of the equiaxed grains in the upper part of the strand is shown in Figure 3.7. On the one hand, when the necessary conditions are achieved in the undercooled region, the inoculants are activated as equiaxed grains (Figure 3.7 (a)). On the other hand, the

fragments generated in the mushy zone near the columnar tip front provide the source of equiaxed grains (Figure 3.7(b)). Analysis of the results showed that the M-EMS-induced flow appeared to impact crystal fragmentation very effectively. The created equiaxed grains will continue to grow in the undercooled region (Figure 3.7(c)) or be remelted in the superheated zone (Figure 3.7(d)). The remelting process is accompanied by a reduction in grain size. Once the grain size is reduced to a critical value ( $d_{\text{critical}}$ ), the equiaxed grain will be destructed (Figure 3.7(e)).

The experimental macrograph of the as-cast structure is shown in Figure 3.8(a), and the simulated macrostructure is displayed in Figure 3.8(b). The profile of the columnar zone shows a satisfactory agreement with the one of the as-cast structure, while the equiaxed zone is somehow underestimated by the simulation. Contour of the macrosegregation index ( $c_{\text{mix}}^{\text{index}}$ ) is exhibited in Figure 3.8(c). Because of the accumulation of the equiaxed grains, negative segregation is observed in the central equiaxed zone. Positive segregation occurs at the border of the columnar zone, and a trail of negative segregation (so-called ‘white band’) is found in the subsurface region of the billet.

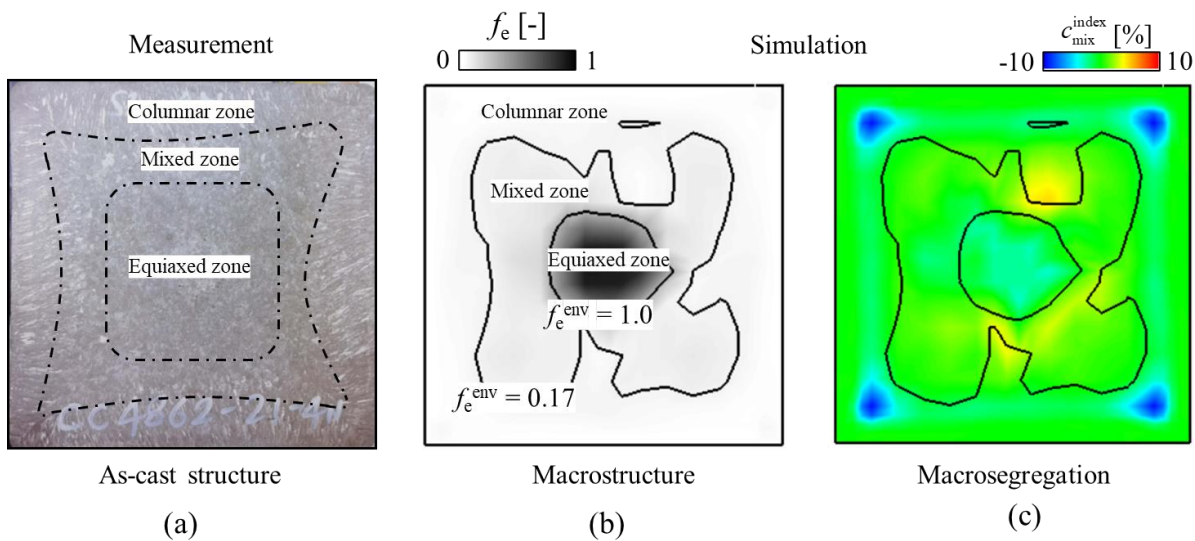


**Figure 3.8.** (a) Macrograph of the as-cast structure; (b) simulated macrostructure; (c) simulated macrosegregation index  $c_{\text{mix}}^{\text{index}}$ .

### 3.3 Evaluation of the coupling schemes between the flow field and electromagnetic field

The purpose of this study is to validate the computational magnetohydrodynamic (MHD) methods that are typically employed for the steel CC process and evaluate the coupling schemes between the flow field and electromagnetic (EM) field. Detailed information refers to Paper 5 of Part II.

Three different MHD calculation methods and coupling schemes are shown in Figure 3.9. Instead of directly solving Maxwell's equations, the analytical equations [64, 146–149], as shown in Figure 3.9(a), are employed to calculate the Lorentz force  $\vec{F}_L$  (composed of  $\vec{F}_\theta$  and  $\vec{F}_r$ ). Specifically, the external magnetic field  $\vec{B}_0$  and its distribution  $f(z)$  should be known in advance. The relative motion between the liquid and magnetic field has been considered by a factor of  $(1 - \omega_\ell / \omega_B)$ .

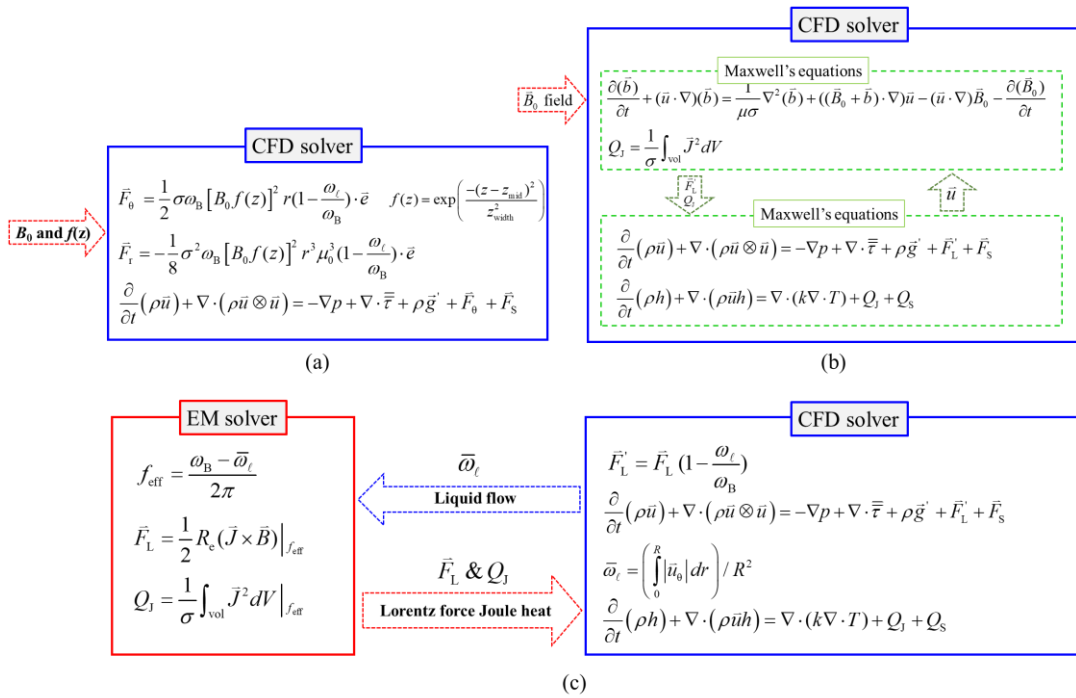


**Figure 3.9.** Sketch of different MHD calculation methods and coupling schemes: (a) Analytical solution; (b) Coupled simulation via ANSYS Fluent add-on MHD module; and (c) Iteration scheme between EM and CFD solvers.

As depicted in Figure 3.9(b), the ANSYS Fluent add-on MHD module provides one coupled method for MHD calculations, but  $\vec{B}_0$  should be measured or calculated via ANSYS

Maxwell software in advance. The electrical conductivity of the liquid melt is dependent on the local temperature  $T$ . The combined magnetic field  $\vec{B}$  is a sum of external magnetic field  $\vec{B}_0$  and induced magnetic field  $\vec{b}$ , i.e.,  $\vec{B} = \vec{B}_0 + \vec{b}$ . The  $\vec{b}$  will be updated by the forced flow ( $\vec{u}$ ). The coupling between  $\vec{B}$ ,  $\vec{u}$ , and  $T$  is automatically solved in ANSYS Fluent. An iteration scheme between the EM and computational fluid dynamic (CFD) solvers as shown in Figure 3.9(c). According to Roplekar and Dantzig [147],  $\vec{F}_L$  was modified by multiplying  $(1 - \omega_\ell / \omega_B)$  before applying it as a source term for the Navier–Stokes equation. Then, the calculated averaged liquid rotating angular velocity,  $\bar{\omega}_\ell = \left( \int_0^R |\bar{u}_\theta| dr \right) / R^2$ , was used to modify the effective frequency of the magnetic field,  $f_{\text{eff}} = (\omega_B - \bar{\omega}_\ell) / 2\pi$ .

Three different laboratory experiments were conducted on an upward Bridgman furnace equipped with a rotating magnetic field (RMF). The RMF was generated by a two-pole inductor charged by a three-phase alternating current (AC). Detailed information on the furnace is available in the Reference [163]. As shown in Figure 3.10(a), the diameter of the iron-core of the inductor is 230 mm, and its height is equal to 300 mm. The first experiment was performed without loading any sample, the  $\vec{B}$  field along the axis and in the azimuthal directions was measured with GM08 Gaussmeter (Hirts Magnetics). As schematically shown in Figure 3.10(b), the solid samples (Cu, Al, and AlSi7) in the second experiment are suspended in the inductor and fixed by an insulated organic sample holder (PA6 polyamide). With the RMF load, the induced Lorentz force on the sample is transported to a digital dynamometer via the sample holder. The pull (force) exerted on the sample under different values of  $|\vec{B}|$  were measured. Hence, the *Pull* is calculated as  $\text{Pull} = \text{Friction}(0.34 \text{ N}) + \text{Force}$ . The torque  $\tau = \text{Pull} * R$ , where  $R$  denotes the radius of the sample. To measure the flow velocity, a so-called pressure compensation method is applied to measure the RMF-induced rotating angular speed [164]. This experiment was performed at room temperature with cold alloy Ga75In25 (Figure 3.10(c)). The inner diameter of the tank was 25 mm, and its height was 100 mm. By measuring the level-difference ( $\Delta H$ ) after loading the RMF, the rotating angular liquid velocity ( $\bar{\omega}_\ell$ ) can be calculated.



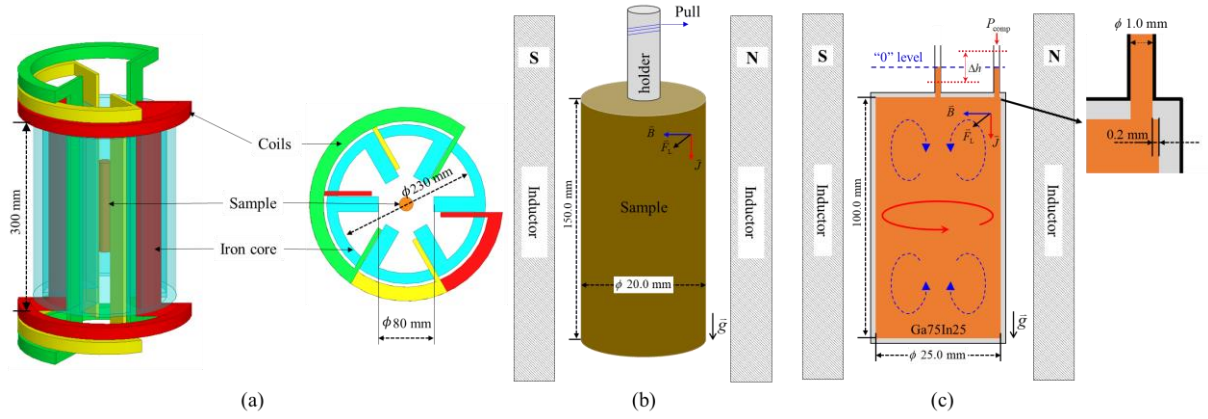


**Figure 3.10.** Schematic of experiment setup. (a) Layout of the inductor and sample position; (b) sketch of torque measurement; (c) sketch of liquid velocity measurement.

As shown in Figure 3.11(a), the calculated  $|\vec{B}|$  along the axis of the inductor for the case without sample loading matches the experimental measurements quite well. When a copper sample ( $H = 150$  mm,  $R = 10$  mm) is loaded, the  $\vec{B}$  field in the sample is subject to the skin effect, and the calculated  $|\vec{B}|$  along the axis of the sample should be reduced by approximately 13 mT. The calculated  $\tau$  for solid samples of three metal/alloys (Cu, Al, and AlSi7) as a function of  $\vec{B}$  is compared with those obtained via experiments as shown in Figure 3.11(b). For all samples,  $\tau$  increases exponentially with  $|\vec{B}|$ . The simulation results are in excellent agreement with the measurements.

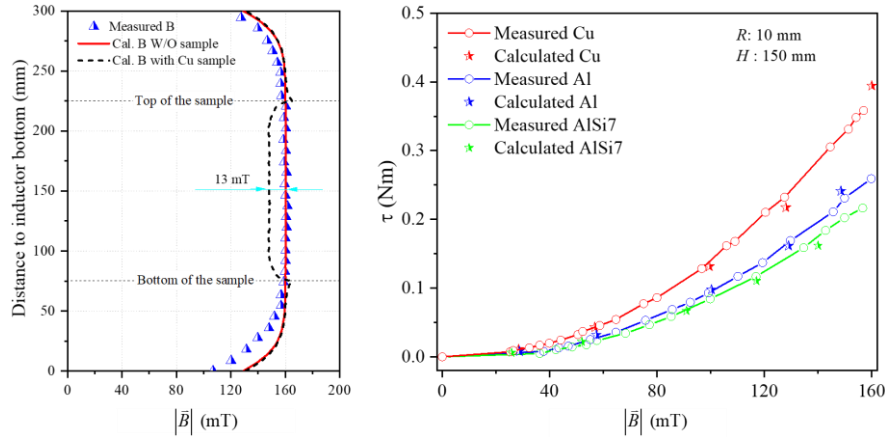


**Figure 3.11.** Experiment-simulation comparison of  $|\vec{B}|$  ( $f = 50$  Hz,  $I = 5700$  A) and  $\tau$ . (a)  $|\vec{B}|$  along the axis of the inductor. (b)  $\tau$  for solid samples of three metal/alloys (Cu, Al, and AlSi7).

The calculated  $\bar{\omega}_\ell$  as a function of  $|\vec{B}|$  with different MHD methods and modification strategies is shown in Figure 3.12. With the analytical solution (Figure 3.9(a)), the calculated

$\bar{\omega}_\ell$  is overestimated by ca. 34.4 %. With the ANSYS Fluent addon MHD module, (Figure 3.9(b)),  $\bar{\omega}_\ell$  shows good agreement with the experimental measurements. With the iteration scheme between EM and CFD solvers (Figure 3.9(c)), different modification strategies were performed to check their effect on the calculation accuracy. Evidently,  $\bar{\omega}_\ell$  differs significantly if modification strategies of  $\vec{F}_L$  are varied. The calculated  $\bar{\omega}_\ell$  is overestimated by ca. 66.2 % without any modification and iteration. If  $\vec{F}_L$  is solely modified by a factor of  $(1 - \omega_\ell / \omega_B)$ ,  $\bar{\omega}_\ell$  is overestimated by ca. 29.6 %. Hence, only when the modification and iteration are conducted,  $\bar{\omega}_\ell$  can reproduce the experimental results.

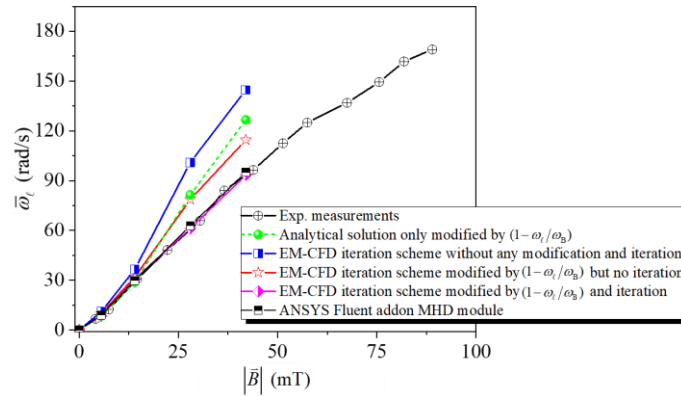


**Figure 3.12.** Comparisons of the angular velocities  $\bar{\omega}_\ell$  between experiment and different MHD methods and coupling schemes.

The analytical solution for the  $\vec{F}_L$  corresponds to easy-to-implement method with highest computation efficiency, but it is limited to the low-frequency cases. The ANSYS Fluent add-on MHD module provides the highest calculation accuracy, but there are drawbacks of excessively high computation cost, incompatibility for multiphase solidification problem, and the external magnetic field should be measured or calculated elsewhere. To ensure the calculation accuracy, an iteration scheme is proposed in the third method. Given that  $\bar{\omega}_\ell$  is not uniform along the axis direction of the CC strand, and that the iteration procedure must be conducted manually. Thus, it is not recommended to use the iteration scheme in the simulation of CC process. The necessary calculation accuracy can still be realized (Figure 3.8) by the scheme without iteration but considering the modification to  $\vec{F}_L$ ,  $\vec{F}_L' = \vec{F}_L (1 - \omega_\ell / \omega_B)$ .

### 3.4 Solidification principle of the SCC

The extended three-phase mixed columnar-equiaxed solidification model has been verified by making the comparisons with the laboratory experiments and the real industrial scale billet continuous casting. Additionally, the accuracy of the coupling scheme between the fluid field and electromagnetic field has been addressed in §3.3. The main purpose of this study is to understand the solidification principle of the SCC using the extended numerical model. Detailed information refers to Paper 4 of Part II.

As schematically shown in Figure 3.13, SCC includes two stages: withdrawing and solidification. Following the CC technique, the withdrawing (pouring) process can be efficiently controlled by the implementation of a SEN for mold filling, water-cooled mold and secondary cooling (air or water spray) for shell formation, and EMS for flow and superheat dissipation. Following the IC technique, when the as-filled and partially solidified casting is put aside for the remaining solidification, further measures can be implemented, e.g., thermal or electric hot topping, shielding or isolating, and even EMS, to control the shrinkage porosity, potential cracks, as-cast structure and macrosegregation.

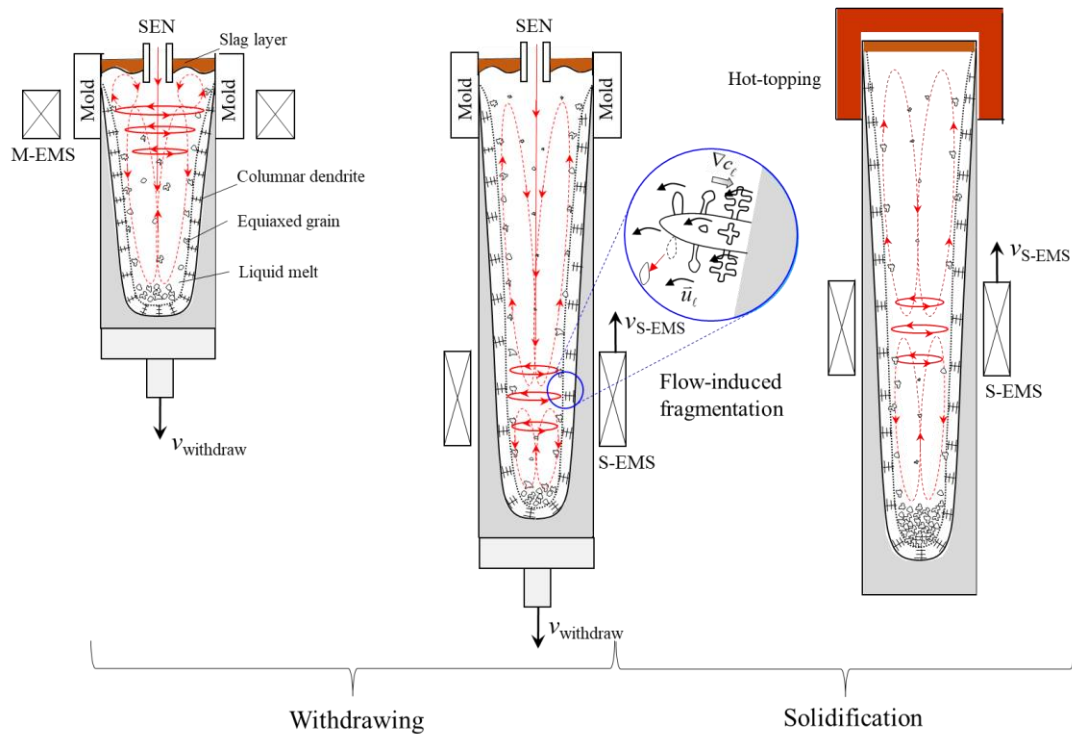


**Figure 3.13.** Schematic of processes for large vertical steel casting.

The typical 3D flow pattern and solidification results under the effect of M-EMS at the early stage of withdrawing (1500 s) are shown in Figure 3.14. A streamline is shown in Figure 3.14(a) to demonstrate the complexity of the flow pattern of the liquid melt. The jet flow coming from the bottom port of the SEN was reversed and returned to the upper mold region. It then rotated and flowed downward along the columnar solidification front. Finally, it returned to the M-EMS region along the center of the casting. Under the effect of such a forced flow, crystal fragments were generated in the mushy zone, especially in the area where M-EMS is operative (Figure 3.14(b)). The simultaneous solidification/remelting phenomenon of equiaxed grains at different positions inside the casting was observed (Figure 3.14(c)). As shown in Figure 3.14(d), the remelting of the columnar dendrites was negligible, whereas the solidification rate of the columnar dendrites was much larger than that of the equiaxed grains.

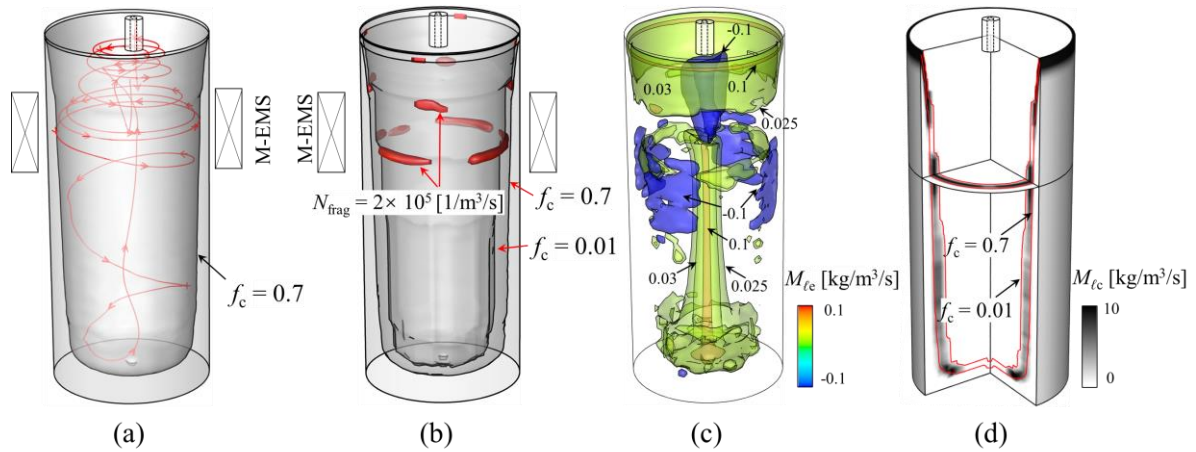


**Figure 3.14.** 3D flow pattern and solidification results of the casting during withdrawing at 1500 s. (a) A streamline of the liquid melt to demonstrate the flow pattern, the iso-surface of  $f_c = 0.7$  is drawn to show the shape of the solid shell; (b) one iso-surface of  $N_{\text{frag}} = 2 \times 10^5$  [1/m<sup>3</sup>/s] to show the distribution of the created fragments in the mushy zone; (c) net mass transfer rate between liquid melt and equiaxed grains ( $M_{t_e}$ ) with positive for solidification and negative for remelting; (d) net mass transfer rate between liquid melt and columnar dendrites ( $M_{t_c}$ );

During the late stage of withdrawing (at 3000 s), the M-EMS was turned off, followed by the activation of the S-EMS. The S-EMS is installed at a start position of 0.5 m above the casting bottom, but it moves upward at a predefined speed of  $7.9 \times 10^{-4}$  m/s relative to the casting. The solidification results at the late stage of the withdrawing ( $t = 5500$  s), when the strand was withdrawn to a length of 8.25 m, are depicted in Figure 3.15. The S-EMS-driven primary rotating flow induces a secondary flow (Figure 3.15(a)). The maximal  $|\bar{u}_\ell|$

( $|\bar{u}_{\ell-\max}| = 1.96 \text{ m/s}$ ) appears at the solidification front near the center of the stirrer (Figure 3.15(c)). Under the effect of S-EMS, columnar dendrites were fragmented near the front of the mushy zone (Figure 3.15(d)). Given birth by these fragments, the equiaxed grains grew and sedimented to the casting bottom along the solidification front (Figure 3.15(e)). Some equiaxed grains could also be brought back to the S-EMS region along the middle-radius region of the casting by the lower recirculation loop. Additionally, the superheated region was extended to the stirred area under the effect of the upper recirculation loop. Some equiaxed grains exposed in the superheated region were re-melted (Figure 3.15(f)) and further destroyed (Figure 3.15(g)), while others continued to solidify and accumulated in the undercooled liquid (Figure 3.15(h)). As depicted in Figure 3.15(i), a slight negative macrosegregation ( $c_{\text{mix}}^{\text{index}} = -6 \%$ ) was formed in the as-solidified shell, and the liquid in the center was enriched with solute.

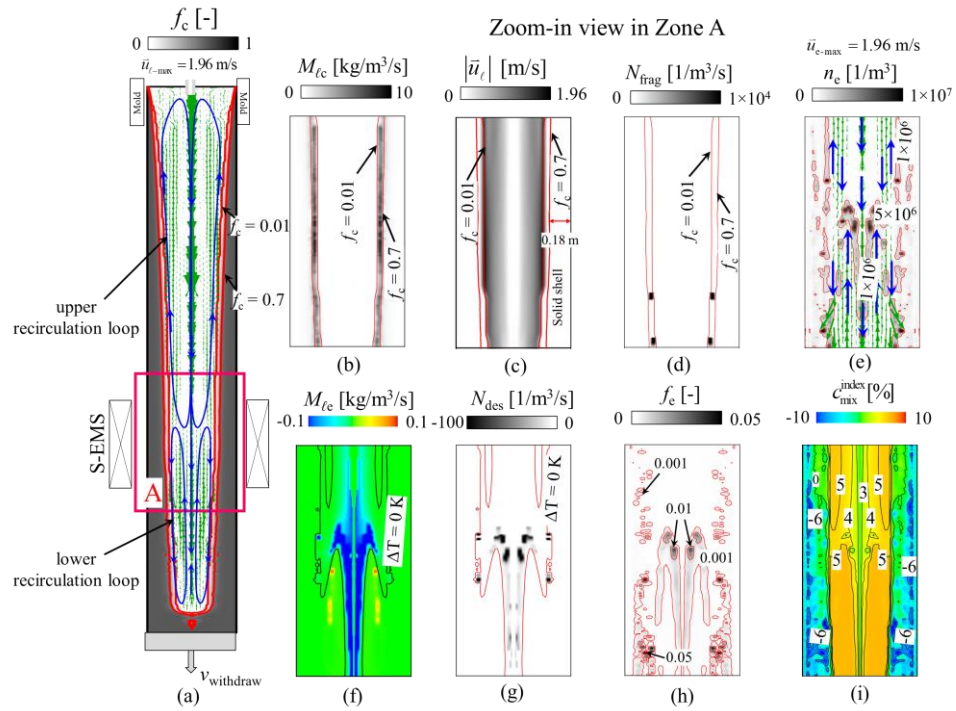


**Figure 3.15.** Solidification results during the late stage of withdrawing of a SCC at  $t = 5500 \text{ s}$ . (a) Contour of  $f_c$  overlaid by vectors of  $\bar{u}_\ell$ . Two isolines are drawn for  $f_c = 0.01$  and  $f_c = 0.7$ . The solidification results in the S-EMS stirred area, as marked by the red rectangle A in (a) are shown in (b)-(i); (b)  $M_{f_c}$ ; (c) contour of  $|\bar{u}_\ell|$ ; (d)  $N_{\text{frag}}$ ; (e) contour of  $n_c$  overlaid by vectors of  $\bar{u}_c$ ; (f)  $M_{f_c}$ , and the isoline of  $\Delta T = 0 \text{ K}$  is drawn to distinguish the superheated and undercooled regions; (g)  $N_{\text{des}}$ ; (h)  $f_c$ ; (i)  $c_{\text{mix}}^{\text{index}}$ .

After the termination of the withdrawing process, the partially solidified casting was put aside for the remaining solidification. In addition to the S-EMS, hot-topping and shielding were applied to decrease the solidification rate of the casting, especially in the top region. With the upward movement of the S-EMS, the upper recirculation loop is compressed (shortened), whereas the lower recirculation loop is elongated (Figure 3.16(a)). The solid shell grew gradually towards the casting center (Figure 3.16(b)). Because of the increase in the shell thickness, the maximal  $|\bar{u}_\ell|$  ( $|\bar{u}_{\ell-\max}| = 1.0 \text{ m/s}$ ) is decreased by 48.9 % (Figure 3.16(c)) compared to the result at 5500 s (Figure 3.15(c)). The fragmentation rate also decreased (Figure 3.16(d)). As the superheat has been fully dissipated in the liquid core (Figure 3.16(g)), no remelting and destruction of the equiaxed grains occurs. The equiaxed grains transported from the lower part of the casting (Figure 3.16(e)) will survive (Figure 3.16(h)) and solidify (Figure 3.16(f)) in the central liquid pool. Mixing the solute-enriched melt with the solute-depleted equiaxed grains (from the lower part of the casting) by the S-EMS-induced flow is beneficial for homogenizing the solute element in the casting center (Figure 3.16(i)).

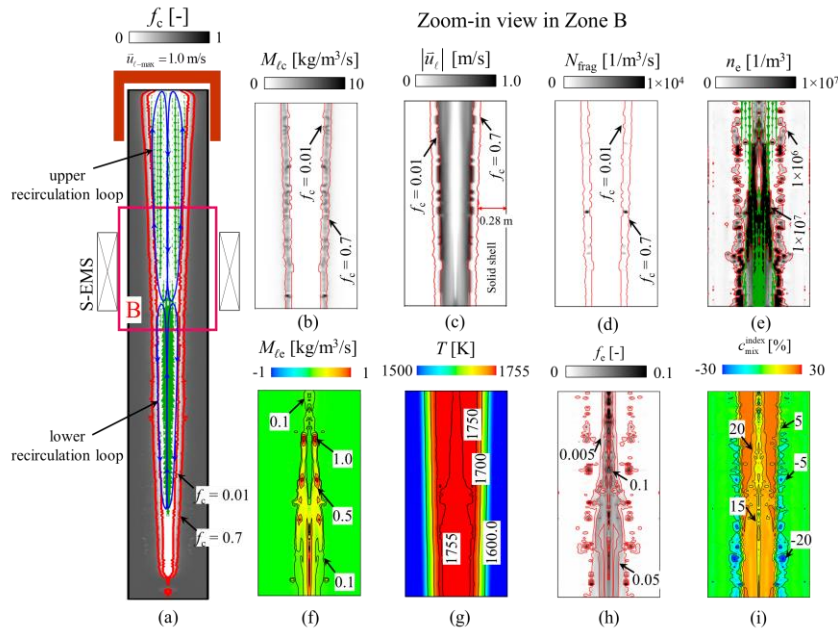


**Figure 3.16.** Solidification results during solidification stage of a SCC at  $t = 9500 \text{ s}$ . (a) Contour of  $f_c$  overlaid by vectors of  $\bar{u}_\ell$ , and two isolines are drawn for  $f_c = 0.01$  and  $f_c = 0.7$ . Zoom-in views of the solidification results in the S-EMS stirred area, as marked by the red rectangle B in (a), are shown in (b)-(i). (b)  $M_{ic}$ ; (c) contour of  $|\bar{u}_\ell|$ ; (d)  $N_{frag}$ ; (e) contour of  $n_c$  overlaid by vectors of  $\bar{u}_\ell$ ; (f)  $M_{ic}$ ; (g) temperature field  $T$ ; (h)  $f_c$ ; (i)  $c_{mix}^{index}$ .

## 4. Main conclusions of the Ph.D works

A previously proposed three-phase mixed columnar-equiaxed solidification model was extended and used to investigate the formation mechanism of the as-cast structure and macrosegregation in semi-continuous casting (SCC) of steel. The model was validated with the Sn-Pb benchmark casting experiments at the laboratory scale and the continuous casting (CC) of a steel billet at the industrial scale. Then, different EM-CFD coupling schemes between the flow field and the electromagnetic field were also evaluated by comparing the experimental and simulation results. Finally, the refined model was used to study the solidification principle of SCC in a large format ( $\phi 1 \text{ m} \times 10 \text{ m}$ ). The main conclusions are drawn as follows.

1. To ‘reproduce’ the experimental results of the laboratory benchmark casting (Sn-Pb) and the continuous casting of steel billet, it is found to be essential to include following key features in the solidification model:
  - three phases which include liquid melt, equiaxed and columnar;
  - fragmentation of the columnar dendrites, which give birth to the equiaxed grains;
  - transport of the equiaxed grains;
  - growth and remelting/destruction of the equiaxed grains;
  - a proper coupling scheme between the electromagnetic field and multiphase flow.
2. Simulations of both laboratory casting of Sn-Pb and continuous casting of steel billet have shown that the forced flow induced by the electromagnetic stirring plays an important role in homogenizing the temperature field and promoting the equiaxed grains formation through the fragmentation mechanism, and consequently, facilitates the columnar-to-equiaxed transition.
3. Simultaneous solidification, transport, and remelting phenomena of equiaxed grains represent an important species/energy transport mechanism during solidification. For example, in the Sn-Pb laboratory benchmark casting, equiaxed grains grow in the undercooled melt, while some equiaxed grains are brought by the TMF-induced flow to the superheated region and re-melted. In the steel billet strand ( $195 \text{ mm} \times 195 \text{ mm}$ ), some equiaxed grains are brought by the M-EMS-induced swirling flow into the central superheated zone and re-melted. It is verified that ignoring the remelting of equiaxed grains in the superheated region in the solidification model will lead to an overestimation of the

temperature in the liquid melt, and it will cause an error in the calculation of the as-cast structure and macrosegregation.

4. Through the parameter studies of the CC of the steel billet (195 mm × 195 mm), it is found that the shielding effect of the copper mold, electrical isolation at the strand-mold interface, and relatively high electrical conductivity of the strand shell affect the M-EMS efficiency. Especially, the electric current path through the strand-mold interface is found to be more important. Considering that: 1) the slag layer in the strand-mold gap is mostly in the solid state, which has a relatively lower conductivity, and 2) an air gap may occasionally form between the strand and mold, the strand-mold interface should be treated as an electrically isolating wall.
5. By evaluating different EM–CFD coupling schemes, it is found that 1) the analytical solution corresponds to easy-to-implement method, but it cannot account for the eddy effect, hence, it is limited to the low-frequency cases; 2) the ANSYS Fluent add-on MHD module provides the highest calculation accuracy, but it is incompatible with the Eulerian–Eulerian multiphase approach; 3) the iteration scheme between EM and CFD solvers considers the eddy current and flow effect on the EM field, and the necessary calculation accuracy can still be realized without iteration in the CC or SCC processes.



## 5. Reference

- [1] A. Einchinger, H.P. Kogler, A. Puhlinger, G. Hrazeder, S. Hahn, F. Wimmer. Semi-continuous casting technology combining technological advantages of two different casting practices. *9<sup>th</sup> Eur. Contin. Cast. Conf.*, **2017**, pp. 267–276.
- [2] S. Michelic, M. Riedler. Production of jumbo blooms by semi-continuous casting: challenges, feasibility, and future potential. *Berg Hüttenmänn. Monatsh.*, vol. 161, **2016**, pp. 39–44.
- [3] J. Penn, P. Pennerstorfer, A. Jungbauer. New generation of continuous casting plants with intelligent manufacturing strategy. *Berg Hüttenmänn. Monatsh.*, vol. 163, **2018**, pp. 11–17.
- [4] K. Mramor, R. Vertnik, B. Šarler. Meshless approach to the large-eddy simulation of the continuous casting process. *Eng. Anal. Boundary Elem.*, vol. 138, **2022**, pp. 319–338.
- [5] R. Vertnik, B. Šarler. Solution of a continuous casting of steel benchmark test by a meshless method. *Eng. Anal. Boundary Elem.*, vol. 45, **2014**, pp. 45–61.
- [6] M. Mramor, R. Vertnik, B. Šarler. Development of three-dimensional LES based meshless model of continuous casting of steel. *Metals*, vol. 12, **2022**, 1750.
- [7] A.Z. Lorbiecka, R. Vertnik, H. Gjerkeš, G. Manojlovič, B. Senčič, J. Cesar, B. Šarler. Numerical modeling of grain structure in continuous casting of steel. *Comput., Mater. Continua*, vol. 8, **2009**, pp. 195–208.
- [8] H. Liu, Z. Wang, H. Qiu. Numerical simulation of fluid flow and solidification in a vertical round bloom caster using a four-port SEN with mold and strand electromagnetic stirring. *ISIJ Int.*, vol. 60, **2020**, pp. 1924–1937.
- [9] X. Li, Z. Zhang, M. Lv, M. Fang, K. Liu. Numerical simulation of the fluid flow, heat transfer, and solidification in ultrahigh speed continuous casting billet mold. *Steel Res. Int.*, vol. 93, **2022**, 2100673.
- [10] Q. Dong, J. Zhang, Y. Yin, H. Nagaumi. Numerical simulation of macrosegregation in billet continuous casting influenced by electromagnetic stirring. *J. Iron Steel Res. Int.*, vol. 29, **2022**, pp. 612–627.
- [11] L. Zhang, Z. Wang, C. Xu, S. Li, X. Ai, J. Li. A vertical continuous casting machine for large blooms. *Ironmaking Steelmaking*, vol. 46, **2019**, pp. 742–746.
- [12] J. Wang, F. Wang, Y. Zhao, J. Zhang, W. Ren. Numerical simulation of 3D-microstructures in solidification processes based on the CAFE method. *Int. J. Miner. Metall. Mater.*, vol. 16, **2009**, pp. 640–645.
- [13] A. Burelko, J. Falkus, W. Kapturkiewicz, K. Sołek, P. Drożdż, M. Wróbel. Modeling of the grain structure formation in the steel continuous ingot by CAFE method. *Arch. Metall. Mater.*, vol. 57, **2012**, pp. 379–384.
- [14] Y. Luo, J. Zhang, X. Wei, C. Xiao, Z. Hu, Y. Yuan, S. Chen. Numerical simulation of solidification structure of high carbon SWRH77B billet based on the CAFE method. *Ironmaking Steelmaking*, vol. 39, **2012**, pp. 26–30.
- [15] J. Fang, X. Liu, Y. Fan, M. Xie, Y. Chen, Y. Yang, Y. Duan, S. Chen. Numerical simulation of solidification structures of Ag–28Cu–1Ni alloy through continuous casting based on three-dimensional CAFE method. *Mater. Trans.*, vol. 61, **2020**, pp. 1230–1238.

- [16] Z. Wang, S. Luo, W. Wang, M. Zhu. Numerical simulation of solidification structure of continuously cast billet with grain motion. *Metall. Mater. Trans. B*, vol. 51, **2020**, pp. 2882–2294.
- [17] Z. Zhang, M. Wu, H. Zhang, S. Hahn, F. Wimmer, A. Ludwig, A. Kharicha. Modeling of the as-cast structure and macrosegregation in the continuous casting of a steel billet: Effect of M-EMS. *J. Mater. Process. Technol.*, vol. 301, **2022**, 117434.
- [18] Z. Zhang, M. Wu, H. Zhang, A. Ludwig, A. Kharicha. The role of mold electromagnetic stirring in the dissipation of superheat during the continuous casting of billets. *Steel Res. Int*, vol. 93, **2022**, 2200065.
- [19] D. Jiang, M. Zhu, L. Zhang. Numerical simulation of solidification behavior and solute transport in slab continuous casting with S-EMS. *Metals*, vol. 9, **2019**, 452.
- [20] D. Jiang, M. Zhu. Flow and solidification in billet continuous casting machine with dual electromagnetic stirrings of mold and the final solidification. *Steel Res. Int*, vol. 86, **2015**, pp. 993–1003.
- [21] D. Jiang, L. Zhang, M. Zhu. Center segregation evolution in slab continuous casting with mechanical reduction: a 3D simulation. *Steel Res. Int.*, vol. 93, **2022**, 2100569.
- [22] D. Jiang, M. Zhu. Center segregation with final electromagnetic stirring in billet continuous casting process. *Metall. Mater. Trans. B*, vol. 48, **2017**, pp. 444–455.
- [23] D. Jiang, M. Zhu. Solidification structure and macrosegregation of billet continuous casting process with dual electromagnetic stirrings in mold and final stage of solidification: a numerical study. *Metall. Mater. Trans. B*, vol. 47, **2016**, pp. 3446–3458.
- [24] Y. Yao, Z. Liu, Z. B. Li, L. Xiao, Y. Gan. Effect of steel strip feeding on the columnar-equiaxed solidification in a large continuous casting round bloom. *J. Mater. Res. Technol.*, vol. 20, **2022**, pp. 1770–1785.
- [25] M. Wu, A. Vakhrushev, E. Karimi-Sibaki, A. Kharicha, A. Ludwig. Advanced process simulation of solidification and melting. *Berg Hüttenmänn. Monatsh.*, vol. 159, **2014**, pp. 30–40.
- [26] T. Sjökvist, M. Göransson, P. Jönsson, P. Cowx. Influence of ferromanganese additions on microalloyed engineering steel. *Ironmaking Steelmaking*, vol. 30, **2003**, pp. 73–80.
- [27] K. Riyahimalayeri. Slag, steel, ladle and non-metallic inclusions equilibria in an ASEA-SKF ladle furnace. Doctoral dissertation, KTH Royal Institute of Technology, **2012**.
- [28] Steel ingots and their casting during steelmaking. Retrieved from <https://www.ispatguru.com/steel-ingots-and-their-casting-during-steelmaking>. in **2023**.
- [29] Steel Statistical Yearbook. World Steel Association. *Economics Committee*. **2018**.
- [30] L. Zhang, B.G. Thomas. State of the art in the control of inclusions during steel ingot casting. *Metall. Mater. Trans. B*, vol. 37, **2006**, pp. 733–761.
- [31] E. Fuchs, P. Jonsson. Inclusion characteristics in bearing steel before and during ingot casting. *High Tem. Mater. Processes*, vol. 19, **2000**, pp. 333–344.
- [32] J.D. Hunt. Steady state columnar and equiaxed growth of dendrites and eutectic. *Mater. Sci. Eng.*, vol. 65, **1984**, pp. 75-83.
- [33] M.A. Martorano, C. Beckermann, C.A. Gandin. A solutal interaction mechanism for the columnar-to-equiaxed transition in alloy solidification. *Metall. Mater. Trans. A*, vol. 34, **2003**, pp. 1657–1674.

- [34] G. Lesoult. Macrosegregation in steel strands and ingots: Characterisation, formation and consequences. *Mater. Sci. Eng. A*, vol. 413, **2005**, pp. 19–29.
- [35] M. Wu, A. Ludwig, A. Kharicha. Simulation of as-cast steel ingots. *Steel Res. Int*, vol. 89, **2018**, 1700037.
- [36] E. Niyama, T. Uchida, M. Morikawa, S. Saito. A method of shrinkage prediction and its application to steel casting practice. *AFS Int. Cast Met. J.*, vol. 9, **1982**, pp. 52–63.
- [37] M. Tkadlečková, K. Michalek, P. Klus, K. Gryc, V. Sikora, M. Kováč. Testing of numerical model settings for simulation of steel ingot casting and solidification. *20<sup>th</sup> Anniv. Int. Conf. Metall. Mater. Metal*, Brno, Czech Republic, **2011**, pp. 61–67.
- [38] M. Tkadlečková, P. Machovčák, K. Gryc, P. Klus, K. Michalek, L. Socha, M. Kováč. Setting a numerical simulation of filling and solidification of heavy steel ingots based on real casting conditions. *Mater. Technol.*, vol. 46, **2012**, pp. 399–402.
- [39] P. Lan, J. Zhang. Numerical analysis of macrosegregation and shrinkage porosity in large steel ingot. *Ironmaking Steelmaking*, vol. 41, **2014**, pp. 598–606.
- [40] M. Riedler, S. Michelic, C. Bernhard. Formation of shrinkage porosity during solidification of steel: Numerical simulation and experimental validation. *IOP Conf. Ser.: Mater. Sci. Eng.*, vol. 143, **2016**, 012035.
- [41] J. Yang, Y. Wang, H. Shen, B. Liu. Numerical simulation of central shrinkage crack formation in a 234-t steel ingot. *China Foundry*, vol. 14, **2017**, pp. 365–372.
- [42] M. Riedler, S. Michelic, C. Bernhard. Numerical simulation and experimental validation of the formation of shrinkage cavity during solidification of steel. *25<sup>th</sup> Anniv. Int. Conf. Metall. Mater.*, **2016**, pp. 97–103.
- [43] G. Ehlen, A. Ludwig, P. Sahn, A. Bührig-Polaczek. Split-solid-model to simulate the formation of shrinkage cavities and macrosegregations in steel casting. *Model. Cast., Weld. Adv. Solidif. Processes X, Proc. Int. Conf. 10<sup>th</sup>*, Destin, FL, USA, **2003**, 285.
- [44] L. Hartmann, C. Ernst, J. Klung. Simulation of ingot casting processes at Deutsche Edelstahlwerke GmbH®. *IOP Conf. Ser.: Mater. Sci. Eng.*, vol. 27, **2012**, 012063.
- [45] J. Odehnal, P. Ludvík, T. Studecký, P. Michálek. Development of universal mould geometry for the teeming of cylindrical iron-base alloy ingots. *Metals*, vol. 11, **2021**, 471.
- [46] K.D. Carlson, C. Beckermann. Prediction of shrinkage pore volume fraction using a dimensionless Niyama criterion. *Metall. Mater. Trans. A*, vol. 40, **2009**, pp. 163–175.
- [47] J. Wang, P. Fu, H. Liu, D. Li, Y. Li. Shrinkage porosity criteria and optimized design of a 100-ton 30Cr2Ni4MoV forging ingot. *Mater. Des.*, vol. 35, **2012**, pp. 446–456.
- [48] S. Qian, X. Hu, Y. Cao, X. Kang, D. Li. Hot top design and its influence on feeder channel segregates in 100-ton steel ingots. *Mater. Des.*, vol. 87, **2015**, pp. 205–214.
- [49] N. Ghodrati, M. Baiteche, A. Loucif, P.I. Gallego, M. Jean-Benoit, M. Jahazi. Influence of hot top height on macrosegregation and material yield in a large-size cast steel ingot using modeling and experimental validation. *Metals*, vol. 12, **2022**, 1906.
- [50] N.Y. Kim, D.C. Ko, Y. Kim, S.W. Han, I.Y. Oh, Y.H. Moon. Feasibility of reduced ingot hot-top height for the cost-effective forging of heavy steel ingots. *Materials*, vol. 13, **2020**, 2916.
- [51] J. Laing. Machine for making pipes of lead and other soft metals. *US Patent No.3023*, **1843**.

- [52] H. Bessemer. *British Patent No. 11317*, **1846**.
- [53] S. Mizoguchi, T. Ohashi, T. Saeki. Continuous casting of steel. *Annu. Rev. Mater. Sci.*, vol. 11, **1981**, pp. 151–169.
- [54] S. Louhenkilpi. Continuous casting of steel. *Treatise Process Metall.*, Elsevier, **2014**, pp. 373–434.
- [55] R. Vertnik, K. Mramor, B. Šarler. Solution of three-dimensional temperature and turbulent velocity field in continuously cast steel billets with electromagnetic stirring by a meshless method. *Eng. Anal. Boundary Elem.*, vol. 104, **2019**, pp. 347–363.
- [56] G. Arth, M. Taferner, C. Bernhard, S. Michelic. Experimental und numerical investigations on cooling efficiency of Air-Mist nozzles on steel during continuous casting. *IOP Conf. Ser.: Mater. Sci. Eng.*, vol. 143, **2016**, 012033.
- [57] J. Zhang, D. Chen, C. Zhang, S. Wang, W. Hwang, M. Han. Effects of an even secondary cooling mode on the temperature and stress fields of round billet continuous casting steel. *J. Mater. Process. Technol.*, vol. 222, **2015**, pp. 315–326.
- [58] W. Poppmeier, B. Tarmann, O. Schaaber. Application of alternating electromagnetic fields in the continuous casting of steel. *JOM*, vol. 18, **1966**, pp. 1109–1114.
- [59] H. Takeuchi, Y. Ikehara, T. Yanai, S. Marsumura. Quality improvement of continuously cast stainless steel blooms through electromagnetic stirring. *Tran. Iron Steel Inst. Jpn.*, vol. 63, **1977**, pp. 1287–1296.
- [60] S.H. Asai, N.O. Nishio, I.W. Muchi. Theoretical analysis and model experiments on electromagnetically driven flow in continuous casting. *Tran. Iron Steel Inst. Jpn.*, vol. 22, **1982**, pp. 126–133.
- [61] A.A. Tzavaras, H.D. Brody. Electromagnetic stirring and continuous casting—achievements, problems, and goals. *JOM*, vol. 36, **1984**, pp. 31–37.
- [62] K. Ayata, T. Mori, T. Fujimoto, T. Ohnishi, I. Wakasugi. Improvement of macrosegregation in continuously cast bloom and billet by electromagnetic stirring. *Tran. Iron Steel Inst. Jpn.*, vol. 24, **1984**, pp. 931–939.
- [63] K.I. Suzuki, Y. Shinsho, K. Murata, K. Nakanishi, M. Kodama. Hot model experiments on electromagnetic stirring at about crater end of continuously cast bloom. *Tran. Iron Steel Inst. Jpn.*, vol. 24, **1984**, pp. 940–949.
- [64] K.H. Spitzer, M. Dubke, K. Schwerdtfeger. Rotational electromagnetic stirring in continuous casting of round strands. *Metall. Trans. B*, vol. 17, **1986**, pp. 119–131.
- [65] N. Genma, T. Soejima, T. Saito, M. Kimura, Y. Kaihara, H. Fukumoto, K. Ayata. The linear-motor type in-mold electromagnetic stirring technique for the slab continuous caster. *ISIJ Int.*, vol. 29, **1989**, pp. 1056–1062.
- [66] K.S. Oh, Y. Chang. Macrosegregation behavior in continuously cast high carbon steel blooms and billets at the final stage of solidification in combination stirring. *ISIJ Int.*, vol. 35, **1995**, pp. 866–875.
- [67] S. Kunstreich. Electromagnetic stirring for continuous casting - part 2. *Metall. Res. Technol.*, vol.100, **2003**, pp. 1043–1061.
- [68] Y. Itoh, T. Okajima, H. Maede, K. Tashiro. Refining of solidification structures of continuously cast type 430 stainless steel slabs by electromagnetic stirring. *Tran. Iron Steel Inst. Jpn.*, vol. 22, **1982**, pp. 223–229.

- [69] J.L. Meyer, N. El-Kaddah, J. Szekely, C. Vives, R. Ricou. A comprehensive study of the induced current, the electromagnetic force field, and the velocity field in a complex electromagnetically driven flow system. *Metall. Trans. B*, vol. 18, **1987**, pp. 529–538.
- [70] L. Beitelman. Effect of mold EMS design on billet casting productivity and product quality. *Can. Metall. Q.*, vol. 38, **1999**, pp. 301–309.
- [71] H.K. Moffatt. Electromagnetic stirring. *Phys. Fluids A*, vol. 3, **1991**, pp. 1336–1343.
- [72] H. An, Y. Bao, M. Wang, Q. Yang. Electromagnetic torque detecting for optimization of in-mould electromagnetic stirring in the billet and bloom continuous casting. *Ironmaking Steelmaking*, vol. 46, **2019**, pp. 845–854.
- [73] M. Dubke, K.H. Tacke, K.H. Spitzer, K. Schwerdtfeger. Flow fields in electromagnetic stirring of rectangular strands with linear inductors: part I. theory and experiments with cold models. *Metall. Trans. B*, vol. 19, **1988**, pp. 581–593.
- [74] S.I. Shakhov, K.N. Vdovin. Electromagnetic stirring in continuous-casting machines. *Steel Transl.*, vol. 49, **2019**, pp. 261–264.
- [75] S. Kunstreich. Electromagnetic stirring for continuous casting. *Mater. Res. Technol.*, vol. 100, **2003**, pp. 395–408.
- [76] K. Fujisaki, S. Satoh, T. Yamada. Consideration of heat transfer and solidification in 3-D MHD calculation. *IEEE Trans. Magn.*, vol. 36, **2000**, pp. 1300–1304.
- [77] J. Kubota, N. Kubo, T. Ishii, M. Suzuki, N. Aramaki, R. Nishimachi. Steel flow control in continuous slab caster mold by traveling magnetic field. *NKK Tech. Rev.(Jpn.)*, vol. 85, **2001**, pp. 1–9.
- [78] S.W. Han, H.J. Cho, S.Y. Jin, M. Sedén, I.B. Lee, I. Sohn. Effects of simultaneous static and traveling magnetic fields on the molten steel flow in a continuous casting mold. *Metall. Mater. Trans. B*, vol. 49, **2018**, pp. 2757–2769.
- [79] S.M. Cho, B.G. Thomas. Electromagnetic forces in continuous casting of steel slabs. *Metals*, vol. 9, **2019**, 471.
- [80] K. Okazawa, T. Toh, J. Fukuda, T. Kawase, M. Toki. Fluid flow in a continuous casting mold driven by linear induction motors. *ISIJ Int.*, vol. 41, **2001**, pp. 851–858.
- [81] H. Yu, M. Zhu. Influence of electromagnetic stirring on transport phenomena in round billet continuous casting mould and macrostructure of high carbon steel billet. *Ironmaking Steelmaking*, vol. 39, **2012**, pp. 574–584.
- [82] Z. Yang, B. Wang, X. Zhang, Y. Wang, H. Dong, Q. Liu. Effect of electromagnetic stirring on molten steel flow and solidification in bloom mold. *J. Iron Steel Res. Int.*, vol. 21, **2014**, pp. 1095–1103.
- [83] B. Ren, D. Chen, H. Wang, M. Long, Z. Han. Numerical simulation of fluid flow and solidification in bloom continuous casting mould with electromagnetic stirring. *Ironmaking Steelmaking*, vol. 42, **2015**, pp. 401–408.
- [84] B. Ren, D. Chen, H. Wang, M. Long. Numerical analysis of coupled turbulent flow and macroscopic solidification in a round bloom continuous casting mold with electromagnetic stirring. *Steel Res. Int.*, vol. 86, **2015**, pp. 1104–1115.

- [85] B. Yang, A. Deng, Y. Li, X. Xu, E. Wang. Numerical simulation of flow and solidification in continuous casting process with mold electromagnetic stirring. *J. Iron Steel Res. Int.*, vol. 26, **2019**, pp. 219–229.
- [86] V.K. Gupta, P.K. Jha, P.K. Jain. Numerical investigation into flow and solidification behavior of billet continuous casting with and without mold electromagnetic stirring. *Heat Transf.*, vol. 51, **2022**, pp. 909–928.
- [87] T. Campanella, C. Charbon, M. Rappaz. Grain refinement induced by electromagnetic stirring: a dendrite fragmentation criterion. *Metall. Mater. Trans. A*, vol. 35, **2004**, pp. 3201–3210.
- [88] H. Wu, N. Wei, Y. Bao, G. Wang, C. Xiao, J. Liu. Effect of M-EMS on the solidification structure of a steel billet. *Int. J. Miner., Metall. Mater.*, vol. 18, **2011**, pp. 159–164.
- [89] X. Geng, X. Li, F. Liu, H. Li, Z. Jiang. Optimisation of electromagnetic field and flow field in round billet continuous casting mould with electromagnetic stirring. *Ironmaking Steelmaking*, vol. 42, **2015**, pp. 675–682.
- [90] H. An, Y. Bao, M. Wang, L. Zhao. Effects of electromagnetic stirring on fluid flow and temperature distribution in billet continuous casting mould and solidification structure of 55SiCr. *Metall. Res. Technol.*, vol. 115, **2018**, 103.
- [91] Y. Wang, L. Zhang, W. Yang, S. Ji, Y. Ren. Effect of mold electromagnetic stirring and final electromagnetic stirring on the solidification structure and macrosegregation in bloom continuous casting. *Steel Res. Int.*, vol. 92, **2021**, 2000661.
- [92] D. Jiang, L. Zhang, Y. Wang. Effect of mold electromagnetic stirring on solidification structure and solute segregation in continuous casting bloom. *J. Iron Steel Res. Int.*, vol. 29, **2022**, pp. 124–131.
- [93] H. Yu, M. Zhu. Effect of electromagnetic stirring in mold on the macroscopic quality of high carbon steel billet. *Acta Metall. Sin. (Engl. Lett.)*, vol. 22, **2009**, pp. 461–467.
- [94] B. Wang, W. Chen, Y. Chen, Y. Feng. Coupled numerical simulation on electromagnetic field and flow field in the round billet mould with electromagnetic stirring. *Ironmaking Steelmaking*, vol. 42, **2015**, pp. 63–69.
- [95] D. Jiang, L. Zhang. A new method to reduce the shielding effect of copper mold in the bloom continuous casting with M-EMS. *JOM*, vol. 74, **2022**, pp. 1601–1609.
- [96] Y. Xu, X. Xu, Z. Li, T. Wang, A. Deng, E. Wang. Dendrite growth characteristics and segregation control of bearing steel billet with rotational electromagnetic stirring. *High Tem. Mater. Processes*, vol. 36, **2017**, pp. 339–346.
- [97] H. Liu, Y. Chen, H. Qiu, Z. Wang. Numerical simulation of coupled fluid flow and solidification in a curved round bloom continuous caster with a combined rotary electromagnetic stirring. *Ironmaking Steelmaking*, vol. 49, **2022**, pp. 506–521.
- [98] M.R. Bridge, G.D. Rogers. Structural effects and band segregate formation during the electromagnetic stirring of strand-cast steel. *Metall. Trans. B*, vol. 15, **1984**, pp. 581–589.
- [99] C. Xiao, J. Zhang, Y. Luo, X. Wei, L. Wu, S. Wang. Control of macrosegregation behavior by applying final electromagnetic stirring for continuously cast high carbon steel billet. *J. Iron Steel Res. Int.*, vol. 20, **2013**, pp. 13–20.

- [100] S. Luo, F. Piao, D. Jiang, W. Wang, M. Zhu. Numerical simulation and experimental study of F-EMS for continuously cast billet of high carbon steel. *J. Iron Steel Res. Int.*, vol. 21, **2014**, pp. 51–55.
- [101] Y. Xu, R. Xu, Z. Fan, C. Li, A. Deng, E. Wang. Analysis of cracking phenomena in continuous casting of 1Cr13 stainless steel billets with final electromagnetic stirring. *Int. J. Miner., Metall. Mater.*, vol. 23, **2016**, pp. 534–541.
- [102] S. Shakhov. Methodology for development and testing of electromagnetic stirring systems in billet and bloom CCMs. *Metallurgist*, vol. 65, **2021**, pp. 368–374.
- [103] F. Wimmer, H. Thöne, P. Pennerstorfer. New vertical bloom caster. *Metall. Res. Technol.*, vol. 112, **2015**, 101.
- [104] L. Zhang, C. Xu, C. Wang, T. Wang, X. Zhang, H. Wu. The simulation of mould metallurgical behaviour under electromagnetic stirring for vertical large bloom. *Ironmaking Steelmaking*, vol. 48, **2021**, pp. 1220–1225.
- [105] H. Wu, C. Xu, C. Lei, T. Wang, Y. Gao, X. Zhang, H. Jin. Numerical simulation and industrial experiment of the fluid flow and heat transfer in large vertical round billets with helical final electromagnetic stirring. *JOM*, **2022**, pp. 1–11.
- [106] L. Zhang, C. Xu, J. Zhang, T. Wang, J. Li, S. Li. The simulation and optimization of an electromagnetic field in a vertical continuous casting mold for a large bloom. *Metals*, vol. 10, **2020**, 516.
- [107] T. Wang, L. Zhang, H. Wu, X. Zhang, Y. Jin, P. Yang, C. Xu. Effect of mold electromagnetic stirring on the flow and solidification of  $\Phi$  800 mm round blooms. *Processes*, vol. 10, **2022**, 430.
- [108] H. Wu, C. Xu, H. Jin, Y. Gao, X. Zhang, Y. Jin. Effect of different positions of final electromagnetic stirring for  $\phi$ 800mm vertical round billet on fluid flow and heat transfer. *Appl. Phys. A: Mater. Sci. Process.*, vol. 128, **2022**, 108.
- [109] K.S. Oh, J.S. Lee, S.J. Kim, J.Y. Choi. Development of a large ingot continuous caster. *Metall. Res. Technol.*, vol. 112, **2015**, 203.
- [110] S. Lee. State of the Art Technology in Slab Continuous Casting. *Berg Hüttenmänn. Monatsh.*, vol. 163, **2018**, pp. 3–10.
- [111] M. Knabl, K. Eynatten, M. Kubin, A. Scheriau, H. Holzgruber. Supersized ESR—strategies for a further optimization and size increase of the process. *Berg Hüttenmänn. Monatsh.*, vol. 163, **2018**, pp. 355–360.
- [112] J. Dong, J. Cui, Q. Le, G. Lu. Liquidus semi-continuous casting, reheating and thixoforming of a wrought aluminum alloy 7075. *Mater. Sci. Eng: A*, vol. 345, **2003**, pp. 234–242.
- [113] R. Nadella, D. Eskin, Q. Du, L. Katgerman. Macrosegregation in direct-chill casting of aluminium alloys. *Prog. Mater. Sci.*, vol. 53, **2008**, pp. 421–480.
- [114] Z. Shao, Q. Le, Z. Zhang, J. Cui. A new method of semi-continuous casting of AZ80 Mg alloy billets by a combination of electromagnetic and ultrasonic fields. *Mater. Des.*, vol. 32, **2011**, pp. 4216–4224.
- [115] D. Eskin, A. Jafari, L. Katgerman. Contribution of forced centreline convection during direct chill casting of round billets to macrosegregation and structure of binary Al–Cu aluminium alloy. *Mater. Sci. Technol.*, vol. 27, **2011**, pp. 890–896.
- [116] A. Kazup, V. Karpati, B. Hegedus, Z. Gacsi. Semi-continuous casting and microstructure investigation of the AlSi12 alloy. *IOP Conf. Ser.: Mater. Sci. Eng.*, vol. 903, **2020**, 012012.

- [117] V. Karpati, B. Hegedus, A. Kazup, T. Ferenczi, D. Molnar, Z. Gacsi. Semi-continuous casting of aluminium alloys. *IOP Conf. Ser.: Mater. Sci. Eng.*, vol. 903, **2020**, 012017.
- [118] H. Jiang, H. Zhang, Q. Ke, J. Cui. Direct-chill semi-continuous casting process of three-layer composite ingot of 4045/3004/4045 aluminum alloys. *Trans. Nonferrous Met. Soc. China*, vol. 21, **2011**, pp. 1692–1697.
- [119] S. Guo, J. Cui, Q. Le, Z. Zhao. The effect of alternating magnetic field on the process of semi-continuous casting for AZ91 billets. *Mater. Lett.*, vol. 59, **2005**, pp. 1841–1844.
- [120] X. Chen, Y. Jia, Q. Liao, W. Jia, Q. Le, S. Ning, F. Yu. The simultaneous application of variable frequency ultrasonic and low frequency electromagnetic fields in semi continuous casting of AZ80 magnesium alloy. *J. Alloys Compd*, vol. 774, **2019**, pp. 710–720.
- [121] J. Ni, C. Beckermann. A volume-averaged two-phase model for transport phenomena during solidification. *Metall. Trans. B*, vol. 22, **1991**, pp. 349–361.
- [122] C. Beckermann, R. Viskanta. Mathematical modeling of transport phenomena during alloy solidification. *Appl. Mech. Res.*, vol. 46, **1993**, pp. 1–27.
- [123] C. Beckermann. Modeling segregation and grain structure development in equiaxed solidification with convection. *JOM*, vol. 49, **1997**, pp. 13–17.
- [124] A. Ludwig, M. Wu. Modeling of globular equiaxed solidification with a two-phase approach. *Metall. Mater. Trans. A*, vol. 33, **2002**, pp. 3673–3383.
- [125] M. Wu, A. Ludwig, A. Bührig-Polaczek, M. Fehlbier, P.R. Sahm. Influence of convection and grain movement on globular equiaxed solidification. *Int. J. Heat Mass Transf.*, vol. 46, **2003**, pp. 2819–2832.
- [126] M. Wu, A. Ludwig. A three-phase model for mixed columnar-equiaxed solidification. *Metall. Mater. Trans. A*, vol. 37, **2006**, pp. 1613–31.
- [127] M. Wu, A. Ludwig. Using a three-phase deterministic model for the columnar-to-equiaxed transition. *Metall. Mater. Trans. A*, vol. 38, **2007**, pp. 1465–1475.
- [128] M. Wu, A. Fjeld, A. Ludwig. Modelling mixed columnar-equiaxed solidification with melt convection and grain sedimentation—Part I: Model description. *Comput. Mater. Sci.*, vol. 50, **2010**, pp. 32–42.
- [129] J. Li, M. Wu, J. Hao, A. Ludwig. Simulation of channel segregation using a two-phase columnar solidification model—Part I: Model description and verification. *Comput. Mater. Sci.*, vol. 55, **2012**, pp. 407–418.
- [130] M. Wu, A. Ludwig, A. Kharicha. A four phase model for the macrosegregation and shrinkage cavity during solidification of steel ingot. *Appl. Math. Modell.*, vol. 41, **2017**, pp. 102–120.
- [131] M. Wu, A. Ludwig, A. Kharicha. Volume-averaged modeling of multiphase flow phenomena during alloy solidification. *Metals*, vol. 9, **2019**, 229.
- [132] N. Ahmad, J. Rappaz, J.L. Desbiolles, T. Jalanti, M. Rappaz, H. Combeau, G. Lesoult, C. Stomp. Numerical simulation of macrosegregation: a comparison between finite volume method and finite element method predictions and a confrontation with experiments. *Metall. Mater. Trans. A*, vol. 29, **1998**, pp. 617–630.
- [133] H. Combeau, M. Založnik, S. Hans, P.E. Richy. Prediction of macrosegregation in steel ingots: Influence of the motion and the morphology of equiaxed grains. *Metall. Mater. Trans. B*, vol. 40, **2009**, pp. 289–304.



- [134] A. Kumar, M. Založnik, H. Combeau. Prediction of equiaxed grain structure and macrosegregation in an industrial steel ingot: comparison with experiment. *Int. J. Adv. Eng. Sci. Appl. Math.*, vol. 2, **2010**, pp. 140–148.
- [135] A. Kumar, M. Založnik, H. Combeau. Study of the influence of mushy zone permeability laws on macro- and meso-segregations predictions. *Int. J. Therm. Sci.*, vol. 54, **2012**, pp. 33–47.
- [136] Y. Souhar, V. F. De Felice, C. Beckermann, H. Combeau, M. Založnik. Three-dimensional mesoscopic modeling of equiaxed dendritic solidification of a binary alloy. *Comput. Mater. Sci.*, vol. 112, **2016**, pp. 304–317.
- [137] A.B. Phillion, M. Založnik, I. Spindler, N. Pinter, C.A. Aledo, G. Salloum-Abou-Jaoude, H.N. Thi, G. Reinhart, G. Boussinot, M. Apel, H. Combeau. Evolution of a mushy zone in a static temperature gradient using a volume average approach. *Acta Materialia*, vol. 141, **2017**, pp. 206–216.
- [138] K.O. Tveito, A. Pakanati, M. M'hamdi, H. Combeau, M. Založnik. A simplified three-phase model of equiaxed solidification for the prediction of microstructure and macrosegregation in castings. *Metall. Mater. Trans. A*, vol. 49, **2018**, pp. 2778–2794.
- [139] A. Pakanati, K.O. Tveito, M. M'hamdi, H. Combeau, M. Založnik. Application of an equiaxed grain growth and transport model to study macrosegregation in a DC casting experiment. *Metall. Mater. Trans. A*, vol. 50, **2019**, pp. 1773–1786.
- [140] S. Sachi, M. Založnik, H. Combeau, C.A. Gandin, M. Genneson, J. Demurger, M. Stoltz, I. Poitroult. Analysis of columnar-to-equiaxed transition experiment in lab scale steel casting by a multiphase model. *IOP Conf. Ser.: Mater. Sci. Eng.*, vol. 529, **2019**, 012039.
- [141] M. Rappaz. Modelling of microstructure formation in solidification processes. *Int. Mater. Rev.*, vol. 34, **1989**, pp. 93–124.
- [142] Y. Zheng, M. Wu, A. Kharicha, A. Ludwig. Incorporation of fragmentation into a volume average solidification model. *Modell. Simul. Mater. Sci. Eng.*, vol. 26, **2017**, 015004.
- [143] H. Zhang, M. Wu, C.M. Rodrigues, A. Ludwig, A. Kharicha, A. Rónaföldi, A. Roósz, Z. Veres, M. Svéda. Dendrite fragmentation mechanism under forced convection condition by rotating magnetic field during unidirectional solidification of AlSi7 alloy. *Acta Materialia*, vol. 241, **2022**, 118391.
- [144] H. Zhang, M. Wu, P. Schumacher, C.M. Rodrigues, A. Ludwig, A. Kharicha. Modelling melting and grain destruction phenomena during globular equiaxed solidification. *Appl. Math. Modell.*, vol. 97, **2021**, pp. 821–838.
- [145] J. Lipton, M.E. Glicksman, W. Kurz. Dendritic growth into undercooled alloy metals. *Mater. Sci. Eng.*, vol. 65, **1984**, pp. 57–63.
- [146] A. Noeppel, A. Ciobanas, X. Wang, K. Zaidat, N. Mangelinck, O. Budenkova, A. Weiss, G. Zimmermann, Y. Fautrelle. Influence of forced/natural convection on segregation during the directional solidification of Al-based binary alloys. *Metall. Mater. Trans. B*, vol. 41, **2010**, pp. 193–208.
- [147] J.K. Roplekar, J.A. Dantzig. A study of solidification with a rotating magnetic field. *Int. J. Cast Metals Res.*, vol. 14, **2001**, pp. 79–95.

- [148] H. Zhang, M. Wu, Z. Zhang, A. Ludwig, A. Kharicha, A. Rónaföldi, A. Roósz, Z. Veres, M. Svéda. Experimental evaluation of MHD modeling of EMS during continuous casting. *Metall. Mater. Trans. B*, vol. 53, **2022**, pp. 2166–2181.
- [149] P.A. Davidson, J.C. Hunt. Swirling recirculating flow in a liquid-metal column generated by a rotating magnetic field. *J. Fluid Mech.*, vol. 185, **1987**, pp. 67–106.
- [150] ANSYS Fluent. Magnetohydrodynamics (MHD) module manual, **2009**.
- [151] M. Javurek, M. Barna, P. Gittler, K. Rockenschaub, M. Lechner. Flow modelling in continuous casting of round bloom strands with electromagnetic stirring. *Steel Res. Int.*, vol. 79, **2008**, pp. 617–626.
- [152] P.A. Galdiz, J.U. Palacios, J.L. Arana, B.G. Thomas. Round continuous casting with EMS-CFD coupled. *Eur. Contin. Cast. Conf.*, Graz, Austria, **2014**.
- [153] H. Wang, M. Zhu, H. Yu. Numerical analysis of electromagnetic field and flow field in high casting speed slab continuous casting mold with traveling magnetic field. *J. Iron Steel Res. Int.*, vol. 17, **2010**, pp. 25–30.
- [154] S. Li, P. Lan, H. Tang, Z. Tie, J. Zhang. Study on the electromagnetic field, fluid flow, and solidification in a bloom continuous casting mold by numerical simulation. *Steel Res. Int.*, vol. 89, **2018**, 1800071.
- [155] S. Li, Z. Han, J. Zhang. Numerical modeling of the macrosegregation improvement in continuous casting blooms by using F-EMS. *JOM*, vol. 72, **2020**, pp. 4117–4126.
- [156] W. Zhang, S. Luo, Y. Chen, W. Wang, M. Zhu. Numerical simulation of fluid flow, heat transfer, species transfer, and solidification in billet continuous casting mold with M-EMS. *Metals*, vol. 9, **2019**, 66.
- [157] Y. Wang, L. Zhang, W. Chen, Y. Ren. Three-dimensional macrosegregation model of bloom in curved continuous casting process. *Metall. Mater. Trans. B*, vol. 52, **2021**, pp. 2796–2805.
- [158] Q. Fang, H. Zhang, J. Wang, P. Zhao, G. Wu, H. Ni. Effect of final electromagnetic stirring on flow, solidification, and solute transport in continuous casting bloom. *JOM*, vol. 73, **2021**, pp. 2698–2708.
- [159] B. Ren, D. Chen, W. Xia, H. Wang, Z. Han. Numerical simulation of electromagnetic field in round bloom continuous casting with final electromagnetic stirring. *Metals*, vol. 8, **2018**, 903.
- [160] D.J. Hebditch, J.D. Hunt. Observations of ingot macrosegregation on model systems. *Metall. Mater. Trans. B*, vol. 5, **1974**, pp. 1557–1564.
- [161] L. Hachani, K. Zaidat, Y. Fautrelle. Experimental study of the solidification of Sn–10 wt.% Pb alloy under different forced convection in benchmark experiment. *Int. J. Heat Mass Transf.*, vol. 85, **2015**, pp. 438–454.
- [162] A. Ludwig, M. Stefan-Kharicha, A. Kharicha, M. Wu. Massive formation of equiaxed crystals by avalanches of mushy zone segments. *Metall. Mater. Trans. A*, vol. 48, **2017**, pp. 2927–2931.
- [163] A. Rónaföldi: Hungary University of Miskolc, Hungary, doctoral dissertation, **2008**.
- [164] A. Rónaföldi, A. Roósz, Z. Veres. Determination of the conditions of laminar/turbulent flow transition using pressure compensation method in the case of Ga75In25 alloy stirred by RMF. *J. Crystal Growth*, vol. 564, **2021**, 126078.

## **Part II: Publications**



**Paper included in this thesis (hyperlinked to the pdf-file of each article):**

- [1] **Z. Zhang**, M. Wu, H. Zhang, S. Hahn, F. Wimmer, A. Ludwig, A. Kharicha. [Modeling of the as-cast structure and macrosegregation in the continuous casting of a steel billet: Effect of M-EMS](#). *J. Mater. Process. Technol.*, vol. 301, 2022, pp. 117434.
- [2] **Z. Zhang**, M. Wu, H. Zhang, A. Ludwig, A. Kharicha. [The role of mold electromagnetic stirring in the dissipation of superheat during the continuous casting of billets](#). *Steel Res. Int.*, vol. 93, 2022, pp. 2200065.
- [3] **Z. Zhang**, M. Wu, H. Zhang, A. Ludwig, A. Kharicha. Effect of forced convection on the formation of the as-cast structure and macrosegregation of Sn-10wt.% Pb alloy: a numerical study. *Int. J. Heat Mass Transf.*, accepted and in press.
- [4] **Z. Zhang**, M. Wu, H. Zhang, S. Hahn, F. Wimmer, A. Ludwig, A. Kharicha. Solidification principle in large vertical steel casting under the effect of EMS, *Metall. Mater. Trans. B*, under review.
- [5] H. Zhang, M. Wu, **Z. Zhang**, A. Ludwig, A. Kharicha, A. Rónaföldi, A. Roósz, Z. Veres, M. Svéda. [Experimental evaluation of MHD modeling of EMS during continuous casting](#). *Metall. Mater. Trans. B*, vol. 53, 2022, pp. 2166–2181.

**Author’s contribution table**

	Idea	Model & simulation	Result analysis	Paper writing
Paper 1	80%	90%	90%	90%
Paper 2	90%	90%	80%	80%
Paper 3	90%	90%	90%	80%
Paper 4	80%	90%	80%	80%
Paper 5	50%	50%	50%	50%

## Paper not included in this thesis

- [6] **Z. Zhang**, M. Wu, H. Zhang, E. Karimi-Sibaki, A. Ludwig, A. Kharicha. [Modeling mixed columnar-equiaxed solidification of Sn-10wt. % Pb alloy under forced convection driven by travelling magnetic stirring](#). *IOP Conf. Ser.: Mater. Sci. Eng.*, vol. 861, 2020, pp. 012024.
- [7] H. Zhang, M. Wu, **Z. Zhang**, A. Ludwig, A. Kharicha. [Influence of crystal fragmentation on the formation of microstructure and macrosegregation during directional solidification under forced convection condition](#). *IOP Conf. Ser.: Mater. Sci. Eng.*, vol. 861, 2020, pp. 012048.
- [8] A. Ludwig, C. M. G. Rodrigues, **Z. Zhang**, H. Zhang, E. Karimi-Sibaki, H. Barati, A. Vakhrushev, M. Al-Nasser, M. Wu, A. Kharicha. [Important key process simulations in the field of steel metallurgy](#). *Berg Hüttenmänn. Monatsh.*, vol. 167, 2022, pp. 2–9.
- [9] M. Wu, **Z. Zhang**, H. Zhang, A. Ludwig, A. Kharicha. Flow-enhanced remelting of settling/floating globular crystals during mixed columnar-equiaxed solidification. *16<sup>th</sup> Int. Conf. Modell. Cast., Weld. Adv. Solidif. Processes*, 2023, Accepted.

## **Paper 1**

### **Modeling of the as-cast structure and macrosegregation in the continuous casting of a steel billet: Effect of M-EMS**

Zhao Zhang, Menghuai Wu, Haijie Zhang, Susanne Hahn,  
Franz Wimmer, Andreas Ludwig, Abdellah Kharicha

Journal of Materials Processing Technology

Volume 301, 2022, 117434







## Modeling of the as-cast structure and macrosegregation in the continuous casting of a steel billet: Effect of M-EMS

Zhao Zhang<sup>a</sup>, Menghuai Wu<sup>a,\*</sup>, Haijie Zhang<sup>a</sup>, Susanne Hahn<sup>b</sup>, Franz Wimmer<sup>b</sup>,  
Andreas Ludwig<sup>a</sup>, Abdellah Kharicha<sup>a</sup>

<sup>a</sup> Chair of Simulation and Modelling of Metallurgical Processes, Department of Metallurgy, University of Leoben, A-8700 Leoben, Austria

<sup>b</sup> Primetals Technologies Austria GmbH, Turmstrasse 44, A-4031 Linz, Austria

### ARTICLE INFO

Associate Editor: Prof. Alan A. Luo

#### Keywords:

M-EMS  
Continuous casting  
Billet  
Solidification  
As-cast structure  
Macrosegregation

### ABSTRACT

Mold electromagnetic stirring (M-EMS) has been introduced into the continuous casting of steel billets to promote the formation of a central equiaxed zone; however, the formation mechanism of the equiaxed crystals and the effect of M-EMS on crystal transport are not fully understood. Currently, a three-phase volume average model was used to study the solidification in a billet continuous casting (195 mm × 195 mm). The modeling results showed that the main function of M-EMS in this type of billet casting is to promote superheat dissipation in the mold region, leaving the liquid core out of the mold region undercooled. Although both, heterogeneous nucleation and crystal fragmentation, are considered to be the origins of equiaxed crystals, M-EMS appeared to impact crystal fragmentation more effectively. A small portion of equiaxed crystals could be brought by the M-EMS induced swirling flow into the superheated zone (upper mold region) and remelted; most equiaxed crystals settled in the lower undercooled zone, where they continued to grow and form a central equiaxed zone. These simultaneous phenomena represent an important species/energy transport mechanism, influencing the as-cast structure and macrosegregation. Negative segregation occurred in the central equiaxed zone, positive segregation occurred at the border of the columnar zone, and a trail of negative segregation occurred in the subsurface region of the billet. Finally, parameter studies were performed, and it was found that the shielding effect of the copper mold, electrical isolation at the strand-mold interface, and relatively high electrical conductivity of the strand shell affect the M-EMS efficiency.

### 1. Introduction

The solidification of continuous casting is governed by extremely complex and co-related phenomena, including melt flow, heat transfer, species transport, formation of the initial strand shell in the mold region, formation of equiaxed crystals by nucleation and/or crystal fragmentation, and transport of the equiaxed crystals. According to Du et al. (2021), the solidification in the continuous casting also affects the strand-mold interfacial condition (friction state), which in turn influences the heat transfer and the build-up of stress and strain in the casting. A comprehensive review on the modeling and simulation of continuous casting was made by Thomas (2018). Mold electromagnetic stirring (M-EMS) has been introduced into continuous casting to optimize fluid flow and heat transfer, to obtain the desired strand quality. As early as 1980s, Ayata et al. (1984) performed series of field experiments to investigate the effect of electromagnetic stirring (EMS) on the

macrosegregation in continuously cast bloom and billet. A wider central equiaxed crystal zone with less negative segregation was obtained with the implementation of M-EMS. Kunstreich (2003a) presented a historical review of EMS in billet, bloom and slab casters as well as some physical mechanisms of electromagnetism and fluid flow. Meanwhile, the metallurgical principles (the stirring intensity, white band and center segregation) and a review of the industrial applications and results were presented by Kunstreich (2003b). However, theoretical interpretations to the early industry practice (plant trials and field experiments), regarding the functionalities of M-EMS in billet/bloom castings, sometimes led to confusion, because some casting results from the industry practice seemed contradictory. For example, Wang et al. (2014), based on a billet casting (185 mm × 185 mm) found that M-EMS alone could sufficiently increase the central equiaxed zone from 10 to 15 % in the non-stirring case to over 45 % with the M-EMS. Wu et al. (2011), based on a billet casting (160 mm × 200 mm) with M-EMS

\* Corresponding author.

E-mail address: [menghuai.wu@unileoben.ac.at](mailto:menghuai.wu@unileoben.ac.at) (M. Wu).

<https://doi.org/10.1016/j.jmatprotec.2021.117434>

Received 7 September 2021; Received in revised form 3 November 2021; Accepted 16 November 2021

Available online 19 November 2021

0924-0136/© 2021 The Author(s). Published by Elsevier B.V. This is an open access article under the CC BY license (<http://creativecommons.org/licenses/by/4.0/>).

alone, found that primary and secondary dendrite arm spacings decreased greatly as increasing the electromagnetic torque, which was beneficial to the columnar-to-equiaxed transition (CET). The center segregation and porosity of billets were reduced correspondingly. However, Ayata et al. (1984), based on another billet (125 mm × 125 mm), found that M-EMS alone could only work for middle carbon steel, and for the low and high carbon steels the M-EMS has to be combined with final electromagnetic stirring (F-EMS) to achieve the desired solidification result in the central equiaxed zone. Li et al. (2006), based on a bloom casting (380 mm × 280 mm) of high carbon steel, confirmed that M-EMS worked only in combination with F-EMS. There were even rare cases where M-EMS was not recommended. Wang et al. (2021), based on a bloom casting (510 mm × 390 mm) of 20CrMnTi steel, found that F-EMS alone (without M-EMS) was sufficient to achieve optimal casting result. Interestingly, a study of An et al. (2019), based on a bloom casting (220 mm × 260 mm), shown that in addition to the combination of M-EMS and F-EMS, a so-called mechanical soft reduction (MSR) had to be implemented to get desired quality in the central region of the bloom. Li et al. (2020) also suggested a hot-core heavy reduction rolling (HHR<sup>2</sup>) technology could be implemented during the continuous casting process. They found that both the microstructure homogeneity and uniformity of mechanical properties along the thickness of the plate were obviously improved by using the HHR<sup>2</sup> process. Du et al. (2008), based on a bloom casting (220 mm × 260 mm), found that the central segregation of blooms with the special combined electromagnetic stirring mode (i.e., M-EMS and F-EMS with alternating rotation direction) could be significantly reduced. A primary reason for the above contradictory results regarding M-EMS is as follows. For the commercial interest, some sensitive details about the casting process were protected from publications such as the casting format (dimensions and section geometry), M-EMS operation parameters, alloy details, and even casting parameters (temperature and speed). This missing information is critical for understanding this process. The main reason for the above contradictory results is that the formation mechanism of the equiaxed crystals and the effect of M-EMS on crystal transport are not fully understood.

It is not possible to observe the solidification process during continuous casting with field experiments owing to the harsh environment and high cost. Therefore, numerical modeling has become an effective tool for this purpose. The first numerical model, which combines the solutions of the Maxwell, Navier-Stokes, and  $k-\epsilon$  turbulence equations, was introduced by Spitzer et al. (1986). This early model provides valuable information for the initial stirrer design. Follow-up numerical studies focused on parameter optimization of the M-EMS process. An et al. (2018) used a three-dimensional mathematic model to investigate the effect of the applied electrical current density and frequency on melt flow. The inner quality of as-cast billet (180 mm × 180 mm) was significantly improved under the optimal parameter of 320 A and 3 Hz. Wang et al. (2020a) developed a coupled model to study the effect of stirrer position on electromagnetic field distribution, fluid flow, temperature distribution, inclusion removal and mold-level fluctuation in billet (180 mm × 220 mm) continuous casting. They found that the lower stirrer position could promote the superheat dissipation, reduce the probability of slag entrapment, and increase the removal ratio of inclusions. Trindade et al. (2002) investigated the shielding effect of copper mold based on a finite-element model, and found the increase of operating copper temperature gave rise to a magnetic field increase. Unfortunately, the above studies ignored solidification, which should be included in the solution.

The importance of considering solidification in numerical models for continuous casting has been addressed recently. Janik and Dyja (2004) used an enthalpy-based mixture model to analyze the temperature field and the growth of solid shell. They found that a three-dimensional numerical analysis is necessary because the heat flux density is not equal to zero in the casting direction. A coupled magnetohydrodynamic (MHD) model was used by Li et al. (2018) to study the characteristics of the electromagnetic field, turbulent flow, and solidification in the mold, and

it was demonstrated that the area of flow field influenced by M-EMS decreased remarkably when solidification was considered. Trindade et al. (2017) used a numerical model based on finite volume element method to investigate the fluid flow and temperature distribution. They found that M-EMS decreased the temperature in the strand center and locally reduced the shell thickness due to the increase of tangential velocity close to the walls. Zhang et al. (2019) used a multi-physical mathematical model to investigate the macro transport phenomena in a billet continuous casting. They found that the high-temperature zone shifted upward with increasing M-EMS current density, and the subsurface negative segregation due to the intensive wash effects of the flow on the initially solidified shell became more severe. Fang et al. (2017) used a multiphysics numerical model to study the effect of M-EMS on flow, temperature field, solidification behavior and solute concentration field in bloom casting (380 mm × 280 mm). They found that the distribution of temperature, solute, and solidified shell was more uniform in the M-EMS effective region. However, they did not find the improvement of the centerline segregation by the M-EMS in this bloom casting. Zappulla et al. (2020) used a multiphysics model to determine the realistic temperature and stress distributions in the solidifying shell of stainless steel. They found that the stresses arising during solidification of the stainless steel include a second subsurface compression peak through the shell thickness. A common drawback of previous models is that the multiphase nature of solidification was simplified. Only the formation of the strand shell was considered, while the formation of equiaxed crystals and their transport by the M-EMS-induced flow were ignored.

The importance of the proper implementation of M-EMS in solidification models was also numerically studied. For example, the copper mold has a lower electrical conductivity at the operating temperature (~150 °C) than at room temperature. This implies that the shielding effect of the copper mold on M-EMS could be overestimated by considering the electrical conductivity of the mold at room temperature. Sun and Zhang (2014) used a coupled mathematical model to study the macrosegregation and macroscale transport phenomena in the bloom continuous casting of high-carbon GCr 15 bearing steel. They found that the mold temperature should be set as 423 K to meet the real continuous casting condition. Thomas et al. (2015) performed several laboratory experiments, in combined with large eddy simulations (LESs) to investigate the effect of ruler electromagnetic braking (EMBr) on transient flow phenomena. They found that the flow stability problems with realistic conducting walls were lessened greatly compared to insulated walls. Wang et al. (2020b) observed that if the strand mold gap were ignored (i.e., ideal conductivity was assumed for the strand mold interface) in the bloom continuous casting with M-EMS, an unrealistic distribution (double peaks) of the electromagnetic force would be predicted along the casting direction.

In this study, a three-phase volume average model was used to study the mixed columnar-equiaxed solidification during the continuous casting of a billet. This study focused on the effect of M-EMS on the melt flow, heat and mass transfer, formation of the strand shell, and formation and transport of equiaxed crystals. The ultimate goal is to develop and validate a numerical tool that can predict the as-cast structure and macrosegregation in continuously cast steel billets.

## 2. Mathematical model

The industry process of continuous casting referred to a continuous production procedure for steel by solidification, but the formation of the as-cast structure and macrosegregation is by no means a steady state process, especially when complex melt flow under the effect of M-EMS is involved. Some early modeling approaches were based on the calculation of steady state thermal field to project the as-cast structural information in the strand, e.g., Peel and Pengelly (1968) predicted the solidification and temperature profile in the continuous casting of aluminium by solving the steady conduction equation, Laitinen and

Neittaanmäki (1988) used a steady-state nonlinear parabolic-type model to simulate the multiphase heat transfer during solidification in continuous casting of steel. A thin horizontal slice model based on the steady state thermal field was also recently used to study the mold transient heat transfer behavior, which was reported by Wang et al. (2012). However, when the dynamics of flow and solidification are of primary interest, the continuous casting process must be considered transiently. Thomas (2018) made a review of the state of the art in modeling these phenomena. And further emphasized the transient character in nature of the continuous casting process.

Schematic of continuous casting under the effect of M-EMS is shown in Fig. 1: (a) the start stage of casting with the zoom-in view of the mixed columnar-equiaxed solidification, (b) the quasi-steady stage of casting. Considering the transient nature of multiphase flow and structure formation, the solidification process must be modelled transiently, and the numerical calculation must be performed from the start stage until the quasi-steady state of the casting, i.e. when the casting is withdrawn till sufficient length ( $> 10.75$  m for the current casting format). When the process approaches quasi-steady state, the modeling results of the casting domain are analyzed with highlight.

### 2.1. Solidification model

A three-phase volume average model (Fig. 1 (a)), which was developed by Wu and Ludwig (2006), was used in this study. The governing equations of the solidification model, are summarized in Table 1, but descriptions of the source terms and exchange terms are presented by Wu and Ludwig (2006) in detail elsewhere. Main features/assumptions are as follows.

(1) The three phases are the steel melt ( $f_l$ ), the columnar phase ( $f_c$ ) from which the strand shell is built, and the equiaxed crystal grains, which are treated as an additional disperse continuum phase ( $f_e$ ). Their volume fractions sum up to one.

(2) The columnar phase is assumed to develop directly from the strand surface. The position of the columnar tip front is traced dynamically according to the Lipton-Glicksman-Kurz model reported by Lipton et al. (1984). The columnar phase moves at a predefined casting velocity.

(3) The equiaxed grains originate from two mechanisms: heterogeneous nucleation and crystal fragmentation. The former occurs by activating the existing nucleation seeds (inoculants) with the necessary

undercooling, and the latter described by Zheng et al. (2018) is based on the flow-enhanced remelting of dendrites near the columnar tip front.

(4) A simplified envelope scheme described by Wu et al. (2019) is used to treat the dendrite morphology of the equiaxed grains. The volume ratio of the solid dendrite to the equiaxed grain envelope ( $f_{si}$ ) is set to 0.3. Remelting of equiaxed grains is considered. According to Zhang et al. (2021), only the diffusion-controlled dissolution is considered in the current study, the thermally-controlled melting process described by Han and Hellawell (1997) is ignored due to the relatively lower superheat in the current casting process.

(5) The CET occurs when the volume fraction of the equiaxed grain envelope reaches the criterion ( $f_e^{env} = f_e/f_{si} = 0.49$ ) at the columnar tip front.

(6) Solidification shrinkage is ignored, and the thermosolutal convection is modelled using the Boussinesq approach.

(7) Volume-averaged concentrations of the melt ( $c_l$ ), equiaxed grains ( $c_e$ ), and columnar dendrites ( $c_c$ ) are calculated. The macrosegregation is characterized by the segregation index  $c_{mix}^{index} = (c_{mix} - c_0) \times 100/c_0$ , where  $c_0$  is the initial concentration and  $c_{mix}$  is the mixture concentration,  $c_{mix} = (f_l \rho_l c_l + f_e \rho_e c_e + f_c \rho_c c_c) / (f_l \rho_l + f_e \rho_e + f_c \rho_c)$ .

(8) The M-EMS-induced Lorentz force is calculated based on the Maxwell equations and added to the momentum equations of both, liquid melt and equiaxed phase. Due to the electromagnetic field period being much shorter than the momentum response time of the liquid/equiaxed phases, the Lorentz force (Eq. (26)) is time-averaged, which was described in detail by Li et al. (2019). In addition, to consider the effect of fluid flow on the electromagnetic field, the Lorentz force is modified by considering a factor that is related to the relative velocity between the rotational magnetic field and the tangential velocity of the melt/equiaxed phase, Eq. (7) in Table 1.

### 2.2. Model implementation of billet casting

A schematic of billet continuous casting with M-EMS is shown in Fig. 2. The steel composition was Fe-C-Cr-Mn, but was simplified as a binary alloy with a nominal carbon concentration of 0.53 wt.%. The material properties and operational parameters are listed in Table 2. The casting geometry (195 mm  $\times$  195 mm) corresponded to that of an industrial process. The calculation domain was limited to only 12 m from the meniscus, which covers the mold region and three subsequent secondary cooling zones (Z1 - Z3). A five-port submerged entry nozzle

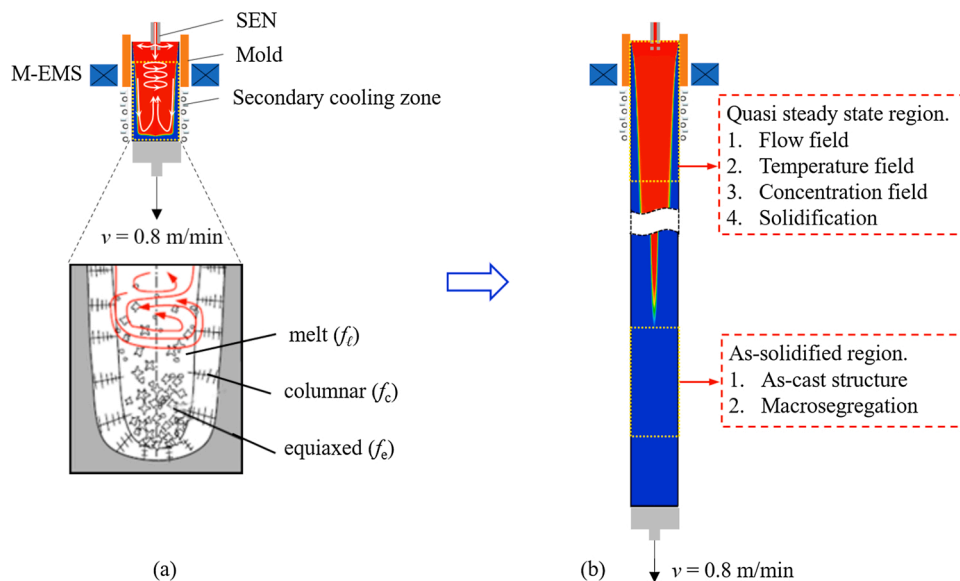


Fig. 1. Schematic of continuous casting process under the effect of M-EMS: (a) Start state of the casting with the zoom-in view of mixed columnar-equiaxed solidification; (b) Quasi-steady stage of the casting.

**Table 1**  
Governing equations of the three-phase solidification model.

Governing equations	Symbols
<p>1. Mass conservations:</p> $\frac{\partial}{\partial t}(f_\ell \rho_\ell) + \nabla \cdot (f_\ell \rho_\ell \vec{u}_\ell) = -M_{\ell e} - M_{\ell c} \quad (1)$ $\frac{\partial}{\partial t}(f_e \rho_e) + \nabla \cdot (f_e \rho_e \vec{u}_e) = M_{\ell e} + M_{cc} \quad (2)$ $\frac{\partial}{\partial t}(f_c \rho_c) = M_{\ell c} - M_{cc} \quad (3)$ $f_\ell + f_e + f_c = 1 \quad (4)$	<p><math>f_\ell, f_e, f_c</math>, volume fraction of different phase [-]  <math>\rho_\ell, \rho_e, \rho_c</math>, density [kg m<sup>-3</sup>]  <math>\vec{u}_\ell, \vec{u}_e</math>, velocity vector [m s<sup>-1</sup>]  <math>M_{\ell e}, M_{\ell c}</math>, net mass transfer rate (solidification) [kg m<sup>-3</sup> s<sup>-1</sup>]  <math>M_{cc}</math>, net mass transfer rate (fragmentation) [kg m<sup>-3</sup> s<sup>-1</sup>]</p>
<p>2. Momentum conservations:</p> $\frac{\partial}{\partial t}(f_\ell \rho_\ell \vec{u}_\ell) + \nabla \cdot (f_\ell \rho_\ell \vec{u}_\ell \otimes \vec{u}_\ell) = +f_\ell \rho_\ell \vec{g}' + f_\ell \vec{F}_L - \vec{U}_{\ell e} - \vec{U}_{\ell c} \quad (5)$ $-f_\ell \nabla p + \nabla \cdot \vec{\bar{\tau}}_\ell$ $\frac{\partial}{\partial t}(f_e \rho_e \vec{u}_e) + \nabla \cdot (f_e \rho_e \vec{u}_e \otimes \vec{u}_e) = +f_e \rho_e \vec{g}' + f_e \vec{F}_L + \vec{U}_{\ell e} + \vec{U}_{ce} \quad (6)$ $-f_e \nabla p + \nabla \cdot \vec{\bar{\tau}}_e$ $\vec{F}_L = \vec{F}_L \left(1 - \frac{\vec{u}_0}{2\pi f r}\right) \quad (7)$	<p><math>\vec{\bar{\tau}}_\ell, \vec{\bar{\tau}}_e</math>, stress-strain tensors [kg m<sup>-1</sup> s<sup>-1</sup>]  <math>p</math>, pressure [N m<sup>-2</sup>]  <math>\vec{g}</math>, gravity [m s<sup>-2</sup>]; <math>\vec{g}'</math>, deduced gravity [m s<sup>-2</sup>]  <math>\vec{F}_L, \vec{F}'_L</math>, Lorentz force and modified Lorentz force [N m<sup>-3</sup>]  <math>\vec{U}_{\ell e}, \vec{U}_{\ell c}, \vec{U}_{ce}</math>, momentum exchange rate [kg m<sup>-2</sup> s<sup>-2</sup>]  <math>\vec{u}_0</math>, tangential velocity [m s<sup>-1</sup>]  <math>f</math>, frequency of the applied current [Hz]  <math>r</math>, radial coordinate [m]</p>
<p>3. Species conservations:</p> $\frac{\partial}{\partial t}(f_\ell \rho_\ell c_\ell) + \nabla \cdot (f_\ell \rho_\ell \vec{u}_\ell c_\ell) = \quad (8)$ $\nabla \cdot (f_\ell \rho_\ell D_\ell \nabla c_\ell) - C_{\ell e} - C_{\ell c}$ $\frac{\partial}{\partial t}(f_e \rho_e c_e) + \nabla \cdot (f_e \rho_e \vec{u}_e c_e) = \quad (9)$ $\nabla \cdot (f_e \rho_e D_e \nabla c_e) + C_{\ell e} + C_{ce}$ $\frac{\partial}{\partial t}(f_c \rho_c c_c) = \nabla \cdot (f_c \rho_c D_c \nabla c_c) + C_{\ell c} - C_{ce} \quad (10)$	<p><math>c_\ell, c_e, c_c</math>, species concentration [-]  <math>D_\ell, D_e, D_c</math>, diffusion coefficient [m<sup>2</sup> s<sup>-1</sup>]  <math>C_{\ell e}, C_{\ell c}, C_{ce}</math>, species exchange rate [kg m<sup>-3</sup> s<sup>-1</sup>]</p>
<p>4. Enthalpy conservations:</p> $\frac{\partial}{\partial t}(f_\ell \rho_\ell h_\ell) + \nabla \cdot (f_\ell \rho_\ell \vec{u}_\ell h_\ell) = \quad (11)$ $\nabla \cdot (f_\ell k_\ell \nabla T_\ell) - Q_{\ell e} - Q_{\ell c}$ $\frac{\partial}{\partial t}(f_e \rho_e h_e) + \nabla \cdot (f_e \rho_e \vec{u}_e h_e) = \quad (12)$ $\nabla \cdot (f_e k_e \nabla T_e) + Q_{\ell e} + Q_{ce}$ $\frac{\partial}{\partial t}(f_c \rho_c h_c) = \nabla \cdot (f_c k_c \nabla T_c) + Q_{\ell c} - Q_{ce} \quad (13)$	<p><math>h_\ell, h_e, h_c</math>, enthalpy [J kg<sup>-1</sup>]  <math>k_\ell, k_e, k_c</math>, thermal conductivity [W m<sup>-1</sup> K<sup>-1</sup>]  <math>Q_{\ell e}, Q_{\ell c}, Q_{ce}</math>, energy exchange rate [J m<sup>-3</sup> s<sup>-1</sup>]</p>
<p>5. Formation/transport of the equiaxed grains</p> $\frac{\partial}{\partial t} n_{eq} + \nabla \cdot (\vec{u}_e n_{eq}) = N_{nu} + N_{frag} + N_{des} \quad (14)$ $\frac{\partial}{\partial t} n_{in} + \nabla \cdot (\vec{u}_\ell n_{in}) = -N_{nu} - N_{des} \quad (15)$	<p><math>n_{eq}</math>, equiaxed number density [m<sup>-3</sup>]  <math>n_{in}</math>, inoculant number density [m<sup>-3</sup>]  <math>N_{nu}</math>, heterogeneous nucleation rate [m<sup>-3</sup> s<sup>-1</sup>]  <math>N_{frag}</math>, crystals fragmentation rate [m<sup>-3</sup> s<sup>-1</sup>]  <math>N_{des}</math>, equiaxed crystals destruction rate [m<sup>-3</sup> s<sup>-1</sup>]  <math>m</math>, slope of liquidus in phase diagram [K (wt.%)<sup>-1</sup>]  <math>\Delta T</math>, constitutional undercooling [K]  <math>\Delta T_N</math>, undercooling for maximum equiaxed nucleation rate [K]  <math>\Delta T_\sigma</math>, Gaussian distribution width of nucleation law [K]  <math>\gamma</math>, fragmentation coefficient [-]  <math>\lambda_2</math>, secondary dendritic arm spacing [m]  <math>v_{Re}</math>, grain grow speed (negative value during remelting) [m s<sup>-1</sup>]  <math>\sigma_g</math>, geometric standard deviation of the lognormal distribution [-]  <math>x</math>, grain diameter of different size classed [m]  <math>\hat{d}_e</math>, geometric mean of the grain size [m]</p>
<p>5.1 Heterogeneous nucleation</p> $N_{nu} = \frac{D(\Delta T)}{Dt} \frac{dn_{eq}}{d(\Delta T)} \quad (16)$ $\frac{D(\Delta T)}{Dt} = \frac{\partial(\Delta T)}{\partial t} + m \cdot \vec{u}_\ell \cdot \nabla c_\ell - \vec{u}_\ell \cdot \nabla T_\ell \quad (17)$ $\frac{dn_{eq}}{d(\Delta T)} = \frac{n_{in}}{\sqrt{2\pi} \Delta T_\sigma} e^{-\frac{1}{2} \left(\frac{\Delta T - \Delta T_N}{\Delta T_\sigma}\right)^2} \quad (18)$	
<p>5.2 Crystals fragmentation</p> $N_{frag} = \frac{-\gamma \cdot (\vec{u}_\ell - \vec{u}_e) \cdot \nabla c_\ell}{\frac{\pi}{6} (\lambda_2 f_c)^3} \quad (19)$	
<p>5.3 Remelting/grain-destruction</p> $N_{des} = v_{Re} \frac{dn_{eq}}{dx} \Big _{x=d_{e,critical}} \quad (20)$ $\frac{dn_{eq}}{dx} = \frac{n_{eq}}{\sqrt{2\pi} \sigma_g \cdot x} e^{-\frac{1}{2} \left(\frac{\ln(x) - \ln(\hat{d}_e)}{\sigma}\right)^2} \quad (21)$ $v_{Re} = \frac{D_\ell (c_\ell^* - c_\ell)}{R_e (1 - k) c_\ell^*} \quad (22)$	
<p>6. Electromagnetic field:</p> $\vec{B} = \mu_0 \mu_r \vec{H} \quad (23)$ $\nabla \times \vec{E} = -\frac{\partial \vec{B}}{\partial t} \quad (24)$ $\vec{J} = \sigma \vec{E} \quad (25)$ $\vec{F}_L = \frac{1}{2} R_c (\vec{J} \times \vec{B}) \quad (26)$	<p><math>\vec{B}</math>, magnetic flux density [T]  <math>\vec{B}^*</math>, conjugate magnetic flux density [T]  <math>\vec{H}</math>, magnetic field intensity [A m<sup>-1</sup>]  <math>\mu_0</math>, magnetic permeability in vacuum [T m A<sup>-1</sup>]  <math>\mu_r</math>, relative magnetic permeability [-]  <math>\vec{E}</math>, electric field intensity [V m<sup>-1</sup>]  <math>\vec{J}</math>, induced current density [A m<sup>-2</sup>]  <math>\sigma</math>, electrical conductivity [Ω<sup>-1</sup> m<sup>-1</sup>]  <math>\vec{F}_L</math>, time-averaged Lorentz force [N m<sup>-3</sup>]  <math>R_c</math>, the real part of a complex number [-]</p>

(SEN) was used. *On-site* measurement of the magnetic flux density along the axis (Line 1) of the continuous casting machine with an empty mold at room temperature was performed to validate the configuration of the M-EMS stirrer. The numerically calculated electromagnetic field agreed satisfactorily with the measurements (Fig. 2(c)). A convective heat transfer thermal boundary condition was used in the mold region, and heat flux thermal boundary conditions were used in the secondary cooling zones (Z1 – Z3) and for commercial reasons, the values are omitted. No-slip flow boundary conditions were employed for the melt and equiaxed phase along the mold walls. The strand mold interface was treated electrically isolating.

### 2.3. Numerical procedure

The calculation is performed from the start of the casting. The casting is withdrawn downward vertically with a casting speed of 0.8 m/min, and the casting bending is ignored. In the current casting format, the metallurgical length, the as-cast structure and macrosegregation on cross-section (2 m above the casting bottom by considering the end effect of continuous casting) are unchanged after the casting has been withdrawn to a length of 10.75 m. It means the casting has reached a quasi-steady state afterwards. To ensure this point, the casting continues to be withdrawn to 12 m in length. All the modeling results of the casting domain are analyzed at this moment.

The M-EMS and flow solidification calculations were decoupled. First, the electromagnetic field was calculated using ANSYS Electronics. By solving the Maxwell equations, the magnetic flux density, electric current density, and time-averaged Lorentz force were obtained, but only the Lorentz force was exported for the subsequent flow solidification calculation, which was performed using ANSYS Fluent. The field of the Lorentz force was first interpolated into the mesh system of ANSYS Fluent, then weighted by the corresponding phase volume fraction (melt, equiaxed or columnar), and finally added as a source term to the momentum conservation equation of each phase via User-Defined Functions (UDF). To consider the effect of the motion of metal phases on the induced Lorentz force, a simple modification was made by considering a factor that is related to the relative velocity between the rotational magnetic field and the tangential velocity of the corresponding phase (Eq. (7)). For each time step (0.005 s), 20 iterations were conducted to decrease the normalized residuals of the continuity, momentum conservation, volume fraction, species transport, and user-defined scalar conservation equations to values below the convergence limit of  $10^{-4}$  and those of the enthalpy conservation equations to below  $10^{-7}$ . Local mesh refinements were performed near the strand wall and strand center. The minimum mesh size was set to 5 mm. The total number of finite volume elements was 529200. The eighteen “transport”

quantities,  $f_\ell, f_c, f_s, u_{\ell,x}, u_{\ell,y}, u_{\ell,z}, u_{c,x}, u_{c,y}, u_{c,z}, C_\ell, C_c, C_s, T_\ell, T_c, T_s, n_{eq}, n_{in}$  and pressure  $p$ , are obtained by solving the eighteen conservation equations, which are summarized in Table 1. All phases share a single pressure field, The pressure correction equation is obtained by using the “Phase Coupled SIMPLE” algorithm. To solve these multiphase coupled equations, one three-dimensional (3D) calculation (withdrawal of the casting of 12 m) required 45 days on a high-performance cluster (2.6 GHz, 28 cores).

## 3. Results

### 3.1. Flow field

The typical transient flow pattern of the steel melt inside the strand with M-EMS is shown in Fig. 3. The time-averaged Lorentz force is shown in Fig. 3(a). A symmetric Lorentz force distribution in the vertical section was obtained. The maximum force occurred near the strand surface, and decreased exponentially toward the strand center. Section views of the Lorentz force at the middle of the M-EMS system (Fig. 3 (a.2)-(a.3)) show nearly (but not perfect) axis symmetry. This deviation from perfect axis symmetry was due to the configuration of the stirrer, whose six poles were not geometrically consistent with the four corners of the strand section. Fig. 3(b) shows the complexity of the 3D flow pattern using streamlines. Four representative streamlines were analyzed in detail (Fig. 3(c)). Type A/B: The melt coming from the bottom and one side port of the SEN went directly downward. After one or two cycles of circulation in the M-EMS region, the melt continued to flow downward along the solidification front. Type C: The melt coming from one side port of the SEN impinged on the strand shell and turned upward toward the meniscus. Because it was confined by the meniscus, the melt turned back to the M-EMS region and underwent several rotations; then, it flowed spirally upward. Mainly restricted by the M-EMS, the melt could only flow back to the position near the bottom of the SEN and then flow downward to the M-EMS region. A so called “upper secondary spiral-shaped recirculation loop” was formed. This type of flow pattern was also reported by Natarajan and El-Kaddah (2004). They used a finite element analysis to investigate the electromagnetic and fluid flow phenomena in rotary electromagnetic stirring of steel. They found that the secondary flow promoted mixing beyond the region confined by the stirrer, and the extent of mixing depended on the frequency of the applied rotating magnetic field. Type D: The melt coming from one side port of the SEN flowed downward into the M-EMS region and underwent several rotations. It then flowed spirally downward along the solidification front and returned to the M-EMS region along the strand core. A so called “lower secondary spiral-shaped recirculation loop” was formed. Note that the above typical streamlines developed

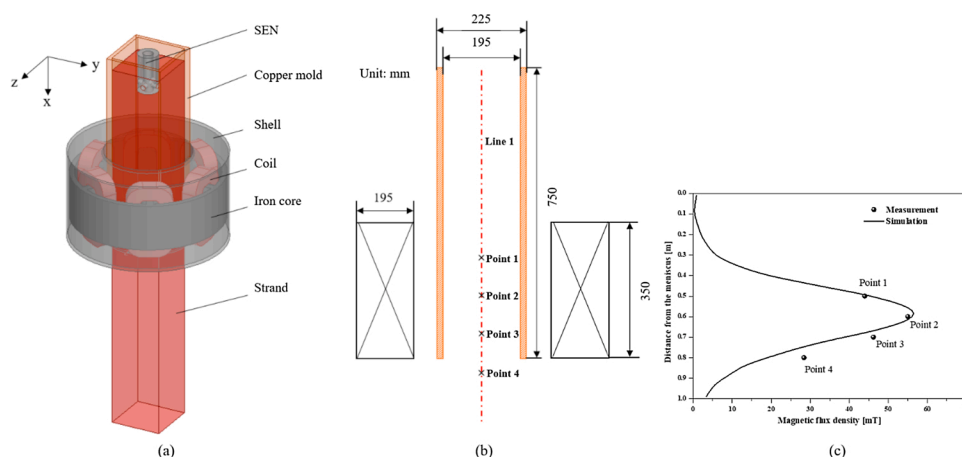


Fig. 2. (a) Schematic of billet continuous casting with M-EMS; (b) Dimensions and relative positions between the mold and M-EMS system; (c) Distribution of the measured and simulated magnetic flux densities along Line 1.

**Table 2**  
Material properties and process parameters<sup>a</sup>.

Material properties	Symbols	Units	
Nominal concentration	$c_0$	wt.%	0.53
Liquidus temperature	$T_L$	K	1688.15
Solidus temperature	$T_S$	K	1593.15
Melting temperature	$T_M$	K	1720.15
Liquid density	$\rho_\ell$	kg m <sup>-3</sup>	7035.0
Density difference between melt and equiaxed crystals	$\Delta\rho$	kg m <sup>-3</sup>	150.0
Latent heat	$L$	kJ kg <sup>-1</sup>	220.0
Specific heat	$c_p$	J kg <sup>-1</sup> K <sup>-1</sup>	800.0
Thermal conductivity	$k_\ell, k_w, k_c$	W m <sup>-1</sup> K <sup>-1</sup>	33.0
Diffusion coefficient in liquid	$D_\ell$	m <sup>2</sup> s <sup>-1</sup>	$2 \times 10^{-8}$
Diffusion coefficient in solid	$D_s$	m <sup>2</sup> s <sup>-1</sup>	$1 \times 10^{-9}$
Thermal expansion coefficient of the melt	$\beta_T$	K <sup>-1</sup>	$4.5 \times 10^{-5}$
Solutal expansion coefficient of the melt	$\beta_C$	wt.% <sup>-1</sup>	0.02
Equilibrium partition coefficient of carbon	$k$	–	0.252
Liquidus slope	$m$	K(wt.%) <sup>-1</sup>	-60.37
Electric conductivity of strand (melt)	$\sigma_\ell$	S m <sup>-1</sup>	$7.6 \times 10^5$
Electric conductivity of strand (solid)	$\sigma_s$	S m <sup>-1</sup>	$8.2 \times 10^5$
Electric conductivity of mold (423 K) (Li et al. (2018))	$\sigma_{m-423}$	S m <sup>-1</sup>	$3.18 \times 10^7$
Electric conductivity of mold (298 K) (Li et al. (2018))	$\sigma_{m-298}$	S m <sup>-1</sup>	$4.7 \times 10^7$
Primary dendritic arm spacing	$\lambda_1$	m	$1.85 \times 10^{-4}$
Secondary dendritic arm spacing	$\lambda_2$	m	$4.8 \times 10^{-5}$
Viscosity	$\mu_\ell$	kg m <sup>-1</sup> s <sup>-1</sup>	0.006
Gibbs Thomson coefficient	$\Gamma$	–	$3.3 \times 10^{-7}$
Initial inoculant number density	$n_{in}^0$	m <sup>-3</sup>	$1 \times 10^9$
Initial equiaxed number density	$n_{eq}^0$	m <sup>-3</sup>	$1 \times 10^6$
Undercooling for maximum equiaxed nucleation rate	$\Delta T_N$	K	5.0
Gaussian distribution width (nucleation)	$\Delta T_\sigma$	K	3.0
Packing limit for equiaxed crystals	$f_{e,packing}$	–	0.637
Volume ratio of solid dendrite to equiaxed grain envelope	$f_{si}$	–	0.3
Fragmentation coefficient	$\gamma$	–	$3.0 \times 10^{-5}$
<b>Process parameters</b>			
Strand format	$D$	m	0.195 × 0.195
Mold length	$H_m$	m	0.75
Secondary cooling zone length (Z1)	$H_1$	m	xxx
Secondary cooling zone length (Z2)	$H_2$	m	xxx
Secondary cooling zone length (Z3)	$H_3$	m	xxx
Casting speed	$V_c$	m min <sup>-1</sup>	0.8
Pouring temperature	$T_p$	K	1708.15
AC electric current	$I$	A	xxx
M-EMS frequency	$f$	Hz	3.0

<sup>a</sup> For commercial reasons, some process parameters, including the thermal boundary conditions, are omitted.

transiently, and could change from one type to another dynamically. Further, the velocity (motion) of the equiaxed phase was not identical to that of the melt flow (Section 3.2).

For comparison, the flow pattern for the case without M-EMS is shown in Fig. 3 (d). The jet from the bottom port of the SEN flowed downward directly. Meanwhile, the melt from the side ports of the SEN impinged on the strand shell first and then split into two streams: one turned upward toward the meniscus, forming vortices below the meniscus, and the other turned downward along the solidification front. The downward flow along the solidification front drove an upward flow in the strand center.

### 3.2. Temperature field and solidification

The transient solidification process together with the temperature/velocity fields for the case with M-EMS are shown in Fig. 4. For

comparison, the temperature field for the case without M-EMS is shown in Fig. 4(d). The analysis area was limited to 2 m from the meniscus, covering the mold region and two secondary cooling zones (Z1 and Z2).

As shown in Fig. 4(a), one important role of the M-EMS is to confine the superheated region to the mold region, leaving the liquid core below the mold undercooled. The superheated region is indicated by the enclosed liquidus isotherm (1688.15 K). Owing to the rotational electromagnetic force, the downward jet flow coming from the bottom exit of the SEN was brought back to the upper part of the mold region along the solidification front (Fig. 4(a), Zoom A). In contrast to the case with M-EMS, the superheated region in the case without M-EMS can extend through the liquid core of the strand far below the mold region (Fig. 4(d)). Similar phenomenon was also observed in direct chill casting of aluminium by Jia et al. (2020). They found that the melt temperature decreased rapidly in the presence of electromagnetic field (EMF). Thus, a shallower depth of the liquid sump was obtained.

Fig. 4(b) shows the contour of the volume fraction of the columnar phase ( $f_c$ ) overlaid with the melt velocity ( $\vec{u}_\ell$ ). An isoline ( $f_c = 0.3$ ) was used to approximate the shell thickness, and another isoline ( $f_c = 0.95$ ) was used to define the columnar solidification front. Therefore, the mushy zone thickness is the distance between the two isolines. Near the middle height of the M-EMS system, the swirling flow was confined by the solidified shell (Fig. 4(b), Zoom B). The high-temperature melt coming from the side ports of the SEN impinged on the strand shell and split into two opposite streams: one upward and one downward. The upward stream was confined between the strand shell, meniscus, and SEN, forming an upper vortex. The upper vortex played an important role in preventing the solidification of the meniscus. The downward stream was blocked by the upper recirculation loop generated by the M-EMS, and thus, a small lower vortex was formed (Fig. 4(b), Zoom A). In the secondary cooling zone, the lower recirculation loop generated by the M-EMS accelerated the downward flow along the solidification front, which in turn drove the melt backward into the mold region along the strand center (Fig. 4(b), Zoom C). After encountering the jet flow from the bottom exit of the SEN, the two parts of the melt joined together and were conducted toward the solidification front by the upper/lower recirculation loops (Fig. 4(b), Zoom A).

Fig. 4(c) shows the contour of the volume fraction of the equiaxed phase ( $f_e$ ) overlaid with the velocity vector of the equiaxed phase ( $\vec{u}_e$ ). A small portion of equiaxed crystals, which were generated by heterogeneous nucleation/crystal fragmentation near the columnar solidification front, was carried to the upper mold region by the upper recirculation loop (Fig. 4(c), Zoom A) and partially remelted in the superheated zone. At approximately 0.29 m below the meniscus, some equiaxed crystals could temporarily survive when they were brought into the lightly undercooled zone (Fig. 4(c), Zoom D). In the secondary cooling zone, most equiaxed crystals settled down and continued to grow during settling (Fig. 4(c), Zoom C).

The temperature profiles along the centerline and strand surface are plotted in Fig. 5, and a comparison is made between the cases with and without M-EMS. Without M-EMS, two large flow recirculation loops (Fig. 4(d), Zone A) were created on the vertical half-plane of the strand. The left recirculation loop consistently brought the cooler melt (still superheated) to the strand center. However, the cooling effect was so weak that the temperature along the centerline at the mold exit was 1706.9 K. Therefore, only 1.25 K of superheat was dissipated (Fig. 5(a)). The right recirculation loop brought hotter melt toward the solidification front, raising the surface temperature ( $T = 1431.15$  K) at the position 0.25 m below the meniscus (Fig. 5(b)). The area of influence was only maintained for a short distance to the position 0.34 m ( $T = 1452.83$  K) below the meniscus. Subsequently, the surface temperature dropped rapidly (Fig. 5(b)). For the case with M-EMS, two large recirculation loops were generated: one upper recirculation loop above the M-EMS system and one lower recirculation loop below the M-EMS system. The upper recirculation loop drove the cooler melt along the solidification

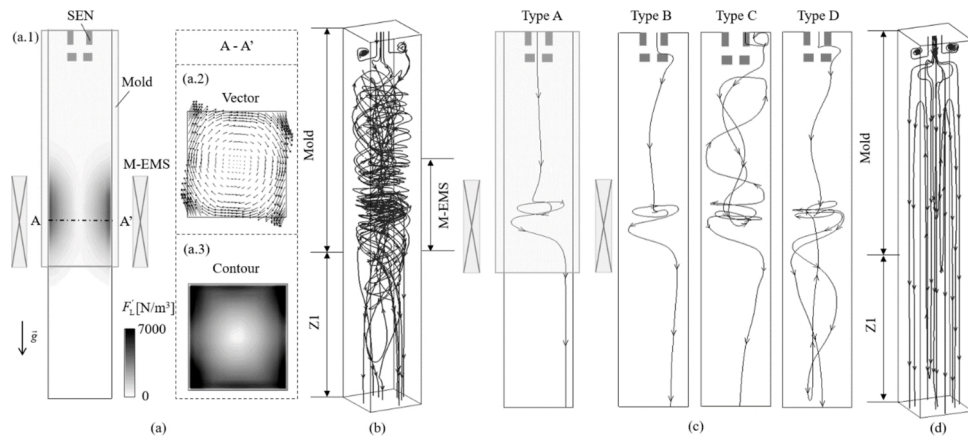


Fig. 3. Melt flow during solidification of the steel billet with M-EMS. (a) Time-averaged Lorentz force distributions on three sections; (b) Streamlines of the melt flow; (c) Four types of streamlines shown separately; (d) For comparison, the flow pattern (streamlines) without M-EMS is also shown.

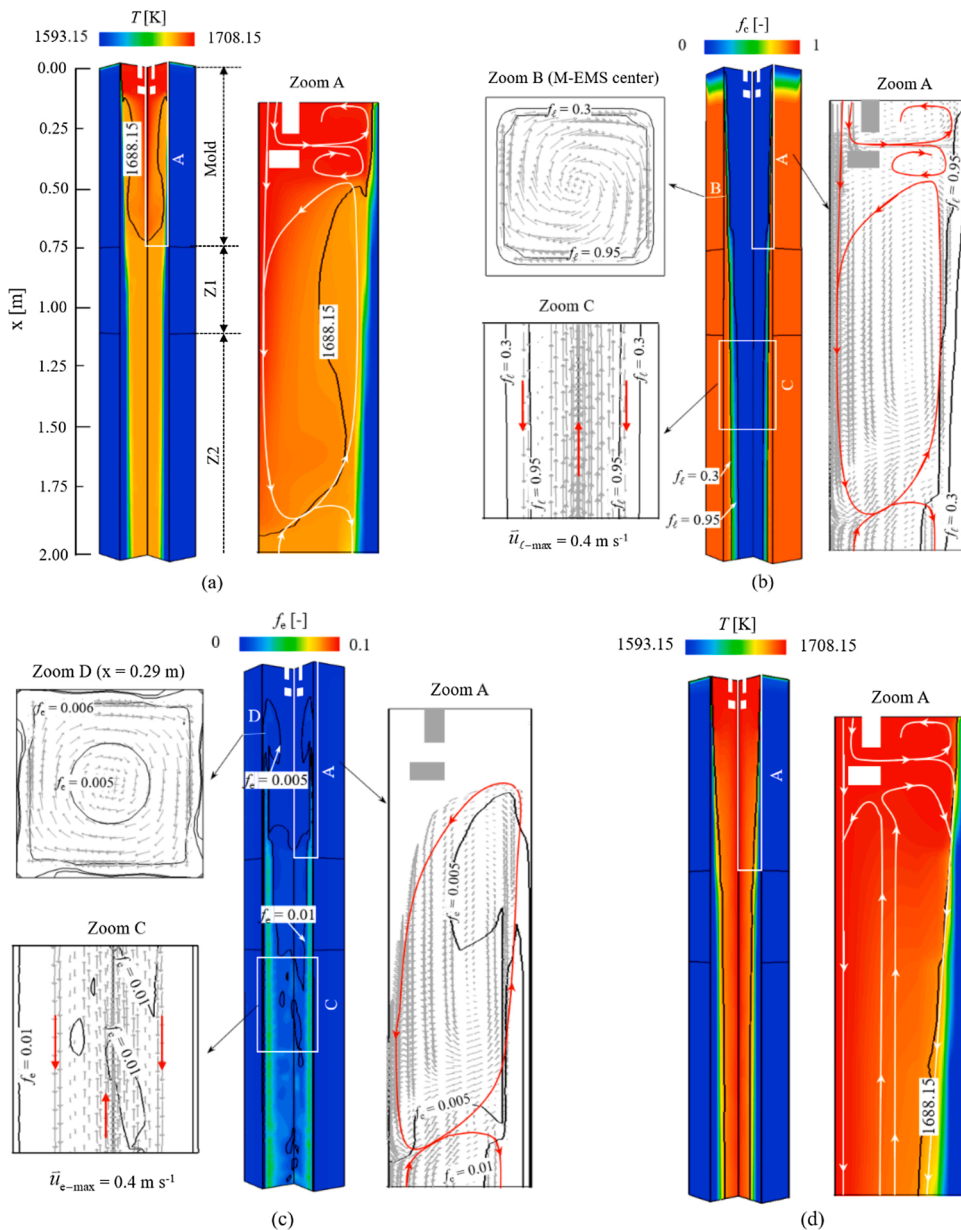


Fig. 4. Transient solidification process in the upper part of the strand with M-EMS. (a)  $T$  field overlaid with the liquidus isotherm (1688.15 K), indicating the superheated zone; (b) Volume fraction of the columnar phase ( $f_c$ ) overlaid with  $\vec{u}_l$  vectors (white) and streamlines (red) schematically highlighting the flow direction; (c) Volume fraction of the equiaxed phase ( $f_e$ ) overlaid with  $\vec{u}_e$  vectors (white) and streamlines (red) schematically highlighting the direction of motion of the equiaxed phase. (d) For comparison, the temperature field for the case without M-EMS is shown. (For interpretation of the references to colour in this Figure legend, the reader is referred to the web version of this article).

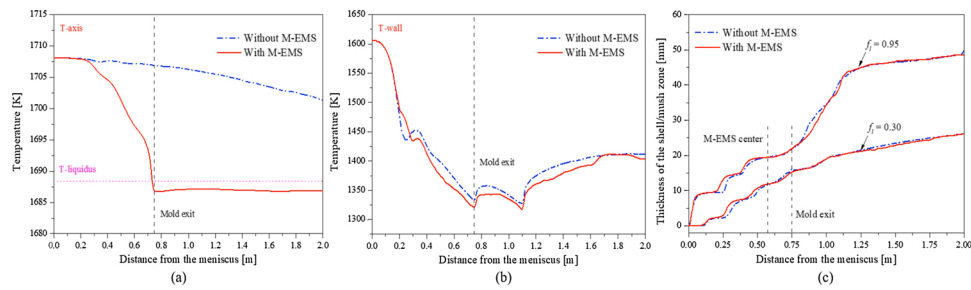


Fig. 5. Comparisons of  $T$  profiles and thicknesses of the strand shell and mushy zone between the two cases: with and without M-EMS. (a)  $T$  profiles along the strand centerline and (b)  $T$  profiles along the strand surface. (c) Thicknesses of the solid shell/mushy zone.

front to the center of the strand, which substantially decreased the temperature of the liquid core. The centerline temperature at the mold exit was 1686.79 K, which is lower than the liquidus temperature (Fig. 5 (a)). This indicates that the area outside the mold region was entirely undercooled. Another role of the upper recirculation loop was to inhibit the downward flow of the melt coming from the side ports of the SEN; a small part of the melt was blocked near the SEN (Fig. 4(a)). Consequently, the temperature decreased drastically along the casting direction. One interesting finding is that for the case with M-EMS, the surface temperature of the strand in most of the mold region was slightly lower than that in the case without M-EMS. This implies that M-EMS may not increase the heat transfer rate from the strand surface to the water-cooled copper mold. In contrast, it may even slightly reduce the cooling rate from the strand surface to the mold. The surface integral of the heat flux over the entire strand surface area in the mold region was calculated, and a comparison was made between the two cases (with and without M-EMS). The results verified the above statement: M-EMS does not increase the heat transfer rate from the strand surface to the water-cooled copper mold. However, M-EMS induced flow is beneficial for the temperature homogenization in the strand. It means that the temperatures of liquid (near the solidification front) and the solid shell in the secondary cooling zone are raised under the effect of M-EMS. Part of the thermal energy (the superheat which is presented in the long hot core region for the case without applying M-EMS) is transferred to the sensible energy and stored in the solid shell and liquid phase (near the solidification front).

Fig. 5(c) shows the evolution of the solid strand shell/mushy zone thicknesses. M-EMS slightly promoted the growth of the solid shell/mushy zones above the M-EMS center, while it inhibited their growth below the M-EMS center. This phenomenon is related to the flow pattern (Fig. 3 and Fig. 4). The upper recirculation loop generated by M-EMS inhibited the downward flow of the hotter melt coming from the side ports of the SEN and drove the cooler melt upward along the solidification front. This type of flow reduces the temperature near the solidification front, which is beneficial for the growth of the strand shell/mushy zone. In contrast, the lower recirculation loop generated by M-EMS brought the hotter melt from the strand center to the solidification front and delayed the growth of the solid shell/mushy zone. The thickness of the strand shell at the mold exit was 15.26 mm with M-EMS and 16.67 mm without M-EMS. Some steps can also be observed in the curves, which were not only due to the flow effect but were also attributed to the mesh size. In this study, a relatively refined mesh (5 mm) was used near the strand wall to calculate the growth of the solid shell/mushy zone; a relatively coarse mesh (7 mm) was used for the inner part. Note that the curves should become smoother after further mesh refinement, but the calculation cost would drastically increase, considering that the current 3D calculation required 45 days on a high-performance cluster (2.6 GHz, 28 cores).

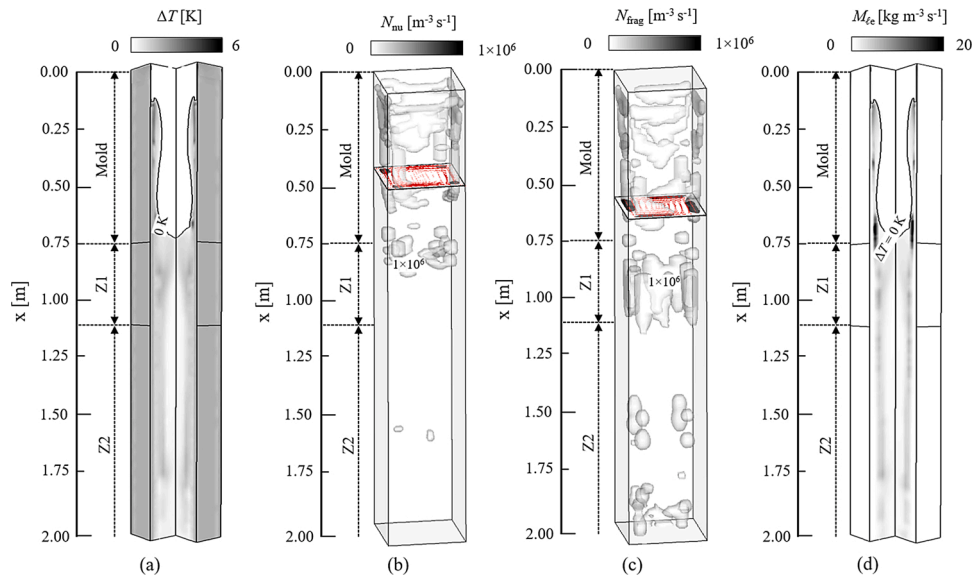
### 3.3. Origin/solidification and remelting/destruction of equiaxed crystals

Fig. 6(a) shows the contour of the constitutional undercooling of the

strand,  $\Delta T = T_f + m \cdot c_\ell - T$ , where  $\Delta T$  considers both, the liquid concentration and temperature. The undercooled and superheated regions are separated by the isoline  $\Delta T = 0$  K. Fig. 6(b) displays the distribution of the heterogeneous nucleation rate ( $N_{nu}$ ). When the necessary nucleation conditions are achieved in the undercooled region, the inoculants are activated as equiaxed crystals. Once the local inoculants are consumed, no heterogeneous nucleation will occur at this site. However, if some inoculants are brought to this site by flow from other regions, nucleation can continue again. Therefore, the distributions of  $N_{nu}$  and  $\Delta T$  were very different; the former was continuous and smooth, whereas the latter was uneven and random, and mostly located in the upper part of the casting (the undercooling area). Fig. 6(c) shows the contour of the crystal fragmentation rate ( $N_{frag}$ ). The fragments were located more frequently in the mushy zone near the columnar tip front along the length of the strand. Analysis of the results showed that the M-EMS-induced flow appeared to impact crystal fragmentation very effectively. To further study the role of M-EMS,  $N_{nu}$  and  $N_{frag}$  under the conditions with and without M-EMS are quantitatively compared in Table 3. Here, the volume integrals of time-averaged  $N_{nu}$  and  $N_{frag}$  (over a time interval of 7 s) in different cooling zones were performed. With M-EMS, the total creation rate of the crystal number density by the mechanism of fragmentation ( $N_{frag}$ , sum over the mold, Z1, and Z2 regions) was approximately  $1.5 \times 10^5$  [ $s^{-1}$ ], which is approximately one order of magnitude higher than that of the case without M-EMS. However, the total creation rate of the crystal number density by the mechanism of nucleation ( $N_{nu}$ ) was similar for both cases; that is, M-EMS did not increase (or even slightly reduce) the total  $N_{nu}$ . The conclusion is that M-EMS increases the quantity of equiaxed crystals via crystal fragmentation. Regardless, most of the fragmentation events occurred in the mold region owing to the stirring effect of M-EMS. Fig. 6(d) shows the net mass transfer rate from the liquid melt to the equiaxed crystals ( $M_{\ell e}$ ). Once equiaxed crystals form, they will continue to grow or be remelted depending on the local thermal and solutal environment. This indicates that the M-EMS-induced swirling flow provides a favorable growth environment for equiaxed crystals out of the mold region by accelerating superheat dissipation. Most of the newly formed equiaxed crystals settle into the undercooled secondary cooling zone, where they continue to grow and form the central equiaxed zone.

During the growth of equiaxed crystals, remelting/destruction of the crystals occurs when they are transported to the superheated melt region. The process involves two steps: reduction in crystal size (remelting) and destruction (disappearance) of the crystals. Fig. 7(a) displays the contour of  $\Delta T$ ; only the region with a negative value of  $\Delta T$  (superheating) is depicted, and the region with a positive value of  $\Delta T$  (undercooling) is omitted. Fig. 7(b) shows the distribution of  $M_{\ell e}$ . Here again, only the region with a negative value of  $M_{\ell e}$  (remelting) is shown. A small portion of the newly formed equiaxed crystals was transported to the superheated region, driven by the melt flow (Fig. 4(c)). There, remelting occurred, which was accompanied by a decrease in the local temperature and a negative  $M_{\ell e}$ . In addition, the melting of low-concentration crystals can dilute the liquid concentration at the center of the strand. Once the crystal size is reduced to a critical value (Eq. 20),





**Fig. 6.** (a) Contour of the constitutional undercooling  $\Delta T$ ; (b) Heterogeneous nucleation rate  $N_{nu}$ ; (c) Crystal fragmentation rate  $N_{frag}$ ; (d) Net mass transfer rate from the melt to the equiaxed crystals  $M_{fe}$  (solidification).

**Table 3**

Time-averaged heterogeneous nucleation rate and crystal fragmentation rate in various cooling zones.

Mechanism		Mold region	Z1	Z2	Total
Heterogeneous nucleation rate [ $s^{-1}$ ]	With M-EMS	95474.63	10392.85	441.63	106309.11
	Without M-EMS	112719.39	17837.36	7797.13	138353.88
Crystal fragmentation rate [ $s^{-1}$ ]	With M-EMS	99498.49	42017.89	5138.75	146655.13
	Without M-EMS	6712.56	5498.22	2026.22	14237.00

the equiaxed crystals will be destroyed and converted into inoculants (Eqs. 14–15). Fig. 7(c) depicts the distribution of the destruction rate of equiaxed crystals ( $N_{des}$ ); its profile is similar to that of the remelting rate of the crystals.

### 3.4. As-cast structure and macrosegregation

Fig. 8(a) displays an experimental macrograph of the as-cast structure (with M-EMS). The columnar, mixed, and equiaxed regions are

marked with dotted lines based on the authors' subjective judgment of the macrograph. Fig. 8(b) shows the simulated macrostructure for the case with M-EMS, and Fig. 8(c) displays the simulated macrostructure for the case without M-EMS. For the simulation cases, the equiaxed zone is marked by the isoline of the equiaxed grain envelope:  $f_e^{env} = 1.0$ ; the columnar and mixed zones are distinguished by the isoline of the equiaxed grain envelope:  $f_e^{env} = 0.17$ . In this study, the equiaxed zone ratio was defined as the area ratio of the equiaxed zone to the entire cross section (195 mm  $\times$  195 mm). When M-EMS was applied, the profile of

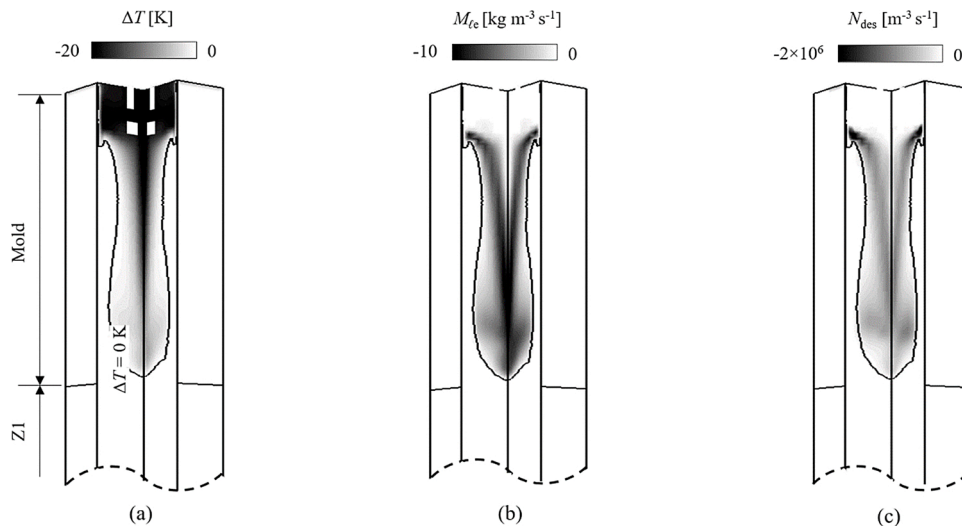


**Fig. 7.** (a) Contour of the undercooling degree  $\Delta T$  (negative scale). (b) Net mass transfer rate from the melt to the equiaxed crystals  $M_{fe}$  (remelting). (c) Destruction rate of the equiaxed crystals  $N_{des}$ . The simulation result is shown in grey-scale, with dark for the superheated region and remelting/destruction rate. Only the simulation results in the superheated region are shown. The results in the undercooled region with nucleation and fragmentation are not shown.

the columnar zone showed a satisfactory agreement with the one of the as-cast structure. The experimentally measured area ratio of the equiaxed zone was approximately 22.03 % (Fig. 8(a)), while the simulated value was 12.6 % (Fig. 8(b)), the equiaxed zone was underestimated by the simulation. Without M-EMS, the equiaxed zone ratio was relatively low (2.3 %); that is, the entire strand section was nearly full of the columnar structure. This would lead to the generation of centerline porosity.

Fig. 9(a) depicts the contour of the macrosegregation index for the two cases: with and without M-EMS. Fig. 9(b) shows the distribution of the macrosegregation index along the symmetry line (Line 2) of the strand section. Because of the accumulation of equiaxed crystals, negative segregation occurred in the central equiaxed zone, positive segregation occurred at the border of the columnar zone, and a trail of negative segregation (white band) occurred in the subsurface region of the billet. For the case without M-EMS, the macrosegregation was weaker, and severe negative segregation only occurred in the central equiaxed zone. The averaged surface integrals of the macrosegregation index ( $\sum \Delta A \cdot c_{\text{mix}}^{\text{index}} / \sum \Delta A$ ) at the strand section were performed for the two cases. The value is -0.024 % for the case with M-EMS, and -0.03129 % for the case without M-EMS.

## 4. Discussion

### 4.1. Transport phenomenon caused by solidification, migration, and remelting of equiaxed crystals

During the continuous casting of steel billets under M-EMS, the formation, growth, migration, and remelting of equiaxed crystals in the mold region represent an important mechanism of mass and energy transport, which impacts the as-cast structure and macrosegregation. As schematically shown in Fig. 10(a), the equiaxed crystals can (1) originate mainly from fragmentation ( $N_{\text{frag}}$ ) in the intensive M-EMS region and partially from nucleation ( $N_{\text{nu}}$ ) in the upper mold region, (2) grow in the undercooled zone along the columnar tip front, (3) migrate to the central superheated region below the SEN owing to the special flow pattern (M-EMS-induced circulation loop between the SEN and the stirrer), and (4) finally remelt in the strand center. The modeling results of  $N_{\text{nu}}$ ,  $N_{\text{frag}}$ ,  $f_e$ ,  $M_{\ell e}$ , and  $N_{\text{des}}$  are also shown in Fig. 10(a)-(b), which support the above statement. Typically, the as-formed equiaxed crystals, which are heavier than the liquid, settle downward. However, the swirling flow and recirculation loop induced by M-EMS greatly influence the motion of these crystals. A small portion of equiaxed crystals was brought to the upper part of the mold region and remelted/destroyed in the superheated region.

It is known that the solidification of equiaxed crystals releases latent heat and rejects the solute element (the solute partition coefficient  $k <$

1). In contrast, the remelting of equiaxed crystals absorbs latent heat and dilutes the solute concentration. These two events, that is, solidification and remelting, occur in different locations: one at the solidification front and one in the strand center. Therefore, the migration of equiaxed grains, which bridges the above two events, represents an important energy/species transport mechanism. To demonstrate the importance of the above mechanism, one more simulation case was considered, where remelting/destruction was not factored. Fig. 11 compares the  $T$  field, net mass transfer rate ( $M_{\ell e}$ ), and liquid concentration field ( $c_{\ell}$ ), between two simulation cases: one with and one without remelting. The undercooling zone in the upper part of the mold region, which was caused when the upper recirculation loop generated by M-EMS (Fig. 4(a)) was larger when remelting was considered (Fig. 11(a)). In other words, the superheated region was somehow “compressed” toward the strand center owing to the cooling effect (absorption of latent heat) induced by the remelting of equiaxed crystals. The nominal concentration of the melt from the SEN was 0.0053. As shown in Fig. 11(c),  $c_{\ell}$  in the superheated region was higher when the remelting of equiaxed crystals was considered. The modeling results in Fig. 11 may not sufficiently demonstrate the differences between the two cases because the differences in  $T$  and  $c_{\ell}$  can subsequently impact further solidification in the secondary cooling zones of the strand. In summary, the solidification, migration, and remelting of equiaxed crystals play a vital role in the redistribution of energy (temperature) and liquid concentration. It should be acknowledged that omitting these phenomena results in considerable error in the prediction of the final as-cast structure and macrosegregation.

### 4.2. Consideration of the state-dependent electrical conductivity of the solidified shell

Steel has a higher electrical conductivity ( $\sigma$ ) in the solid state than that in the liquid state, and the difference in  $\sigma$  is approximately 7.8 % for this alloy. This implies that the electric current path induced by M-EMS may vary during the evolution of the solid shell. To understand the influence of the state-dependent  $\sigma$  on the efficiency of M-EMS, two simulation cases were compared. The first case assumed a uniform electrical conductivity ( $7.6 \times 10^5$  S/m), independent of the liquid/solid state. The second case used the state-dependent electrical conductivity for different regions; that is, the as-solidified shell used the value of the solid state ( $8.2 \times 10^5$  S/m). To achieve the second case, an iterative calculation between two software packages (ANSYS Electronics and ANSYS Fluent) was performed. The profile of the solid shell calculated from the first case was taken as a reference to update the distribution of the Lorentz force with ANSYS Electronics, considering the state-dependent  $\sigma$ . The updated Lorentz force was used to calculate the solidification of the strand. Fig. 12 shows the time-averaged magnitude of the magnetic flux density ( $B$ ), induced electrical current density ( $J$ ), and

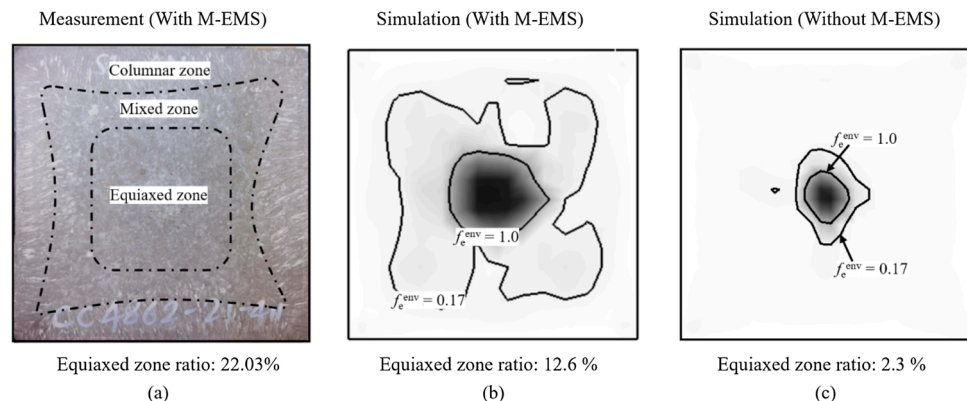


Fig. 8. (a) Macrograph of the as-cast structure with M-EMS. (b) Simulated macrostructure for the case with M-EMS. (c) Simulated macrostructure for the case without M-EMS.

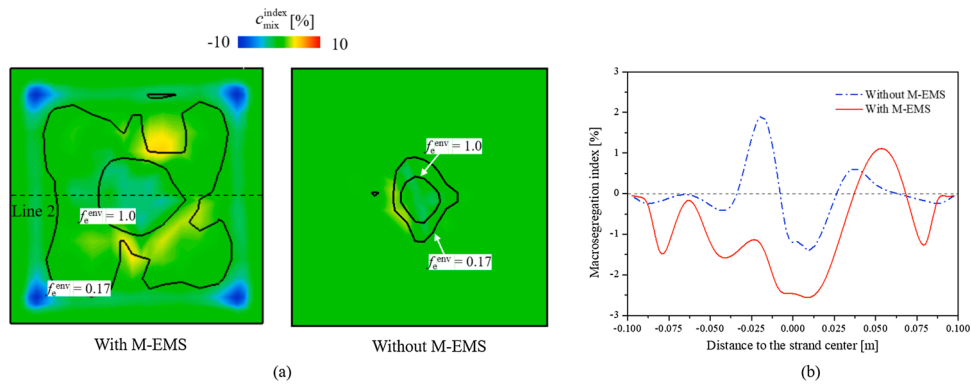


Fig. 9. (a) Contour of the macrosegregation index for the two cases: with and without M-EMS; (b) Distribution of the macrosegregation index along the centerline (Line 2) of the strand section.

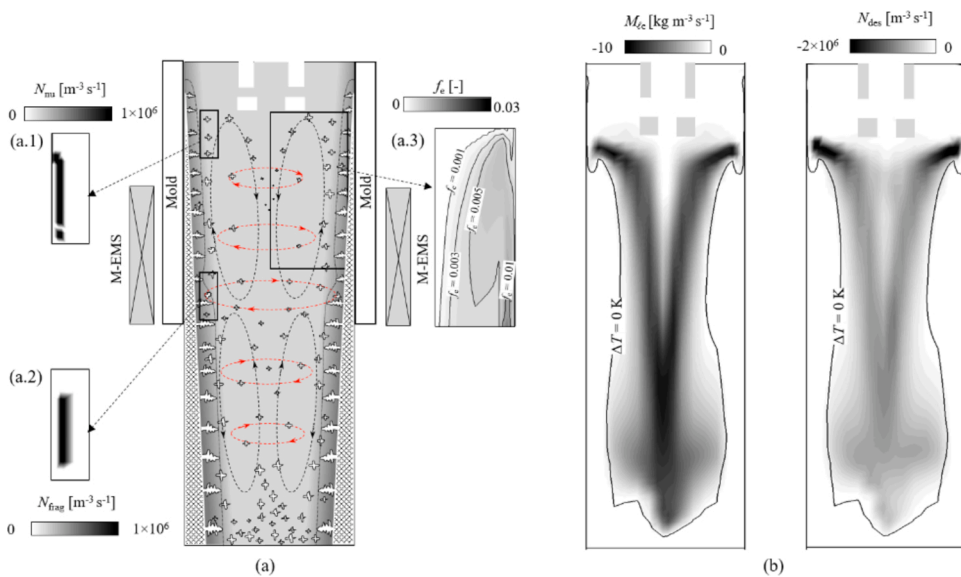


Fig. 10. (a) Schematic of the mass/energy transport mechanism through the formation/growth, migration, and remelting of equiaxed crystals under the effect of M-EMS. The red/black dashed lines highlight the motion/migration direction of equiaxed crystals, and the black dotted line defines the columnar tip front. (b) Calculated remelting rate ( $M_{re}$ ) and grain destruction rate ( $N_{des}$ ) of equiaxed crystals in the superheated region. Only the range with negative values of  $M_{re}$  and  $N_{des}$ , indicating remelting and grain destruction, is shown. (For interpretation of the references to colour in this Figure legend, the reader is referred to the web version of this article)

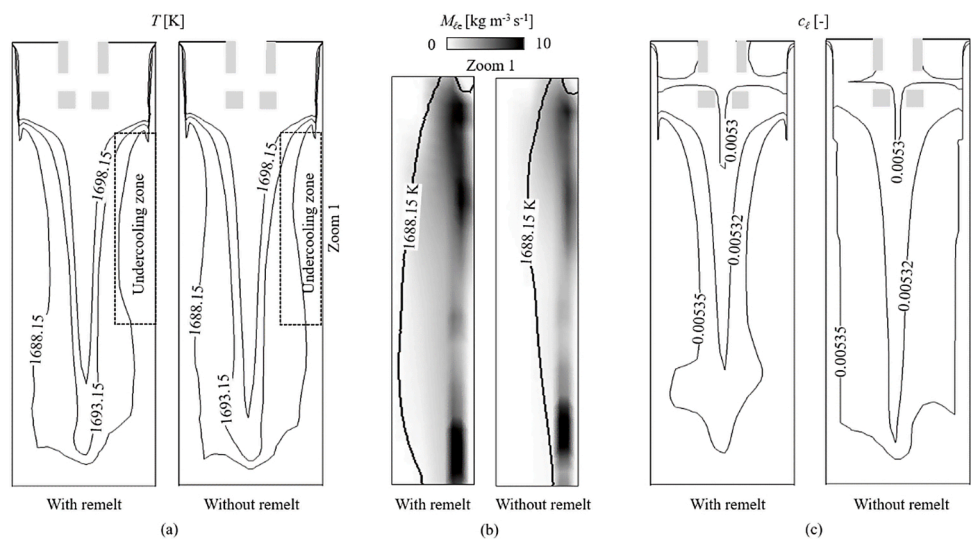


Fig. 11. Effect of remelting on the temperature ( $T$ ) and liquid concentration ( $c_l$ ) fields, and a comparison of two simulation cases: one considering remelting, and one ignoring remelting. (a)  $T$  field and net mass transfer rate ( $M_{re}$ ). (b) Liquid concentration ( $c_l$ ).

Lorentz force ( $F_L$ ) in the strand. No significant differences were found between the two cases. The Lorentz force in the melt front of the solidified shell in the second case was only 3% lower than that in the first case. Such a small difference in  $F_L$  did not significantly impact the initial solidification of the strand.

#### 4.3. Shielding effect of the copper mold

The shielding effect of the copper mold on the rotational magnetic field depends on the operating temperature of the mold because its electrical conductivity ( $\sigma_m$ ) is a function of temperature. To understand the influence of the shielding effect on the operating efficiency of M-EMS, two simulation cases were compared. The first case assumed a mold operating temperature of 298 K (corresponding to  $\sigma_{m-298} = 4.7 \times 10^7$  S/m); the second case used a mold operating temperature of 423 K (corresponding to  $\sigma_{m-423} = 3.18 \times 10^7$  S/m). Fig. 13(a) displays the time-averaged results of the magnetic flux density ( $B$ ) and induced current density ( $J$ ) on the mold surface for the two mold temperatures.  $B$  was minimally affected by the mold operating temperature, but  $J$  displayed a large difference between the two cases. The difference in the peak value of  $J$  at the edge of the mold reached approximately 35%. The induced  $J$  created a secondary magnetic field directed opposite to the applied magnetic field. Thus, a so-called “shielding effect” was induced, and the applied magnetic field was weakened in the strand. Fig. 13(b) shows the contour of the Lorentz force ( $F_L$ ) on the central longitudinal plane of the strand. Because of the stronger mold shielding effect at 298 K than that at 423 K, the  $F_L$  of the strand was visibly lower, resulting in an approximately 23.6% reduction in  $F_L$  at the solidification front. This subsequently influenced the initial solidification in the mold region. For the shielding effect at room temperature (298 K), the average solid fraction in the strand of the mold region was reduced by 0.37% compared to that at 423 K. In other words, to model the solidification of continuous casting under M-EMS properly, the shielding effect of the copper mold at an elevated operating temperature should be considered.

#### 4.4. Electrical current path through the strand mold interface

During the continuous casting of steel, there is a slag layer between the strand and the copper mold. It is known that the electrical conductivity of the slag affects the electric current path, thereby influencing the M-EMS efficiency. Here, two extreme simulation cases are compared: conducting wall (i.e., the strand–mold interface is an ideal electrical conductor) and isolating wall (i.e., the strand–mold interface is an ideal electrical insulator). The modeling results for the two cases are shown in Fig. 14. The  $B$  fields were almost identical, but the  $J$  fields were extremely different between the two cases. The electrical conductivity of the mold ( $3.18 \times 10^7$  S/m) was considerably higher (38.78 $\times$ ) than that

of the strand ( $8.2 \times 10^5$  S/m). The path of the induced electric current depends strongly on the strand–mold interface condition. As shown in Fig. 14(b), the induced current inside the strand was confined in the strand when the isolating wall condition was applied, while when the conducting wall condition was applied, the induced electric current was largely confined near the mold. For the latter case with a conducting wall, the maximum  $J$  occurred at the mold exit. When the isolating wall was applied,  $F_L$  showed a symmetric distribution and reached the maximum value at the strand surface in the middle section of the stirrer. However, for the conducting wall condition, three  $F_L$  peaks were observed: one at the strand surface in the middle section of the stirrer and two on the strand surface near the mold exit. Overall, the  $F_L$  generated in the strand was relatively low when the conducting wall condition was applied. In the isolating wall case, the average solid fraction in the strand of the mold region was predicted to be approximately 0.61% more than that of the conducting wall case. The actual electrical conductivity of the strand–mold gap is unknown. Considering that (1) the slag layer in the strand–mold gap is mostly in the solid state, which has a relatively lower conductivity, and (2) an air gap may occasionally form between the strand and mold, the strand–mold interface should be treated as an electrically isolating wall.

#### 4.5. Model uncertainty analysis

Although the three-phase solidification model has been consistently evaluated against different industry castings and laboratory experiments by Wu et al. (2019), this study is the first of its kind to apply it to solidification in billet continuous casting with M-EMS. The agreement between the as-cast structure of the simulation and that of the experiment (Fig. 8(a)-(b)) may only be considered as demonstrative, because the modeling results are largely dependent on the modeling parameters, which are partially unknown. Among others, such as the temperature-dependent thermophysical properties and thermal boundary conditions, the main uncertain parameters are the heterogeneous nucleation parameters ( $n_{in}^0$ ,  $\Delta T_N$ , and  $\Delta T_\sigma$ ) and the coefficient that governs crystal fragmentation ( $\gamma$ ). The criterion for the estimation of the nucleation parameters is based on the industry practice whereby a dominant columnar structure should appear in the billet in the as-cast strand for the case without M-EMS; hence, the number of potential nucleation sites should be relatively small ( $n_{in}^0 = 10^9 \text{ m}^{-3}$ ). Both, industry practice and the current simulations (Table 3) agree that the main origin of equiaxed crystals with M-EMS is crystal fragmentation; therefore, the determination of  $\gamma$  becomes more crucial. The topic of M-EMS-induced crystal fragmentation, as the origin of equiaxed crystals in continuously cast steel, is actually under-researched. Here,  $\gamma$  ( $3.0 \times 10^{-5}$ ) was obtained through a parameter study by matching the as-cast structure of the simulation with the experimental one shown in Fig. 8(a).

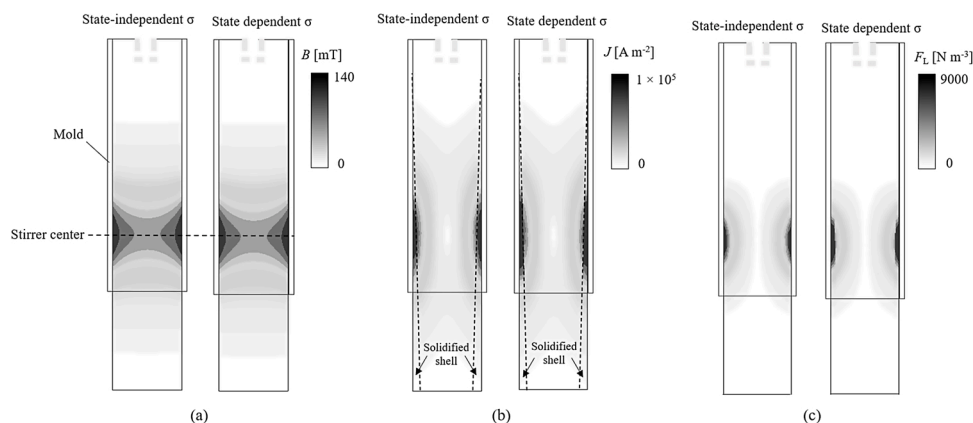
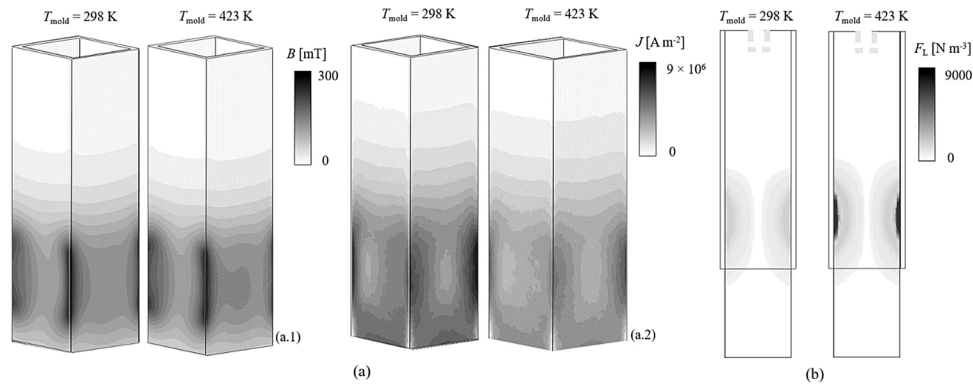
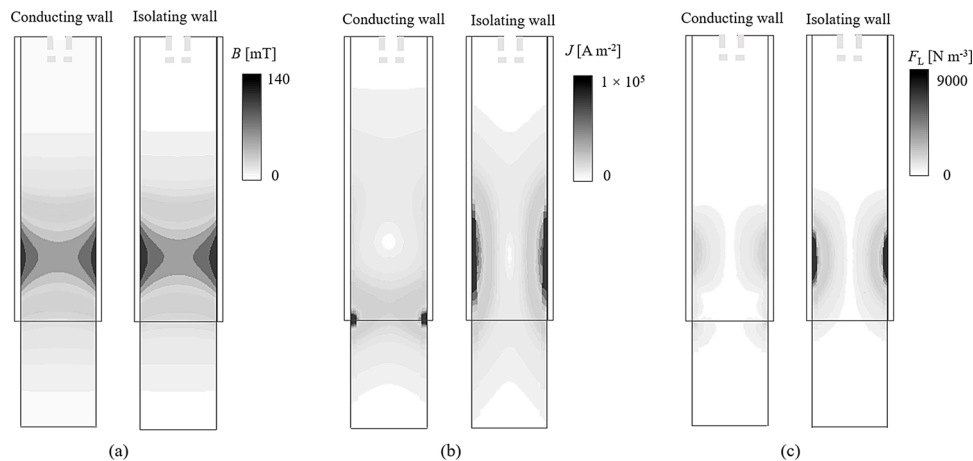


Fig. 12. Time-averaged magnitude of (a) magnetic flux density ( $B$ ), (b) induced electrical current density ( $J$ ), and (c) Lorentz force ( $F_L$ ). Two simulation cases are compared, that consider and ignore the state-dependent electrical conductivity ( $\sigma$ ).



**Fig. 13.** (a) Time-averaged magnitude of electromagnetic fields on the mold surface at two different mold temperatures: (a.1) magnetic flux density ( $B$ ) and (a.2) induced current density ( $J$ ). (b) Contour of the Lorentz force ( $F_L$ ) on the central longitudinal plane of the strand.



**Fig. 14.** Time-averaged magnitude of the (a) magnetic flux density ( $B$ ), (b) induced electrical current density ( $J$ ), and (c) Lorentz force ( $F_L$ ). Two simulation cases are compared: conducting wall (i.e., the strand–mold interface is an ideal electrical conductor) and isolating wall (i.e., the strand–mold interface is an ideal electrical insulator).

Note that for both simulation cases (with and without M-EMS), the same set of nucleation and fragmentation parameters was used.

Another important parameter that significantly impacts macrosegregation, as induced by equiaxed crystal sedimentation, is the volume ratio of the solid dendrite to the equiaxed grain envelope ( $f_{\text{si}}$ ). Because more porous dendritic crystals (smaller  $f_{\text{si}}$ ) tend to pack earlier, that is, at a lower volume fraction of solid ( $f_e$ ), the induced negative macrosegregation ( $c_{\text{mix}}^{\text{index}}$ ) in the central equiaxed zone is less intensive. A recent numerical parameter study showed that the intensity of the negative segregation in the equiaxed sedimentation zone is linearly proportional to  $f_{\text{si}}$ . Furthermore,  $f_{\text{si}}$  is alloy-dependent. Owing to the lack of experimental data (macrosegregation map) for the alloy in this casting format, a value of 0.3 for  $f_{\text{si}}$  was arbitrarily chosen in this study. This implies that the calculated macrosegregation intensity (Fig. 9), particularly in the central equiaxed zone, was quantitatively inaccurate. However, the calculated segregation pattern is qualitatively reliable because the model considers key mechanisms of macrosegregation in the casting process.

## 5. Conclusion

A three-phase solidification model was used to investigate mixed columnar–equiaxed solidification in the continuous casting of a steel billet under the effect of M-EMS. The major contribution of this work is to demonstrate the role of M-EMS in the control of mold flow, which further impacts superheat dissipation, crystal fragmentation, and the

subsequent formation of the as-cast structure and macrosegregation. The following conclusions were drawn.

- (1) In billet casting using existing casting geometry ( $195 \times 195$  mm), M-EMS played the following two roles: i) to accelerate superheat dissipation in the mold region, leaving the liquid core out of the mold region largely undercooled, and ii) to promote the formation of equiaxed crystals through M-EMS-induced crystal fragmentation. These roles were fulfilled synergistically, to result in a central equiaxed zone: the latter led to the origin and formation of equiaxed crystals, and the former promoted the survival and further growth of equiaxed crystals in the secondary cooling zone. By explicitly noting the casting format, we stress that the above roles will change with the casting size and geometry.
- (2) The central equiaxed structure observed in the practice of billet casting with M-EMS was attributed to crystal fragmentation rather than heterogeneous nucleation. The numerical model verified that the crystal fragmentation rate is very sensitive to the M-EMS implementation, whereas the heterogeneous nucleation rate was not.
- (3) A small portion of equiaxed crystals could be brought by the M-EMS-induced swirling flow into the superheated zone and remelted. These simultaneous phenomena (solidification at one location and grain migration and remelting at another location) represent an important species/energy transport mechanism, which impacts the as-cast structure and compositional heterogeneity.

- (4) Numerical parameter studies were performed to investigate the shielding effect of the copper mold at different operating temperatures, including the effect of the (solid/liquid) state-dependent electrical conductivity of the strand and the effect of the electric current path through the strand–mold interface. Only the electric current path through the strand–mold interface was found to be of critical importance, and it significantly affected the M-EMS efficiency.

Although a satisfactory agreement between the numerically calculated and experimentally determined as-cast structure was achieved, the current modeling results can only be considered qualitative because some modeling parameters were estimated based on a numerical parameter study. Further laboratory or in-plant experiments are required to quantify these parameters.

#### Author declaration

The authors declare that they have no known competing financial interests or personal relationships that could have appeared to influence the work reported in this paper.

#### CRediT authorship contribution statement

**Zhao Zhang:** Conceptualization, Methodology, Software, Investigation, Writing - original draft, Visualization. **Menghuai Wu:** Conceptualization, Methodology, Software, Writing - review & editing, Project administration, Funding acquisition. **Haijie Zhang:** Methodology, Software. **Susanne Hahn:** Validation, Funding acquisition. **Franz Wimmer:** Investigation. **Andreas Ludwig:** Resources, Supervision. **Abdellah Kharicha:** Software, Formal analysis.

#### Declaration of Competing Interest

None.

#### Acknowledgements

The authors acknowledge the financial support from the Austria Research Promotion Agency (FFG) through the Bridge 1 project (No. 868070) as well as the technical support of the industrial partner Primetals Technologies Austria GmbH.

#### References

- An, H., Bao, Y., Wang, M., Zhao, L., 2018. Effects of electromagnetic stirring on fluid flow and temperature distribution in billet continuous casting mould and solidification structure of 55SiCr. *Metall. Res. Technol.* 115, 103–115. <https://doi.org/10.1051/metal/2017075>.
- An, H., Bao, Y., Wang, M., Yang, Q., Huang, Y., 2019. Improvement of centre segregation in continuous casting bloom and the resulting carbide homogeneity in bearing steel GCr15. *Ironmak. Steelmak.* 46, 896–905. <https://doi.org/10.1080/03019233.2019.1604614>.
- Ayata, K., Mori, T., Fujimoto, T., Ohnishi, T., Wakasugi, I., 1984. Improvement of macrosegregation in continuously cast bloom and billet by electromagnetic stirring. *Trans. Iron Steel Inst. Japan* 24, 931–939. <https://doi.org/10.2355/isijinternational1966.24.931>.
- Du, W.D., Wang, K., Song, C.J., Li, H.G., Jiang, M.W., Zhai, Q.J., Zhao, P., 2008. Effect of special combined electromagnetic stirring mode on macrosegregation of high strength spring steel blooms. *Ironmak. Steelmak.* 35, 153–156. <https://doi.org/10.1179/030192307X239533>.
- Du, F., Zhang, K., Li, C., Chen, W., Zhang, P., Wang, X., 2021. Investigation on non-uniform friction behaviors of slab during continuous casting based on an inverse algorithm. *J. Mater. Process. Technol.* 288, 116871. <https://doi.org/10.1016/j.jmatprotec.2020.116871>.
- Fang, Q., Ni, H., Wang, B., Zhang, H., Ye, F., 2017. Effects of EMS induced flow on solidification and solute transport in bloom mold. *Metals (Basel)*. 7, 72. <https://doi.org/10.3390/met7030072>.
- Han, Q., Hellawell, A., 1997. Primary particle melting rates and equiaxed grain nucleation. *Metall. Mater. Trans. B Process Metall. Mater. Process. Sci.* 28, 169–173. <https://doi.org/10.1007/s11663-997-0139-7>.

- Janik, M., Dyja, H., 2004. Modelling of three-dimensional temperature field inside the mould during continuous casting of steel. *J. Mater. Process. Technol.* 157–158, 177–182. <https://doi.org/10.1016/j.jmatprotec.2004.09.026>.
- Jia, Y., Hou, J., Wang, H., Le, Q., Lan, Q., Chen, X., Bao, L., 2020. Effects of an oscillation electromagnetic field on grain refinement and Al8Mn5 phase formation during direct-chill casting of AZ31B magnesium alloy. *J. Mater. Process. Technol.* 278, 116542. <https://doi.org/10.1016/j.jmatprotec.2019.116542>.
- Kunstreich, S., 2003a. Electromagnetic stirring for continuous casting - Part 1. *Rev. Metall. Cah. D'Informations Tech.* 100, 395–408. <https://doi.org/10.1051/metal:2003198>.
- Kunstreich, S., 2003b. Electromagnetic stirring for continuous casting - Part 2. *Rev. Metall. Cah. D'Informations Tech.* 100, 1043–1061. <https://doi.org/10.1051/metal:2003113>.
- Laitinen, E., Neittaanmäki, P., 1988. On numerical simulation of the continuous casting process. *J. Eng. Math.* 22, 335–354. <https://doi.org/10.1007/BF00058513>.
- Li, J., Wang, B., Ma, Y., Cui, J., 2006. Effect of complex electromagnetic stirring on inner quality of high carbon steel bloom. *Mater. Sci. Eng. A* 425, 201–204. <https://doi.org/10.1016/j.msea.2006.03.061>.
- Li, S., Lan, P., Tang, H., Tie, Z., Zhang, J., 2018. Study on the electromagnetic field, fluid flow, and solidification in a bloom continuous casting mold by numerical simulation. *Steel Res. Int.* 89, 1800071. <https://doi.org/10.1002/srin.201800071>.
- Li, S., Xiao, H., Wang, P., Liu, H., Zhang, J., 2019. Analysis on electromagnetic field of continuous casting mold including a new integral method for calculating electromagnetic torque. *Metals (Basel)*. 9, 946. <https://doi.org/10.3390/met9090946>.
- Li, H., Gong, M., Li, T., Wang, Z., Wang, G., 2020. Effects of hot-core heavy reduction rolling during continuous casting on microstructures and mechanical properties of hot-rolled plates. *J. Mater. Process. Technol.* 283, 116708. <https://doi.org/10.1016/j.jmatprotec.2020.116708>.
- Lipton, J., Glicksman, M.E., Kurz, W., 1984. Dendritic growth into undercooled alloy metals. *Mater. Sci. Eng.* 65, 57–63. [https://doi.org/10.1016/0025-5416\(84\)90199-X](https://doi.org/10.1016/0025-5416(84)90199-X).
- Natarajan, T.T., El-Kaddah, N., 2004. Finite element analysis of electromagnetic and fluid flow phenomena in rotary electromagnetic stirring of steel. *Appl. Math. Model.* 28, 47–61. [https://doi.org/10.1016/S0307-904X\(03\)00114-8](https://doi.org/10.1016/S0307-904X(03)00114-8).
- Peel, D.A., Pengelly, A.E., 1968. Heat transfer, solidification, and metallurgical structure in the continuous casting of aluminum. *Proc. of 1st SP Conf. in 1967. The Solidification of Metals* 186–196.
- Spitzer, K.H., Dubke, M., Schwerdtfeger, K., 1986. Rotational electromagnetic stirring in continuous casting of round strands. *Metall. Trans. B* 17, 119–131. <https://doi.org/10.1007/BF02670825>.
- Sun, H., Zhang, J., 2014. Study on the macrosegregation behavior for the bloom continuous casting: Model development and validation. *Metall. Mater. Trans. B*. 45, 1133–1149. <https://doi.org/10.1007/s11663-013-9986-6>.
- Thomas, B.G., 2018. Review on modeling and simulation of continuous casting. *Steel Res. Int.* 89, 1700312. <https://doi.org/10.1002/srin.201700312>.
- Thomas, B.G., Singh, R., Vanka, S.P., Timmel, K., Eckert, S., Gerbeth, G., 2015. Effect of single-ruler electromagnetic braking (EMBr) location on transient flow in continuous casting. *J. Manuf. Sci. Prod.* 15, 93–104. <https://doi.org/10.1515/jmsp-2014-0047>.
- Trindade, L.B., Vilela, A.C.F., Filho, A.F.F., Vilhena, M.T.M.B., Soares, R.B., 2002. Numerical model of electromagnetic stirring for continuous casting billets. *IEEE Trans. Magn.* 38, 3658–3660. <https://doi.org/10.1109/TMAG.2002.804804>.
- Trindade, L.B., Nadalon, J.E.A., Contini, A.C., Barroso, R.C., 2017. Modeling of solidification in continuous casting round billet with mold electromagnetic stirring (M-EMS). *Steel Res. Int.* 88, 1600319. <https://doi.org/10.1002/srin.201600319>.
- Wang, X., Tang, L., Zang, X., Yao, M., 2012. Mold transient heat transfer behavior based on measurement and inverse analysis of slab continuous casting. *J. Mater. Process. Technol.* 212, 1811–1818. <https://doi.org/10.1016/j.jmatprotec.2012.04.001>.
- Wang, S., Alvarez De Toledo, G., Välimaa, K., Louhenkilpi, S., 2014. Magneto-hydrodynamic phenomena, fluid control and computational modeling in the continuous casting of billet and bloom. *ISIJ Int.* 54, 2273–2282. <https://doi.org/10.2355/isijinternational.54.2273>.
- Wang, X., Zheng, S., Liu, Z., Zhu, M., 2020a. Numerical simulation on multiple physical fields behaviors in billet continuous casting with different stirrer positions. *Steel Res. Int.* 91, 1900415. <https://doi.org/10.1002/srin.201900415>.
- Wang, Y., Chen, W., Jiang, D., Zhang, L., 2020b. Effect of the gap between copper mold and solidified shell on the fluid flow in the continuous casting strand with mold electromagnetic stirring. *Steel Res. Int.* 91, 1900470. <https://doi.org/10.1002/srin.201900470>.
- Wang, Y., Zhang, L., Yang, W., Ji, S., Ren, Y., 2021. Effect of mold electromagnetic stirring and final electromagnetic stirring on the solidification structure and macrosegregation in bloom continuous casting. *Steel Res. Int.* 92, 2000661. <https://doi.org/10.1002/srin.202000661>.
- Wu, M., Ludwig, A., 2006. A three-phase model for mixed columnar-equiaxed solidification. *Metall. Mater. Trans. A*. 37, 1613–1631. <https://doi.org/10.1007/s11661-006-0104-0>.
- Wu, H.J., Wei, N., Bao, Y.P., Wang, G.X., Xiao, C.P., Liu, J.J., 2011. Effect of M-EMS on the solidification structure of a steel billet. *Int. J. Miner. Metall. Mater.* 18, 159–164. <https://doi.org/10.1007/s12613-011-0416-y>.
- Wu, M., Ludwig, A., Kharicha, A., 2019. Volume-averaged modeling of multiphase flow phenomena during alloy solidification. *Metals (Basel)* 9, 229. <https://doi.org/10.3390/met9020229>.
- Zappulla, M.L.S., Cho, S.M., Koric, S., Lee, H.J., Kim, S.H., Thomas, B.G., 2020. Multiphysics modeling of continuous casting of stainless steel. *J. Mater. Process. Technol.* 278, 116469. <https://doi.org/10.1016/j.jmatprotec.2019.116469>.

- Zhang, W., Luo, S., Chen, Y., Wang, W., Zhu, M., 2019. Numerical simulation of fluid flow, heat transfer, species transfer, and solidification in billet continuous casting mold with M-EMS. *Metals (Basel)* 9, 66. <https://doi.org/10.3390/met9010066>.
- Zhang, H., Wu, M., Schumacher, P., Rodrigues, C.M.G., Ludwig, A., Kharicha, A., 2021. Modelling melting and grain destruction phenomena during globular equiaxed solidification. *Appl. Math. Model.* 97, 821–838. <https://doi.org/10.1016/j.apm.2021.04.024>.
- Zheng, Y., Wu, M., Kharicha, A., Ludwig, A., 2018. Incorporation of fragmentation into a volume average solidification model. *Model. Simul. Mater. Sci. Eng.* 26, 015004 <https://doi.org/10.1088/1361-651X/aa86c5>.





## **Paper 2**

# **The Role of Mold Electromagnetic Stirring (M-EMS) in the Dissipation of Superheat During the Continuous Casting of Billets**

Zhao Zhang, Menghuai Wu, Haijie Zhang,  
Andreas Ludwig, Abdellah Kharicha

Steel Research International

Volume 93, 2022, 2200065



# The Role of Mold Electromagnetic Stirring in the Dissipation of Superheat during the Continuous Casting of Billets

Zhao Zhang, Menghuai Wu,\* Haijie Zhang, Andreas Ludwig, and Abdellah Kharicha

A two-phase solidification model coupling mold electromagnetic stirring (M-EMS) is used to investigate the initial solidification in the mold region of billet continuous casting. One novelty of this numerical study is to quantify how the M-EMS induces primary and secondary flows, interacting with the jet flows coming from the submerged entry nozzle, and how those flows further influence the dissipation of superheat and the initial solidification. The role of the M-EMS in speeding up the superheat dissipation in the mold region, known from previous studies and casting practices, is quantitatively verified. Additionally, some new knowledge regarding the M-EMS is found. The total heat transfer rate from the strand surface to the water-cooled copper mold is not affected by the M-EMS; with the M-EMS, the superheat effect on the solid growth can only be detected in the out-of-the-mold region, while the shell growth inside the mold region is quite independent of the superheat; a strong M-EMS tends to accelerate the growth of the solid shell in the mold region, but delays its growth in the secondary cooling zones. The aforementioned new findings may only be valid for the case of the current billet casting, to be confirmed for other casting formats/parameters.

Mold electromagnetic stirring (M-EMS), as an additional engineering measure, has been widely used to optimize fluid flow and heat transfer, and hence to control as-cast structures and macrosegregation.<sup>[5–11]</sup> The swirling flow generated by M-EMS can effectively speed up the superheat dissipation in the mold region, and as a consequence, the equiaxed nuclei originating from crystal fragmentation or heterogeneous nucleation can survive the superheat and form the central equiaxed zone.<sup>[12,13]</sup>

Due to the harsh environment and high cost of field experiments, numerical modeling has become an effective tool for investigating transport behavior with M-EMS. Yu et al.<sup>[14]</sup> developed a mathematical model to investigate the effect of M-EMS on the flow field, temperature profile, and inclusion trajectories in round billet continuous casting. They found that the core temperature was dramatically reduced with M-EMS. An et al.<sup>[15]</sup> proposed a 3D


mathematical model to study the effect of current intensity and frequency on fluid flow, and the simulation results also indicated that M-EMS tends to accelerate superheat dissipation. However, solidification was ignored in the above studies.

Ren et al.<sup>[16]</sup> developed a mathematical model to investigate the influence of M-EMS on fluid flow, heat transfer, and solidification in round bloom continuous casting. They found that M-EMS prevents the superheated jet from moving downward and thus accelerates superheat dissipation in the mold region. Li et al.<sup>[17]</sup> proposed a coupled magnetohydrodynamics (MHD) model to study the electromagnetic field, fluid flow, and solidification with M-EMS in bloom continuous casting. The maximum melt swirling flow velocity was found to be remarkably decreased when considering solidification. Meanwhile, the M-EMS-induced swirling flow was beneficial for preventing the superheated melt from moving down into the liquid core below. Trindade et al.<sup>[18]</sup> used a coupled numerical model to study the fluid flow, temperature distribution, and solidification of round billet continuous casting under M-EMS. They found that M-EMS tends to decrease the temperature in the strand center and locally reduce the shell thickness due to the increase in the tangential velocity close to the wall. However, common drawbacks of the previous models are as follows: 1) they used a relatively rough mixture-based model to study the solidification characteristics. The solid shell is simply calculated based on the lever rule, which omits some important

## 1. Introduction

During the continuous casting of billets, a steel melt is poured into a water-cooled copper mold with a certain superheat. Superheat is defined as the sensible energy contained in the melt above the liquidus,<sup>[1]</sup> but it is often simply referred to as the temperature difference above the liquidus. It is generally recognized that casting with a low superheat is beneficial for minimizing centerline segregation by facilitating the formation of a central equiaxed zone.<sup>[2–4]</sup>

Z. Zhang, M. Wu, H. Zhang, A. Ludwig, A. Kharicha  
Simulation and Modelling of Metallurgical Processes  
Department of Metallurgy  
Montanuniversitaet Leoben  
Franz-Josef-Str. 18, 8700 Leoben, Austria  
E-mail: menghuai.wu@unileoben.ac.at

 The ORCID identification number(s) for the author(s) of this article can be found under <https://doi.org/10.1002/srin.202200065>.

© 2022 The Authors. Steel Research International published by Wiley-VCH GmbH. This is an open access article under the terms of the Creative Commons Attribution-NonCommercial-NoDerivs License, which permits use and distribution in any medium, provided the original work is properly cited, the use is non-commercial and no modifications or adaptations are made.

DOI: 10.1002/srin.202200065

characteristic features, i.e., the columnar tip growth velocity and the flow-solidification interaction in the mushy zone; 2) the flow-EMS coupling is simplified. On one hand, the solid shell, which has a higher electrical conductivity than the liquid melt, is ignored when calculating the Lorentz force. On the other hand, the effect of melt flow on the Lorentz force is ignored. The original Lorentz force should be reduced under the effect of a rotating melt flow. Ignorance of this modification would overestimate the melt flow. Dong et al.<sup>[19]</sup> developed a magnetohydrodynamic model to investigate the effect of fluid flow on the magnetic field, induced current, and electromagnetic force. They found that the flow field in the mold has a certain influence on the magnetic field, the effect of fluid flow in M-EMS calculation should not be ignored. However, the mixture solidification model used in their study failed to treat the columnar tip growth and the flow-solidification interaction in the mushy zone accurately.

In this study, a two-phase columnar solidification model is used to investigate the superheat dissipation in billet continuous casting under the effect of M-EMS. The evolution of the solid shell of the strand is considered using the two-phase model as columnar dendritic structures, whose front is dynamically tracked. The flow-solidification interaction in the mushy zone, and its effect on the formation of macrosegregation are considered. Importantly, a proper coupling scheme between the electromagnetic field and the melt flow is used to treat the flow-EMS integration, i.e., the tangential velocity of the melt that follows the rotational magnetic field would reduce the Lorentz force. Additionally, state-dependent electrical conductivity is used for liquid melts and solid shells, i.e., the solid shell is electrically more conductive than the liquid melt. Parameter studies were performed by varying the superheat and M-EMS electric current intensity.

## 2. Model Description

### 2.1. Basis Assumptions

A two-phase columnar solidification model is presented to study the initial solidification of the billet strands. The governing equations of the solidification model, are summarized in **Table 1**, and details of the model are described elsewhere.<sup>[20–23]</sup> The main features/assumptions are given below. 1) Two phases are defined: liquid melt ( $\ell$ ) and solid columnar dendrites ( $c$ ). Their volume fractions ( $f_\ell, f_c$ ) sum up to one. The velocity of the liquid melt is obtained by solving the corresponding Navier–Stokes equations, and the motion of the columnar phase is set constant (equal to the casting speed); 2) The columnar dendrites are assumed to develop directly from the strand surface. The position of the columnar tip front is explicitly treated according to the Lipton–Glicksman–Kurz model<sup>[24]</sup>; 3) Since the magnetic Reynolds used in the current study is relatively large (0.0463). In addition, the liquid rotating angular speed ( $\omega_\ell = 4.27 \text{ rad s}^{-1}$ ) is about 22% of the magnetic rotating angular speed ( $\omega_B = 18.85 \text{ rad s}^{-1}$ ). Thus, it is necessary to consider the effect of melt flow on the electromagnetic force. The time-averaged rotational electromagnetic force ( $\vec{F}_L$ ) is calculated based on the Maxwell equations. To consider the interaction between the melt flow and the magnetic field, the electromagnetic force

is modified by considering the relative motion between the rotation magnetic field and the tangential velocity of the melt,  $\vec{F}'_L = \vec{F}_L(1 - \vec{u}_0/(2\pi f \cdot r))$ , where  $\vec{u}_0$  is the tangential component of the melt velocity,  $f$  is the M-EMS frequency and  $r$  is the radial coordinate.  $\vec{F}'_L$  is implemented in the model; 4) Volume-averaged concentrations of the liquid melt ( $c_\ell$ ) and solid columnar dendrites ( $c_c$ ) are calculated. Macrosegregation is characterized by the segregation index,  $c_{\text{mix}}^{\text{index}} = (c_{\text{mix}} - c_0) \times 100/c_0$ , in which  $c_0$  is the initial concentration and  $c_{\text{mix}}$  is the mixture concentration,  $c_{\text{mix}} = (f_\ell \rho_\ell c_\ell + f_c \rho_c c_c)/(f_\ell \rho_\ell + f_c \rho_c)$ ; and 5) Solidification shrinkage is ignored, and the thermal-solutal convection of melt is modeled with the Boussinesq approach.

### 2.2. Geometry and Boundary Conditions

**Figure 1a** reveals the geometrical configuration of billet continuous casting with M-EMS. The dimensions and relative positions between the mold and M-EMS are shown in **Figure 1b**. The distribution of simulated and measured magnetic flux density along the axis-line of mold in the absence of strand are displayed in **Figure 1c**. A satisfactory simulation-experiment agreement is obtained. The stirrer is fed using a three-phase alternative current (AC) with a frequency of 3 Hz. The current intensity is set to 430 A for the reference case. The casting format is 195 mm  $\times$  195 mm, referring to an industrial process. Since the current study focuses on the initial state of solidification, i.e., the formation of a solid shell in the mold region and solidification in the first and second cooling regions, the entire calculation domain (length of the strand) is limited to only 3 m from the meniscus. A 3D calculation (3 m long) requires 7 days on a high-performance cluster (2.6 GHz, 28 cores). For commercial reasons, the composition of the industrial alloy is omitted, but it is simplified as an equivalent binary alloy with a nominal composition of Fe–0.53 wt.%C. The pouring temperature of the reference case is set to 1708.15 K. Parameter studies will be performed by varying the pouring temperature (1698.15–1718.15 K) and M-EMS intensity (200–600 A). A five-port submerged entry nozzle (SEN) is applied, with M-EMS located at the bottom of the mold. On-site measurements of the magnetic flux density along the axis on the continuous casting machine of an empty mold at room temperature were made, which were used to validate the electromagnetic calculation (ANSYS-Maxwell). A satisfactory agreement was obtained between the calculation and measurement. A constant heat transfer coefficient was applied in the mold region to calculate the heat extraction from the strand surface to the copper mold. The heat flux thermal boundary conditions are used in the secondary cooling zones and for commercial reasons, the values are omitted. The strand-mold interface is regarded as electrically isolating. The material properties are listed in **Table 2**.

### 2.3. Numerical Procedure

Electromagnetic-computational fluid dynamics (EM-CFD) iteration was conducted on two commercial software programs, namely ANSYS-Maxwell and ANSYS-Fluent. The ANSYS Fluent add-on MHD module provides a coupled calculation scheme, but the original magnetic field ( $\vec{B}_0$ ) must be provided

**Table 1.** Governing equations of the two-phase columnar solidification model.

Governing equations	Symbols
1. Mass conservations	$f_l, f_c$ , volume fraction of liquid and columnar phases [-] $\rho_l, \rho_c$ , density of liquid and columnar phases [ $\text{kg m}^{-3}$ ] $\vec{u}_l$ , velocity vector of the liquid [ $\text{m s}^{-1}$ ] $M_{lc}$ , net mass transfer rate [ $\text{kg m}^{-3} \text{s}^{-1}$ ]
$\frac{\partial}{\partial t}(f_l \rho_l) + \nabla \cdot (f_l \rho_l \vec{u}_l) = -M_{lc} \quad (1)$	
$\frac{\partial}{\partial t}(f_c \rho_c) = M_{lc} \quad (2)$	
$f_l + f_c = 1 \quad (3)$	
2. Momentum conservations	$\vec{\tau}_i$ , stress-strain tensors [ $\text{kg m}^{-1} \text{s}^{-1}$ ] $p$ , pressure [ $\text{N m}^{-2}$ ] $\vec{g}, \vec{g}'$ , gravity and deduced gravity [ $\text{m s}^{-2}$ ] $\rho_l^b$ , density for buoyancy force [ $\text{kg m}^{-3}$ ] $\rho_l^{\text{ref}}$ , reference density [ $\text{kg m}^{-3}$ ] $T^{\text{ref}}$ , reference temperature [K] $c^{\text{ref}}$ , reference concentration [-] $\beta_T$ , thermal expansion coefficient [ $\text{K}^{-1}$ ] $\beta_c$ , solutal expansion coefficient [ $\text{wt}\%^{-1}$ ] $\vec{F}_L, \vec{F}_L'$ , Lorentz force and modified Lorentz force [ $\text{N m}^{-3}$ ] $\vec{U}_{lc}$ , momentum exchange rate [ $\text{kg m}^{-2} \text{s}^{-2}$ ] $\vec{u}_\theta$ , tangential velocity [ $\text{m s}^{-1}$ ] $f$ , frequency of the applied current [Hz] $r$ , radial coordinate [m]
$\frac{\partial}{\partial t}(f_l \rho_l \vec{u}_l) + \nabla \cdot (f_l \rho_l \vec{u}_l \otimes \vec{u}_l) = -f_l \nabla p + \nabla \cdot \vec{\tau}_l + f_l \rho_l \vec{g}' + f_l \vec{F}_L' - \vec{U}_{lc} \quad (4)$	
$\vec{g}' = \frac{\rho_l^b(T, c_l) - \rho_l^{\text{ref}}}{\rho_l^{\text{ref}}} \vec{g} \quad (5)$	
$\rho_l^b(T, c_l) = \rho_l^{\text{ref}} \cdot (1 + \beta_T \cdot (T^{\text{ref}} - T_l) + \beta_c \cdot (c^{\text{ref}} - c_l)) \quad (6)$	
$\vec{F}_L' = \vec{F}_L \left(1 - \frac{\vec{u}_\theta}{2\pi f \cdot r}\right) \quad (7)$	
3. Species conservations	$c_l, c_c$ , species concentration of liquid and columnar phases [-] $D_l, D_c$ , diffusion coefficient of liquid and columnar phases [ $\text{m}^2 \text{s}^{-1}$ ] $C_{lc}$ , species exchange rate [ $\text{kg m}^{-3} \text{s}^{-1}$ ]
$\frac{\partial}{\partial t}(f_l \rho_l c_l) + \nabla \cdot (f_l \rho_l \vec{u}_l c_l) = \nabla \cdot (f_l \rho_l D_l \nabla c_l) - C_{lc} \quad (8)$	
$\frac{\partial}{\partial t}(f_c \rho_c c_c) = \nabla \cdot (f_c \rho_c D_c \nabla c_c) + C_{lc} \quad (9)$	
4. Enthalpy conservations	$h_l, h_c$ , enthalpy of liquid and columnar phases [ $\text{J kg}^{-1}$ ] $k_l, k_c$ , thermal conductivity of liquid and columnar phases [ $\text{W m}^{-1} \text{K}^{-1}$ ] $Q_{lc}$ , energy exchange rate [ $\text{J m}^{-3} \text{s}^{-1}$ ]
$\frac{\partial}{\partial t}(f_l \rho_l h_l) + \nabla \cdot (f_l \rho_l \vec{u}_l h_l) = \nabla \cdot (f_l k_l \nabla \cdot T_l) - Q_{lc} \quad (10)$	
$\frac{\partial}{\partial t}(f_c \rho_c h_c) = \nabla \cdot (f_c k_c \nabla \cdot T_c) + Q_{lc} \quad (11)$	
5. Electromagnetic field	$\vec{B}$ , magnetic flux density [T] $\vec{B}^*$ , conjugate magnetic flux density [T] $\vec{H}$ , magnetic field intensity [ $\text{A m}^{-1}$ ] $\mu_0$ , magnetic permeability in vacuum [ $\text{T m A}^{-1}$ ] $\mu_r$ , relative magnetic permeability [-] $\vec{E}$ , electric field intensity [ $\text{V m}^{-1}$ ] $\vec{J}$ , induced current density [ $\text{A m}^{-2}$ ] $\sigma$ , electrical conductivity [ $\Omega^{-1} \text{m}^{-1}$ ] $\vec{F}_L$ , time-averaged Lorentz force [ $\text{N m}^{-3}$ ] $R_e$ , the real part of a complex number [-]
$\vec{B} = \mu_0 \mu_r \vec{H} \quad (12)$	
$\nabla \times \vec{E} = -\frac{\partial \vec{B}}{\partial t} \quad (13)$	
$\vec{J} = \sigma \vec{E} \quad (14)$	
$\vec{F}_L = \frac{1}{2} R_e(\vec{J} \times \vec{B}^*) \quad (15)$	

either by EM calculation (ANSYS-Maxwell) or experimental measurement. Because of the explicit temporal resolution of  $\vec{B}_0$ , the time step for the numerical simulation should be very small. The additional calculation of the induced magnetic field ( $\vec{b}$ ) equations and their interaction with the momentum equations and energy equations are computationally costly. Additionally, the add-on MHD module in ANSYS Fluent is not compatible with the Eulerian-Eulerian approach, which is used for the multi-phase solidification problem.<sup>[25]</sup> Thus, another relatively simple but reasonable method was used. First, the time-averaged Lorentz force ( $\vec{F}_L$ ) was calculated using ANSYS-Maxwell with

the assumption that the calculation domain is full of stationary melt. Then,  $\vec{F}_L$  was interpolated into the mesh system of ANSYS-Fluent, weighted by the corresponding phase volume fraction (melt, columnar), and finally added as a source term to the momentum conservation equation of each phase via user-defined functions (UDFs). To consider the interaction between the melt flow and magnetic field,  $\vec{F}_L$  was modified by considering a factor that is related to the relative velocity between the rotational magnetic field and the tangential velocity of the melt (Equation (7)). The calculations of the melt flow, heat transfer and solute transport were coupled in ANSYS-Fluent.

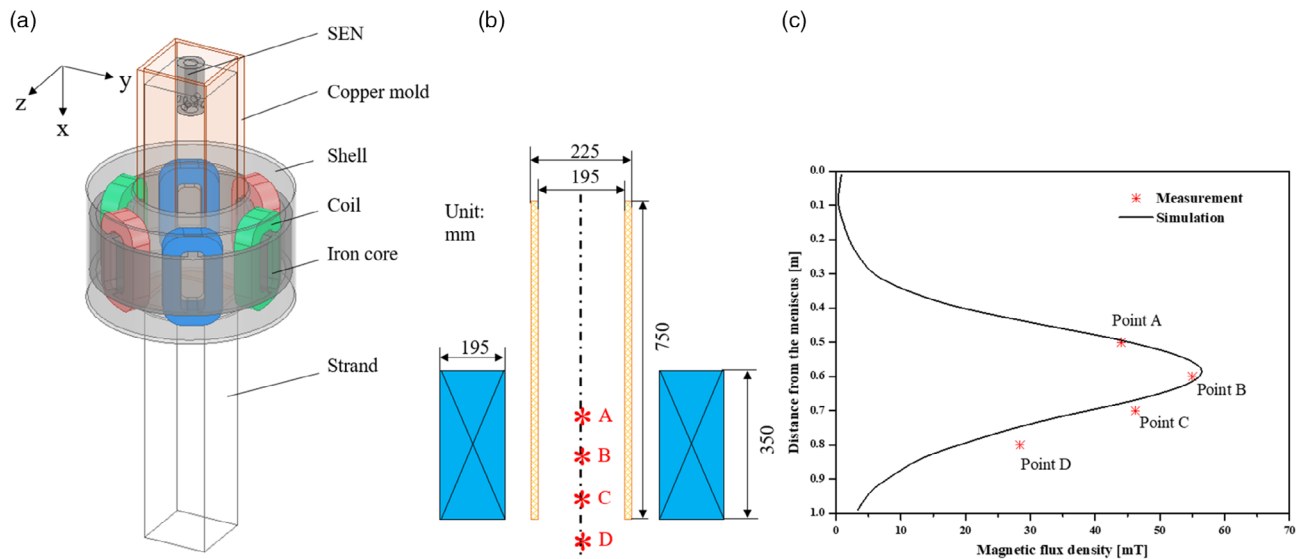


**Figure 1.** a) Geometrical configuration of billet continuous casting with M-EMS; b) dimensions and relative positions between the mold and M-EMS; c) distributions of simulated and measured magnetic flux density along the axis-line of mold in the absence of strand.

**Table 2.** Material properties.

Material properties	Symbols	Units	Values
Nominal concentration	$c_0$	wt.%	0.53
Liquidus temperature	$T_L$	K	1688.15
Solidus temperature	$T_S$	K	1593.15
Liquid density	$\rho_l$	$\text{kg m}^{-3}$	7035.0
Latent heat	$L$	$\text{kJ kg}^{-1}$	220.0
Specific heat	$c_p$	$\text{J kg}^{-1} \text{K}^{-1}$	800.0
Thermal conductivity	$k_l, k_s$	$\text{W m}^{-1} \text{K}^{-1}$	33.0
Diffusion coefficient in liquid	$D_l$	$\text{m}^2 \text{s}^{-1}$	$2.0 \times 10^{-8}$
Diffusion coefficient in solid	$D_s$	$\text{m}^2 \text{s}^{-1}$	$1.0 \times 10^{-9}$
Thermal expansion coefficient of the melt	$\beta_T$	$\text{K}^{-1}$	$4.5 \times 10^{-5}$
Solutal expansion coefficient of the melt	$\beta_C$	$\text{wt.}\%^{-1}$	0.02
Equilibrium partition coefficient of carbon	$k$	-	0.252
Electric conductivity of strand (melt)	$\sigma_l$	$\text{S m}^{-1}$	$7.6 \times 10^5$
Electric conductivity of strand (solid)	$\sigma_s$	$\text{S m}^{-1}$	$8.2 \times 10^5$
Electric conductivity of copper mold	$\sigma_m$	$\text{S m}^{-1}$	$3.18 \times 10^7$
Primary dendritic arm spacing	$\lambda_1$	m	$1.85 \times 10^{-4}$
Secondary dendritic arm spacing	$\lambda_2$	m	$4.8 \times 10^{-5}$
Viscosity	$\mu_l$	$\text{kg m}^{-1} \text{s}^{-1}$	0.006
Gibbs Thomson coefficient	$\Gamma$	m K	$3.3 \times 10^{-7}$
Casting speed	$V_c$	$\text{m min}^{-1}$	0.8

After the casting reached a quasi-steady state, the profile of the solid shell was exported from ANSYS-Fluent and then imported to ANSYS-Maxwell to recalculate  $\vec{F}_L$ . The solid shell used a relatively higher electrical conductivity ( $8.2 \times 10^5 \text{ S m}^{-1}$ ) than the stationary melt ( $7.6 \times 10^5 \text{ S m}^{-1}$ ). The recalculated  $\vec{F}_L$  was

exported from the ANSYS-Maxwell and then interpolated to ANSYS-Fluent to recalculate the melt flow, heat transfer, and solute transport. When the casting process approaches the quasi-steady state again, the simulation results are analyzed with highlight.

## 3. Results

### 3.1. Flow Field

Comparisons of the original Lorentz force and modified Lorentz force are displayed in Figure 2. Distributions of the Lorentz force on the central vertical plane of the strand are shown in Figure 2a, and the Lorentz forces on the cross-section plane at the position of the M-EMS center are shown in Figure 2b. Two isolines are plotted to present the solidified shell ( $f_c = 0.7$ ) and columnar solidification front ( $f_c = 0.05$ ). It is clear to see that the two Lorentz forces are basically the same within the solidified shell region where the liquid tangential velocity  $\vec{u}_\theta$  (Equation (7)) is nearly zero. While in the mushy zone and bulk liquid region, the movement of the liquid melt tends to decrease the Lorentz force correspondingly. Profiles of the Lorentz force along the centerline (Line 1) of the M-EMS center plane are shown in Figure 2c. Two isolines are used to define the different solidification regions (bulk liquid, mushy zone, and solid shell). The M-EMS-induced swirling flow is capable to reduce the original Lorentz force by up to 45.34% at the columnar solidification front (0.072 m to the strand center). It is obvious that ignorance of the modification will overestimate the liquid flow and further influence the heat/mass transfer rate during the billet continuous casting.

Figure 3a shows the velocity contour of the flow pattern. To understand the effect of M-EMS, two cases are compared here, namely, without and with M-EMS. The quarter of the calculation domain is cut vertically in Figure 3a to get a better view of the

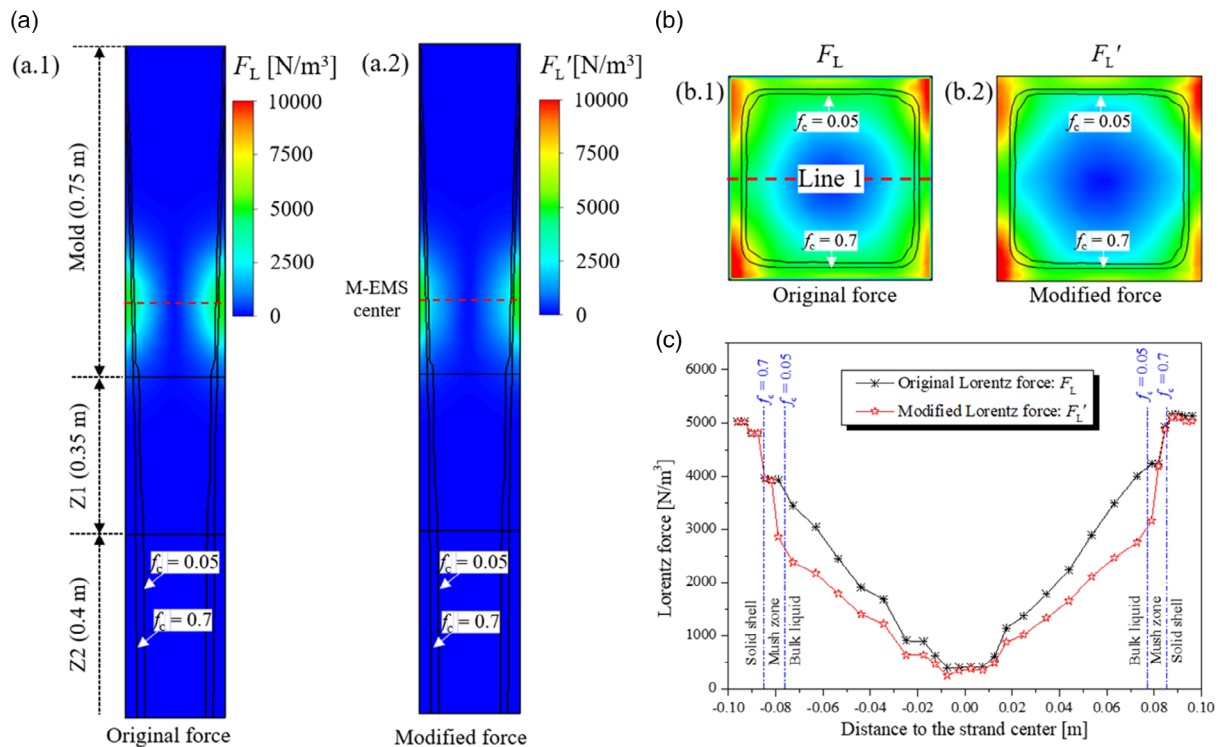


**Figure 2.** a) Distributions of the Lorentz force on the central vertical plane of the strand overlaid with two isolines to present the solid shell ( $f_c = 0.7$ ) and columnar solidification front ( $f_c = 0.05$ ), a.1) original Lorentz force  $\vec{F}_L$ ; a.2) modified Lorentz force  $\vec{F}'_L$ ; b) Lorentz force on cross-sectional plane at the position of M-EMS center, b.1) original Lorentz force  $\vec{F}_L$ ; b.2) modified Lorentz force  $\vec{F}'_L$ ; c) Lorentz force profiles along the centerline (Line 1) of (b).

inner information of the billet strand. Zoom-views of the flow pattern at the upper part of the mold region are shown in Figure 3b, zoom-views of the flow pattern at the lower part of the mold region are displayed in Figure 3c. In addition, the flow patterns on horizontal sections at the position of the M-EMS center are also shown in Figure 3c. Two isolines are also plotted to present the solidified shell ( $f_c = 0.7$ ) and columnar solidification front ( $f_c = 0.05$ ). The analysis area is limited to 1.5 meters from the meniscus, covering the mold region and two secondary cooling zones (Z1 and Z2). The jet flow coming from the side port of the SEN impinges on the strand wall and is split into two opposite streams. The upper stream is confined by the meniscus, forming an upper vortex that plays an important role in preventing the solidification of the meniscus. M-EMS has a small effect on this vortex (Figure 3b). However, the flow patterns below the SEN are strikingly different between the two cases. For the case without M-EMS, the impinging jet coming from the bottom port of the SEN flows straight down, as does the melt near the solidification front. To conserve these two downward flows, an upward flow forms in the middle radius section of the strand (Figure 3b,c). Thus, the left and right recirculation loops are created on the half-vertical plane of the strand. For the case with M-EMS, the melt at the center of the strand (M-EMS region) will be brought to the solidification front and move upward/downward. Figure 3d shows the 3D streamline of the melt. Without M-EMS, the flow pattern is relatively simple, i.e., most of the melt coming from the SEN flows downward and returns back to the mold region along

the mid-radius region. With M-EMS, a typical swirling flow is generated by the stirrer. The melt above the stirrer spirally flows upward to the upper part of the mold region along the solidification front and then returns to the M-EMS region along the centerline of the strand, forming a so-called upper recirculation loop. In contrast, the melt below the stirrer spirally flows downward along the solidification front and then returns to the stirrer region along the centerline of the strand, and a so-called lower recirculation loop is formed. This form of the flow pattern favors the promotion of superheat dissipation and concentration homogeneity.

### 3.2. Temperature Field

Figure 4a shows the temperature field for two cases, without and with M-EMS. The simulation results on vertical symmetrical planes are shown in Figure 4a.1, and the simulation results on horizontal sections at the position of the M-EMS center are shown in Figure 4a.2. The superheat region is highlighted and enclosed by the isotherm of  $T = 1688.15$  K, which refers to the liquidus of the steel with an initial composition of  $c_0$ . It is obvious that, when M-EMS is not applied, the superheat region is extended to far below the mold region along the billet centerline. When M-EMS is applied, the superheat region is confined only in the mold region. Due to the intensive heat transfer rate from strand surface to water-cooled mold, more superheats could be dissipated in this area (Figure 4a.2). The temperature profile

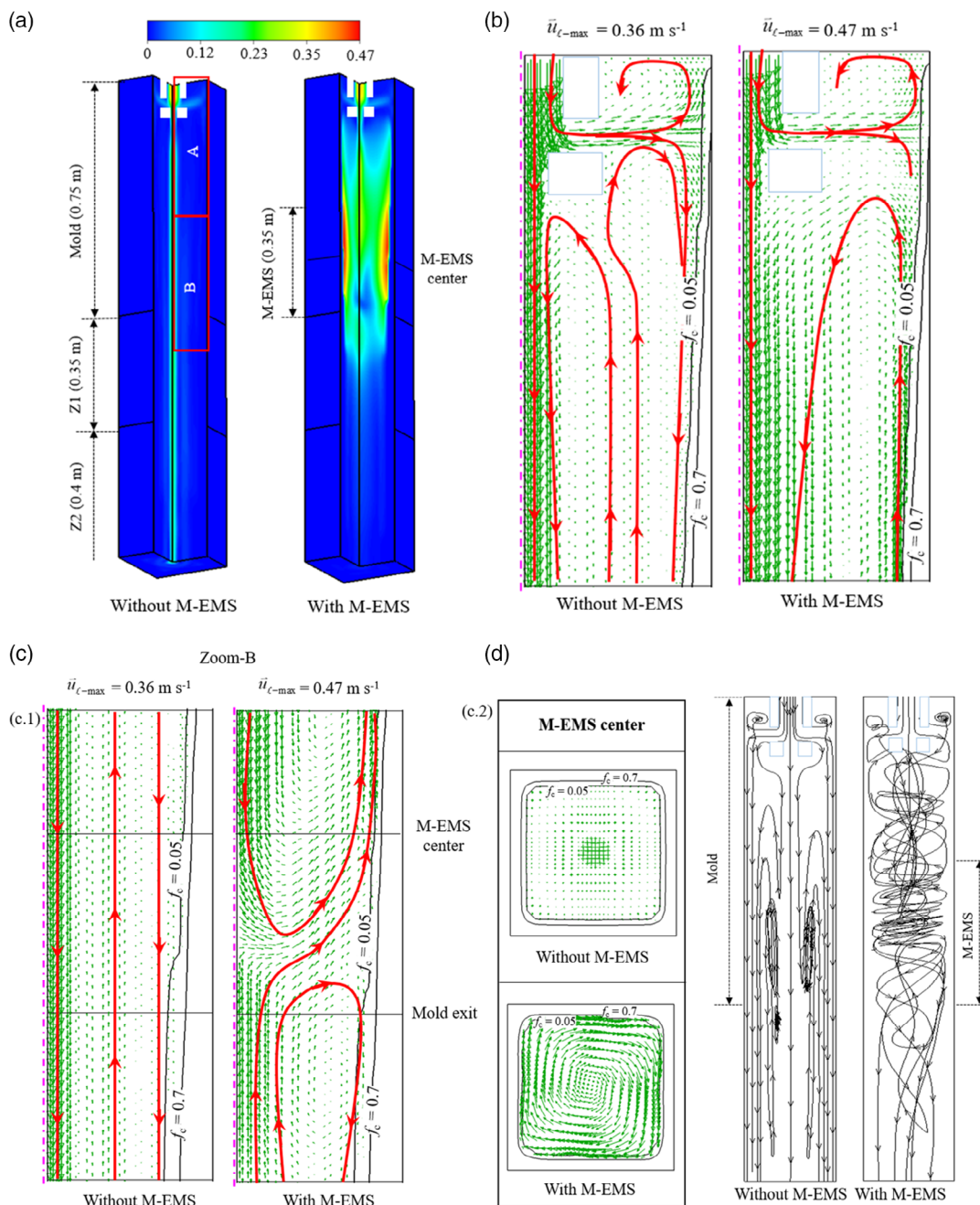


**Figure 3.** Comparison of the velocity fields for two cases: without and with M-EMS. a) Velocity contour of the flow pattern; b) zoom-view of the flow pattern at the upper part of the mold (Zone-A); c) zoom-view of the flow pattern at the lower part of the mold (Zone-B), c.1) on vertical symmetrical planes; c.2) on horizontal sections at the position of the M-EMS center; d) 3D streamline of the melt.

along the axis line of the strand is presented in Figure 4b. The melt enters the mold through SEN at the same temperature (1708.15 K) for both simulation cases. It then suddenly decreases at 0.2 m below the meniscus. For the case without M-EMS, the temperature decreases from 1708.15 to 1705.12 K. This phenomenon can be easily explained by its flow pattern. The left recirculation loop generated on the half vertical plane continuously brings the cooler melt (still superheated) to the strand center (Figure 3b), while the impact region is limited to a small area

below the SEN. Therefore, the temperature curve fluctuates slightly as the distance from the meniscus increases. The temperature is 1705.18 K at the mold exit with a tiny change in the secondary cooling zone. For the case with M-EMS, the temperature decreases from 1708.15 to 1700.96 K at 0.2 m below the meniscus, which is attributed to the M-EMS-induced upper recirculation loop, which carries the cooler melt from the solidification front to the center of the strand. The impact area of the upper recirculation loop extends almost to the entire mold



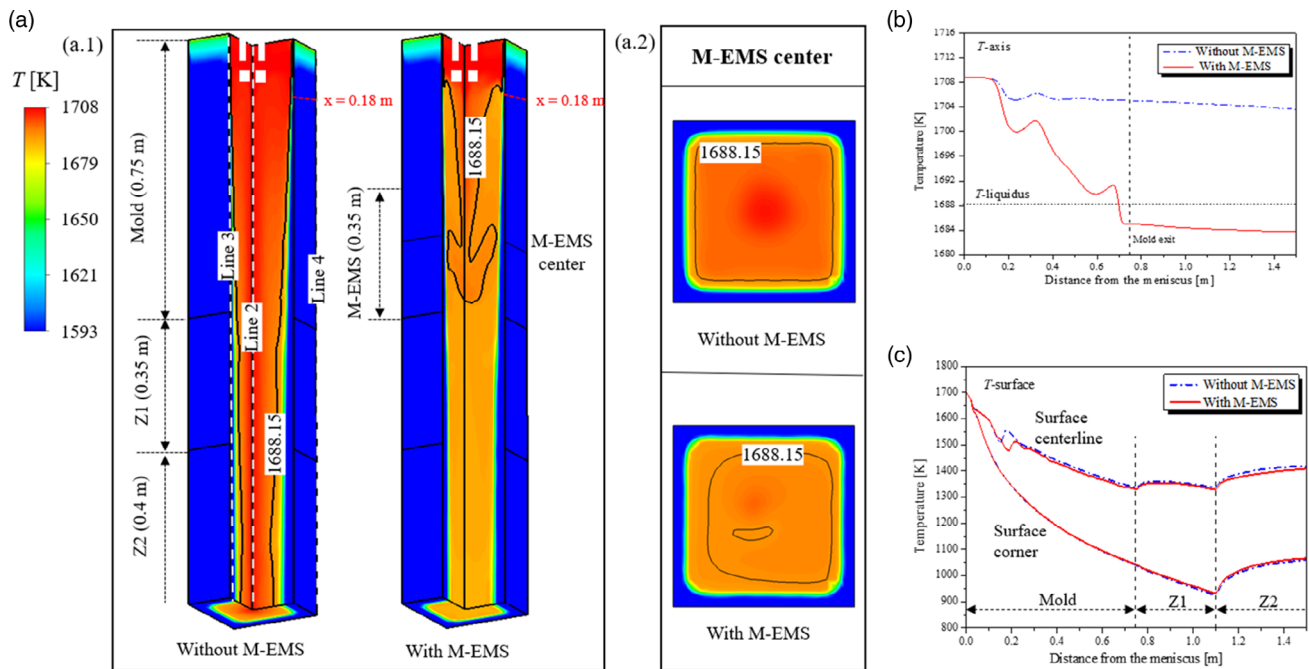


**Figure 4.** Comparison of the temperature distributions for two cases: without and with M-EMS. a) Contours of the temperature field overlaid with the isotherm of 1688.15 K, which refers to the liquidus of the steel with an initial composition  $c_0$ , a.1) vertical symmetrical planes, a.2) horizontal sections at the position of the M-EMS center; b) temperature profiles along the axis-line of the strand (Line 2); c) temperature profiles along the centerline (Line 3) and corner (Line 4) of a strand surface.

region; thus, the temperature decreases continuously as the distance to the meniscus increases. The temperature reaches 1685.03 K ( $\approx 3$  K below the liquidus) at the mold exit (Figure 4b). Only a tiny change in the temperature is found in the secondary cooling zone. This region, a state of undercooling, is beneficial for the survival of crystal fragments created by M-EMS-induced fragmentation of columnar dendrites. Temperature profiles along the centerline of a strand surface are shown in Figure 4c. Below the side port of SEN, the two curves of the surface centerline show opposite trends at 0.18 m below the meniscus, which is mainly caused by the different flow patterns of the two cases. For the case without M-EMS, the rise in temperature is attributed to the right recirculation loop, which carries the high-temperature melt to the solidification front. The cooler melt is spirally brought to the upper mold region along the solidification front by the upper recirculation loop when M-EMS is applied. Another role of the upper recirculation loop is to inhibit the downward flow of the melt coming from the side port of the SEN. These two effects will subsequently reduce the wall temperature of the strand. After this point, the wall temperature is slightly higher for the case without M-EMS. The temperature profiles along the corner of a strand surface of the two cases are also compared in Figure 4c. It seems that M-EMS-induced flow has an ignorable effect on the temperature distribution at the outer surface corner. The two curves almost overlap with one another. Interestingly, the global heat transfer rate from the strand surface to the water-cooled copper mold seems unlikely to be affected by M-EMS. By integrating the heat flux over the total strand surface in the mold region, the value of the integrated heat flow rate is

503905.5 W for the case without M-EMS, and 503588.1 W for the case with M-EMS. The heat flux from the strand to the mold depends on the strand (solid shell) surface temperature. As the M-EMS does not influence the strand surface temperature (Figure 4c), it does not influence the total heat transfer rate from the strand surface to the water-cooled copper mold. The M-EMS-induced flow is beneficial for the temperature homogenization in the liquid core, but the temperature in the shell, especially at the shell surface, is rarely influenced by the M-EMS.

### 3.3. Growth of the Solid Shell/mushy Zone and Formation of Subsurface Macrosegregation

Figure 5a compares the contours of the volume fraction of the solid columnar dendrites ( $f_c$ ) for the two cases without and with M-EMS, with no obvious difference found between them. Contours of the volume fractions of the solid columnar dendrites on the horizontal section at the position of the mold exit are shown in Figure 5b. It seems that M-EMS tends to inhibit the growth of the mushy zone at mold exit. The evolutions of the shell thickness and the mushy zone thickness (the distance between the two isolines  $f_c = 0.7$  and 0.05) along the casting direction for the two cases are compared in Figure 5c. The positions of the mold exit and the M-EMS center are also marked in Figure 5c. It seems that an M-EMS-induced flow slightly promotes the growth of the solid shell/mushy zone above the M-EMS center but inhibits their growth below the M-EMS center. The reason is that the M-EMS-induced upper recirculation loop (Figure 3b) drives the cooler melt upward along the

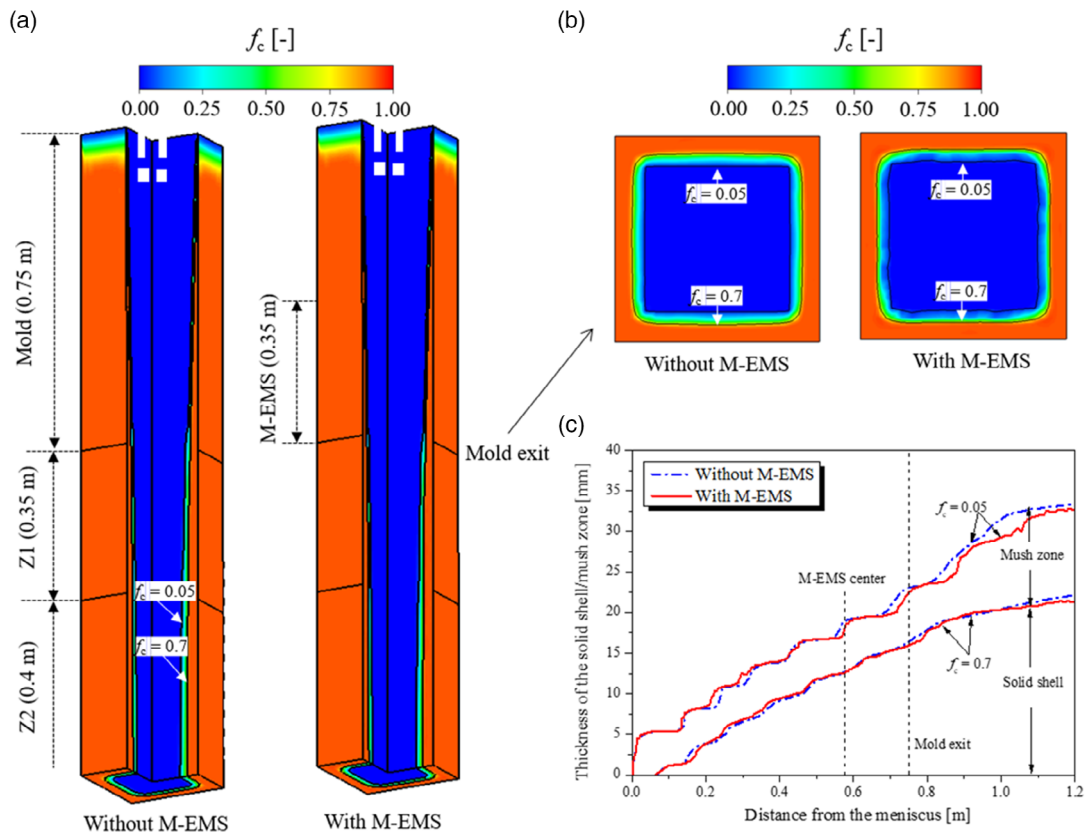


**Figure 5.** Comparison of the thickness of the solid shell and mushy zone of the two cases: without/with M-EMS. a) Contours of the volume fraction of solid columnar dendrites on vertical symmetrical planes; b) contours of the volume fraction of solid columnar dendrites on horizontal sections at the position of mold exit; c) thickness of the solid shell/mushy zone along the casting direction.

solidification front. This type of flow intends to reduce the temperature near the solidification front, which is beneficial for the growth of the solid shell/mushy zone. Conversely, the M-EMS-induced lower recirculation loop (Figure 3c) continuously brings the hotter melt from the stand center to the solidification front and delays the growth of the solid shell/mushy zone. Although a qualitative trend can be observed, the influence of M-EMS-induced flows on the evolution of the solid shell (quantitative results) is not as obvious in the current case with an applied electric current intensity of 430 A for the M-EMS. The thickness of the solid shell at the mold exit is 16.423 mm without M-EMS, and the value is 15.981 mm with M-EMS. The M-EMS-induced flow only reduces the shell thickness by 0.442 mm.

Figure 6a shows the contours of the macrosegregation index for the two cases: without/with M-EMS. Section views of the macrosegregation on the M-EMS center plane are displayed in Figure 6b, and profiles of the macrosegregation along the diagonal line (Line 5) of this plane are shown in Figure 6c. For the case without M-EMS, the macrosegregation is negligible, while for the case with M-EMS, due to the “solute washing” effect, the M-EMS-induced horizontal swirling flow penetrates the mushy zone and sweeps out the solute enriched melt to the bulk liquid. Subsurface negative segregation is formed, with the worst negative segregation appearing near the corner of the strand. It should be noted that the negative segregation is fixed in the solidified shell

(inside of the isoline  $f_c = 0.7$ ). Thus, the degree of negative segregation will not change as solidification progresses. Meanwhile, the solute is slightly enriched in the bulk region (Figure 6c). This solute enrichment cannot be considered to be macrosegregation, since this solute-enriched melt will solidify later to form the center as-cast structure (mostly equiaxed), and the final segregation profile will change correspondingly. This is further discussed in §5.

## 4. Parameter Studies

To further investigate the interplay between M-EMS and superheat, parameter studies were also performed by varying the superheat (10, 15, 20, 25, 30 K) and the M-EMS electric current intensity (200, 300, 430, 500, 600 A).

### 4.1. Superheat

Figure 7 shows the influence of the superheat (10–30 K) on the temperature distribution in the mold and secondary cooling regions. The electric current intensity is kept constant (430 A). The temperature contours on vertical symmetrical planes are shown in Figure 7a. The superheated zone is marked with an isotherm of 1688.15 K, which corresponds to the liquidus of the steel with an initial composition of  $c_0$ . It is obvious that

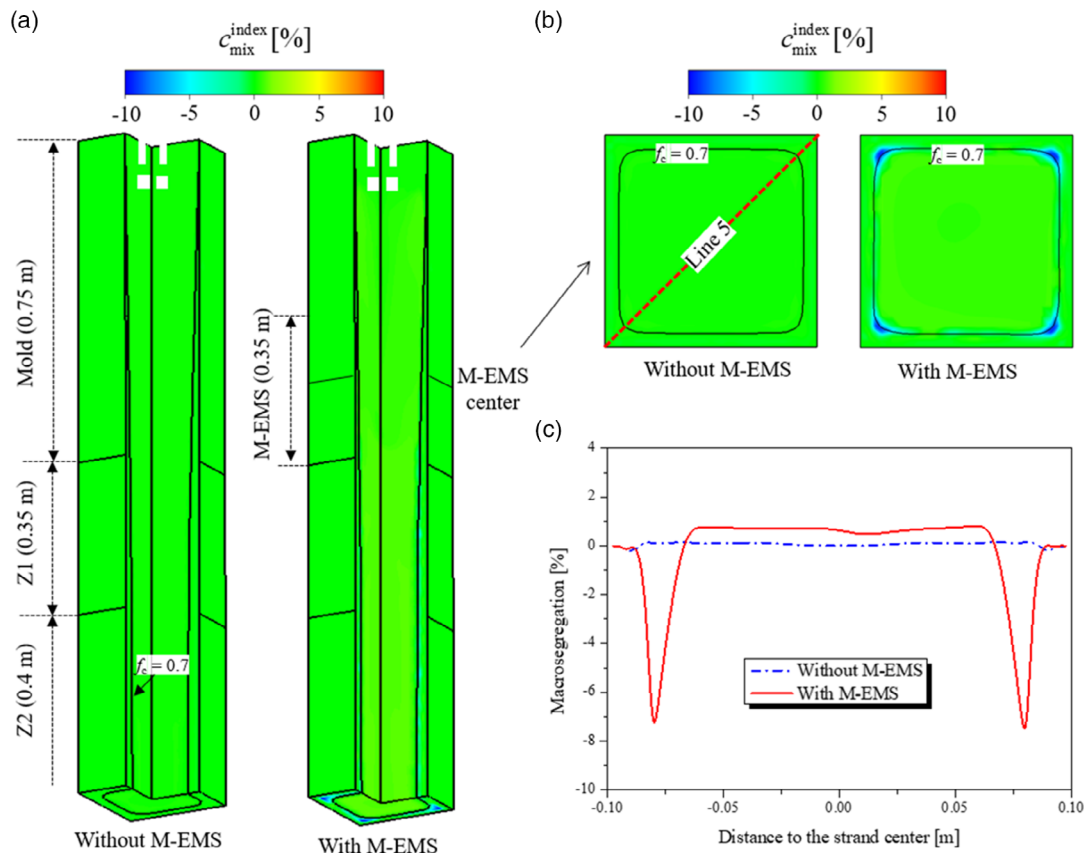


**Figure 6.** Comparison of the macrosegregation between the two cases: without/with M-EMS. a) Contours of the macrosegregation index on vertical symmetry planes and b) on horizontal sections at the position of the M-EMS center; c) macrosegregation profiles along the diagonal line (Line 5) of (b).

the superheated area gradually expands to the entire mold region with increased superheating. When the superheat is 10 K, the upper recirculation loop (Figure 3b) generated by the M-EMS can easily cool the liquid temperature below the liquidus. The superheated region, starting from the SEN, can only extend to two-thirds of the mold region and is only limited to the center of the strand. When the superheat is 30 K, the superheated region extends to almost the entire mold region. The extended superheated region does not favor the growth of solid shells and the heterogeneous nucleation of equiaxed crystals. Furthermore, the crystal fragments will be remelted/destroyed when they are brought into this superheated area.

Figure 7b depicts the temperature profiles along the axis-line of the strand. The temperatures of the melt are almost constant (but different between the five cases with different superheats) in the SEN region and then decrease sharply as they enter the M-EMS region. The superheated areas are mainly confined in the mold region (Figure 7a). The temperatures at the mold exit of the five cases are all below the liquidus temperature, leaving the liquid core out of the mold region undercooled. The temperature differences between the five cases are not as obvious in the secondary cooling zones. The temperature is 1684.16 K at the mold exit and 1684.11 K at 1.27 m below the meniscus of the first case ( $\Delta T = 10$  K), while the value is 1684.71 K at the mold exit and 1684.59 K at 1.27 m below the meniscus of the last case

( $\Delta T = 30$  K). The temperature difference is only  $\approx 0.55$  K at the mold exit and 0.48 K at 1.27 m below the meniscus between the two cases. This means that the influence of the superheat on the temperature distribution in the center of the strand is quite weak in the secondary cooling zones. The temperature profiles along the centerline of a strand surface are shown in Figure 7c. It is interesting to find that the superheat seems to have a tiny effect on the surface temperature in the mold region, but it can significantly raise the surface temperature in the secondary cooling zones with an increased superheat. The reason is that M-EMS tends to homogenize the temperature in the liquid core of the strand, the increased thermal energy is transferred to the sensible energy and stored in the solid shell and liquid phase (near the solidification front) in the secondary cooling zones as increasing the superheat. The temperature is 1391.42 K in the first case ( $\Delta T = 10$  K), and 1426.78 K in the last case ( $\Delta T = 30$  K) at 1.27 m below the meniscus, for a difference of 35.36 K. The higher surface temperature of the last case ( $\Delta T = 30$  K) will delay the growth of the solid shell/mushy zone in the secondary cooling zones.

Figure 8 shows the effect of superheat on the evolution of the solid shell and the mushy zone. The contours of  $f_c$  on the vertical symmetry planes are shown in Figure 8a. It is obvious that the region of the solid shell/mushy zone is compressed by increasing the superheat. Quantitative analyses are conducted to reveal the thickness of the solid shell/mushy zone along the casting

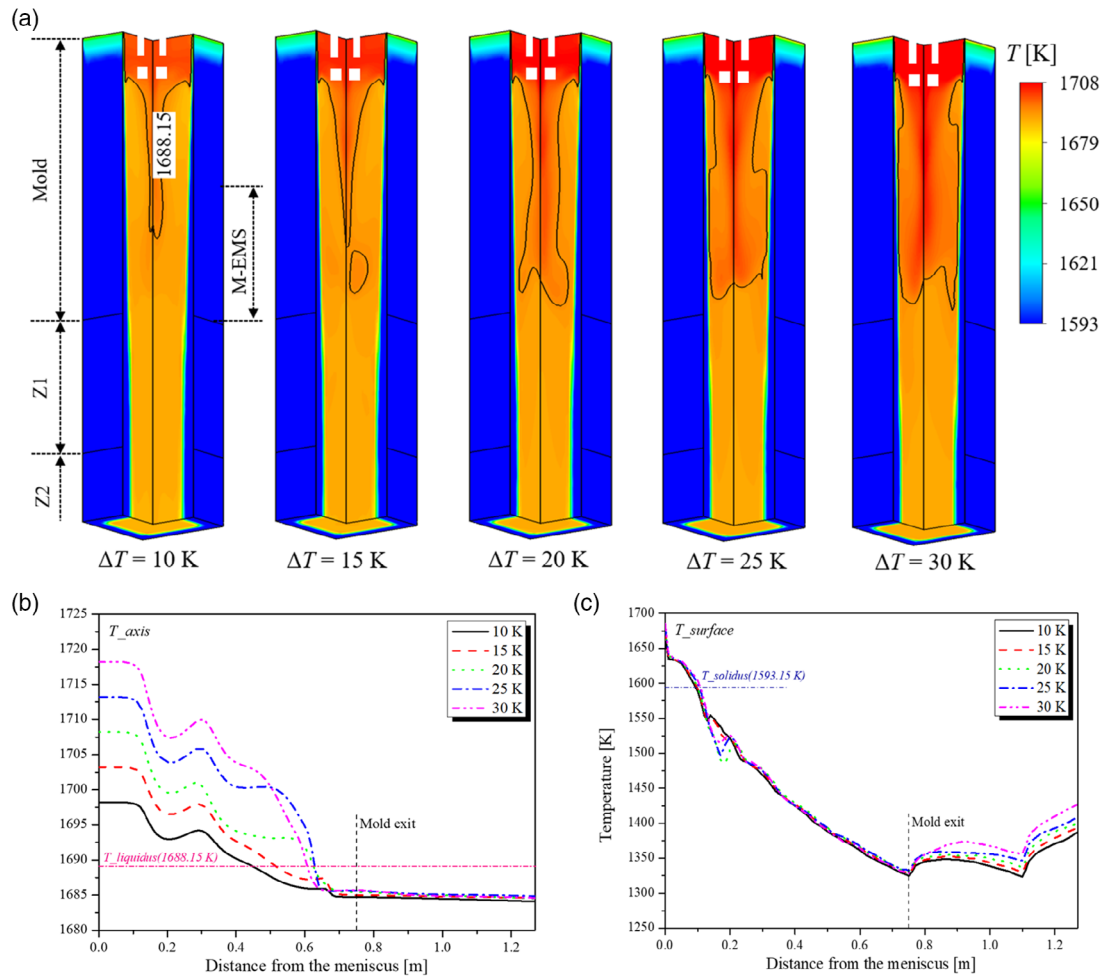


**Figure 7.** Influence of the superheat (10–30 K) on the temperature distribution. M-EMS is kept constant (430 A). a) Temperature contours on the vertical symmetry planes; b) profiles of the temperature along the axis-line of the strand; c) profiles of the temperature along the centerline of a strand surface.

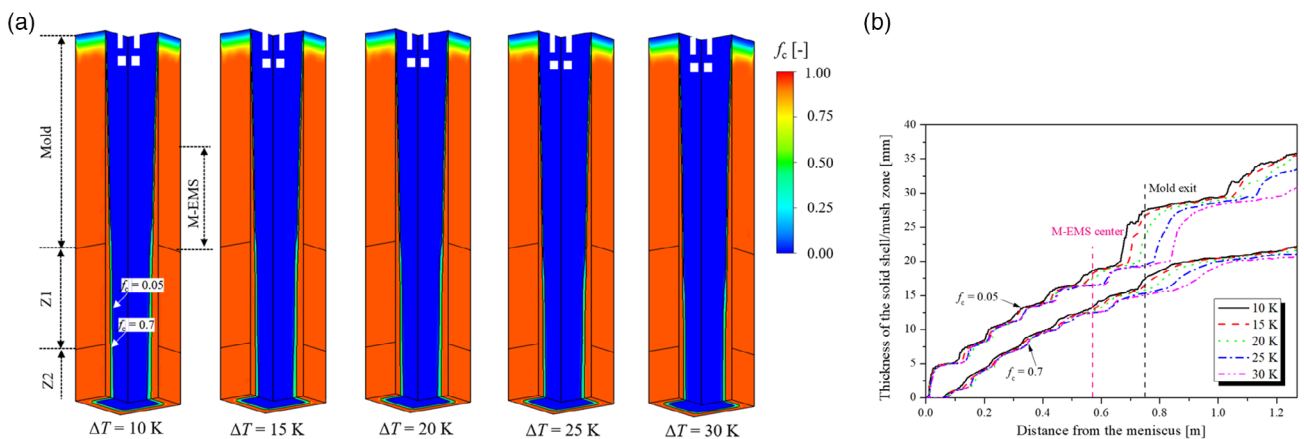


**Figure 8.** Effect of the superheat (10–30 K) on the evolution of the solid shell and mushy zone. a) Contours of  $f_c$  on the vertical symmetry planes; b) thickness of the solid shell/mushy zone along the casting direction.

direction in Figure 8b. As mentioned before, the superheat has a tiny effect on the surface temperature in the mold region. Thus, no large difference in the thickness of the solid shell/mushy zone

can be found in this area. However, starting from the secondary cooling zones, the enormous surface temperature distinctions of the five cases will definitely influence the growth of the solid

shell/mushy zone. The thickness of the solid shell at the mold exit is 17.38 mm in the first case ( $\Delta T = 10$  K) and 15.14 mm in the last case ( $\Delta T = 30$  K). Increasing the superheat by 20 K will reduce the solid shell thickness by 2.24 mm at the mold exit. It is, therefore, concluded that the higher superheat is not beneficial for the growth of the solid shell, especially in the secondary cooling zones. A similar conclusion also applies to the growth of the mushy zone; the columnar solidification front ( $f_c = 0.05$ ) is compressed by increasing the superheat.

#### 4.2. Electric Current Intensity

Figure 9 presents the influence of the electric current intensity (200–600 A) of M-EMS on the temperature distribution in the mold and secondary cooling regions. The superheat is kept constant (20 K). Figure 9a displays the contours of the temperature on the vertical symmetry planes. It can be seen that the superheated region is shifted upward with an increasing electric current intensity of M-EMS. This is conducive to accelerating the dissipation of the superheat.

Figure 9b shows the temperature profiles along the axis-line of the strand. For the case where the electric current intensity is equal to 200 A, the relatively weak stirring intensity is not sufficient to decrease the axis temperature below the liquidus temperature at the mold exit. The superheated region, therefore, extends to the secondary cooling zones until the position 1 m below the meniscus. For the other four cases (300–600 A), the stirring intensity is powerful enough to decrease the axis temperature below the liquidus temperature at the mold exit and leave the liquid core out of the mold region undercooled. When the current intensity is sufficiently large ( $>430$  A), a further increase in the electric current intensity will no longer influence the core temperature in the secondary cooling zones. The temperature profiles along the centerline of a strand surface are shown in Figure 9c. It seems that increasing the electric current intensity is prone to decreasing the surface temperature in the mold region, but it is prone to increase the surface temperature in the secondary cooling zones. This phenomenon can also be explained by the flow patterns shown in Figure 2b,c. The M-EMS-induced upper recirculation loop, which tends to bring the cooler melt to the upper part of the mold region along

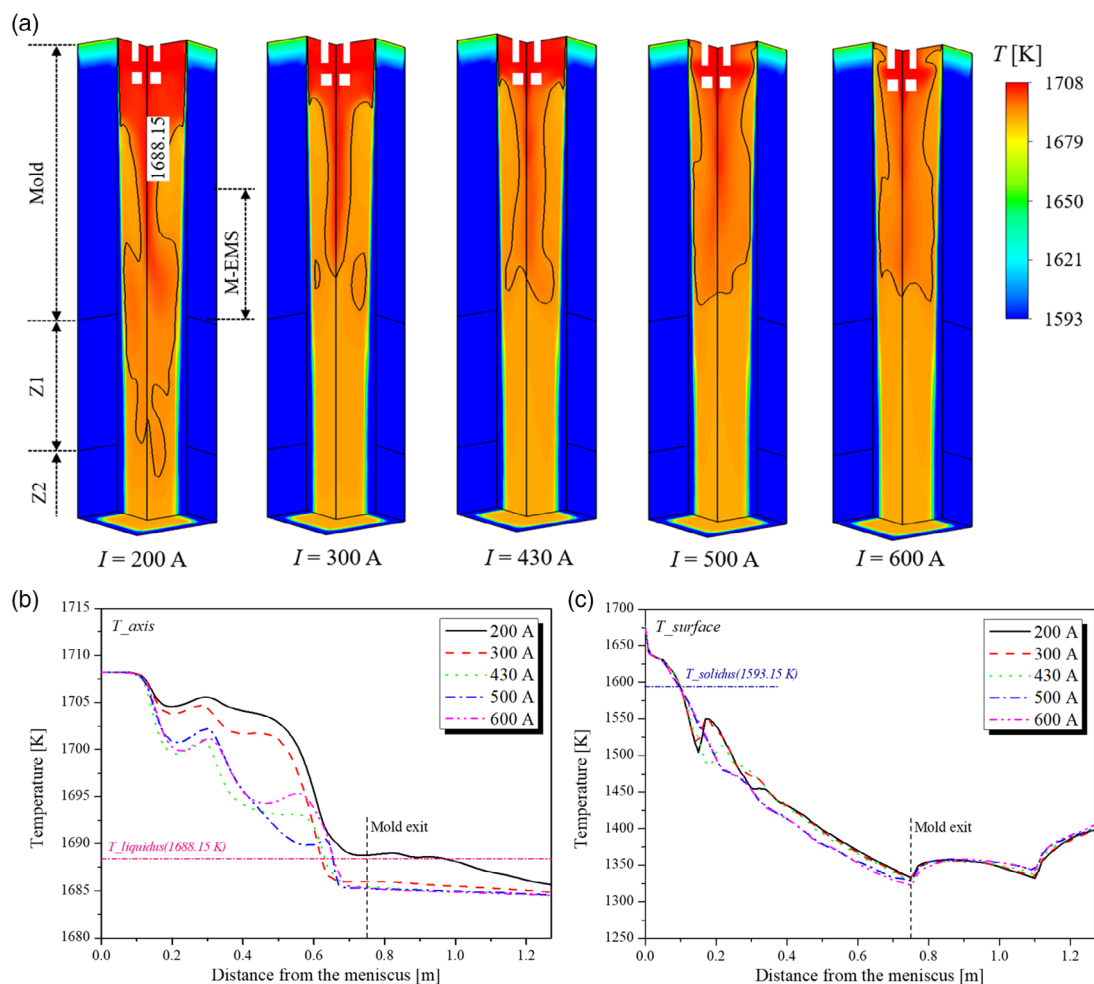


**Figure 9.** Influence of the electric current intensity (200–600 A) of M-EMS on the temperature distribution. The superheat is kept constant (20 K). a) Contours of the temperature on the vertical symmetry planes; b) profiles of the temperature along the axis-line of the strand; c) profiles of the temperature along the centerline of a strand surface.

the solidification front, will be enhanced with an increasing electric current intensity. This will cause a drop in the surface temperature in the mold region. Similarly, the enhanced lower recirculation loop tends to raise the surface temperature in the secondary cooling zone by increasing the electric current intensity.

Figure 10 displays the effect of the electric current intensity (200–600 A) of M-EMS on the evolution of the solid shell/mushy zone. The contours of  $f_c$  on the vertical symmetry planes are shown in Figure 10a. For a quantitative comparison, the thickness of the solid shell/mushy zone along the casting direction of the five cases is plotted in Figure 10b. By increasing the electric current intensity, the lower surface temperature tends to facilitate the growth of the solid shell/mushy zone in the mold region (this is more obvious when the current intensity is larger than 430 A). It will further be beneficial for the fragmentation of solid columnar dendrites and increases the number of equiaxed grains. In contrast, the higher surface temperature tends to delay the growth of the solid shell/mushy zone in the secondary cooling zones (this is more obvious when the current intensity is larger than 430 A).

## 5. Discussion

In this work, a two-phase (liquid, columnar) solidification model is used to investigate the superheat dissipation in billet continuous casting under the effect of M-EMS. Superheat dissipation is an important message for analyzing the growth of solid shells and hence further affects the possible formation of subsurface macrosegregation. However, one must state that the formation/growth, migration and remelting/destruction of equiaxed crystals play an important role during the continuous casting of billet strands. It is true that to understand the formation of the final as-cast structure and macrosegregation in the billet, a three-phase mixed columnar-equiaxed model is needed. This was done by the authors in a previous paper.<sup>[26]</sup> Demonstratively, the calculated as-cast structure is shown in Figure 11, and satisfactory agreement with the field experiment was obtained. The columnar zone, mixed zone, and equiaxed zone of the calculated as-cast structure are distinguished by two isolines of equiaxed grain envelope:  $f_e^{env} = 1.0$  and  $f_e^{env} = 0.17$ .  $f_e^{env} = f_e/f_{si}$ , where  $f_e$  is the volume fraction of equiaxed crystals, and  $f_{si}$  is the volume ratio of solid dendrites to equiaxed grain envelope ( $f_{si} = 0.3$  in

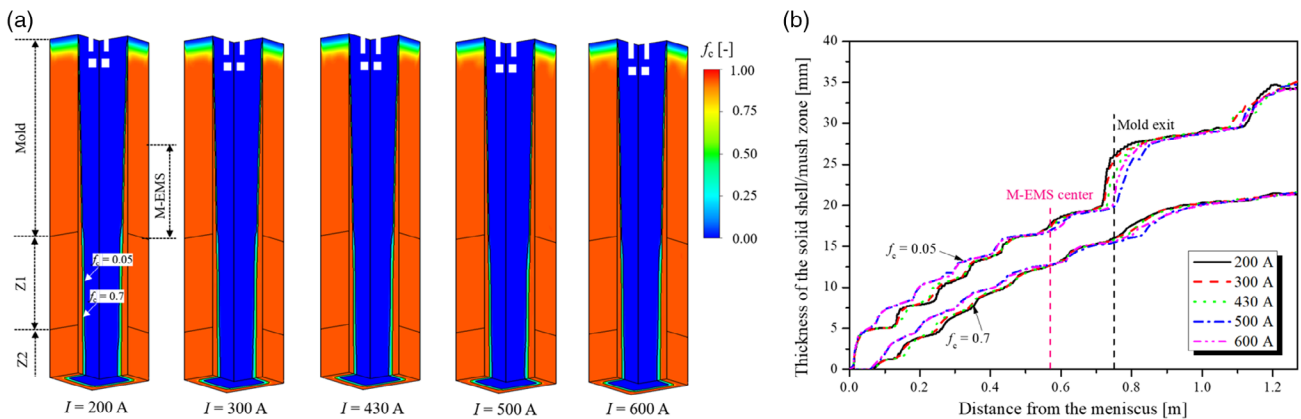


**Figure 10.** Effect of the electric current intensity (200–600 A) of M-EMS on the evolution of the solid shell and mushy zone. a) Contours of  $f_c$  on vertical symmetry planes; b) thickness of the solid shell/mushy zone along the casting direction.

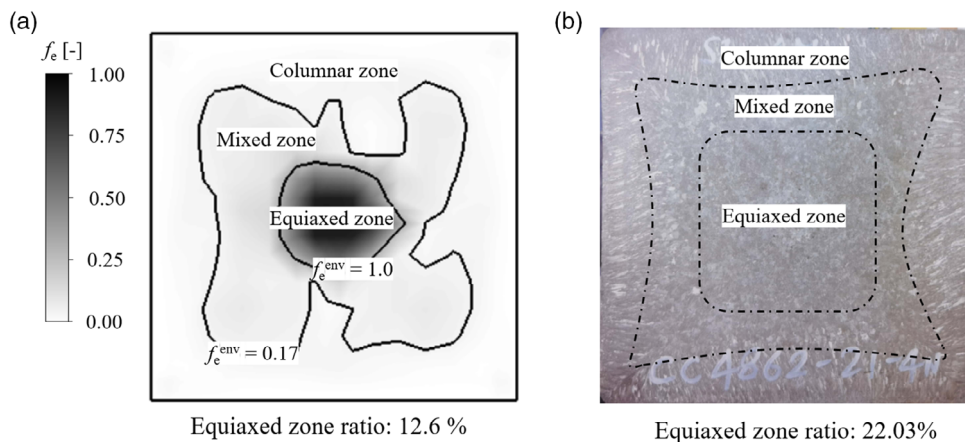


**Figure 11.** a) Calculated distribution of equiaxed crystals overlaid with two isolines of the equiaxed grain envelope:  $f_e^{env} = 1.0$  and  $f_e^{env} = 0.17$ ; b) as-cast structure. Reproduced with permission.<sup>[26]</sup> Copyright 2022, Elsevier.

this calculation). Two mechanisms (heterogeneous nucleation<sup>[20]</sup> and fragmentation of dendrites<sup>[27]</sup>) contributed to the source of equiaxed crystals, wherein the initial inoculant number density ( $n_{in}^0$ ) is set as  $1 \times 10^9$ , and the fragmentation coefficient ( $\gamma$ ) is set as  $3.0 \times 10^{-5}$ .

The reason why the current study is only limited to the two-phase model is due to the calculation cost. A 3D calculation of a full length of casting ( $\approx 12$  m) with the three-phase model requires 45 days on a high-performance cluster (2.6 GHz, 28 cores), while a 3D calculation for the initial solidification of a part of the strand (3 m long) with the two-phase model only needs 7 days of calculation time. It is not wise to conduct parameter studies on such a time-consuming case (three-phase, 12 m). The calculations based on the two-phase model can also effectively reflect the effect of M-EMS on the superheat dissipation during the continuous casting of billets. **Figure 12a** depicts the temperature fields of the two cases (without/with M-EMS) by using the two-phase model in a 3 m calculation domain. **Figure 12b** shows the temperature fields of the two cases (without/with M-EMS) by using the three-phase model in a 12 m calculation domain. The same conclusion could be drawn by analyzing the simulation results of the two simulation models:

the role of M-EMS in the dissipation of superheat during the continuous casting of billets is to speed up the superheat dissipation in the mold region, leaving the liquid core out of the mold region greatly undercooled.

## 6. Conclusion

A two-phase solidification model was used to investigate the effect of M-EMS on the dissipation of superheat in the mold region of billet continuous casting. A proper coupling scheme between the electromagnetic field and the melt flow is used to treat the flow-EMS interaction. The electric conductivity of the material is treated as state-dependent, i.e., the liquid melt and solid shell have different electric conductivities. Parameter studies were also performed by varying the superheat and the electric current intensity of M-EMS. The following new findings were obtained. 1) The M-EMS-induced horizontal swirling flow speeds up the superheat dissipation in the mold region, leaving the liquid core out of the mold region largely undercooled. However, the total heat transfer rate from the strand surface to the water-cooled copper mold is not affected by M-EMS; 2) The growth of the solid shell is not evidently influenced by M-EMS. Subsurface

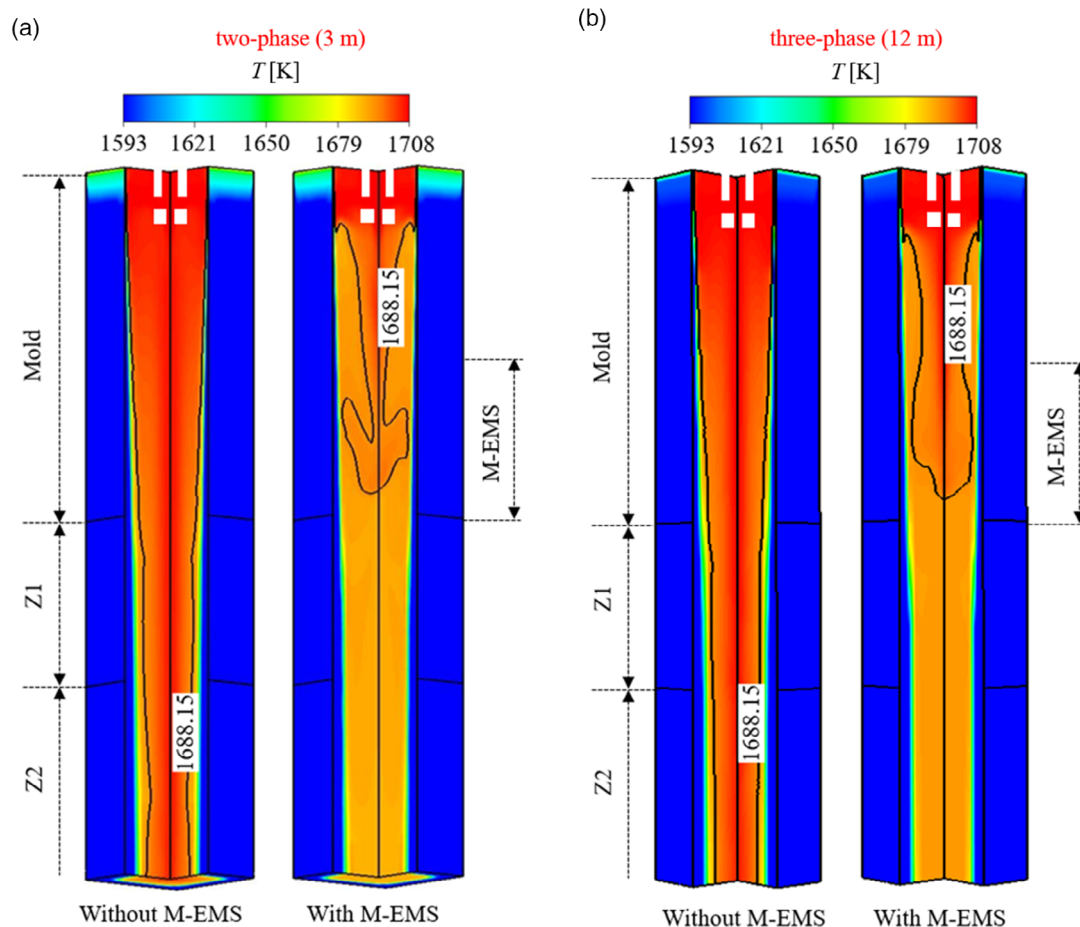


**Figure 12.** Comparison between the two models, i.e., two-phase columnar solidification model versus three-phase mixed columnar-equiaxed solidification model. a) Temperature fields of the two cases (with/without M-EMS) by using the two-phase model in a 3 m calculation domain; b) temperature fields of the two cases (with/without M-EMS) by using the three-phase model in a 12 m calculation domain.

negative segregation near the strand corner is formed due to the M-EMS-induced swirling flow; 3) With the M-EMS, the effect of the melt superheating on the growth of the solid shell/mushy zone can only be detected in the out-of-the-mold region (the larger the superheat is, the slower the shell growth), while the shell growth inside the mold region is minorly influenced by the superheat; and 4) A strong M-EMS with a large electric current intensity tends to accelerate the growth of the solid shell/mushy zone in the mold region but delay the growth of the solid shell/mushy zone in the secondary cooling zones.

The aforementioned findings might conflict with some existing knowledge and may only be valid for the current casting format/parameters, to be confirmed for other casting formats/parameters of different alloys.

## Acknowledgements

The authors acknowledge the financial support from the Austria Research Promotion Agency (FFG) through the Bridge 1 project (No. 868070) as well as the technical support of the industrial partner Primetals Technologies Austria GmbH.

## Conflict of Interest

The authors declare no conflict of interest.

## Data Availability Statement

The data that support the findings of this study are available from the corresponding author upon reasonable request.

## Keywords

continuous casting, electromagnetic stirring, solid shell growth, superheat dissipation

Received: January 24, 2022  
Revised: June 26, 2022  
Published online: July 9, 2022

- [1] X. Huang, B. G. Thomas, F. M. Najjar, *Metall. Mater. Trans. B* **1992**, 23, 339.
- [2] S. K. Choudhary, S. Ganguly, *ISIJ Int.* **2007**, 47, 1759.
- [3] S. K. Choudhary, S. Ganguly, A. Sengupta, V. Sharma, *J. Mater. Process. Technol.* **2017**, 243, 312.
- [4] S. Kunstreich, *Rev. Metall.* **2003**, 100, 1043.
- [5] N. A. Shah, J. J. Moore, *Iron Steelmaker* **1982**, 9, 31.
- [6] N. A. Shah, J. J. Moore, *Iron Steelmaker* **1982**, 9, 42.
- [7] B. Z. Ren, D. F. Chen, H. D. Wang, M. J. Long, Z. W. Han, *Ironmaking Steelmaking* **2015**, 42, 401.
- [8] B. X. Wang, W. Chen, Y. Chen, Y. P. Feng, *Ironmaking Steelmaking* **2015**, 42, 63.
- [9] Y. B. Yin, J. M. Zhang, Q. P. Dong, Q. H. Zhou, *Ironmaking Steelmaking* **2019**, 46, 855.
- [10] N. Genma, T. Soejima, T. Saito, M. Kimura, Y. Kaihara, H. Fukumoto, K. Ayata, *ISIJ Int.* **1989**, 29, 1056.
- [11] Q. Fang, H. Zhang, J. H. Wang, C. Liu, H. W. Ni, *Metall. Mater. Trans. B* **2020**, 51, 1705.
- [12] K. Ayata, T. Mori, T. Fujimoto, T. Ohnishi, I. Wakasugi, *Trans. Iron Steel Inst. Jpn.* **1984**, 24, 931.
- [13] Z. G. Yang, B. Wang, X. F. Zhang, Y. T. Wang, H. B. Dong, Q. Liu, *J. Iron Steel Res. Int.* **2014**, 21, 1095.
- [14] H. Q. Yu, M. Y. Zhu, *Ironmaking Steelmaking* **2012**, 39, 574.
- [15] H. H. An, Y. P. Bao, M. Wang, L. H. Zhao, *Metall. Res. Technol.* **2018**, 115, 103.
- [16] B. Z. Ren, D. F. Chen, H. D. Wang, M. J. Long, *Steel Res. Int.* **2015**, 86, 1104.
- [17] S. X. Li, P. Lan, H. Y. Tang, Z. P. Tie, J. Q. Zhang, *Steel Res. Int.* **2018**, 89, 1800071.
- [18] L. B. Trindade, J. E. A. Nadalon, A. C. Contini, R. C. Barroso, *Steel Res. Int.* **2017**, 88, 1600319.
- [19] Q. P. Dong, J. M. Zhang, Q. Liu, Y. B. Yin, *Steel Res. Int.* **2017**, 88, 1700067.
- [20] M. Wu, A. Ludwig, *Metall. Mater. Trans. A* **2006**, 37, 1613.
- [21] M. Wu, A. Ludwig, A. Kharicha, *Metals* **2019**, 9, 229.
- [22] M. Wu, A. Ludwig, A. Kharicha, *Appl. Math. Model.* **2017**, 41, 102.
- [23] J. Li, M. Wu, J. Hao, A. Ludwig, *Comput. Mater. Sci.* **2012**, 55, 407.
- [24] J. Lipton, M. E. Glicksman, W. Kurz, *Mater. Sci. Eng.* **1984**, 65, 57.
- [25] H. J. Zhang, M. Wu, Z. Zhang, A. Ludwig, A. Kharicha, A. Rónaföldi, A. Roósz, Z. Veres, M. Svéda, *Metall. Mater. Trans. B* **2022**, 1.
- [26] Z. Zhang, M. Wu, H. J. Zhang, S. Hahn, F. Wimmer, A. Ludwig, A. Kharicha, *J. Mater. Process. Technol.* **2022**, 301, 117434.
- [27] Y. J. Zheng, M. Wu, A. Kharicha, A. Ludwig, *Model. Simul. Mater. Sci. Eng.* **2018**, 26, 015004.



## **Paper 3**

### **Effect of forced convection on the formation of the as-cast structure and macrosegregation of Sn-10wt.% Pb alloy: a numerical study**

Zhao Zhang, Menghuai Wu, Haijie Zhang, Andreas Ludwig, Abdellah Kharicha

International Journal of Heat and Mass Transfer

Accepted and in press.



# Effect of forced convection on the formation of the as-cast structure and macrosegregation of Sn-10wt.% Pb alloy: a numerical study

Zhao Zhang, Menghuai Wu\*, Haijie Zhang, Andreas Ludwig, Abdellah Kharicha

Chair of Simulation and Modelling of Metallurgical Processes, Department of Metallurgy, University of Leoben, A-8700, Leoben, Austria.

E-mail: menghuai.wu@unileoben.ac.at

**Abstract:** A series of solidification benchmark experiments based on Sn-10wt.% Pb alloy were performed at the SIMAP Laboratory in Grenoble, France (Hachani et al., 2015) to study the effect of different types of forced convection on the as-cast structure and macrosegregation. Forced convection was achieved by using a traveling magnetic field (TMF). Four cases were investigated: without TMF; TMF in the same direction as natural convection; TMF in the opposite direction as natural convection; and TMF periodically reversed with respect to natural convection. In the current study, a three-phase mixed columnar-equiaxed solidification model was used to “reproduce” the above experiments to understand the flow effect on the as-cast structure formation. The dendrite fragmentation is regarded as the only source of equiaxed grains. Remelting/destruction of equiaxed grains in the superheated melt is considered. The continuous growth of the surviving equiaxed grains and further competition with the as-developed columnar dendrites, leading to columnar-to-equiaxed transition (CET), are included. Except for Case III (i.e., a TMF in the opposite direction as natural convection), satisfactory simulation-experiment agreements in terms of the temperature field, as-cast structure and macrosegregation are obtained for the remaining three cases. Based on the simulation results, it is found that 1) TMF plays an important role in homogenizing the temperature field and promoting the formation of equiaxed grains via fragmentation, consequently facilitating the appearance of CET; 2) TMF tends to generally intensify macrosegregation and increase the number of channel segregations; and 3) the simultaneous solidification/remelting process represents a significant species/energy transport mechanism. Ignoring the remelting of equiaxed grains would lead to an overestimate of the

local temperature in the remelting zone. The reason for the mismatch between the simulation and experimental results obtained for Case III is discussed.

**Keywords:** Traveling magnetic field (TMF); Fragmentation; Remelting; Macrosegregation; As-cast structure.

## 1. Introduction

The electromagnetic field (EMF) has been widely used during the casting process because of its multiple benefits for improving the casting quality: the well-controlled flow field, the homogenization of the temperature/solute field, the promotion of grain nucleation and dendrite fragmentation, the extension of the equiaxed structure and the improvement of the segregation intensity, etc. [1-3]. One typical EMF, i.e., the traveling magnetic field (TMF), which can produce a Lorentz force in one direction, is often used to control the flow pattern (forming the so-called “butterfly” type of flow) and grain structure both in slab continuous casting processes [4-8] and laboratory experiments [9-10].

Various experiments have been performed to investigate the solidification of pure tin and its alloys, e.g., tin-lead (Sn-3 wt.% Pb, Sn-5 wt.% Pb, Pb-48 wt.% Sn) and tin-zinc (Sn-5 wt.% Zn), on the laboratory scale in a rectangular cavity under natural convection [11-17]. The experimental results show that the channel segregations are intensified with increasing cooling rate and initial solute concentration. To investigate the effect of forced convection on the as-cast structure and macrosegregation, similar experiments were performed under TMF conditions [18-21]. Specifically, Hachani et al. [20] performed a series of experiments to study the effect of different types of forced convection on the as-cast structure and macrosegregation. Forced convection was achieved by using the TMF. Four different solidification experiments based on Sn-10wt.%Pb alloy were investigated: without TMF (Case I); TMF in the same direction as natural convection (Case II); TMF in the opposite direction as natural convection (Case III); and TMF periodically reversed with respect to natural convection (Case IV). The temperature field, as-cast structure, and solute distribution of the four cases were analyzed comprehensively, which provided an excellent reference case to validate the simulation model.

Many numerical studies [22-35] have attempted to “reproduce” the above benchmark experiments [11, 15, 17, 20]. A cellular automaton-finite element (CA-FE) solidification model [22-23] was used to simulate the solidification of the benchmark experiment [15]. Satisfactory agreement of the grain morphology was obtained, but the segregation channels could not be predicted. Two-phase volume-averaged (VA) numerical models [24-32] were also used to simulate the benchmark [11, 17]. The segregation channels were excellently reproduced, but because the second solid phase, the equiaxed grains, were ignored, the credibility of the calculation results was weakened. Direct application of the two-phase VA numerical model to the cases under a TMF, makes it more difficult to “reproduce” the as-cast structure and segregation profiles [33-34]. Recently, a three-phase mixed-columnar-equiaxed VA model [35–36] was used to model benchmark Case I of Hachani et al. [20]. The numerical simulation results proved that the motion of equiaxed grains significantly affects the final distribution of the equiaxed grains and macrosegregation profiles. However, both of them ignored the remelting/destruction phenomenon occurred during the casting process. Additionally, compared to benchmark Case I, the cases under the TMF are of high interest and significance, but the simulations raise more challenges under forced convection conditions.

This study continues the work of the current authors [36-37] by including the effect of the TMF. The three-phase mixed columnar-equiaxed solidification model was extended with improved approaches for remelting and grain destruction. The extended model was used to “reproduce” the four cases of Hachani’s benchmark experiments [20]. On this basis, this study focuses on explaining the formation mechanism for the as-cast structure and macrosegregation under the effect of TMFs.

## **2. Model description**

A three-phase mixed columnar-equiaxed solidification model [38-41] was used to investigate the formation of the as-cast structure and macrosegregation of Sn-10wt.% Pb alloy in an experimental benchmark under forced convection conditions [20]. The governing equations for the model have been presented in detail elsewhere [38, 41]. Three phases are considered: liquid melt ( $\ell$ ), equiaxed grains (e) and columnar dendrites (c). Their volume fractions ( $f_\ell, f_e, f_c$ ) sum up to one. Both the liquid melt and equiaxed grains are treated as moving phases, for which the corresponding Navier–Stokes equations are solved to obtain the liquid velocity

( $\bar{u}_\ell$ ) and equiaxed velocity ( $\bar{u}_e$ ). The columnar dendrites are assumed to be composed of a rigid phase, for which the velocity is zero ( $\bar{u}_c \equiv 0$ ). Simple morphologies are assumed for the two solid phases: stepwise cylinders for columnar trunks and spheres for equiaxed grains. To address the drag force and other hydrodynamic interactions between phases, a dendritic envelope ( $f_e^{\text{env}}$ ) is considered for equiaxed grains. The volume ratio of the solid ‘dendrite’ to the dendritic envelop is defined as  $f_{\text{si}} (= f_e / f_e^{\text{env}})$ , which was set as a constant in this study. A diffusion-governed growth kinetic is considered to treat the solidification for both solid phases. The difference between the equilibrium and volume-averaged liquid concentrations ( $c_\ell^* - c_\ell$ ) served as the driving force for solidification. The position of the columnar tip front was traced dynamically based on the Lipton-Glicksman-Kurz (LGK) model [42]. A so-called effective equiaxed viscosity ( $\mu_e$ ), which increases with  $f_e^{\text{env}}$ , was used to model the interaction between the equiaxed grains [43]. When  $f_e^{\text{env}}$  reached a packing limit  $f_{e,\text{packing}}$ , a rigid network of equiaxed grains was built. Additionally, the equiaxed grains were captured by the columnar dendrites and fixed there when the local volume fraction of the columnar phase  $f_c \geq 0.2$ . Solidification shrinkage was ignored. Both thermal-solutal convection and grain sedimentation were modeled using the Boussinesq approach. The volume-averaged concentrations for each phase, i.e.,  $c_\ell$ ,  $c_e$ , and  $c_c$ , were calculated. The macrosegregation was characterized by the segregation index:  $c_{\text{mix}}^{\text{index}} = (c_{\text{mix}} - c_0) \times 100 / c_0$ , in which  $c_0$  is the initial concentration and  $c_{\text{mix}}$  is the mixture concentration with  $c_{\text{mix}} = (f_\ell \rho_\ell c_\ell + f_e \rho_e c_e + f_c \rho_c c_c) / (f_\ell \rho_\ell + f_e \rho_e + f_c \rho_c)$ , where  $\rho_\ell$ ,  $\rho_e$ ,  $\rho_c$  are the densities for each phase. Some important relevant modeling features for the current benchmark are described below.

### 2.1 Dendrite fragmentation

Dendrite fragmentation [44] is considered as the only source of equiaxed grains. The net mass transfer rate from the columnar dendrites to the equiaxed grains due to fragmentation can be calculated using

$$M_{\text{ce}} = -\gamma \cdot (\bar{u}_\ell - \bar{u}_c) \cdot \nabla c_\ell \cdot \rho_e, \quad (1)$$

where  $\gamma$  is the fragmentation coefficient and  $\nabla c_l$  is the liquid concentration gradient. All other contributions to fragmentation, e.g., the curvature effect of the dendrites, latent heat-induced thermal fluctuation, and diffusion in the interdendritic melt, are included in the single fragmentation coefficient  $\gamma$ . The production rate of the number density of fragments is calculated via

$$N_{ce} = \frac{M_{ce}}{\rho_e \cdot \frac{\pi}{6} (d_{e,frag}^0)^3}, \quad (2)$$

where  $d_{e,frag}^0 (= \lambda_2 \cdot f_c)$  is the initial diameter of the fragment and  $\lambda_2$  is the secondary dendrite arm spacing, which must be determined experimentally. Heterogeneous nucleation is ignored here.

## 2.2 Solidification and remelting/destruction of equiaxed grains

The solidification and remelting of equiaxed grains are treated as two asymmetric processes [45], i.e., the remelting process is not simply “inverse solidification”. Schematics of the solute partitioning at the liquid–solid interface and the solute distribution in the liquid and solid during solidification and remelting processes are shown in Figure 1.

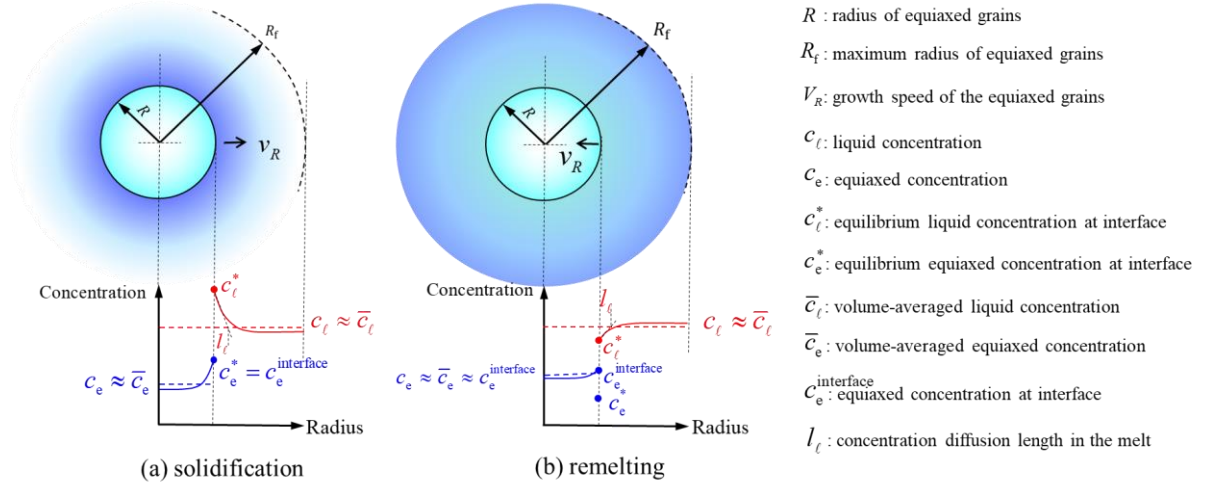


**Figure 1.** Schematic of solute partitioning at the liquid–solid interface and the solute distribution in the liquid and solid: (a) solidification process; (b) remelting process.

- 1) *Solidification*: the growth of the equiaxed grains is governed by diffusion. The net mass transfer rate between the liquid melt and the equiaxed grains during the solidification process is described as

$$M_{l_e} = v_R \cdot (n_{eq} \pi d_e^2) \cdot \rho_e \cdot f_l , \quad (3)$$

where  $n_{eq}$  is the number density of equiaxed grains,  $d_e$  is the grain diameter, and  $v_R$  is the growth speed of equiaxed grains, which yields

$$v_R = \frac{D_l}{l_l} \cdot \frac{(c_l^* - c_l)}{(c_l^* - c_e^*)} , \quad (4)$$

where  $D_l$  is the solute diffusion coefficient in the liquid,  $c_e^*$  is the equilibrium equiaxed concentration at the liquid/solid interface (Figure 1(a)), and  $l_l$  is the diffusion length, which is calculated using

$$l_l = \frac{d_e}{2} (1 - f_e^{\frac{1}{3}}) . \quad (5)$$

- 2) *Remelting and destruction of the equiaxed grains*: the remelting of the equiaxed grains is also governed by solute diffusion [46]. The geometrical impingement factor ( $f_l$ ) is unnecessary during the remelting process, and thereby, Equation (3) is updated for the remelting process.

$$M_{l_e} = v_R \cdot (n_{eq} \pi d_e^2) \cdot \rho_e . \quad (6)$$

Unlike the solidification process, the equilibrium concentrations ( $c_l^*$  and  $c_e^*$ ) are lower than the volume-averaged concentrations ( $c_l$  and  $c_e$ ) during the remelting process (Figure 1(b)); thus, it is assumed that the equiaxed concentration at the liquid/solid interface ( $c_e^{interface}$ ) is equal to  $c_e$ , and  $v_{Re}$  is calculated using

$$v_R = \frac{D_l}{l_l} \cdot \frac{(c_l^* - c_l)}{(c_l^* - c_e)} . \quad (7)$$

A significant remelting process occurs when the equiaxed grains are transported into the bulk melt region, where flow might be quite turbulent. The turbulent flow effect on



the remelting process is considered based on the modified diffusion length [47-48], which yields

$$l_\ell = d_e / (2 + 0.6 \cdot \text{Sc}^{1/3} \text{Re}^{1/2}) , \quad (8)$$

where  $\text{Sc} = \mu / \rho_\ell D_\ell$  is the Schmidt number,  $\text{Re} = d_e \rho_\ell |\bar{u}_\ell - \bar{u}_e| / \mu$  is the local Reynolds number, and  $\mu$  is the dynamic viscosity of the liquid melt.

To model the grain destruction, the equiaxed grains are assumed to follow a lognormal size distribution [45]. If a grain is exposed to a superheated liquid, remelting will first lead to a decrease in the diameter of the grain. Once the size class of the equiaxed grains due to remelting becomes smaller than the critical value of the grain size ( $d_{e,\text{critical}}$ ), the equiaxed grains will be destructed. The destruction rate for the grains can be calculated using

$$n_{\text{des}} = v_R \left. \frac{dn_{\text{eq}}}{dx} \right|_{x=d_{e,\text{critical}}} , \quad (9)$$

$$\text{with } \frac{dn_{\text{eq}}}{dx} = \frac{n_{\text{eq}}}{\sqrt{2\pi} \cdot \sigma \cdot x} \cdot e^{-\frac{1}{2} \left( \frac{\ln(x) - \ln(\hat{d}_e)}{\sigma} \right)^2} , \quad (10)$$

where  $\sigma$  is the geometric standard deviation of the lognormal distribution, the dummy variable ( $x$ ) corresponds to the equiaxed grain diameter of different size classes, and  $\hat{d}_e$  is the geometrical mean of the grain size. However, only the volume-averaged grains diameter  $d_e$ , which is not equal to  $\hat{d}_e$ , could be obtained through the volume-averaged method. Thus, a further assumption was made in this study, the variation in  $d_e$  and  $\hat{d}_e$  due to remelting follows the same trend, i.e.,  $d(\hat{d}_e) / dt \approx d(d_e) / dt$ , which can be estimated by remelting rate of equiaxed grains ( $v_R$ ).

### 2.3 One-way coupling of the electromagnetic field and flow field

A one-way coupling approach between the electromagnetic field and flow field was adopted. The electromagnetic field was calculated using ANSYS Maxwell, and the flow field was solved using ANSYS Fluent.

Firstly, the time-averaged Lorentz force was calculated using ANSYS Maxwell,

$$\bar{F} = \frac{1}{2}(\bar{J} \times \bar{B}^*). \quad (11)$$

The Lorentz force is composed of the forces in three directions ( $F_x$ ,  $F_y$ , and  $F_z$ ), but it acts mainly in the x direction. Thus, to consider the relative motion between the Lorentz force in the x direction ( $F_x$ ) and the x-velocity component of the melt/equiaxed phase,  $F_x$  was modified using

$$F'_x = F_x \cdot \left(1 - \frac{u_x}{u_{B,x}}\right), \quad (12)$$

where  $F'_x$  is the modified Lorentz force in the x direction,  $u_x$  is the x-velocity of the melt/equiaxed phases, and  $u_{B,x}$  is the moving velocity of the TMF. The Lorentz forces in other two directions ( $F_y$ ,  $F_z$ ) would keep as original. Then, the Lorentz forces ( $F'_x$ ,  $F_y$ ,  $F_z$ ) were weighted by the corresponding phase volume fraction ( $f_\ell$ ,  $f_e$ ) and finally used as the source terms ( $F'_{x,\ell}$ ,  $F'_{x,e}$ ,  $F_{y,\ell}$ ,  $F_{y,e}$ ,  $F_{z,\ell}$ ,  $F_{z,e}$ ) for the momentum conservation equations of each phase via User-Defined Functions (UDFs).

$$F'_{x,\ell} = F'_x \cdot f_\ell, \quad F'_{x,e} = F'_x \cdot f_e, \quad (13)$$

$$F_{y,\ell} = F_y \cdot f_\ell, \quad F_{y,e} = F_y \cdot f_e, \quad (14)$$

$$F_{z,\ell} = F_z \cdot f_\ell, \quad F_{z,e} = F_z \cdot f_e. \quad (15)$$

### 3. Benchmark configuration

#### 3.1 Experimental procedure

The experiments were conducted by another research group at the SIMAP Laboratory in Grenoble, France [20]. The Sn-10 wt.% Pb alloy was solidified in a quasi-two-dimensional rectangular ( $100 \times 60 \times 10 \text{ mm}^3$ ) mold. As shown in Figure 2(a), two heat exchangers were arranged beside the two lateral walls of the sample to control the input/extraction of the heat. The heating and cooling history of the two exchangers designed for the experiment is demonstrated in Figure 2(b). A temperature difference of 40 K was assigned between the two exchangers during the cooling stage, and the cooling rates were equal to 0.03 K/s. An array of fifty thermocouples was placed onto the front surface of the sample to record the temperature evolution. A second array of sixteen thermocouples was arranged onto the back surface to

confirm that the temperature variations in the thickness direction remain small, i.e., the temperature field of the sample follows a quasi-two-dimensional pattern. Nine thermocouples were arranged onto the left and right exchangers, respectively, to measure the heat flux extracted from the sample. As presented in Figure 2(a), the linear motor used to generate the TMF was placed 5 mm beneath the sample. A three-phase alternative current (AC) with a constant frequency ( $f = 50$  Hz) and current intensity ( $I = 8.2$  A) was used to feed the power. For a more detailed introduction of the benchmark setup, refer to [20].

Once the coils were charged, a magnetic field was produced. If a conductive casting sample was loaded, an induced current was generated in the sample. The interaction between the magnetic field and induced current produced a Lorentz force, which drove the liquid to flow. The magnetic flux density ( $B$ ) was measured along the x-axis (3 mm above the motor) without loading the sample. As schematically shown in Figure 2(c), four different solidification experiments for Sn-10 wt.% Pb alloy were performed to investigate the effect of different types of forced convection on the as-cast structure and macrosegregation.

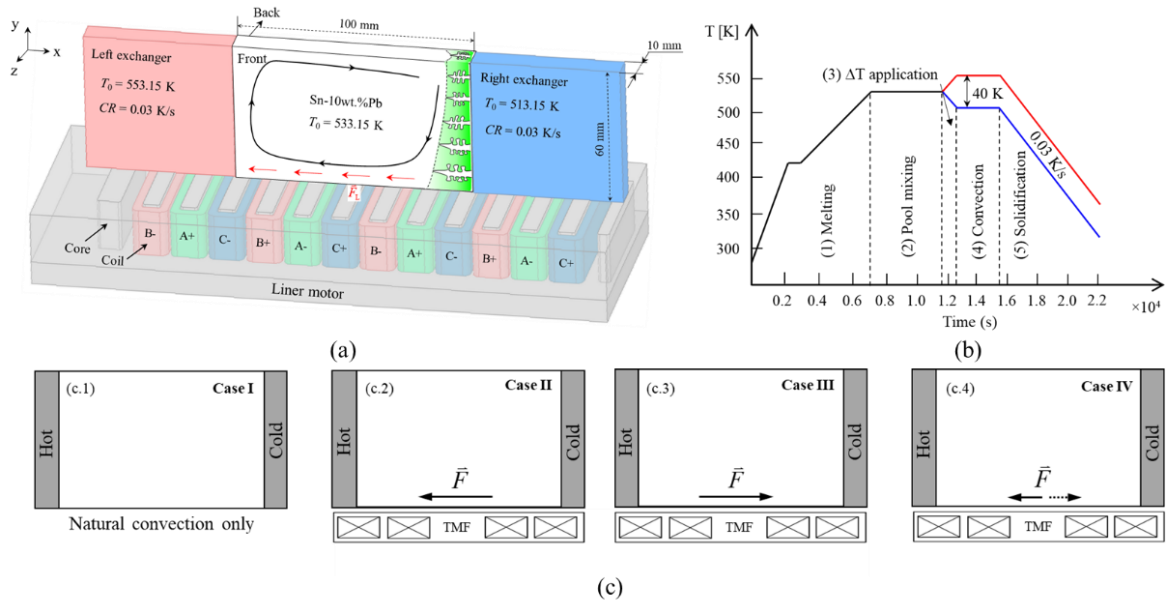


**Figure 2.** (a) Schematic view of the experimental facility used for the benchmark [20]; (b) heating and cooling history of the two exchangers; (c) four different stirring modes. (c.1) Case I: natural convection only; (c.2) Case II: TMF aligned along the same direction as the natural convection; (c.3) Case III: TMF aligned along the opposite direction as the natural convection; (c.4) Case IV: TMF imposed in an alternative direction with a frequency of 0.0625 Hz (stirring in one direction for 8 s)

During the solidification process, evolutions of the temperature field were recorded and analyzed. Temperature maps for the selected area ( $x$ : 0.5 cm – 9.5 cm;  $y$ : 1 cm – 5 cm) of the front surface (Figure 2(a)) at three different solidification times ( $t = 540$  s,  $t = 900$  s, and  $t = 1440$  s) were revealed [20].  $t = 0$  s corresponds to the first appearance of the liquidus of the alloy with an initial composition of  $c_0$ . After the castings completely solidified, the as-cast structures for the four cases were obtained through metallurgic analyses, which consisted of several passes of polishing with abrasive paper and chemical attack with a mixture of 75% Vol HCl (37 mol%/v) and 25% Vol HNO<sub>3</sub> (69.5%) [15]. A chemical method coupled using the Inductive Coupled Plasma (ICP) technique was used to obtain the quantitative results for the solute distribution, and the profiles for the macrosegregation were revealed by X-ray analysis along the thickness direction [20].

### 3.2 Numerical procedure

A full-scale inductor (Figure 2(a)) was built to perform the electromagnetic calculation using the commercial software ANSYS Maxwell. Firstly, the magnetic field ( $B$ ) along the x-axis without sample loading was calculated and compared with the measurements. Then, the conductive casting sample ( $\sigma = 1.86 \times 10^6 \Omega^{-1} \text{ m}^{-1}$ ) was loaded 5 mm above the linear motor. The time-averaged  $\vec{F}$  was calculated by solving Maxwell's equations, and the extracted  $\vec{F}$  was interpolated into the mesh system of ANSYS Fluent.  $F_x$  was modified by multiplying  $(1 - u_x / u_{B,x})$  to consider the relative motion between the Lorentz force in the x direction and the x-velocity component of the corresponding phase (Equation (12)). It was then weighted by the corresponding phase volume fraction ( $f_l, f_e$ ) and used as a source term in the momentum conservation equations for each phase (Equation (13) and Equation (14)). Unlike the electromagnetic field calculation, only the casting domain was solved for the flow and solidification. Four simulations corresponding to Hachani's four experiments (Cases I-IV) [20] were conducted. The simulations started from the last stage (solidification) in Figure 2(b), and the melt was assumed to have a homogeneous temperature ( $T = 533.15$  K) and concentration (Sn – 10 wt.% Pb) distribution before solidification. A convective heat transfer boundary condition ( $h = 2000 \text{ W/m}^2 \cdot \text{K}$ ) was used for the two lateral walls. At the beginning of the simulation, the left exchanger temperature was set as 553.15 K, and the right exchanger was set as 513.15 K. The cooling rate for the right exchanger was set to be 0.03 K/s, which is identical to the experimental value. The cooling rate for the left exchanger was experimentally

reported to be 0.03 K/s, but here it was set to be 0.033 K/s. The reason for this modification will be discussed in detail in §5.4. Adiabatic boundary conditions were used for the remaining four walls. The liquid was assumed to be incompressible with a constant density and viscosity. The no-slip flow boundary condition was applied for the melt and equiaxed grains along all the sample walls. The thermodynamic/physical properties used in the current simulations are listed in Table 1.

**Table 1.** Thermo-dynamic/physical properties.

Property/parameters	Symbol	Units	Values	Ref.
Nominal Pb concentration of the alloy	$c_0$	wt.%Pb	10.0	[20]
Liquidus temperature (Sn-10 wt.%Pb)	$T_{liq}$	K	492.61	[20]
Melting temperature of pure Sn	$T_f$	K	505.15	[20]
Initial temperature	$T_0$	K	533.15	[20]
Partition coefficient	$k$	-	$6.56 \times 10^{-2}$	[20]
Liquidus slope	$m$	K (wt.%Pb) <sup>-1</sup>	-1.2826	[20]
Eutectic temperature	$T_{eut}$	K	456.57	[20]
Eutectic concentration	$c_{eut}$	wt.%Pb	38.1	[20]
Reference density	$\rho_{ref}$	kg m <sup>-3</sup>	7000.0	[20]
Liquid density (buoyancy force)	$\rho_\ell$	kg m <sup>-3</sup>	$\rho_{ref}(1 - \beta_T(T_\ell - T_{ref}) - \beta_C(c_\ell - c_{ref}))$	
Solid density for both solid phases	$\rho_e, \rho_c$	kg m <sup>-3</sup>	7310.0	
Thermal expansion coefficient	$\beta_T$	K <sup>-1</sup>	$6.0 \times 10^{-5}$	[17]
Solutal expansion coefficient	$\beta_C$	(wt.%Pb) <sup>-1</sup>	$-5.3 \times 10^{-3}$	[17]
Primary dendrite arm spacing	$\lambda_1$	m	$2.25 \times 10^{-4}$	[35]
Secondary dendrite arm spacing	$\lambda_2$	m	$6.5 \times 10^{-5}$	[17]
Diffusion coefficient in liquid	$D_\ell$	m <sup>2</sup> s <sup>-1</sup>	$4.5 \times 10^{-9}$	[35]
Latent heat	$L$	J kg <sup>-1</sup>	$6.1 \times 10^4$	[17]
Specific heat	$c_p^\ell, c_p^e, c_p^c$	J (kg K) <sup>-1</sup>	260.0	[17]

Thermal conductivity	$k_\ell, k_e, k_c$	$\text{W(m K)}^{-1}$	55.0	[17]
Viscosity	$\mu_\ell$	Pa s	$1.0 \times 10^{-3}$	[20]
Gibbs-Thomson coefficient	$\Gamma$	m K	$6.5 \times 10^{-8}$	[35]
Solid fraction in the dendritic envelope	$f_{si}$	-	0.5	[35]
Packing limit	$f_{e,packing}$	-	0.637	[35]

\*Super/subscripts  $\ell$ ,  $e$ , and  $c$  indicate different phases.

A hexahedron mesh with a mesh size of 1 mm was used in the current study, and the total mesh number was 60,000. Regarding the flow calculation, for each timestep ( $\Delta t = 0.005$  s), 40 iterations were needed to decrease the normalized residuals for the continuity, momentum conservation equations to values below the convergence limit of  $10^{-4}$  and those for the enthalpy conservation equations to below  $10^{-7}$ . All simulations were performed in parallel using a high-performance computing cluster (2.6 GHz, 28 cores). One three-dimensional (3D) calculation required 7 days of computing time.

## 4. Simulation results

### 4.1 $B$ field and distribution of the Lorentz force

Figure 3(a) shows a comparison of the  $B$  field along the x-axis (3 mm above the motor) determined by calculation and measurement in the absence of the casting sample. Satisfactory agreement is obtained between the two datasets. The oscillation of the  $B$  field is caused by the arrangement of the magnets at the bottom of the device. The distribution of the time-averaged Lorentz force on the casting (solid-state with no movement) surface of Case II is shown in Figure 3(b). The profile of the magnitude ( $|F|$ ) of the Lorentz force along Line 1 (Figure 3(b)) is plotted in Figure 3(c). The maximal  $|F|$  ( $728 \text{ N/m}^3$ ) appears at the bottom of the sample, and it exponentially declines along the sample height. The effective zone for the Lorentz force is limited to within a distance of 10 mm above the sample bottom.

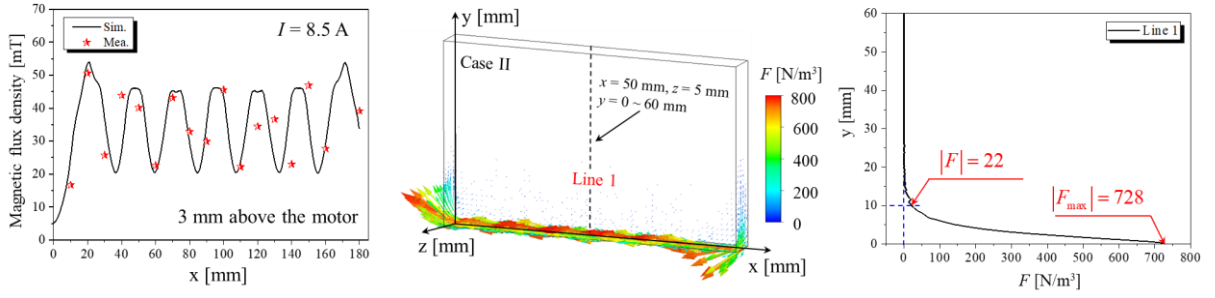


**Figure 3.** (a) Comparison of the measured and calculated  $B$  in the absence of the casting sample along the  $x$ -axis (3 mm above the linear motor); (b) distribution of the time-averaged Lorentz force on the casting surface of Case II; (c) profile of the magnitude ( $|F|$ ) of the Lorentz force along Line 1 shown in (b).

#### 4.2 Solidification sequence

To illustrate the TMF-induced flow and its effect on the formation of the as-cast structure and macrosegregation, the solidification sequence was analyzed for the middle vertical section based on Case II shown in Figure 4. In this case, the Lorentz force acts in the same direction as natural convection. Schematic views of the liquid flow pattern and solidification process are shown in Figure 4(a.x). Figure 4(b.x) shows the calculated temperature field. The liquid velocity overlaid with  $f_c$  and the equiaxed velocity overlaid with  $f_e$  are presented in Figures 4(c.x) - (d.x), respectively. Figure 4(e.x) shows the contour of  $M_{\ell e}$  to demonstrate the simultaneous solidification and remelting phenomena. The induced macrosegregation profiles are displayed in Figure 4(f.x).

The simulation results at 180 s are shown in Figures 4(a.1) - (f.1). As the superheat dissipates from the right wall, the temperature gradually drops below the liquidus temperature on the right side (Figure 4(b.1)). The red isoline of the constitutional undercooling ( $\Delta T = T_f + m \cdot c_\ell - T$ ) that equals 0 K is plotted to separate the superheated and undercooling zones. The columnar dendrites initialize from the right wall and grow along the direction of the temperature gradient (Figure 4(c.1)). A clockwise flow pattern is formed under a combination of the thermo-solutal buoyancy and Lorentz force of the TMF (Figure 4(c.1)). The maximum liquid velocity ( $\bar{u}_{\ell, \max} = 0.1$  m/s) is observed near the bottom-left corner. In the columnar-liquid mushy zone, especially near the columnar tip region, the equiaxed grains are generated through fragmentation (Figure 4(d.1)). At this moment, because the equiaxed grains are much heavier than the liquid melt, i.e., the density difference between the equiaxed grains and liquid

melt ( $\Delta\rho$ ) is positive ( $\Delta\rho = \rho_e - \rho_l > 0$ ), the grains tend to sediment to the bottom of the sample. Due to the strong TMF-induced flow, some equiaxed grains are brought to the left superheated region (Figure 4(d.1)), whereas the grains that are generated in or are brought to the deep mushy zone ( $f_c > 0.2$ ) are captured by the columnar phase. From Figures 4(b.1) and 4(e.1), the equiaxed grains grow ( $M_{le} > 0$ ) in the undercooled melt near the solidification front and remelt ( $M_{le} < 0$ ) in the left superheated liquid. A slightly negative segregation is observed along the right wall (Figure 4(f.1)).

At 540 s, the sample is further cooled down (Figure 4(b.2)). The columnar dendrites grow to 1/3 of the sample width, and  $f_e$  is increased to 20% (Figures 4(c.2)-(d.2)). Although the superheated region (e.g., the lower-right and upper-left corners) is extended due to the enrichment of the solute in the bulk liquid, the maximum superheat is decreased by 1.29 K compared to the results obtained at 180 s. Similar to the results shown in Figure 4(e.1), remelting of equiaxed grains occurs mainly near the left wall, but the remelting rate is significantly reduced in Figure 4(e.2). At this moment, some channel segregations initialize from the right-bottom region of the mushy zone (Figure 4(f.2)).

The superheat is totally dissipated from the sample (Figure 4(b.3)) at 900 s. The columnar dendrites and equiaxed grains grow competitively in the remaining undercooled melt. The enrichment of the solute element (Pb) in the melt (Figure 4(f.3)) makes the liquid melt denser, which decreases the  $\Delta\rho$  and even reverses it ( $\Delta\rho < 0$ ), i.e., the liquid melt is heavier than the equiaxed grains. It becomes easier for equiaxed grains to float upwards along the left wall of the sample (Figure 4(d.3)). Some of the equiaxed grains are brought back to the columnar tip front. The growth of such equiaxed grains inhibits the advancement of the columnar dendrites accordingly (Figure 4(c.3)), leading to the columnar-to-equiaxed transition (CET).



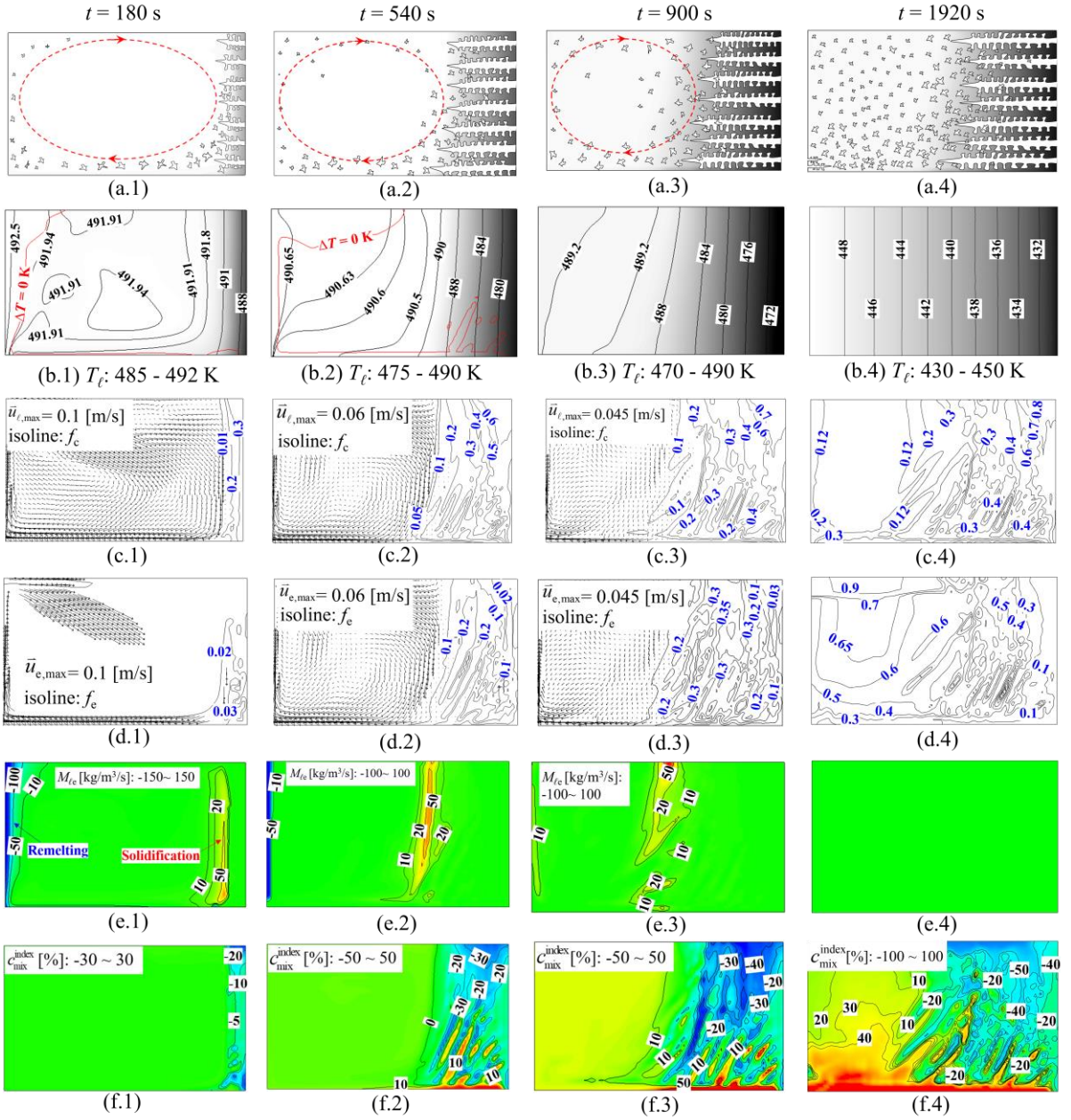


**Figure 4.** Solidification sequence (on the middle vertical plane) of Case II: (a.x) Schematic views of the liquid flow pattern and dendrite growth; (b.x) contour and isolines (in black) of  $T$  (in K) overlaid with the red isoline of  $\Delta T = 0$  K; (c.x) liquid velocity overlaid with the isolines of  $f_c$ ; (d.x) velocity of equiaxed grains overlaid with the isolines of  $f_c$ ; (e.x) contours of  $M_{te}$ , red for solidification and blue for remelting; (f.x) contours of  $c_{mix}^{index}$  [%], red for positive segregation and blue for negative segregation.

The sample is fully solidified at 1920 s. As presented in Figure 4(c.4), the columnar dendrites take the right side, and the remaining part is mostly occupied by the equiaxed grains. In the upper left corner of the sample (Figure 4(d.4)), the sample is solidified as a fully equiaxed

grain structure. Serious positive segregation is found in the lower-left corner, which indicates the presence of a high-volume fraction of eutectics. Several channel segregations can be observed in the lower-right corner (Figure 4(f.4)).

### 4.3 Calculated temperature fields and comparison with experiments

Comparison of the temperature field determined from the measurement and simulation results for all four cases (I - IV) for the selected area of the front surface ( $x$ : 0.5 cm – 9.5 cm;  $y$ : 1 cm – 5 cm) at three different solidification times are shown in Figures 5–7. The  $DT$  is defined as the difference between the maximum temperature and the minimum temperature of the measured region. The solidification front is indicated by the isoline of  $f_c = 0.1$  in the simulation results. Satisfactory agreements between the measurements and simulation results are obtained.

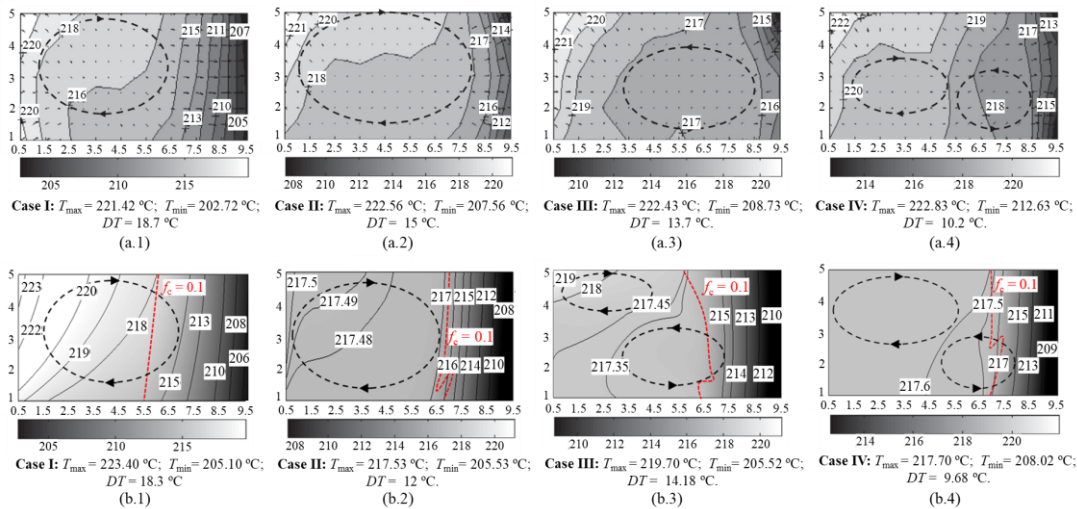


**Figure 5.** Comparison of the temperature field (in °C) for the four cases (I - IV) determined by measurements and the simulation for the front surface of the sample at 540 s, (a.x) the measurement results, (b.x) the simulation results. The black dashed lines show the direction of the liquid convection, and the red dashed lines show the position of the solidification front (isoline of  $f_c = 0.1$ ). (a.x) is reprinted from publication [20], with permission from Elsevier.

As shown in Figures 5(a.1)–5(b.1), in Case I, the isotherms are distorted following the direction (clockwise) of the fluid flow. The maximum temperature appears at the top-left corner, and the measured and calculated  $DT$  values are equal to 18.7 °C and 18.3 °C (Figures 5(a.1) - 5(b.1)), respectively. Compared to Case I, the enhanced convection due to the TMF in Case II leads to a more uniform temperature field, i.e., the measured  $DT$  is decreased from 18.7 °C to 15 °C (Figure 5(a.2)), and the calculated  $DT$  is decreased from 18.3 °C to 12 °C (Figure 5(b.2)). For Case III, the reversed forced convection (the anticlockwise vortex at the

lower part of the sample in Figure 5(b.3)) bends the isotherms to the right side in the lower part of the sample. The  $DT$  for this case is decreased to 14 °C. According to the simulation results, the maximum temperature in the top-left corner of Case III is caused by another small clockwise vortex, which is developed in the top-left part (Figure 5(b.3)). For Case IV, two vortices with different flow directions are predicted. Their flow directions vary with time due to the periodic change in the Lorentz force. Comparing the  $DT$  for the four cases, the periodically reversed stirring mode shows the highest efficiency in homogenizing the temperature field.

The measured and calculated temperature field at 900 s is shown in Figure 6. The measured temperature field (isotherms and  $DT$ ) for the four cases can also be well “reproduced” by the simulations. Because of the reduced liquid flow velocity in the mushy zone, the isotherms are almost vertical on the right side. Regarding  $DT$ , a similar trend to that for the previous time (540 s) is found, i.e., the TMF tends to homogenize the temperature by decreasing  $DT$ .

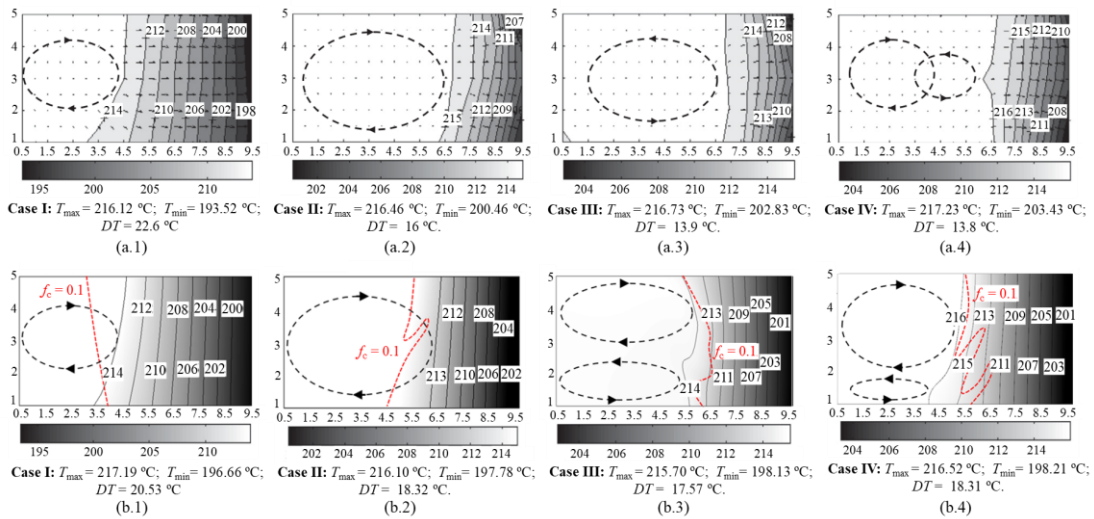


**Figure 6.** Comparison of the temperature field (in °C) for the four cases (I - IV) determined by measurements and simulation for the front surface of the sample at 900 s, (a.x) the measurement results, (b.x) the simulation results. The black dashed lines show the direction of the liquid convection, and the red dashed lines show the position of the solidification front (isoline of  $f_c = 0.1$ ). (a.x) is reprinted from publication [20], with permission from Elsevier.

At 1440 s (Figure 7), it is interesting to note the existence of isotherms corresponding to the temperature level ranging from 204 to 210 °C on the left side, which indicates that the initial heat flux flowing into the sample from the left wall is reversed to flow out of the sample. This condition is favorable for the onset of the second solidification front from the left wall.

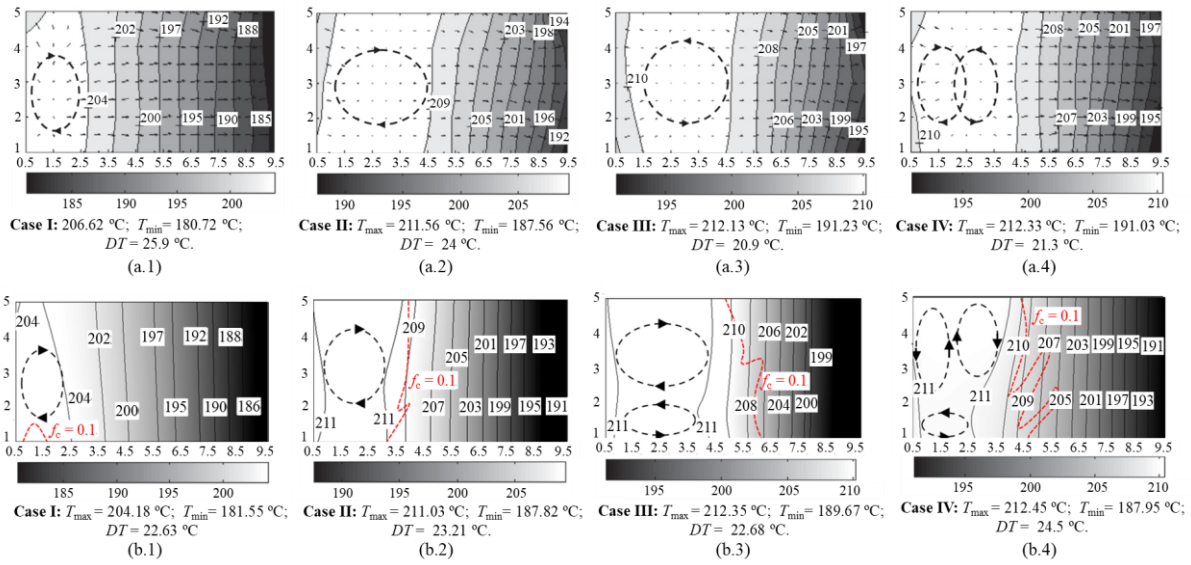


**Figure 7.** Comparison of the temperature field (in °C) for the four cases (I - IV) determined by measurements and simulation for the front surface of the sample: (a.x) the measured results at 1440 s, (b.1) the simulation results at 1440 s, (b.2) the simulation results at 1280 s, (b.3) the simulation results at 1200 s, and (b.4) the simulation results at 1300 s. The black dashed lines show the direction of the liquid convection, and the red dashed lines show the position of the solidification front (isoline of  $f_c = 0.1$ ). (a.x) is reprinted from publication [20], with permission from Elsevier.

Notably, the indicated flow patterns at three solidification times in Case III are different for the experiment and the simulation. One more vortex is found in the liquid pool by the simulation.

#### 4.4 As-cast structure

The metallographic analysis of the as-cast structures in the laboratory experiment is shown in Figure 8(a.x). The calculated distributions of  $f_c$  and  $f_e$  are depicted in Figures 8(b.x) - (c.x). Satisfactory simulation-experiment agreements are achieved for Cases I, II, and IV but not for Case III. The mismatch for Case III will be discussed in detail in §5.3. For Case I, Figures 8(a.1) - (b.1), the upwind tilting of the columnar dendrites dominates the as-cast structure, and the equiaxed grains are mainly distributed in the segregation channels and in a band on the left part of the sample (Figure 8(c.1)). For Case II, the equiaxed zone is greatly extended (Figure 8(a.2)) compared to Case I. The left half of the sample is solidified as equiaxed grains (Figure 8(c.2)), and the right half is solidified as columnar dendrites (Figure 8(b.2)). For Case IV, the equiaxed region is further extended (Figures 8(a.4) and (c.4)), and columnar dendrites are facilitated in the two right-hand corners (Figure 8(b.4)).

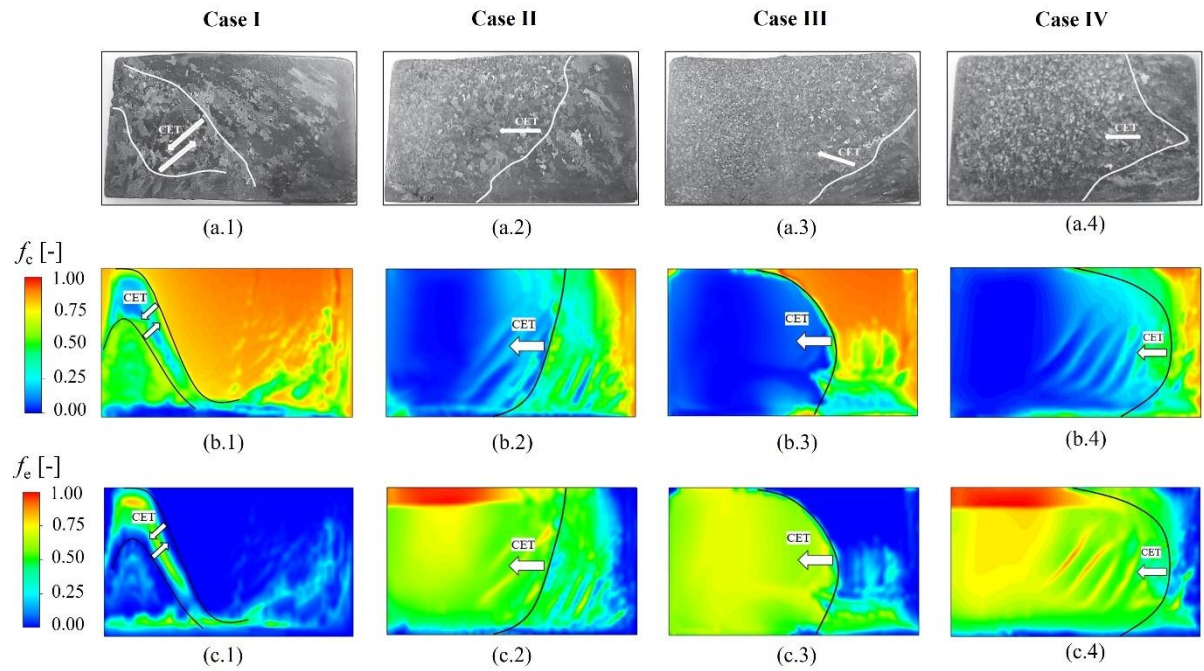


**Figure 8.** Comparison of the as-cast structure for the four cases (I - IV) based on metallographic analysis in laboratory experiments (a.x) and the simulated volume fraction of columnar dendrites (b.x) and equiaxed grains (c.x). (a.x) is reprinted from publication [20], with permission from Elsevier.

#### 4.5 Macrosegregation

The experimentally measured macrosegregation profiles obtained by X-radiography and digital processing methods are shown in Figures 9(a.x) and 9(b.x), respectively. The calculated segregation profiles obtained by averaging the Pb concentrations for ten cross-section planes along the thickness direction are presented in Figure 9(c.x). The simulation results agree well with the experimental measurements except for Case III. The possible reason for this mismatch in Case III will be discussed in detail in §5.3. For Cases I, II, and IV, several channel segregations [24–25, 49–50] are formed in the right part of the sample. Negative segregation is mainly observed in the upper right region, and positive segregation locates in the left-bottom region. Compared to the result of Case I (Figure (a.1)-(c.1)), the location of the strongest positive segregation is pushed to the left-bottom corner in Case II (Figures (a.2)-(c.2)), while the periodically reversed convection (Case IV) is observed to shift this positive segregation to the central-bottom area (Figures (a.4)-(c.4)). By integrating the macrosegregation index in the calculation domain, the global macrosegregation index ( $GMI = \iiint_{vol} |c_{mix}^{index}| dv$ ) is determined to be 38.17% for Case I. By applying the TMF, the GMI

is increased to 39.45% for Case II and 39.77% for Case IV. It is found that macrosegregation is generally intensified by the TMF.

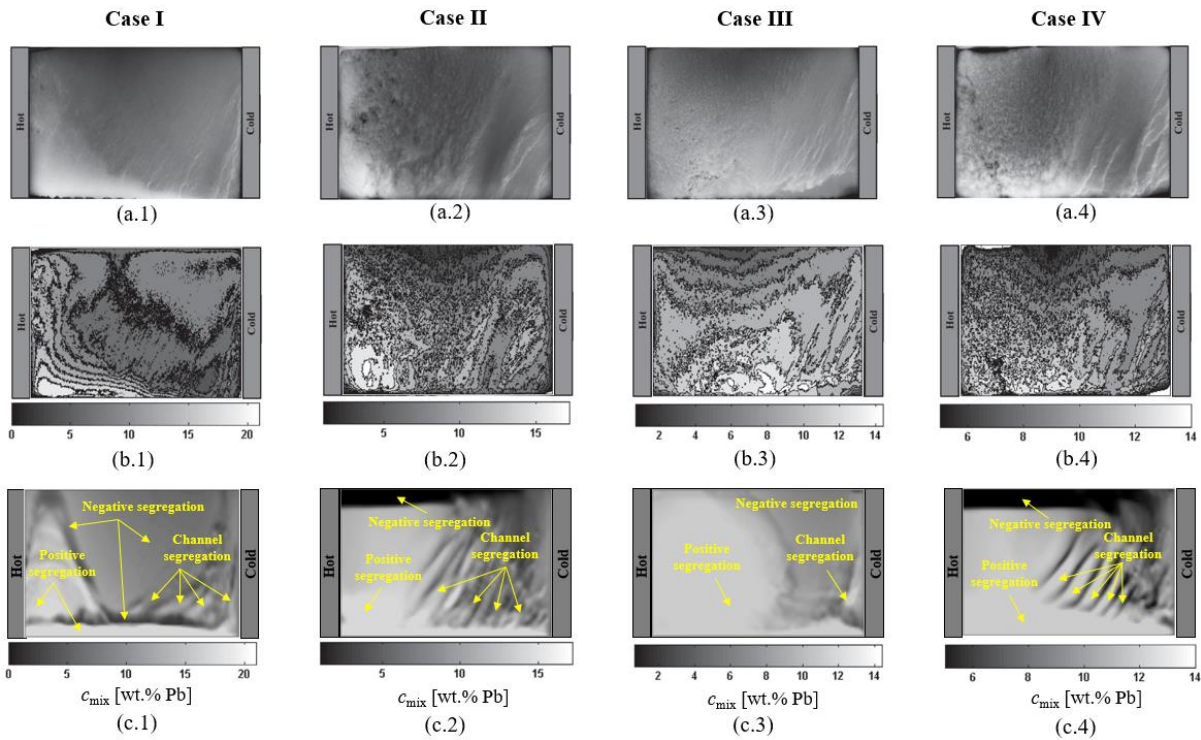


**Figure 9.** Macrosegregation maps obtained for the sample under the effect of different electromagnetic stirring modes: (a.x) X-radiography of the as-solidified ingot; (b.x) Pb concentration map digitally processed from (a.x); (c.x) simulated mean Pb concentration through the thickness direction. (a.x) and (b.x) are reprinted from publication [20], with permission from Elsevier.

3D views of the simulated channel segregations for the four cases are revealed by the isosurface of  $c_{mix} = 11$  wt.% Pb, as shown in Figure 10. The results are colored by  $c_{mix}$  from 2 wt.% Pb to 18 wt.% Pb. Channel segregations are clearly observed for the four cases. The TMF leads to an increase in the number of channel segregations (Figures 10(b) and 10(d)).

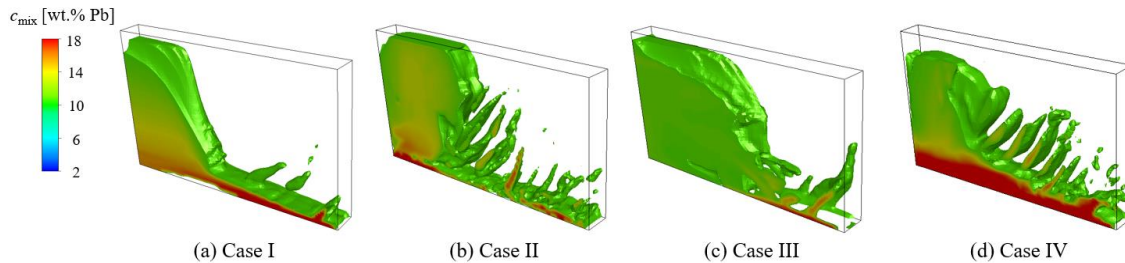


**Figure 10.** 3D views of the isosurfaces of  $c_{mix} = 11$  wt.% Pb for the four cases (I - IV). The results are colored by  $c_{mix}$ .

As mentioned above, Case III cannot be well reproduced in the current study. Good agreement has been achieved for Case I, as reported previously [39]. Here, a quantitative comparison of the Pb concentration determined from simulation results and measurements focuses on Case II and Case IV, as shown in Figures 11 and 12. Fifty cores ( $\phi$  0.5 cm  $\times$  1 cm) distributed along five horizontal lines were extracted by drilling holes ( $\phi$  0.5 cm  $\times$  1 cm) from the as-solidified sample along the thickness direction. A chemical method coupled with the Inductive Coupled Plasma (ICP) technique was used to determine the mean value for the Pb concentration at each point. The simulated Pb concentrations (blue box), averaged in the volumes (0.4 cm  $\times$  0.4 cm  $\times$  1 cm) corresponding to the same positions of the experiment, are compared with those of the experiment in Figure 11 and 12. The simulated results coincide with the measurement results very well. A similar tendency for the macrosegregation distribution determined by the simulations and measurements is observed. To capture more information about the segregation, the mean concentrations along the five horizontal lines (Figures 11(a), 12(a)) are also plotted. The simulation curves also show a good agreement with the measurement results. Nevertheless, the fluctuation of the red lines, which indicates the channel segregation, cannot be detected by using this analysis method. The reason for this is due to the core size ( $\phi$  0.5 cm) of the chemical analysis, which is too large for capturing the channel segregation phenomena.

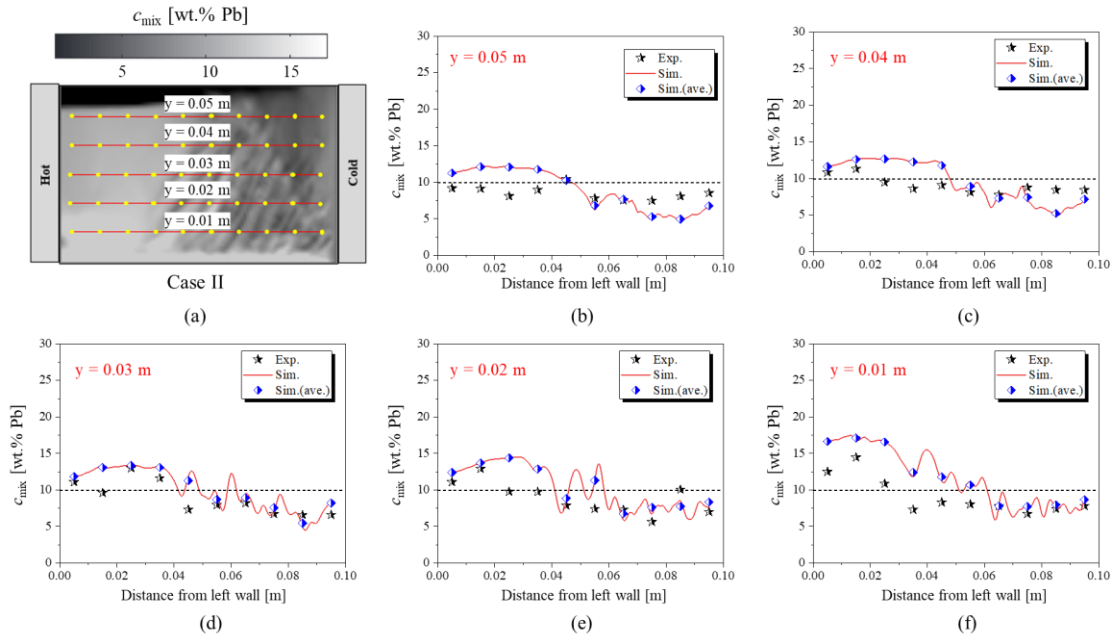


**Figure 11.** Quantitative comparison of the Pb concentration ( $c_{\text{mix}}$ ) for Case II determined from the measurement data obtained using the ICP (Inductive Coupled Plasma) technique and simulation results. (a) Contour of the simulated Pb concentration; (b)-(f) correspond to the results obtained at five different horizontal lines,  $y = 0.05$  m,  $0.04$  m,  $0.03$  m,  $0.02$  m, and  $0.01$  m. The experimental points show the averaged Pb concentrations in the drilling holes ( $\phi 0.5$  cm  $\times$  1 cm). The points of simulation show the averaged Pb concentrations in the volumes ( $0.4$  cm  $\times$   $0.4$  cm  $\times$  1 cm) corresponding to the experimental positions.

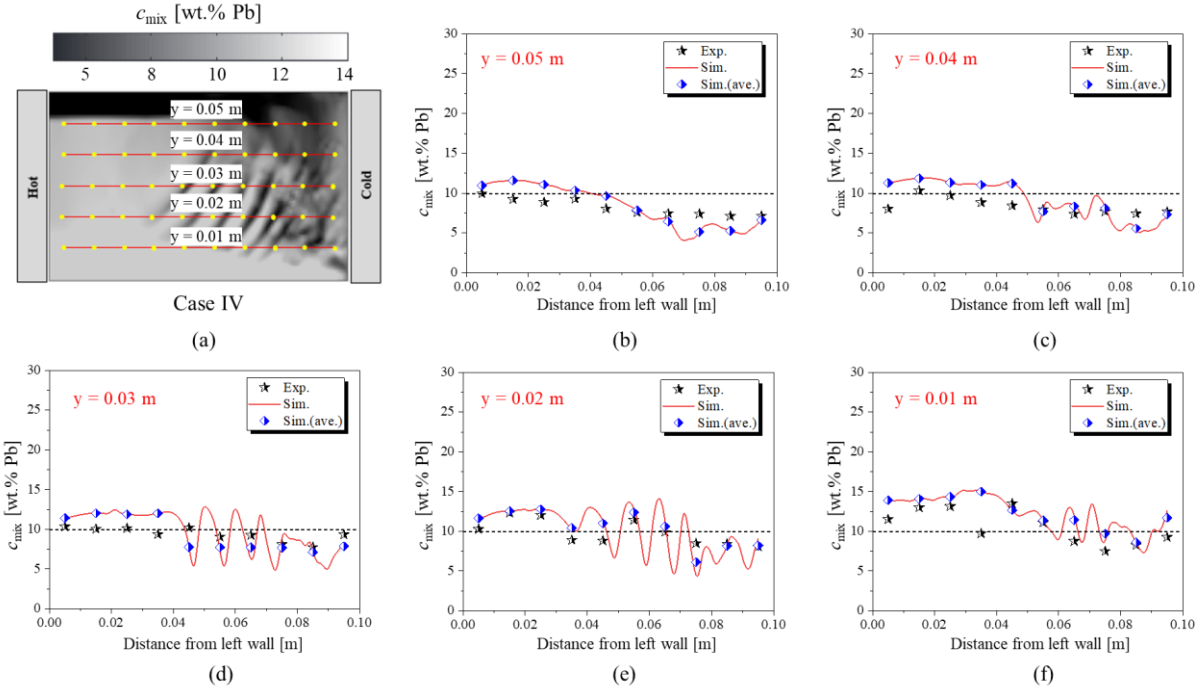


**Figure 12.** Quantitative comparison of the Pb concentration ( $c_{\text{mix}}$ ) for Case IV determined from the measurement data obtained using the ICP (Inductive Coupled Plasma) technique and simulation results. (a) Contour of the simulated Pb-concentration; (b)-(f) correspond to the results at five different horizontal lines,  $y = 0.05$  m,  $0.04$  m,  $0.03$  m,  $0.02$  m, and  $0.01$  m. The experimental points show the averaged Pb concentrations in the drilling holes ( $\phi 0.5$  cm  $\times$  1 cm). The points of simulation show the averaged Pb concentrations in the volumes ( $0.4$  cm  $\times$   $0.4$  cm  $\times$  1 cm) corresponding to the experimental positions.

## 5. Discussion

### 5.1 Effect of TMF-induced convection on the evolution of the columnar tip front

Figure 13 shows the profiles of the columnar tip front ( $f_c = 0.01$ ) at the early stage of solidification ( $t = 120$  s) for the four different cases. The isotherms overlaid with the liquid velocity in vector are plotted on the central vertical section.



For Case I, natural convection acts in the sample. The isotherms are distorted, and the lowest temperature appears at the bottom-right corner. The columnar dendrites solidify and extend to the left side (Figure 13(a)). The profile of the columnar tip front is consistent with that of the isotherm. For Case II, natural convection is strengthened by the TMF. The isotherms are more distorted. The high-temperature melt coming from the upper-left corner impinges the middle part of the right cold wall. It, consequently, influences the isotherms near the columnar tip front, i.e., the temperature in the middle part of the right-cold wall is slightly higher than that at the two right-hand corners. Thus, the growth speed of the columnar tip front at the two right-hand corners is faster than that at the middle part of the right wall (Figure 13(b)).

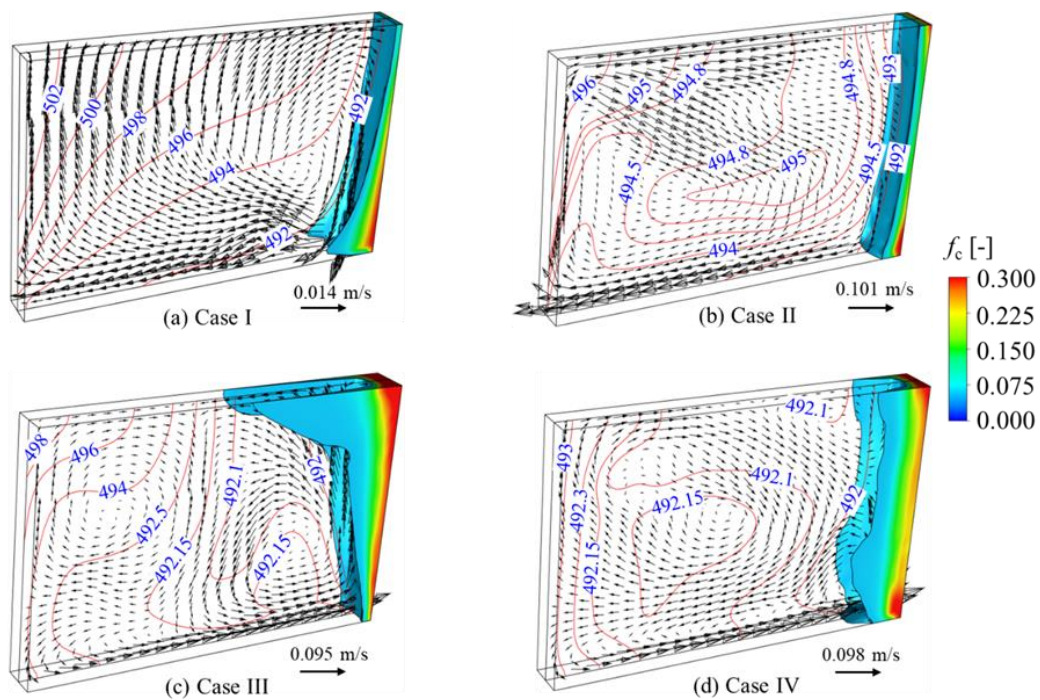


**Figure 13.** Influence of TMF-induced convection on the columnar tip front, which is defined by the isosurface of  $f_c = 0.01$  at the early stage of solidification ( $t = 120$  s) for the four cases: (a) Case I; (b) Case II; (c) Case III; and (d) Case IV. The isotherms overlaid with the liquid velocity in vector are plotted on the central vertical plane of the sample.

Two vortices with opposite directions are formed in Case III (Figure 13(c)): the first vortex locates on the left side in the clockwise direction, while the other one locates on the right side in the anti-clockwise direction. This kind of flow pattern in Case III is not indicated by the experiment (Figure 5(a.3), Figure 6(a.3), Figure 7(a.3)). The right-anticlockwise convection transports the cooler melt to the upper-right corner along the right wall. The lowest

temperature appears at the upper-right corner, where the columnar tip front is facilitated to grow (Figure 13(c)). When the periodically reversed stirring is applied (Case IV), the flow direction near the columnar tip front is also reversed periodically. When an anticlockwise flow is induced, the aggregation of the cooler melt at the upper-right corner promotes the growth of the columnar dendrites in this area. When a clockwise flow is induced, the growth of columnar dendrites at the bottom-right corner is accelerated. Thus, the columnar tip front preferentially grows from the two corners of the right wall (Figure 13(d)).

Through the above analysis, it should be noted that the forced convection plays an important role in changing the temperature field and further influencing the evolution of the columnar tip front. The final as-cast structure and macrosegregation are closely associated with the flow patterns induced by different types of TMFs.

### *5.2 Importance of remelting/destruction of equiaxed grains*

An additional simulation (Case II-A) was conducted to demonstrate the importance of the remelting/destruction of equiaxed grains and its further impact on the temperature field, formation of the as-cast structure and macrosegregation. All the settings for Case II-A were the same as those for Case II except for ignoring the remelting/destruction of equiaxed grains. The simulation results obtained for Case II and a comparison with Case II-A are shown in Figure 14. The net mass transfer rate from liquid to equiaxed ( $M_{le}$ ) due to remelting overlaid with the isotherms obtained at 120 s is shown in Figures 14(a.1)-(b.1). Only the range with a negative value, indicating the remelting process, is displayed. The equiaxed grains start to remelt if they are exposed in the superheated melt. By integrating  $M_{le}$  over the whole sample region, the remelting rate is determined to reach up to  $4.8 \times 10^{-4}$  kg/s. Correspondingly, the heat dissipation rate due to the consumption of the latent heat from the liquid melt by remelting is equal to 29.3 J/s. As shown in Figure 14(a.1), the isotherms (e.g., 492.6 K and 492.7 K) are distorted in the area where remelting occurs. The average temperature of the liquid is overestimated by 5.13 K in Case II-A, ignoring remelting, compared to Case II, considering remelting of the equiaxed grains. The simulated distributions of  $f_e$  and  $c_{mix}$  in the as-solidified sample for the two cases are shown in Figures 14(a.2)-(b.2) and Figures 14(a.3)-(b.3), respectively. In comparison to Case II, (1) ignoring the remelting of equiaxed grains (Case II-A) leads to an overestimation of  $f_e$  by 15.3% (30.4 g) and an underestimation of  $f_c$  by 34.1% (30.6 g); (2) although some segregation channels are also predicted to be present, as

shown in Figure 14(b.3), the experimentally observed segregation pattern (i.e., the serious positive segregation at the left-bottom corner and the negative segregation at the left-top region, Figure 9(b.2)), cannot be reproduced by Case II-A; (3) the GMI is underestimated by 48% for Case II-A. The accompanying remelting of equiaxed grains during the solidification process represents a significant species/energy transport mechanism. Ignoring the remelting phenomenon would lead to an overestimation of the temperature in the liquid melt. This leads to a further overestimation of the mass of the equiaxed grains and underestimation of macrosegregation.

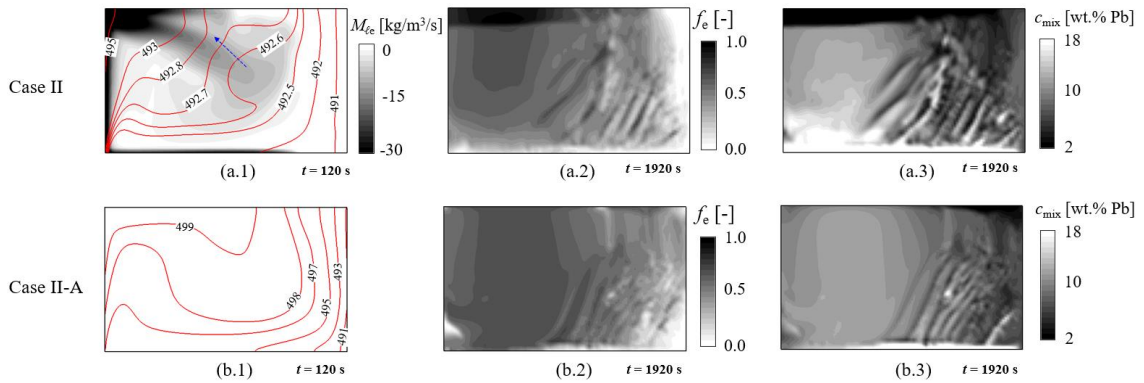


**Figure 14.** Comparison of the simulation results obtained for the two cases (Case II and Case II-A) with (a.x) and without remelting of equiaxed grains (b.x); (a.1)-(b.1) contours of  $M_{fc}$  (negative value due to remelting only) overlaid with isotherms at 120 s; (a.2)-(b.2) as-solidified structure of equiaxed grains ( $f_e$ ) at 1920 s; (a.3)-(b.3) contours of the  $c_{mix}$  at 1920 s.

### 5.3 Simulation-experiment mismatch in Case III

Based on the current numerical model, the experimental results, e.g., the temperature field, as-cast structure and macrosegregation, cannot be “reproduced” for Case III. One reason for this mismatch could be the avalanche phenomenon [51], which probably occurs when the columnar dendrites solidify from the upper-right corner of the ingot in the early stage of solidification. The current model cannot be used to consider this phenomenon.

The evolution of the columnar structure (Case III), which is represented by the isosurface of  $f_c = 0.05$ , is shown in Figure 15. The temperature field overlaid with the liquid velocity in vector is displayed on the central vertical plane. At 50 s, the TMF-induced forced convection, which is in the anti-clockwise direction, transports the high temperature melt along the bottom toward the right cold wall. The melt impinges the bottom-right corner, and then flows to the upper part of the ingot along the right cold wall. The lowest temperature ( $T_{low} = 490.49$  K),

and the associated solidification of the columnar structure should start at the upper-right corner, as shown in Figure 15(a).

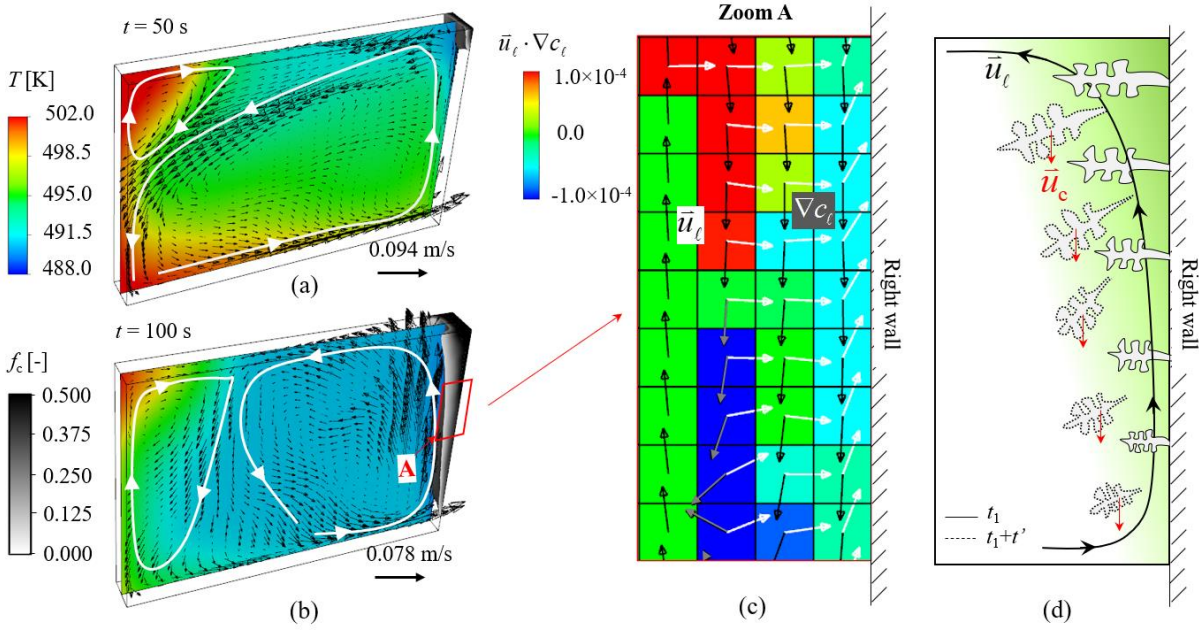


**Figure 15.** Solidification sequence of the columnar dendrites (iso-surface of  $f_c = 0.05$ ) for Case III: (a)  $t = 50$  s; (b)  $t = 100$  s; (c) zoom view of the  $\bar{u}_\ell \cdot \nabla c_\ell$  distribution in Zone A shown in (b). Temperature field overlaid with liquid velocity vector is shown on the central vertical plane; (d) schematic view of the avalanche phenomenon.

At 100 s, the columnar tip front continually grows and extends downwards along the cold wall. The flow pattern is slightly different from that found previously, i.e., the vortex in the upper-left corner is enlarged, while the main vortex is compressed to the right side (Figure 15(b)). A zoomed view of the distribution of  $\bar{u}_\ell \cdot \nabla c_\ell$  near the upper-right corner (Zone A marked in Figure 15(b)) on the central vertical plane is shown in Figure 15(c). The interdendritic flow ( $\bar{u}_\ell$ ) in the direction opposite to the liquid concentration gradient ( $\nabla c_\ell$ ) leads to local remelting. The ‘blue’ region with a negative value of  $\bar{u}_\ell \cdot \nabla c_\ell$ , where the angle between  $\bar{u}_\ell$  and  $\nabla c_\ell$  is larger than  $90^\circ$ , is observed near the right wall. If the remelting of columnar dendrite roots causes massive dendrites to fall off from the right wall, as schematically shown in Figure 15(d), the avalanche phenomenon is likely to occur. However, this phenomenon is still far more complex for the recent model. According to the current model, the growth of the columnar dendrites in the upper-right part is further promoted during the later solidification stage. Finally, the as-solidified columnar dendrites capture the upper-

right part of the sample in Case III (Figure 8(b.3)), leading to a mismatch to the measurement result (Figure 8(a.3)).

Another possible reason why the simulation result for Case III cannot reproduce the as-cast structure is that the heterogeneous nucleation is ignored. The significant role of fragmentation in the generation of equiaxed grains in this benchmark experiment has been addressed by Hachani et al. [20]. Thus, only the fragmentation of columnar dendrites is considered as the source of the equiaxed grains in the current study. However, heterogeneous nucleation, which can serve as another source of equiaxed grains, is likely to occur when the inoculants are exposed to the undercooling environment. Specifically, when the lowest temperature appears at the upper-right corner in the early solidification stage of Case III, the first solid phase can consist of columnar dendrites or equiaxed grains, which are formed through heterogeneous nucleation. If the equiaxed grains can occupy the upper-right corner during the later solidification process, the simulated final as-cast structure will show good agreement with the measurement result.

#### *5.4 Boundary conditions for the two lateral walls*

The temperature history for the two exchangers was monitored during the solidification process [20]. However, due to the thermal contact resistance between the exchangers and sample walls, which is not always constant, the exact temperatures of the two lateral walls ( $T_{\text{wall}}$ ) are unknown and need to be determined. The extrapolation method based on the heat reservation law can be used to calculate  $T_{\text{wall}}$  [31-32]. However, because the exact experimental temperature for the two exchangers is unknown, the use of this method is greatly limited for researchers.

The convective heat transfer boundary condition ( $q = 2000 (T_{\text{wall}} - T_{\text{exch}})$ ) was used in the current study, where  $q$  is the heat flux between the sample and exchanger and  $T_{\text{exch}}$  is the defined exchanger temperature in Figure 2(b). Based on the cooling rates (0.03 K/s) for the two exchangers provided by Hachani et al. [20], the isotherms corresponding to the temperature level ranging from 204 to 210 °C on the left side of the four cases (I-IV) cannot be “reproduced”. Numerical parameter studies were performed by varying the cooling rate for the left exchanger. The best fit to the temperature fields for all four cases is obtained for a cooling rate value of 0.033 K/s (9% higher than 0.03 K/s). Consequently, this cooling rate was used in this study.

## 6. Conclusion

An extended three-phase mixed columnar-equiaxed solidification model was used to simulate the benchmark experiments for Sn-10wt.% Pb alloy [20]. Four cases under different flow conditions (natural convection and/or forced convection with different modes) were investigated. Except for Case III, satisfactory simulation-experiment agreements in terms of the temperature field, as-cast structure and macrosegregation were obtained for the remaining three cases. Based on the simulation results, the following conclusions are drawn.

- (1) To ‘reproduce’ the benchmark experiments [20], the model must at least have the following features: i) three phases (liquid melt, equiaxed grains, and columnar dendrites); ii) dendrite fragmentation, which gives birth to the equiaxed grains; iii) movement of equiaxed grains; iv) growth and remelting/destruction of equiaxed grains exposed to undercooled and superheated liquid; and v) coupling between the TMF and multiphase flow.
- (2) The simultaneous solidification and remelting of equiaxed crystals represent an important species/energy transport mechanism in this laboratory benchmark. Ignoring the remelting of equiaxed grains in the superheated region in a numerical model will lead to an error in the estimation of the as-cast structure and macrosegregation.
- (3) TMF plays an important role in homogenizing the temperature field and promoting equiaxed grain formation through the fragmentation mechanism, and, consequently, facilitates CET.
- (4) TMF is found to generally intensify macrosegregation and increase the number of channel segregations.

The simulation and experimental measurement results obtained for Case III show a mismatch most likely because the avalanche phenomenon and/or heterogeneous nucleation was not taken into account. Further modeling effort is still needed to ‘reproduce’ Case III.

## Declaration of Competing Interest

None.

## Acknowledgements

The authors acknowledge the financial support from the Austrian Research Promotion Agency (FFG) through the project Bridge I (No. 868070) as well as the technical support of the industrial partner Primetals Technologies Austria GmbH.

## Reference

- [1] K. Ayata, T. Mori, T. Fujimoto, T. Ohnishi, I. Wakasugi, Improvement of Macrosegregation in Continuously Cast Bloom and Billet By Electromagnetic Stirring, *Trans. Iron Steel Inst. Japan.* 24 (1984) 931–939. <https://doi.org/10.2355/isijinternational1966.24.931>
- [2] N.A. Shan, J.J. Moore, A review of the effects of electromagnetic stirring (EMS) in continuously cast steel. Part 1, *Iron Steelmak.* 9 (1982) 31-36.
- [3] S. Wang, G. Alvarez De Toledo, K. Välimaa, S. Louhenkilpi, Magneto hydrodynamic phenomena, fluid control and computational modeling in the continuous casting of billet and bloom, *ISIJ Int.* 54 (2014) 2273–2282. <https://doi.org/10.2355/isijinternational.54.2273>
- [4] N. Genma, T. Soejima, T. Saito, M. Kimura, Y. Kaihara, H. Fukumoto, K. Ayata, The linear-motor type in-mold electromagnetic stirring technique for the slab continuous caster, *ISIJ Int.* 29 (1989) 1056-1062. <https://doi.org/10.2355/isijinternational.29.1056>
- [5] K. Fujisaki, In-mold electromagnetic stirring in continuous casting, *IEEE Trans. Ind. Appl.* 37 (2001) 1098–1104. <https://doi.org/10.1109/28.936402>
- [6] K. Okazawa, T. Toh, J. Fukuda, T. Kawase, M. Toki, Fluid flow in a continuous casting mold driven by linear induction motors, *ISIJ Int.* 41 (2001) 851–858. <https://doi.org/10.2355/isijinternational.41.851>
- [7] M. Dubke, K.H. Tacke, K.H. Spitzer, K. Schwerdtfeger, Flow fields in electromagnetic stirring of rectangular strands with linear inductors: Part I. theory and experiments with cold models, *Metall. Trans. B.* 19 (1988) 581–593. <https://doi.org/10.1007/BF02659149>
- [8] M. Dubke, K.H. Tacke, K.H. Spitzer, K. Schwerdtfeger, Flow fields in electromagnetic stirring of rectangular strands with linear inductors: Part II. computation of flow fields in billets, blooms, and slabs of steel, *Metall. Trans. B.* 19 (1988) 595–602. <https://doi.org/10.1007/BF02659150>
- [9] X. Wang, Y. Fautrelle, R. Moreau, J. Etay, A.M. Bianchi, F. Baltaretu, X. Na, Flow, heat and mass transfers during solidification under traveling/rotating magnetic field, *Int. J. Energy Environ. Eng.* 6 (2015) 367–373. <https://doi.org/10.1007/s40095-015-0181-1>
- [10] L. Hachani, R. Boussaa, B. Saadi, X. Wang, K. Zaidat, A. Belgacem-Bouzida, D. Henry, V. Botton, H. Ben Hadid, Y. Fautrelle, Experimental investigation of the natural and forced convection on solidification of Sn-3wt . % Pb alloy using a benchmark experiment, *J. Iron Steel Res. Int.* 19 (2012)

- [11] D.J. Hebditch, J.D. Hunt, Observations of ingot macrosegregation on model systems, *Metall. Mater. Trans. B* 5 (1974) 1557–1564. <https://doi.org/10.1007/BF02646326>
- [12] G. Quillet, A. Ciobanas, P. Lehmann, Y. Fautrelle, A benchmark solidification experiment on an Sn-10%wtBi alloy, *Int. J. Heat Mass Transf.* 50 (2007) 654–666. <https://doi.org/10.1016/j.ijheatmasstransfer.2006.07.030>
- [13] X. Wang, P. Petitpas, C. Garnier, J.P. Paulin, Y. Fautrelle, A quasi two-dimensional benchmark experiment for the solidification of a tin-lead binary alloy, *C. R. Mec.* 335 (2007) 336–341. <https://doi.org/10.1016/j.crme.2007.05.009>
- [14] X. Wang, Y. Fautrelle, An investigation of the influence of natural convection on tin solidification using a quasi two-dimensional experimental benchmark, *Int. J. Heat Mass Transf.* 52 (2009) 5624–5633. <https://doi.org/10.1016/j.ijheatmasstransfer.2009.05.030>
- [15] L. Hachani, B. Saadi, X. Wang, A. Nouri, K. Zaidat, A. Belgacem-Bouzida, L. Ayouni-Derouiche, G. Raimondi, Y. Fautrelle, Experimental analysis of the solidification of Sn-3 wt.%Pb alloy under natural convection, *Int. J. Heat Mass Transf.* 55 (2012) 1986–1996. <https://doi.org/10.1016/j.ijheatmasstransfer.2011.11.054>
- [16] L. Hachani, K. Zaidat, B. Saadi, X. Wang, Y. Fautrelle, Solidification of Sn-Pb alloys: Experiments on the influence of the initial concentration, *Int. J. Therm. Sci.* 91 (2015) 34–48. <https://doi.org/10.1016/j.ijthermalsci.2015.01.007>
- [17] M. Bellet, H. Combeau, Y. Fautrelle, D. Gobin, M. Rady, E. Arquis, O. Budenkova, B. Dussoubs, Y. Duterrail, A. Kumar, C.-A. Gandin, B. Goyeau, S. Mosbah, M. Založnik, Call for contributions to a numerical benchmark problem for 2D columnar solidification of binary alloys, *Int. J. Therm. Sci.* 48 (2009) 2013–2016. <https://doi.org/10.1016/j.ijthermalsci.2009.07.024>
- [18] A. Abdelhakem, L. Hachani, K. Zaidat, I. Sari, Y. Fautrelle, Experimental study of the effect of intermittent electromagnetic stirring on the columnar-equiaxed transition in Sn-10 wt % Pb alloy solidification, *J. Heat Transfer.* 143 (2021) 1–8. <https://doi.org/10.1115/1.4050408>
- [19] L. Hachani, J. Wang, I. Kaldre, G. Salloum Abou-Jaoude, O. Budenkova, G. Reinhart, K. Zaidat, N. Mangelinck, X. Li, H. Nguyen Thi, A. Bojarevics, Z. Ren, L. Buligins, Y. Fautrelle, Magnetic fields, convection and solidification, *Mater. Sci. Forum.* 790 (2014) 375–383. <https://doi.org/10.4028/www.scientific.net/MSF.790-791.375>
- [20] L. Hachani, K. Zaidat, Y. Fautrelle, Experimental study of the solidification of Sn-10 wt.%Pb alloy under different forced convection in benchmark experiment, *Int. J. Heat Mass Transf.* 85 (2015) 438–454. <https://doi.org/10.1016/j.ijheatmasstransfer.2015.01.145>
- [21] K. Zaidat, I. Sari, A. Boumaaza, A. Abdelhakem, L. Hachani, Y. Fautrelle, Experimental investigation of



- the effect of travelling magnetic field on the CET in Sn-10wt.%Pb alloy, *IOP Conf. Ser. Mater. Sci. Eng.* 424 (2018) 012052. <https://doi.org/10.1088/1757-899X/424/1/012052>
- [22] C.-A. Gandin, T. Carozzani, H. Dignonnet, S. Chen, G. Guillemot, Direct modeling of structures and segregations up to industrial casting scales, *JOM* 65 (2013) 1122-1130. <https://doi.org/10.1007/s11837-013-0679-z>
- [23] T. Carozzani, C.-A. Gandin, H. Dignonnet, M. Bellet, K. Zaidat, Y. Fautrelle, Direct simulation of a solidification benchmark experiment, *Metall. Mater. Trans. A* 44 (2013) 873–887. <https://doi.org/10.1007/s11661-012-1465-1>
- [24] J. Li, M. Wu, J. Hao, A. Ludwig, Simulation of channel segregation using a two-phase columnar solidification model - Part I: Model description and verification, *Comput. Mater. Sci.* 55 (2012) 407–418. <https://doi.org/10.1016/j.commatsci.2011.12.037>
- [25] J. Li, M. Wu, J. Hao, A. Kharicha, A. Ludwig, Simulation of channel segregation using a two-phase columnar solidification model - Part II: Mechanism and parameter study, *Comput. Mater. Sci.* 55 (2012) 419–429. <https://doi.org/10.1016/j.commatsci.2011.12.021>
- [26] H. Combeau, M. Bellet, Y. Fautrelle, D. Gobin, E. Arquis, O. Budenkova, B. Dussoubs, Y. Duterrail, A. Kumar, S. Mosbah, T. Quatruvaux, M. Rady, C.-A. Gandin, B. Goyeau, M. Založnik, A numerical benchmark on the prediction of macrosegregation in binary alloys, *Supplemental Proceedings: Materials Fabrication, Properties, Characterization, and Modeling*, 2 (2011) 755-762. <https://doi.org/10.1002/9781118062142.ch91>
- [27] H. Combeau, M. Bellet, Y. Fautrelle, D. Gobin, E. Arquis, O. Budenkova, B. Dussoubs, Y. Du Terrail, A. Kumar, C.-A. Gandin, B. Goyeau, S. Mosbah, T. Quatruvaux, M. Rady, M. Založnik, Analysis of a numerical benchmark for columnar solidification of binary alloys, *IOP Conf. Ser. Mater. Sci. Eng.* 33 (2012) 012086. <https://doi.org/10.1088/1757-899X/33/1/012086>
- [28] S. Ganina, V. Ginkin, O. Budenkova, B. Saadi, L. Hachani, Y. Fautrelle, Comparison of two models for simulation of binary alloy solidification, *Defect Diffus. Forum.* 326 (2012) 599–604. <https://doi.org/10.4028/www.scientific.net/DDF.326-328.599>
- [29] R. Boussaa, O. Budenkova, L. Hachani, X. Wang, B. Saadi, K. Zaidat, H. Ben Hadid, Y. Fautrelle, 2D and 3D numerical modeling of solidification benchmark of Sn-3Pb (%wt.) alloy under natural convection, *CFD Model. Simul. Mater. Process.* (2012) 163–170. <https://doi.org/10.1002/9781118364697.ch19>
- [30] K.O. Tveito, M. M’Hamdi, H. Combeau, M. Založnik, K. Zaidat, X. Wang, B. Saadi, Y. Fautrelle, Numerical analysis of the influence of melting and application of electromagnetic stirring prior to solidification on macrosegregation formation during casting of a binary alloy, *CFD Model. Simul. Mater.* (2012) 253–260. <https://doi.org/10.1002/9781118364697.ch30>

- [31] R. Boussaa, L. Hachani, O. Budenkova, V. Botton, D. Henry, K. Zaidat, H. Ben Hadid, Y. Fautrelle, Macrosegregations in Sn-3 wt%Pb alloy solidification: Experimental and 3D numerical simulation investigations, *Int. J. Heat Mass Transf.* 100 (2016) 680–690. <https://doi.org/10.1016/j.ijheatmasstransfer.2016.04.120>
- [32] A. Abdelhakem, A. Nouri, L. Hachani, Y. Fautrelle, K. Zaidat, Three-dimensional numerical simulation and experimental investigations of benchmark experiment of Sn-10 wt. %Pb alloy solidification under thermosolutal convection, *J. Heat Transfer.* 144 (2022) 042401. <https://doi.org/10.1115/1.4053567>
- [33] T. Wang, L. Hachani, Y. Fautrelle, Y. Delannoy, E. Wang, X. Wang, O. Budenkova, Numerical modeling of a benchmark experiment on equiaxed solidification of a Sn–Pb alloy with electromagnetic stirring and natural convection, *Int. J. Heat Mass Transf.* 151 (2020) 119414. <https://doi.org/10.1016/j.ijheatmasstransfer.2020.119414>
- [34] S. Khelfi, A. Abdelhakem, A. Nouri, L. Hachani, K. Zaidat, Numerical modeling and experimental analysis of benchmark experiment of Sn-10 wt%Pb alloy under forced convection by electromagnetic stirring, *J. Cryst. Growth* 584 (2022) 126575. <https://doi.org/10.1016/j.jcrysgro.2022.126575>
- [35] C. Wang, Z. Liu, B. Li, A three-phase volume-averaged solidification model considering the growth direction of columnar crystals axis, *Int. J. Heat Mass Transf.* 194 (2022) 122974. <https://doi.org/10.1016/j.ijheatmasstransfer.2022.122974>
- [36] Y. Zheng, M. Wu, E. Karimi-Sibaki, A. Kharicha, A. Ludwig, Use of a mixed columnar-equiaxed solidification model to analyse the formation of as-cast structure and macrosegregation in a Sn-10 wt% Pb benchmark experiment, *Int. J. Heat Mass Transf.* 122 (2018) 939–953. <https://doi.org/10.1016/j.ijheatmasstransfer.2018.02.012>
- [37] Z. Zhang, M. Wu, H. Zhang, E. Karimi-Sibaki, A. Ludwig, A. Kharicha, Modeling mixed columnar-equiaxed solidification of Sn- 10wt.%Pb alloy under forced convection driven by travelling magnetic stirring, *IOP Conf. Ser. Mater. Sci.* 861 (2020) 012024. <https://doi.org/10.1088/1757-899X/861/1/012024>
- [38] M. Wu, A. Ludwig, A three-phase model for mixed columnar-equiaxed solidification, *Metall. Mater. Trans. A* 37 (2006) 1613–1631. <https://doi.org/10.1007/s11661-006-0104-0>
- [39] M. Wu, A. Ludwig, Using a three-phase deterministic model for the columnar-to-equiaxed transition, *Metall. Mater. Trans. A* 38 (2007) 1465–1475. <https://doi.org/10.1007/s11661-007-9175-9>
- [40] J. Li, M. Wu, A. Ludwig, A. Kharicha, Simulation of macrosegregation in a 2.45-ton steel ingot using a three-phase mixed columnar-equiaxed model, *Int. J. Heat Mass Transf.* 72 (2014) 668–679. <https://doi.org/10.1016/j.ijheatmasstransfer.2013.08.079>
- [41] M. Wu, A. Ludwig, A. Kharicha, Volume-averaged modeling of multiphase flow phenomena during alloy solidification, *Metals* 9 (2019) 229. <https://doi.org/10.3390/met9020229>

- [42] J. Lipton, M.E. Glicksman, W. Kurz, Dendritic growth into undercooled alloy metals, *Mater. Sci. Eng.* 65 (1984) 57–63. [https://doi.org/10.1016/0025-5416\(84\)90199-X](https://doi.org/10.1016/0025-5416(84)90199-X)
- [43] A. Ludwig, M. Wu, Modeling of globular equiaxed solidification with a two-phase approach, *Metall. Mater. Trans. A* 33 (2002) 3673–3683. <https://doi.org/10.1007/s11661-002-0241-z>
- [44] Y. Zheng, M. Wu, A. Kharicha, A. Ludwig, Incorporation of fragmentation into a volume average solidification model, *Model. Simul. Mater. Sci. Eng.* 26 (2018) 015004. <https://doi.org/10.1088/1361-651X/aa86c5>
- [45] H. Zhang, M. Wu, P. Schumacher, C.M.G. Rodrigues, A. Ludwig, A. Kharicha, Modelling melting and grain destruction phenomena during globular equiaxed solidification, *Appl. Math. Model.* 97 (2021) 821–838. <https://doi.org/10.1016/j.apm.2021.04.024>
- [46] Q. Han, A. Hellawell, Primary particle melting rates and equiaxed grain nucleation, *Metall. Mater. Trans. B* 28 (1997) 169–173. <https://doi.org/10.1007/s11663-997-0139-7>
- [47] J.P. Gu, C. Beckermann, A.F. Giamei, Motion and remelting of dendrite fragments during directional solidification of a nickel-base superalloy, *Metall. Mater. Trans. A* 28 (1997) 1533–1542. <https://doi.org/10.1007/s11661-997-0215-2>
- [48] B. Appolaire, H. Combeau, G. Lesoult, Modeling of equiaxed growth in multicomponent alloys accounting for convection and for the globular/dendritic morphological transition, *Mater. Sci. Eng. A.* 487 (2008) 33–45. <https://doi.org/10.1016/j.msea.2007.11.030>
- [49] A. Kumar, M. Založnik, H. Combeau, G. Lesoult, A. Kumar, Channel segregation during columnar solidification: Relation between mushy zone instability and mush permeability, *Int. J. Heat Mass Transf.* 164 (2021) 120602. <https://doi.org/10.1016/j.ijheatmasstransfer.2020.120602>
- [50] M. Seredyński, J. Banaszek, Coupled enthalpy-porosity and front tracking approach to modeling chemical inhomogeneity in solidifying metal alloys. *Int. J. Heat Mass Transf.* 173 (2021) 121221. <https://doi.org/10.1016/j.ijheatmasstransfer.2021.121221>
- [51] A. Ludwig, M. Stefan-Kharicha, A. Kharicha, M. Wu, Massive formation of equiaxed crystals by avalanches of mushy zone segments, *Metall. Mater. Trans. A* 48 (2017) 2927–2931. <https://doi.org/10.1007/s11661-017-4008-y>



## **Paper 4**

### **Solidification principle in large vertical steel casting under the EMS effect**

Zhao Zhang, Menghuai Wu, Haijie Zhang, Susanne Hahn,  
Franz Wimmer, Andreas Ludwig, Abdellah Kharicha

Metallurgical and Materials Transactions B

Under review



## Solidification principle in large vertical steel casting under the EMS effect

Zhao Zhang <sup>a</sup>, Menghuai Wu <sup>a,\*</sup>, Haijie Zhang <sup>a</sup>, Susanne Hahn <sup>b</sup>, Franz Wimmer <sup>b</sup>, Andreas Ludwig <sup>a</sup>, Abdellah Kharicha <sup>a</sup>

<sup>a</sup> Chair of Simulation and Modelling of Metallurgical Processes, Department of Metallurgy, University of Leoben, Franz-Josef Street 18, A-8700 Leoben, Austria

<sup>b</sup> Primetals Technologies Austria GmbH, Turmstrasse 44, A-4031 Linz, Austria

\*Corresponding author: menghuai.wu@unileoben.ac.at

**Abstract:** The surging demand for large high-quality rotor shafts or similar steel components in heavy industries (energy sector) poses new challenges to steelmakers. Based on the experience of conventional ingot and continuous casting, several new process concepts have been proposed, e.g., vertical continuous casting (VCC), semi-continuous casting (SCC), and segment casting (SC), but none of them are optimally put in operation. The main problems include the control of the as-cast structure and macrosegregation. Electromagnetic stirring (EMS) is necessary to obtain the center equiaxed zone, but EMS-induced multiphase flow can cause severe macrosegregation and uneven distribution of the as-cast structure between equiaxed and columnar. In this study, an advanced mixed columnar-equiaxed solidification model was used to investigate the formation of the as-cast structure and macrosegregation in an example of SCC with a large format (diameter 1 m). The main role of EMS is to create crystal fragments by fragmentation, which is regarded in this work as the only origin of equiaxed grains. The created equiaxed grains are brought by the EMS-induced (primary and secondary) flow and gravity-induced sedimentation to the central/lower part of the casting. The main goal of this study was to understand the solidification principle of SCC. In addition, a numerical parameter study by varying the EMS parameters was also performed to demonstrate the model capability towards the process optimization of SCC.

**Keywords:** Large vertical steel casting; As-cast structure; Macrosegregation; Semi-continuous casting.

## 1. Introduction

The surging demand for large high-quality rotor shafts or similar steel components in heavy industries (energy sector) poses new challenges to steelmakers. The initial form of these components is usually made by casting, but solidification takes an extremely long time, which consequently leads to internal quality problems such as macrosegregation and centerline shrinkage porosity. The existing casting technologies do not work properly for these components. For example, conventional ingot casting (IC) is limited by its length or height, whereas the established continuous casting method (CC) is restricted to a certain cross-section size. Therefore, several new process concepts have recently been proposed, including vertical continuous casting (VCC) <sup>[1-3]</sup>, semi-continuous casting (SCC) <sup>[4-6]</sup> and segment casting (SC) <sup>[7-8]</sup>. Their principal idea is to combine the advantages of both IC and CC, while eliminating their corresponding limitations. As schematically shown in **Figure 1**, the hot melt was poured into a water-cooled mold and the as-solidified shell was withdrawn from the mold vertically to a certain length and height. Then, the as-filled and partially solidified casting was left to cool down for the liquid core to solidify. Following the CC technique, the withdrawing (pouring) process can be efficiently controlled by the implementation of a submerged entry nozzle (SEN) for mold filling, water-cooled mold, and secondary cooling (air or water spray) for shell formation and electromagnetic stirring (EMS) for flow and superheat dissipation. Following the IC technique, when the as-filled and partially solidified casting is put aside for the remaining solidification, further measures can be implemented, such as thermal or electric hot topping, shielding or isolating, and even EMS, to control the shrinkage porosity, potential cracks, as-cast structure, and macrosegregation.

VCC, SCC, and SC differ from each other in their technical details, but a common feature is the application of EMS. Depending on the installed positions, as shown in **Figure 1**, different types of EMS are used, that is, mold-EMS (M-EMS) and strand-EMS (S-EMS). The final EMS (F-EMS) can also be used for VCC <sup>[1, 3]</sup>, but not for SCC and SC. The role of M-EMS is to control the mold flow and superheat dissipation, thereby influencing the rest of the solidification <sup>[9-15]</sup>. The role of S-EMS is to promote a center equiaxed zone <sup>[16-17]</sup>. The S-EMS induces a special flow pattern in the liquid core; the flow interacts with the advancing solidification front and creates crystal fragments via a fragmentation <sup>[18-19]</sup>; in this work the crystal fragments serve as the main (or only) source of the equiaxed crystals; they are finally brought by the S-EMS-induced flow to the casting center to form the equiaxed zone. The principal idea of S-



EMS is simple; however, its industrial implementation is difficult. The flow induced by S-EMS is multiphasic, and the flow-solidification interaction in front of the solidification mushy zone is complex. Under what conditions are crystal fragments created, and what is the fragmentation rate and its dependency on the flow intensity? S-EMS-induced flow leads to a white band [14, 20]. It is also known that the settling equiaxed crystals leads to a sedimentation-induced macrosegregation [21]. S-EMS is a double-edged sword: favorably, it extends the center equiaxed zone, but the macrosegregation induced by or related to the S-EMS-induced multiphase flow is troublesome. This is the reason why none of the above new process concepts are effectively put into operation. Owing to the harsh environment, it is impossible to observe the solidification process and conduct parametric studies based on field experiments.

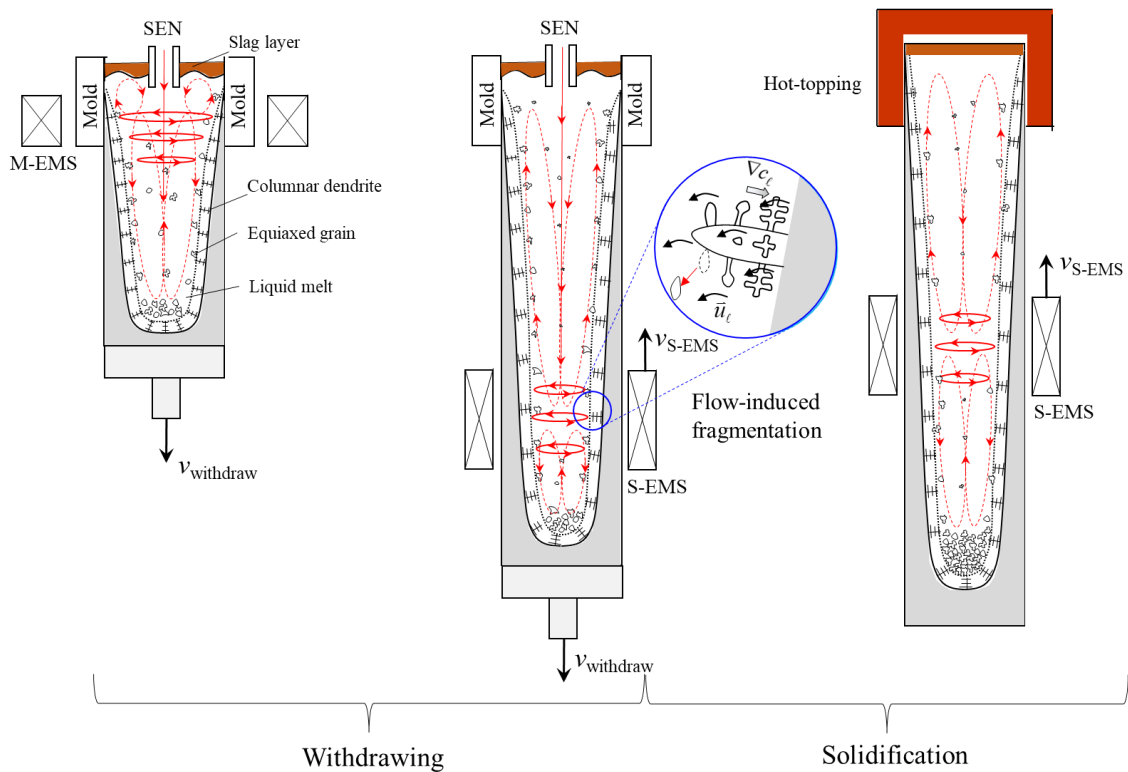


Fig. 1—Schematic of processes for large vertical steel casting.

Numerical modeling is an effective way to study the solidification principles of new processes. Michelic et al. [17] used the ProCAST software to simulate the SC process. As ProCAST is only used for the simulation of the fluid flow of a mixture phase, a relatively rough simulation result (temperature field and profile of the solid shell) was obtained. No as-cast structures or macrosegregations were observed. For a large-section VCC, Zhang et al. [2] used a CAFE model to predict the as-cast structure. Although a similar distribution of the as-cast structure between

the simulation and measurement was claimed to be obtained, the most obvious drawback of this model is that the transport of equiaxed grains, which is extremely important to the solidification process, was ignored. Additionally, the distribution of the macrosegregation of the strand has not been studied. Zhang et al. [22] used the thermal solver in ProCAST to calculate the temperature field and growth of the solid shell and used a CAFE model to calculate the solidification structure. As mentioned before, simplifying the multiphase nature as a mixed phase weakens the capability of the model. Recently, Yao et al. [23] used a three-phase columnar-equiaxed solidification model to simulate the effect of steel strip feeding on the solidification process in the VCC of a round bloom. They found that an increase in the feeding ratio promoted columnar-to-equiaxed transition (CET) and reduced macrosegregation. However, the fragmentation phenomenon, which is crucial for the formation of the central equiaxed zone, was ignored.

To study the solidification principle in large vertical steel casting, a three-phase mixed columnar-equiaxed solidification model, as proposed by Wu et al. [24], was recently extended for flow-induced fragmentation [25] and remelting/destruction of equiaxed grains [26]. The extended model was verified in a steel billet continuous casting, where M-EMS was applied [27]. The current study used the same model for solidification in a large vertical steel casting. As an example, a SCC that includes withdrawing and solidification processes is referred. Both the M-EMS and S-EMS were considered. The final goal is to understand the solidification principle behind the SCC and explore the optimal SCC process via a parameter study.

## 2. Model description and simulation settings

### 2.1 Solidification model

A three-phase mixed columnar-equiaxed solidification model [24, 28–30] was used to investigate the solidification process of the casting. The three phases include liquid melt ( $\ell$ ), equiaxed grains (e), and columnar dendrites (c). Both the liquid melt and equiaxed grains are treated as moving phases, for which the corresponding Navier–Stokes equations are solved for their velocities ( $\bar{u}_\ell, \bar{u}_e$ ). The columnar dendrites are assumed as a rigid phase. However, the position of the columnar tip front is traced dynamically based on the Lipton–Glicksman–Kurz (LGK) model [31]. Simple morphologies for the two solid phases are assumed: cylinders for columnar trunks and spheres for equiaxed grains. To deal the drag force and other hydrodynamic interactions between phases, a dendritic envelop ( $f_e^{\text{env}}$ ) is considered for equiaxed grains. The volume

ratio of the solid ‘dendrite’ to the dendritic envelop is defined as  $f_{si}$  ( $= f_c / f_c^{env}$ ), which was determined by a parameter study. A so-called effective equiaxed viscosity ( $\mu_e$ ), which increases with  $f_c^{env}$ , is used to model the interaction between the equiaxed grains [32]. When  $f_c^{env}$  reaches the packing limit  $f_{c,packing}$ , a rigid network of equiaxed grains is built. Additionally, the equiaxed grains can be captured by the columnar dendrites and fixed there when the local volume fraction of the columnar phase ( $f_c$ ) is above a critical value ( $f_c^{free}$ ). A diffusion-governed growth kinetic is considered to treat the solidification for both solid phases. The difference between the equilibrium and volume-averaged liquid concentrations ( $c_\ell^* - c_\ell$ ) serves as the driving force for the solidification. Remelting of equiaxed grains is also considered [26]. To characterize the macrosegregation, the segregation index is defined:  $c_{mix}^{index} = (c_{mix} - c_0) \times 100 / c_0$ , where  $c_{mix}$  is the mixture concentration with  $c_{mix} = (f_\ell \rho_\ell c_\ell + f_e \rho_e c_e + f_c \rho_c c_c) / (f_\ell \rho_\ell + f_e \rho_e + f_c \rho_c)$ . The governing equations of the model are summarized in **Table I**. The description of the source terms and the exchange terms have been detailed elsewhere [24, 30].

**Table I.** Governing equations of the three-phase columnar-equiaxed solidification model.

Governing equations	Symbols
1. Mass conservations:	
$\frac{\partial}{\partial t}(f_\ell \rho_\ell) + \nabla \cdot (f_\ell \rho_\ell \vec{u}_\ell) = -M_{\ell e} - M_{\ell c}$ (1)	$f_\ell, f_e, f_c$ , volume fraction [-]
$\frac{\partial}{\partial t}(f_e \rho_e) + \nabla \cdot (f_e \rho_e \vec{u}_e) = M_{\ell e} + M_{ce}$ (2)	$\rho_\ell, \rho_e, \rho_c$ , density [kg m <sup>-3</sup> ] $\vec{u}_\ell, \vec{u}_e$ , velocity vector [m s <sup>-1</sup> ]
$\frac{\partial}{\partial t}(f_c \rho_c) = M_{\ell c} - M_{ce}$ (3)	$M_{\ell e}, M_{\ell c}, M_{ce}$ , net mass transfer rate [kg m <sup>-3</sup> s <sup>-1</sup> ]
$f_\ell + f_e + f_c = 1$ (4)	
2. Momentum conservations:	
$\frac{\partial}{\partial t}(f_\ell \rho_\ell \vec{u}_\ell) + \nabla \cdot (f_\ell \rho_\ell \vec{u}_\ell \otimes \vec{u}_\ell) =$ (5)	$\vec{\tau}_\ell$ , stress-strain tensors [kg m <sup>-1</sup> s <sup>-1</sup> ] $p$ , pressure [N m <sup>-2</sup> ]
$-f_\ell \nabla p + \nabla \cdot \vec{\tau}_\ell + f_\ell \rho_\ell \vec{g}'_\ell + f_\ell \vec{F}' - \vec{U}_{\ell e} - \vec{U}_{\ell c}$	$\vec{g}, \vec{g}'_\ell$ gravity and deduced gravity [m s <sup>-2</sup> ]
$\frac{\partial}{\partial t}(f_e \rho_e \vec{u}_e) + \nabla \cdot (f_e \rho_e \vec{u}_e \otimes \vec{u}_e) =$ (6)	$\rho_\ell^b$ , density for buoyancy force [kg m <sup>-3</sup> ] $\rho_\ell^{ref}$ , reference density [kg m <sup>-3</sup> ]
$-f_e \nabla p + \nabla \cdot \vec{\tau}_e + f_e \rho_e \vec{g} + f_e \vec{F}' + \vec{U}_{\ell e} + \vec{U}_{ce}$	$T^{ref}$ , reference temperature [K] $c^{ref}$ , reference concentration [-]
$\vec{g}'_\ell = \frac{\rho_\ell^b(T, c_\ell) - \rho_\ell^{ref}}{\rho_\ell^{ref}} \vec{g}$ (7)	$\beta_T$ , thermal expansion coefficient [K <sup>-1</sup> ]
$\rho_\ell^b(T, c_\ell) = \rho_\ell^{ref} \cdot (1 + \beta_T \cdot (T^{ref} - T_\ell) + \beta_c \cdot (c^{ref} - c_\ell))$ (8)	$\beta_c$ , solutal expansion coefficient [wt.% <sup>-1</sup> ]
	$\vec{U}_{\ell e}, \vec{U}_{\ell c}, \vec{U}_{ce}$ , momentum exchange rate [kg m <sup>-2</sup> s <sup>-2</sup> ] $\vec{F}'$ , modified Lorentz force [N m <sup>-3</sup> ]

---

### 3. Species conservations:

---

$$\frac{\partial}{\partial t}(f_\ell \rho_\ell c_\ell) + \nabla \cdot (f_\ell \rho_\ell \bar{u}_\ell c_\ell) = \quad (9) \quad c_\ell, c_e, c_c, \text{ species concentration [-]}$$

$$\nabla \cdot (f_\ell \rho_\ell D_\ell \nabla c_\ell) - C_{\ell e} - C_{\ell c} \quad D_\ell, D_e, D_c, \text{ diffusion coefficient [m}^2 \text{ s}^{-1}\text{]}$$

$$C_{\ell e}, C_{\ell c}, C_{ce}, \text{ species exchange rate [kg m}^{-3} \text{ s}^{-1}\text{]}$$

$$\frac{\partial}{\partial t}(f_e \rho_e c_e) + \nabla \cdot (f_e \rho_e \bar{u}_e c_e) = \quad (10)$$

$$\nabla \cdot (f_e \rho_e D_e \nabla c_e) + C_{\ell e} + C_{ce}$$

$$\frac{\partial}{\partial t}(f_c \rho_c c_c) = \nabla \cdot (f_c \rho_c D_c \nabla c_c) + C_{\ell c} - C_{ce} \quad (11)$$

### 4. Enthalpy conservations:

---

$$\frac{\partial}{\partial t}(f_\ell \rho_\ell h_\ell) + \nabla \cdot (f_\ell \rho_\ell \bar{u}_\ell h_\ell) = \quad (12)$$

$$\nabla \cdot (f_\ell k_\ell \nabla T_\ell) - Q_{\ell e} - Q_{\ell c} \quad h_\ell, h_e, h_c, \text{ enthalpy [J kg}^{-1}\text{]}$$

$$T_\ell, T_e, T_c \text{ temperature [K]}$$

$$\frac{\partial}{\partial t}(f_e \rho_e h_e) + \nabla \cdot (f_e \rho_e \bar{u}_e h_e) = \quad (13)$$

$$\nabla \cdot (f_e k_e \nabla T_e) + Q_{\ell e} + Q_{ce} \quad k_\ell, k_e, k_c \text{ thermal conductivity [W m}^{-1} \text{ K}^{-1}\text{]}$$

$$Q_{\ell e}, Q_{\ell c}, Q_{ce}, \text{ energy exchange rate [J m}^{-3} \text{ s}^{-1}\text{]}$$

$$\frac{\partial}{\partial t}(f_c \rho_c h_c) = \nabla \cdot (f_c k_c \nabla T_c) + Q_{\ell c} - Q_{ce} \quad (14)$$

### 5. Electromagnetic field

---

$$\vec{B} = \mu_0 \mu_r \vec{H} \quad (15) \quad \vec{B}, \text{ magnetic flux density [T]}$$

$$\nabla \times \vec{E} = -\frac{\partial \vec{B}}{\partial t} \quad (16) \quad \vec{B}^*, \text{ conjugate magnetic flux density [T]}$$

$$\vec{H}, \text{ magnetic field intensity [A m}^{-1}\text{]}$$

$$\vec{J} = \sigma \vec{E} \quad (17) \quad \mu_0, \text{ magnetic permeability in vacuum [T m A}^{-1}\text{]}$$

$$\vec{F} = \frac{1}{2} R_c (\vec{J} \times \vec{B}^*) \quad (18) \quad \mu_r, \text{ relative magnetic permeability [-]}$$

$\vec{E}$ , electric field intensity [V m<sup>-1</sup>]  
 $\vec{J}$ , induced current density [A m<sup>-2</sup>]  
 $\sigma$ , electrical conductivity [ $\Omega^{-1} \text{ m}^{-1}$ ]  
 $\vec{F}$ , time-averaged Lorentz force [N m<sup>-3</sup>]  
 $R_c$ , the real part of a complex number [-]

---

\*Superscripts and subscripts  $\ell$ ,  $e$ , and  $c$  indicate the different phases.

Another important phenomenon, i.e., the origin of equiaxed grains by dendrite fragmentation, is noteworthy. Here, flow-induced dendrite fragmentation [25, 33] is regarded as the only source of equiaxed grains. Heterogenous nucleation appears to be insignificant in such a large vertical steel ingot; hence, it is ignored. The production rate of the number density of fragments  $N_{\text{frag}}$ , that is, the source of equiaxed grains, is calculated as:

$$N_{\text{frag}} = \frac{M_{ce}}{\rho_c \cdot \frac{\pi}{6} (d_{e,\text{frag}}^0)^3}, \quad (19)$$

where  $M_{ce}$  is the net mass transfer rate from columnar dendrites to equiaxed grains via fragmentation.

$$M_{ce} = -\gamma \cdot (\bar{u}_\ell - \bar{u}_c) \cdot \nabla c_\ell \cdot \rho_c. \quad (20)$$

Crystal fragmentation depends on the relative velocity ( $\bar{u}_\ell - \bar{u}_c$ ) and the liquid concentration gradient ( $\nabla c_\ell$ ). All other factors contributing to fragmentation, such as the curvature effect of the dendrites, latent heat-induced thermal fluctuation, and diffusion in the interdendritic melt, are included in the single fragmentation coefficient  $\gamma$ .

## 2.2 Numerical simulation procedure for the SCC

SCC includes two stages: Stage I, withdrawing, and Stage II, solidification. In the real withdrawing process, the mold system, including the submerged entry nozzle (SEN), mold, and M-EMS, is stationary, whereas the as-solidified shell is continuously withdrawn with the casting speed ( $v_{\text{withdraw}}$ ). To model the flow and solidification during the withdrawing stage, the calculation domain, i.e., a region with a liquid melt and a solidified shell, must be treated as a dynamically increasing domain. This type of system is not feasible for the Eulerian solver on which the solidification model is based. Therefore, as shown in **Figure 2**, a unique numerical procedure is used to mimic the withdrawing process. The entire domain of the casting ( $\phi$  1.0 m  $\times$  10 m) is considered in a stationary reference frame. It is assumed that the entire calculation domain is initially filled with steel melt (no flow) at the pouring temperature (1801.15 K). The calculation domain is set stationary while the entire mold system (SEN, mold, and M-EMS) moves at the speed of  $-v_{\text{withdraw}}$ . Meanwhile, the thermal boundary conditions in the different cooling zones (**Figure 2**) move up correspondingly. In particular, a so-called pseudo-slag-SEN region is set as a rigid material and has the initial temperature of the steel melt. As the entire calculation domain is fixed, the upward movement of the pseudo slag-SEN region pushes the steel melt in the upper part of the domain and forces the melt to flow into the lower part of the domain through the SEN. When the mold system and pseudo slag-SEN region reach the top of the calculation domain, i.e., the casting reach the target length (10 m), the withdrawing process terminates, which marks the beginning of the next stage (solidification). During the solidification stage,  $v_{\text{withdraw}}$  is set to zero, and the S-EMS can be applied.

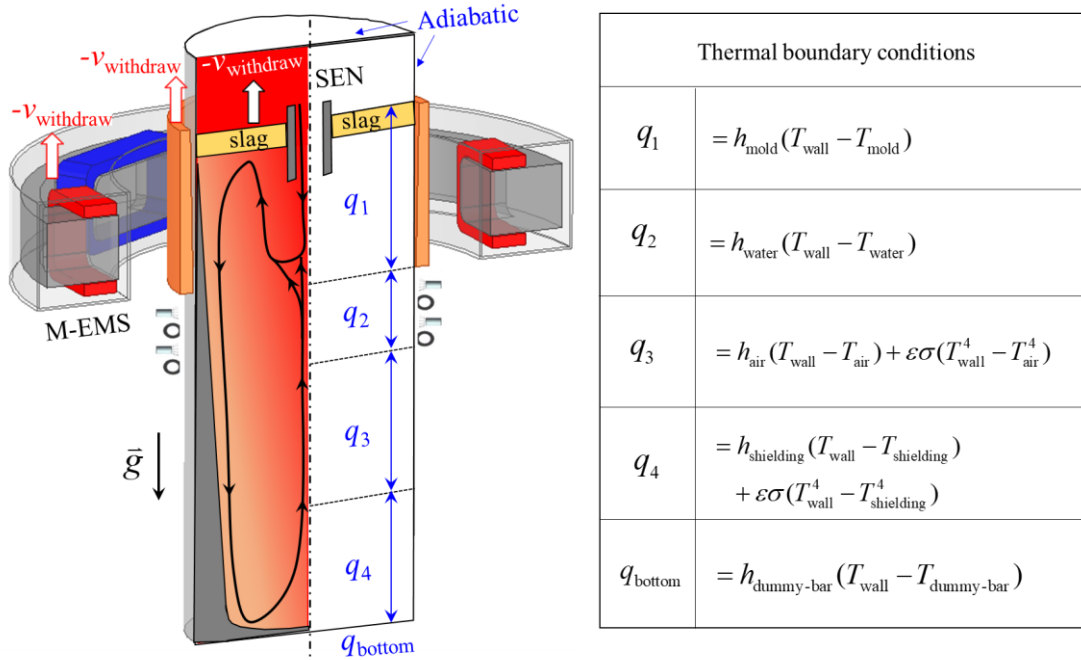


Fig. 2—Configuration of the computation domain of the SCC during the withdrawing process. Left half shows the numerical treatment of withdrawing process; right half marks different cooling zones (thermal boundary conditions).

The convective heat transfer boundary condition (**Figure 2**) is used for the bottom and lateral walls of the strand, and the adiabatic boundary condition is used for the domain above the pseudo slag-SEN region. For commercial reasons, exact values of the boundary conditions are omitted here. The melt was assumed to be incompressible with a constant density. Despite this assumption, thermal-solutal convection is included in the numerical model with a Boussinesq approximation. A no-slip flow boundary condition is applied to the melt and equiaxed grains along the walls. The industrial alloy is a multicomponent (Fe-C-Si-Mn-Cr-Mo), but here it is simplified as a binary alloy of Fe-0.415 wt. %C. The material properties and process parameters are presented in **Table II**.

**Table II.** Material properties and process parameters.

Property/parameters	Symbol	Units	Values
<b>Thermodynamic properties</b>			
Melting point of pure iron	$T_f$	K	1805.15
Liquidus slope	$m$	K (wt. %) <sup>-1</sup>	-91.56
Nominal concentration of alloy	$c_0$	wt. %	0.415
Liquidus temperature with nominal concentration	$T_L$	K	1766.15
Equilibrium partition coefficient	$k$	-	0.283
<b>Thermophysical properties</b>			
Reference density	$\rho_l, \rho_c, \rho_c$	kg m <sup>-3</sup>	7024.0

Liquid-equiaxed density difference	$\Delta\rho$	kg m <sup>-3</sup>	150.0
Thermal expansion coefficient	$\beta_T$	K <sup>-1</sup>	$1.8 \times 10^{-4}$
Solutal expansion coefficient	$\beta_C$	(wt. %) <sup>-1</sup>	$1.4 \times 10^{-2}$
Primary dendritic arm spacing	$\lambda_1$	m	$2.52 \times 10^{-4}$
Secondary dendritic arm spacing	$\lambda_2$	m	$1.4 \times 10^{-5}$
Diffusion coefficient in liquid	$D_\ell$	m <sup>2</sup> s <sup>-1</sup>	$2.0 \times 10^{-8}$
Latent heat	$L$	J kg <sup>-1</sup>	$2.35 \times 10^5$
Specific heat	$c_p^l, c_p^s, c_p^c$	J (kg K) <sup>-1</sup>	850.0
Thermal conductivity	$k_\ell, k_e, k_c$	W(m K) <sup>-1</sup>	34.5, 31.5, 31.5
Viscosity	$\mu_\ell$	Pa s	$5.7 \times 10^{-3}$
Gibbs-Thomson coefficient	$\Gamma$	m K	$2.92 \times 10^{-7}$
<b>Process parameters</b>			
Casting speed	$v_{\text{withdraw}}$	m/s	$1.5 \times 10^{-3}$
Strand diameter	$D$	m	1.0
Calculated strand length	$H$	m	10.0
Effective mold length	$H_m$	m	0.6
Pouring temperature	$T_p$	K	1801.15
<b>EMS parameters</b>			
Current intensity of M-EMS	$I_m$	A	800.0
Current frequency of M-EMS	$f_m$	Hz	1.5
Coil turns of M-EMS	$n_m$	-	82.0
Current intensity of S-EMS	$I_s$	A	800.0
Current frequency of S-EMS	$f_s$	Hz	2.0
Coil turns of S-EMS	$n_s$	-	62.0
<b>Modeling parameters</b>			
Solid fraction in the dendrite envelope	$f_{si}$	-	0.3
Packing limit for equiaxed grains	$f_{e,\text{packing}}$	-	0.637
Critical $f_c$ for free moving equiaxed grains	$f_c^{\text{free}}$	-	0.2
CET criterion	$f_c^{\text{CET}}$	-	0.49
Fragmentation coefficient	$\gamma$	-	$1.0 \times 10^{-7}$

The multiphase flow was solved using the commercial solver ANSYS Fluent. The solidification model described in §2.1 was coded in the solver using user-defined functions (UDFs). The electromagnetic fields, that is, Maxwell equations owing to the effect of M-EMS and S-EMS, were solved based on the ANSYS Maxwell software, which is separated from the flow-solidification solver. Therefore, a unique coupling scheme was applied between the EMS and flow-solidification solvers. First, two full-scale inductors (**Figure 3**) were built. The electromagnetic fields (M-EMS and S-EMS) were calculated using the ANSYS Maxwell software by assuming a stationary melt. The time-averaged Lorentz force ( $\bar{F}$ ) was then exported and interpolated into the flow-solidification solver ANSYS Fluent. To consider the interaction between

the flow and electromagnetic field, a correction to the Lorentz force in the tangential direction ( $F_\theta$ ) was made:

$$F'_\theta = F_\theta \left(1 - \frac{u_\theta}{2\pi f \cdot r}\right), \quad (21)$$

where  $u_\theta$  denotes the tangential velocity of the moving phases (liquid and equiaxed),  $f$  denotes the frequency of the applied current, and  $r$  denotes the radial coordinate. Then, the modified Lorentz force ( $\bar{F}'$ ) was weighted by the corresponding phase volume fraction ( $f_l \bar{F}'$ ,  $f_c \bar{F}'$ ) and finally served as the source terms for the momentum conservation equations of each phase through the UDFs. This coupling method has been verified in previous studies [27, 34].

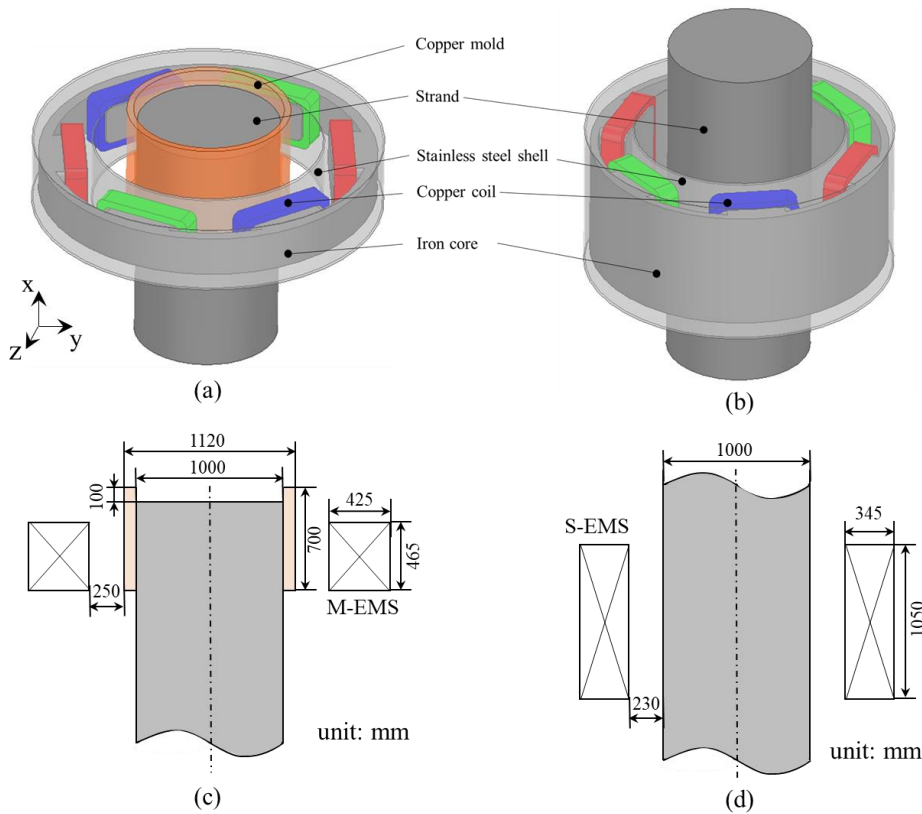


Fig. 3—Settings of the M-EMS (a) and S-EMS (b); and their dimensions and relative positions (c)-(d).

A full-scale three-dimensional (3D) geometry with a tetrahedral mesh (mesh size of 50 mm) was used for the M-EMS and S-EMS calculations. Both 3D and 2D-axisymmetric simulations were performed for the flow and solidification calculations. Because the 3D calculation is highly time-consuming, only a small part of the casting ( $\phi 1.0 \text{ m} \times 3 \text{ m}$ ) was calculated with a relatively coarse mesh to analyze the 3D flow pattern and the corresponding solidification



process. The calculation of the full-scale casting ( $\phi$  1.0 m  $\times$  10 m) was conducted with relatively-fine mesh based on the 2D-axisymmetric geometry. The averaged hexahedral mesh size for the 3D flow and solidification simulation was 24 mm (local mesh near the strand wall and center were refined to ca. 7.5 mm), and the average size of 12.5 mm (local mesh near the strand wall and center were refined to ca. 5 mm) for the 2D-axisymmetric simulation was utilized. The conservation equations for the current multiphase solidification model were iteratively solved using ANSYS Fluent with a time step of 0.005 s. One 2D-axisymmetry calculation ( $\phi$  1.0 m  $\times$  10 m) required 60 days, and one 3D calculation ( $\phi$  1.0 m  $\times$  3 m) required 15 days on a high-performance cluster (2.6 GHz, 28 cores).

### 3. Results

#### 3.1 Global flow pattern and solidification

The typical 3D flow pattern and solidification results during withdrawaling (1500 s) of the SCC casting process are shown in **Figure 4**. The effect of M-EMS on the flow and solidification was analyzed. As depicted in **Figures 4(a.1)** and **(a.2)**, the maximal Lorentz force appears at the casting wall and decreases exponentially towards the casting center. A quantitative analysis of the Lorentz forces ( $|\bar{F}|$ ,  $|\bar{F}'|$ ,  $|f_\ell \bar{F}'|$ ,  $|f_e \bar{F}'|$ ) along the casting radius (Line 1 in **Figure 4(a.2)**) is presented in **Figure 4(a.3)**.  $|\bar{F}|$  and  $|\bar{F}'|$  are the same within the solid shell, where the liquid tangential velocity ( $u_\theta$ ) is zero (**Equation (21)**). In the mushy zone and bulk liquid region, the Lorentz force can be reduced by 29.1 % at the columnar tip front because of the slip motion between the liquid and magnetic field, i.e.,  $|\bar{F}'| = 0.709 |\bar{F}|$ .  $|\bar{F}'|$  is further partitioned among different phases in accordance with their individual volume fractions, that is,  $|f_\ell \bar{F}'|$  and  $|f_e \bar{F}'|$ , as shown in **Figure 4(a.3)**. The liquid flow ( $\bar{u}_\ell$ ) under the M-EMS is depicted by the vector in **Figure 4(b)**. A rotating flow (primary flow) of up to a magnitude of 1.31 m/s is generated near the solidification front. The rotating flow induces a secondary flow. The jet flow coming from a five-port SEN further complicates the liquid flow in the casting. A streamline is shown in **Figure 4(c)** to demonstrate the complexity of the flow pattern of the liquid melt. The jet flow coming from the bottom port of the SEN is reversed and returns to the upper mold region. It then rotates and flows downward along the columnar solidification front. Finally, it returns to the M-EMS region along the center of the casting. Under the effect of such a forced flow, crystal fragments are generated in the mushy zone, especially in the area where M-EMS is operative

(Figure 4(d)). The simultaneous solidification/remelting phenomenon of equiaxed grains at different positions inside the casting is observed, as shown in Figure 4(e). As shown in Figure 4(f), the remelting of the columnar dendrites is negligible, whereas the solidification rate of the columnar dendrites is much larger than that of the equiaxed grains. The distribution of  $f_e$  is shown in Figure 4(g). Further details regarding the solidification process are presented in § 3.2.

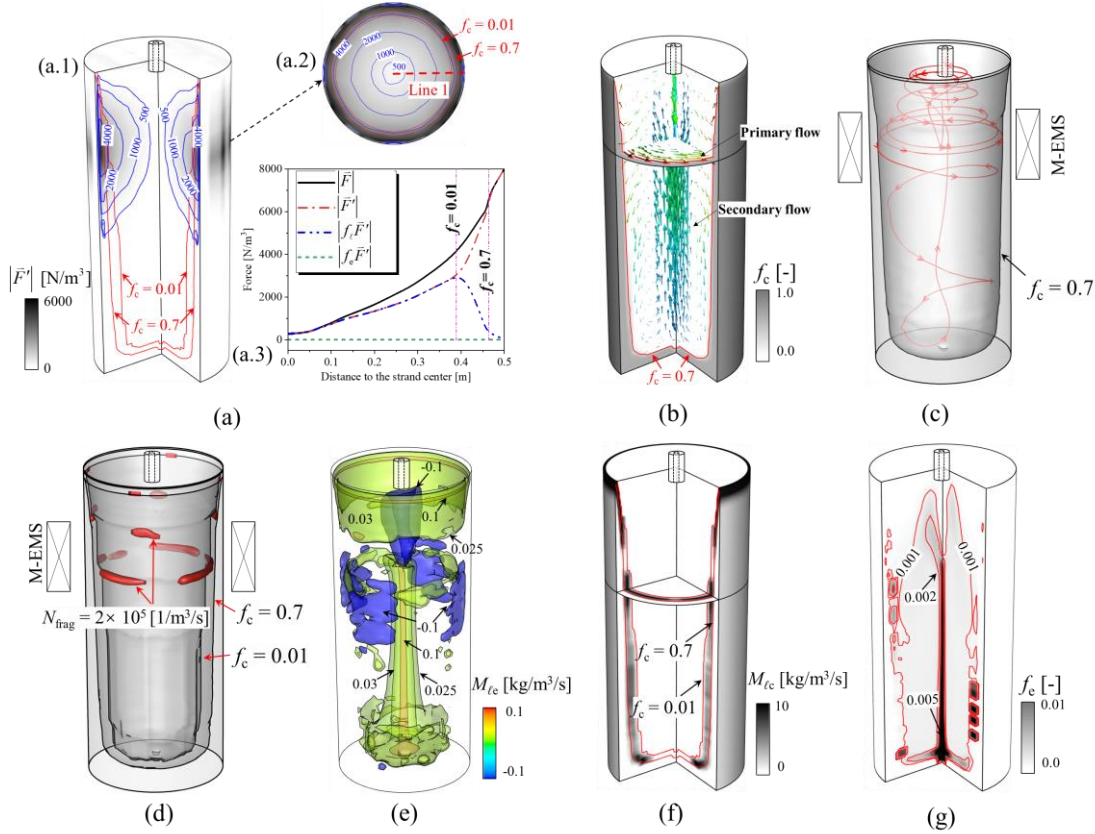


Fig. 4—3D flow pattern and solidification results of the casting during withdrawal (3 m in height) at 1500 s. (a.1) Distribution of the modified Lorentz force ( $|\vec{F}'|$ ); (a.2) distribution of  $|\vec{F}'|$  on the plane 0.55 m below the meniscus; (a.3) profiles of the Lorentz forces ( $|\vec{F}|$ ,  $|\vec{F}'|$ ,  $|f_l \vec{F}'|$ ,  $|f_e \vec{F}'|$ ) along the radius (Line 1 in (a.2)) of the casting; (b) contour of  $f_c$  overlaid by  $\vec{u}_t$  to show the primary/secondary flow induced by M-EMS; (c) one streamline of the liquid melt to demonstrate the flow pattern, the iso-surface of  $f_c = 0.7$  is drawn to show the shape of the solid shell; (d) one iso-surface of  $N_{\text{frag}} = 2 \times 10^{-5}$  [1/m<sup>3</sup>/s] to show the distribution of the created fragments in the mushy zone (confined between two iso-surfaces of  $f_c = 0.01$  and  $f_c = 0.7$ ); (e) different iso-surfaces of  $M_{tc}$  to show the net mass transfer rate between liquid melt and equiaxed grains with positive for solidification and negative for remelting; (f) net mass transfer rate between liquid melt and columnar dendrites ( $M_{tc}$ ); (g) volume fraction of the equiaxed grains  $f_e$ .

The 3D results were obtained from a calculation with a coarse mesh. A 2D-axisymmetric simulation with a fine mesh was also performed, and the 3D and 2D results are compared in Figure 5. It is verified that the 2D simulation can well replicate the 3D simulation in terms of

the flow pattern, profile of the solid shell ( $f_c = 0.7$ ), and temperature field (isoline 1762 K). The main difference between them is that the jet flow coming from the bottom port of the SEN goes deeper in the 2D-axisymmetric simulation (**Figure 5(a)–(b)**). The inertial impact coming from the bottom jet of the SEN is forced to concentrate on the axis by the model for the case of the 2D-axisymmetric simulation; in the 3D simulation, the SEN bottom jet has more freedom; hence, it is stopped earlier by the M-EMS. The maximal liquid velocity ( $|\bar{u}_{t-\max}|$ ) of 2D-axisymmetric simulation is also overestimated by 14.5 % comparing to the 3D simulation.

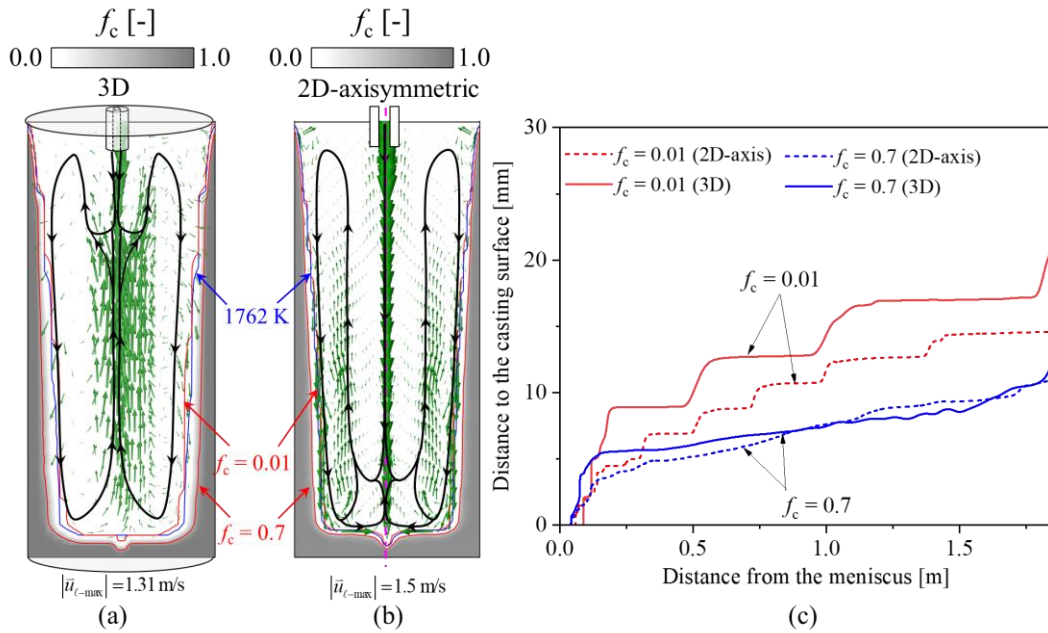


Fig. 5—Comparisons of the simulation results between the (a) 3D and (b) 2D-axisymmetric simulations. (a) Contour of  $f_c$  on the central longitudinal section of the casting overlaid by  $\bar{u}_t$  in green vectors. Two red iso-lines of  $f_c = 0.01$  and  $f_c = 0.7$  are drawn to show the position of the solidification front, and the thickness of the shell. The blue iso-line is for  $T = 1762 \text{ K}$ , and the black streamline is to show the liquid flow pattern on the section; (b) same results as (a) but of the 2D-axisymmetric calculation (one half section is mirrored from the other); (c) profiles of the thickness of the solid shell/mushy zone of the two cases.

The thickness of the solid shell ( $f_c = 0.7$ ) and the position of the solidification front ( $f_c = 0.01$ ) for the two cases are compared in **Figure 5(c)**. The profiles of the solid shell of the 3D and 2D models agree well with each other, whereas the position of the solidification front is overestimated by the 3D model. Owing to the limitation of the computational capacity (hardware), the full 3D calculation can only be completed for the early withdrawing stage ( $\phi 1.0 \text{ m} \times 3 \text{ m}$ ). Thus, for the entire casting ( $\phi 1.0 \text{ m} \times 10 \text{ m}$ ) including both Stage I (withdrawing) and II (solidification), the simulation has to be performed in 2D-axisymmetry. According to the

current 2D-3D comparison, the qualitative nature of the solidification process can be verified, but the quantitative modeling results need to be further evaluated. Therefore, the modeling results presented in the following sections are sufficient for the analysis of the solidification principle, and they may not be referred to as quantitative results for a real SCC casting process.

### 3.2 Solidification in Stage I

#### 3.2.1 Early stage of withdrawing under the effect of M-EMS

Some modeling results of the SCC process at the early stage of the withdrawing stage ( $t = 1500$  s) under M-EMS are presented in **Figure 4**, but a more detailed analysis is presented in **Figure 6**. As depicted in **Figure 6(a)**, under the combined effect of the M-EMS and SEN jet flow, the liquid flows downward along the solidification front and strand center, and these two downward flows drive an upward flow along the middle-radius region of the casting. A solidified shell of a certain thickness is formed owing to the intensive cooling of the copper mold. The solid shell thickness progressively increases during the withdrawing process (**Figure 4(f)** and **6(b)**). The solute partition at the solid-liquid interface during the solidification process leads to a liquid concentration gradient ( $\nabla c_\ell$ ) opposite to the growth direction of the columnar dendritic mushy zone. When the  $\bar{u}_\ell$  and  $\nabla c_\ell$  point in the opposite direction (the angle between them is larger than  $90^\circ$ , e.g., the blue region in **Figure 6(c)**), the interdendritic flow tends to increase the local liquid concentration ( $c_\ell$ )<sup>[27]</sup>. This causes remelting of the columnar dendrites, and thereby the formation of fragments. The contour of the fragmentation rate  $N_{\text{frag}}$  is shown in **Figure 6(d)**. Fragments are mainly produced in the mushy zone near the columnar tip front. According to the 3D calculation in **Figure 4(d)**, the maximal  $N_{\text{frag}}$  is located in the M-EMS-operated region. These fragments operate as the origin of the equiaxed grains. The newly formed equiaxed grains grow and sediment to the casting bottom along the solidification front (**Figure 6(e)**). Most of the equiaxed grains accumulate at the bottom of the casting, while some are transported to the upper mold region by the liquid flow along the middle-radius region of the casting. As shown in **Figure 6(f)**, the equiaxed grains further solidify in the undercooled melt (yellow region in **Figure 6(f)**), and re-melting of the equiaxed grains occurs in the superheated region (blue region in **Figure 6(f)**). The 3D-view of the solidification/remelting process of the equiaxed grains is shown in **Figure 4(e)**. The equiaxed grains decrease in size because of remelting. Once the size class of the equiaxed grains decreases to the critical grain size value

( $d_{c,critical}$ ), the equiaxed grains are destroyed (**Figure 6(g)**). The transient distribution of  $f_e$  is shown in **Figure 6(h)**. Most equiaxed grains accumulate at the bottom of the casting. In the upper center of the casting, no equiaxed grains can survive the superheat.

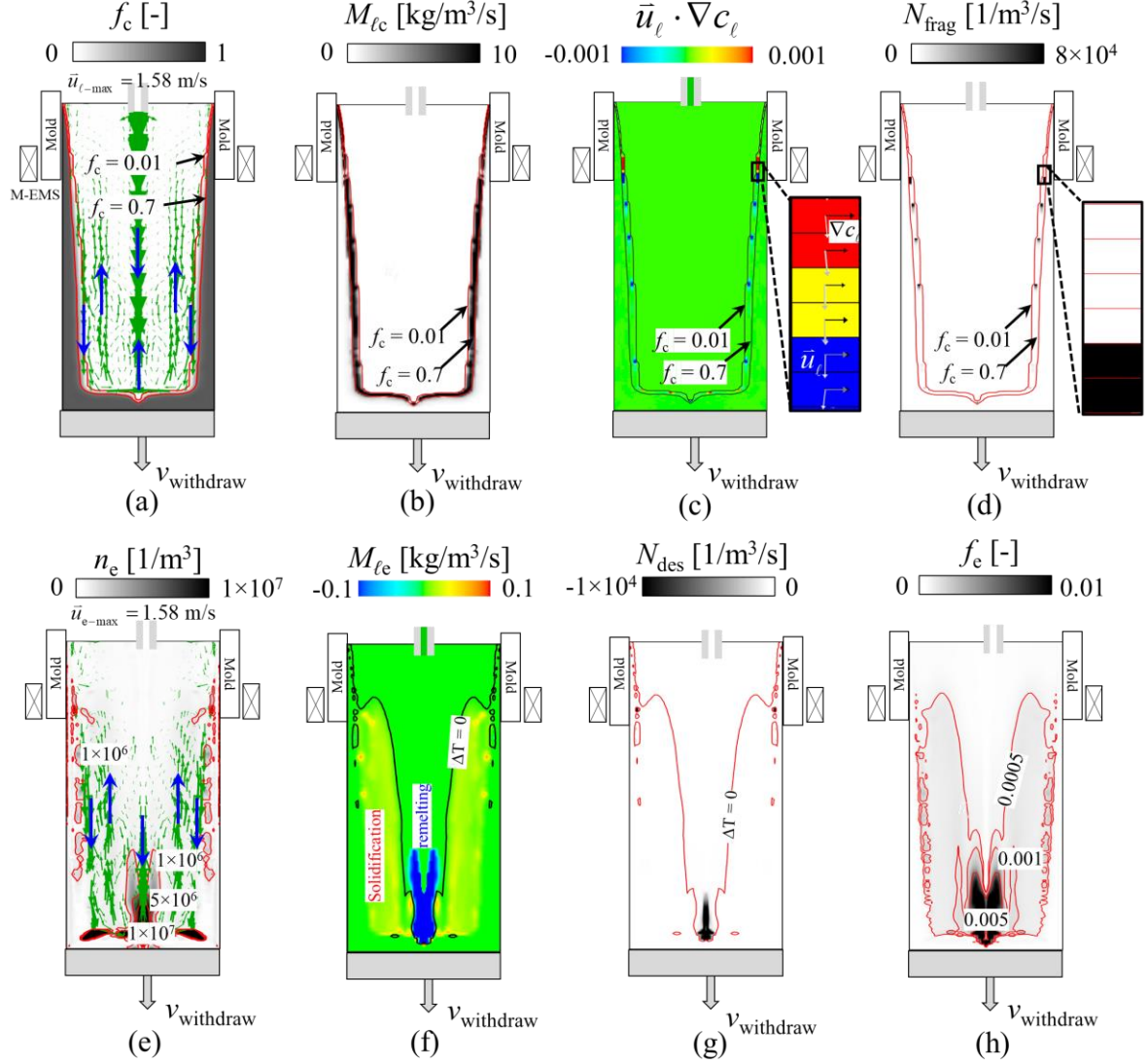


Fig. 6—Solidification results during the early stage of Stage I of a SCC at  $t = 1500$  s. (a) Contour of  $f_c$  overlaid by vectors of  $\bar{u}_l$ , and two isolines are drawn to define the position of the columnar tip front ( $f_c = 0.01$ ) and solid shell ( $f_c = 0.7$ ); (b)  $M_{l_c}$ ; (c) contour of the term  $\bar{u}_l \cdot \nabla c_l$  with red for positive value and blue for negative value; (d)  $N_{frag}$ ; (e) contour of number density of equiaxed grains  $n_e$  overlaid by vectors of  $\bar{u}_e$ ; (f)  $M_{l_e}$  with red for solidification and blue for remelting, and the isoline of  $\Delta T = 0$  is used to distinguish the superheated and undercooled regions; (g) destruction rate of equiaxed grains  $N_{des}$ ; (h)  $f_e$ .

### 3.2.2 Late stage of withdrawing under the effect of S-EMS

During the late stage of withdrawing (at 3000 s), the M-EMS is turned off, followed by the activation of the S-EMS. The S-EMS is installed at a start position of 0.5 m above the casting bottom, but it moves upward at a predefined speed of  $7.9 \times 10^{-4}$  m/s relative to the casting. The solidification results at the late stage of the withdrawing ( $t = 5500$  s), when the strand is withdrawn to a length of 8.25 m, are depicted in **Figure 7**. The front of the solidification mushy zone further advances towards the casting center (**Figure 7(a)**). The S-EMS-driven primary rotating flow induces a meridional flow (secondary flow). As shown by the red rectangle in **Figure 7(a)**, the liquid melt flows away from the center of the stirrer to the top and bottom of the casting along the solidification front and then returns to the stirred area along the central area of the casting. Thus, upper and lower recirculation loops are formed in the liquid core (**Figure 7(a)**). To show more solidification phenomena occurring in the stirred area, zoomed-in views of the simulation results in Zone A (the red rectangle) of **Figure 7(a)** are displayed in **Figure 7(b)–(i)**. In the mushy zone, a positive value of  $M_{\ell c}$  indicates mass transfer from the liquid melt to the columnar dendrites due to solidification (**Figure 7(b)**), which is accompanied by the release of latent heat and rejection of the solute. The contour of the liquid velocity ( $|\bar{u}_{\ell}|$ ) is shown in **Figure 7(c)**. The maximal  $|\bar{u}_{\ell}|$  ( $|\bar{u}_{\ell-\max}| = 1.96$  m/s) appears at the solidification front near the center of the stirrer. The thickness of the solid shell is shown to be 0.18 m at the stirrer center. Under the effect of S-EMS, columnar dendrites are fragmented near the front of the mushy zone (**Figure 7(d)**). Given birth by these fragments, the equiaxed grains grow and sediment to the casting bottom along the solidification front (**Figure 7(e)**). Additionally, some equiaxed grains can be brought back to the S-EMS region along the middle-radius region of the casting by the lower recirculation loop. Without the M-EMS, the S-EMS can change the flow pattern dramatically, thereby modifying the superheated region in the liquid core. The jet flow is accelerated by the upper recirculation loop. A large amount of superheated melt is transported from the bottom port of the SEN to the lower part of the casting. The superheated region is extended to the stirred area, as shown in **Figure 7(f)**. Some equiaxed grains are re-melted (blue region in **Figure 7(f)**) in the superheated melt, while others continue to solidify (yellow region in **Figure 7(f)**) in the undercooled liquid. The remelting process is followed by grain destruction, as shown in **Figure 7(g)**. The distribution of  $f_{\ell}$  is shown in **Figure 7(h)**. Compared with the results of the early withdrawing at 1500 s (**Figure 6(h)**),  $f_{\ell}$  has increased from 1 % to 5 %. The solidification of the columnar/equiaxed grains rejects the solute element into the liquid. As

depicted in **Figure 7(i)**, a slight negative macrosegregation ( $c_{\text{mix}}^{\text{index}} = -6\%$ ) is formed in the as-solidified shell, and the liquid in the center is enriched with solute. Those regions with negative macrosegregation are sometimes referred to as the ‘white band’ owing to the stirring effect of M-EMS and S-EMS.

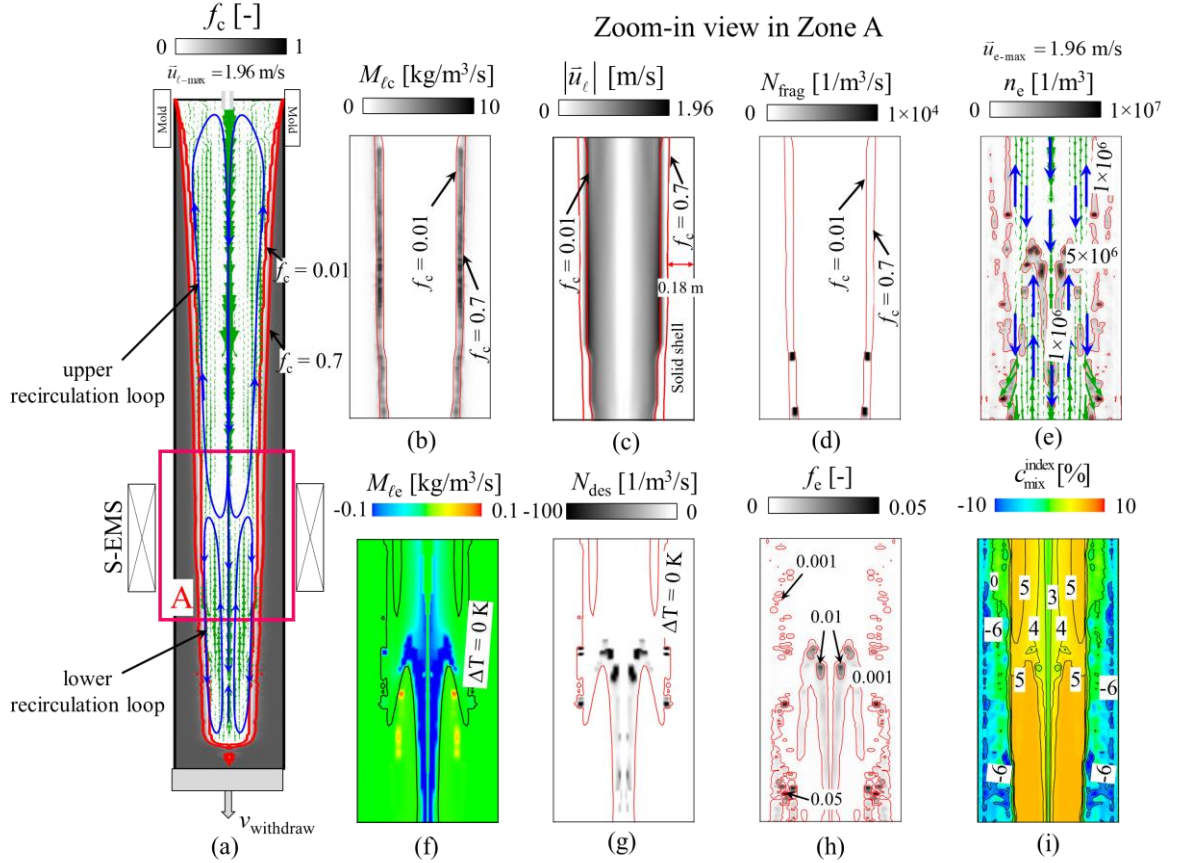


Fig. 7—Solidification results during the late stage of Stage I of a SCC at  $t = 5500$  s. (a) Contour of  $f_c$  overlaid by vectors of  $\vec{u}_\ell$ . Two isolines are drawn for  $f_c = 0.01$  and  $f_c = 0.7$ . The solidification results in the S-EMS stirred area, as marked by the red rectangle A in (a) are shown in (b)-(i); (b)  $M_{lc}$ ; (c) contour of  $|\vec{u}_\ell|$ ; (d)  $N_{\text{frag}}$ ; (e) contour of  $n_e$  overlaid by vectors of  $\vec{u}_\ell$ ; (f)  $M_{lc}$ , and the isoline of  $\Delta T = 0$  is drawn to distinguish the superheated and undercooled regions; (g)  $N_{\text{des}}$ ; (h)  $f_c$ ; (i)  $c_{\text{mix}}^{\text{index}}$ .

### 3.3 Solidification in Stage II

Stage II, the solidification process, marks the termination of the withdrawing process. During this stage, the moving S-EMS operates continuously at a speed of  $7.9 \times 10^{-4}$  m/s, but two additional measures, i.e., hot-topping and shielding, are applied. This requires the adaptation of thermal boundary conditions in the corresponding boundary zones. A summary of the solidification results at 9500 s during Stage II is shown in **Figure 8**. The solidification principle at this stage is similar to the late stage of withdrawing under the effect of S-EMS (**Figure 7**). The

solidification rate, especially in the top region of the casting, is significantly reduced using hot-topping and shielding methods. With the S-EMS slowing approaching the top end of the casting, the upper recirculation loop is compressed (shortened), whereas the lower recirculation loop is elongated (**Figure 8(a)**). The solid shell grows gradually towards the casting center (**Figure 8(b)**), and the shell thickness develops to ca. 0.28 m at the stirrer center area (**Figure 8(c)**). Because of the increase in the shell thickness, the maximal  $|\bar{u}_\ell|$  ( $|\bar{u}_{\ell-\max}| = 1.0$  m/s) is decreased by 48.9 % near the solidification front (**Figure 8(c)**) compared to the result at 5500 s (**Figure 7(c)**). The fragmentation rate is also decreased (**Figure 8(d)**).

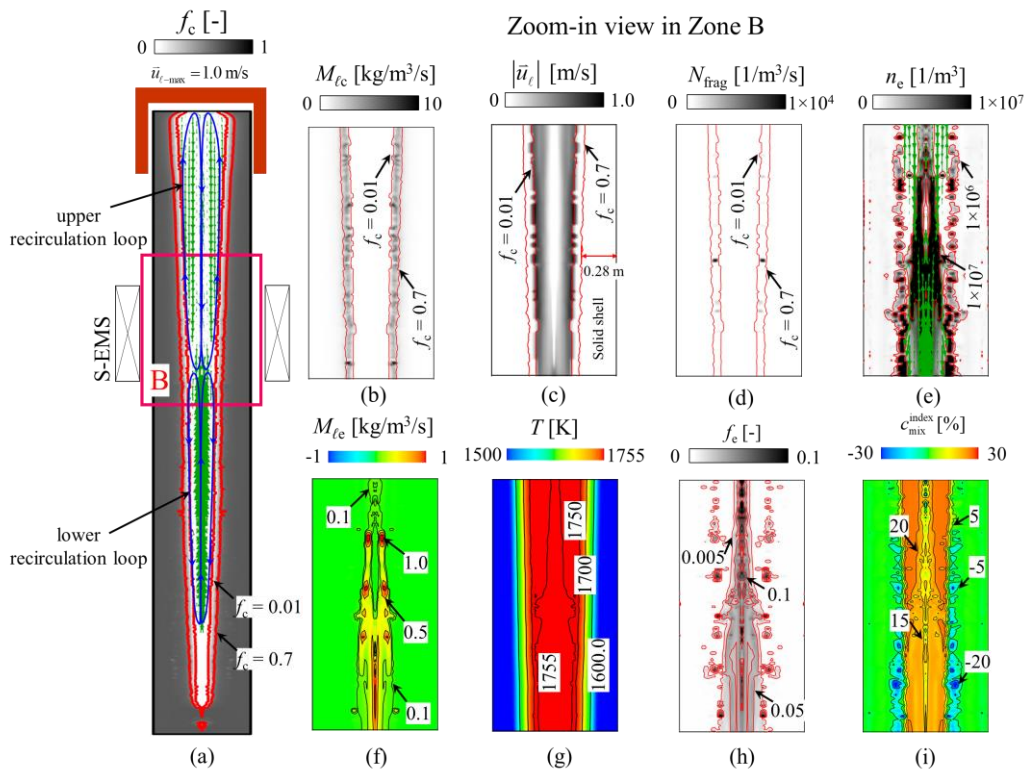


Fig. 8—Solidification results during Stage II of a SCC at  $t = 9500$  s. (a) Contour of  $f_c$  overlaid by vectors of  $\bar{u}_\ell$ , and two isolines are drawn for  $f_c = 0.01$  and  $f_c = 0.7$ . Zoom-in views of the solidification results in the S-EMS stirred area, as marked by the red rectangle B in (a) are shown in (b)-(i). (b)  $M_{fc}$ ; (c) contour of  $|\bar{u}_\ell|$ ; (d)  $N_{frag}$ ; (e) contour of  $n_c$  overlaid by vectors of  $\bar{u}_\ell$ ; (f)  $M_{fc}$ ; (g) temperature field  $T$ ; (h)  $f_c$ ; (i)  $c_{mix}^{index}$ .

Under the effect of S-EMS, the equiaxed grains in the lower part of the casting are transported to the stirred area by the melt flow along the casting center (**Figure 8(e)**). Because the superheat has been fully dissipated in the liquid core, that is,  $T_{\max} < T_L$ , as shown in **Figure 8(g)**, no remelting and destruction of the equiaxed grains occurs. Solidification of the equiaxed grains



can be observed in both the mushy zone and central liquid pool (**Figure 8(f)**), and most of the equiaxed grains are accumulated in the center of the casting (**Figure 8(h)**). Because the equiaxed grains have a relatively lower solute concentration, mixing the solute-enriched melt (from the upper part of the casting) with the solute-depleted equiaxed grains (from the lower part of the casting) with the S-EMS-induced flow is beneficial for homogenizing the solute element in the casting center (**Figure 8(i)**). Additionally, a trail of negative segregation (white band) is observed in the as-solidified shell, which is caused by the stirring effect of the S-EMS.

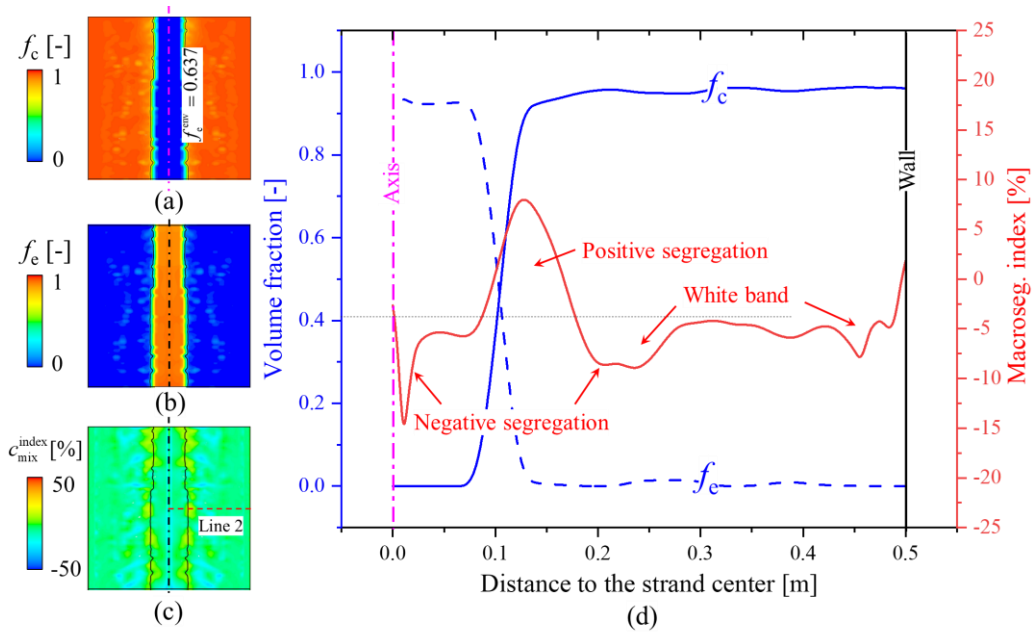


Fig. 9—As-cast structure and macrosegregation in the local area (1.5 ~ 2.5 m from the strand bottom) of the strand. (a)  $f_c$ ; (b)  $f_c$ ; (c)  $c_{\text{mix}}^{\text{index}}$ . (d) profiles of the phase distributions and  $c_{\text{mix}}^{\text{index}}$  along the radius of the strand (Line 2 in (c.2)).

The solidification process is completed at the end of Stage II. A relatively uniform distribution of the as-cast structure and macrosegregation can be achieved, except for the starting and hot-top ends of the strand. The zoomed-in views of the final simulation results in a local area (1.5 m ~ 2.5 m from the strand bottom) are shown in (**Figure 9 (a) – (c)**). Equiaxed grains are formed in the center of the strand (**Figure 9 (b)**), and columnar dendrites are primarily developed in the outer radius region of the strand (**Figure 9 (a)**). A relatively uniform distribution of the macrosegregation index ( $c_{\text{mix}}^{\text{index}}$ ) is observed (**Figure 9 (c)**). The simulation results along Line 2 in **Figure 9 (c)** are shown in **Figure 9 (d)**. Negative segregation is observed in the central equiaxed zone, and positive segregation is observed at the border of the columnar zone. In the columnar zone, two trails of the ‘white band’ (negative segregation), as caused by the S-

EMS and M-EMS, are found in the positions of 0.23 and 0.45 m to the strand center, respectively. This segregation intensity, oscillating in a range between  $\pm 15\%$  of  $c_{\text{mix}}^{\text{index}}$  across the casting section, should fall within the tolerance of most engineering applications of such large steel strands.

#### 4. Discussion

SCC for large steel strands is still in its conception stage, and no experimental results are available to validate the current simulation results. This might have shed some doubt on the modeling results, especially in terms of their quantitative accuracy. It is true that the presented modeling results can only be used to analyze the solidification principle of such large steel strands under the effects of M-EMS and S-EMS. Further experimental evaluation is required to use the current model to design an actual SCC process. For example, some modeling parameters ( $\gamma$ ,  $f_{\text{si}}$ ,  $f_{\text{e,packing}}$ ,  $f_{\text{c}}^{\text{free}}$ , and  $f_{\text{e,CET}}$ ) were assigned based on previous studies. Some of them ( $f_{\text{e,packing}}$ ,  $f_{\text{c}}^{\text{free}}$ ,  $f_{\text{e,CET}}$ ) have been verified for steel ingots and steel continuous castings [21, 24, 27–30, 35]; some of them ( $\gamma$ ,  $f_{\text{si}}$ ) are more sensitive to cast alloys and casting processes [25, 27, 33, 35]. Hence, they should be determined via numerical parameter studies based on sufficient experimental findings. Other points worth mentioning are (1) the limited computation capacity, which does not allow for a full 3D simulation of the whole strand (10 m) with sufficient mesh resolution, and (2) the process parameters of the SCC used in the current model, which have not been verified experimentally.

Despite the above mentioned uncertainties regarding the quantitative accuracy of the modeling results referring to the special processes of SCC, the three-phase mixed columnar-equiaxed solidification model [24, 30] has been validated by the authors for steel ingots of different sizes [29, 36]. After recent extensions for considering the crystal fragmentation [25] and EMS [27, 34], it was successfully used to ‘reproduce’ the laboratory solidification experiments as carried out in Grenoble based on Sn-10wt. % Pb alloy [37–38]. In these solidification experiments, EMS with different configurations of the travelling magnetic field were applied. The same model was also successfully validated for steel billet casting using M-EMS [27, 35].

As the model has been validated and the solidification principle in SCC has been clearly described, if the aforementioned uncertain modeling parameters ( $\gamma$ ,  $f_{\text{si}}$ ) are determined experimentally, the model can be applied to design and optimize the SCC process. To demonstrate such model capability, a numerical parameter study is performed to investigate the

effect of S-EMS moving schemes on the as-cast structure and macrosegregation. Two additional simulations (Cases I and II) are conducted, as shown in **Figure 10**.

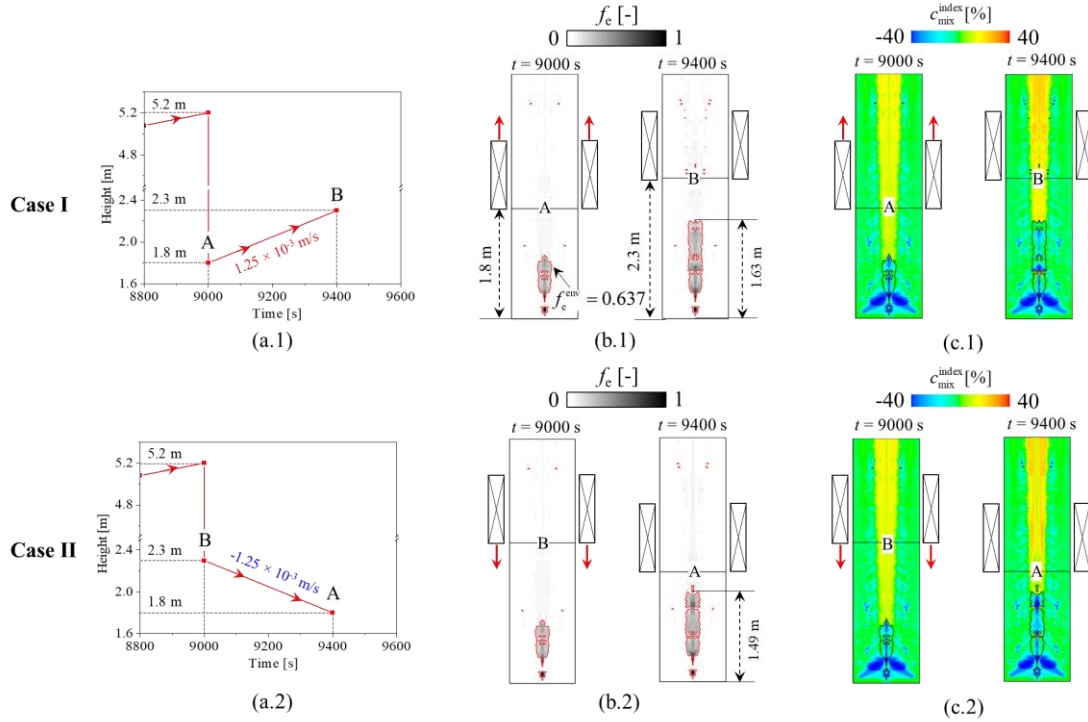


Fig. 10—Parameter study on the S-EMS moving scheme and its influence on the as-cast structure and macrosegregation: Case I – upward motion of S-EMS; Case II – downward motion of S-EMS. (a.1)-(a.2): Definition of the moving schemes of the S-EMS; (b.1)-(b.2): contours of  $f_e$  overlaid with the isoline of  $f_e^{env} = 0.637$  at 9000 s and 9400 s; (c.1)-(c.2) contours of  $c_{mix}^{index}$  at 9000 s and 9400 s.

These two simulations are based on the results of the previous simulation (§ 3.), that is, the calculation results at 9000 s are used as the initial conditions. Different from the previous simulation, the S-EMS is translated from its previous position (ca. 5.2 m above the casting bottom at 9000 s) to lower positions of 1.8 m (Case I) and 2.3 m (Case II), respectively. For Case I, as shown in **Figure 10 (a.1)**, the S-EMS moves upward from Point A (1.8 m) to Point B (2.3 m) at a speed of  $1.25 \times 10^{-3}$  m/s relative to the strand. For Case II, as shown in **Figure 10 (a.2)**, the S-EMS moves downward from Point B (2.3 m) to Point A (1.8 m) at a speed of  $-1.25 \times 10^{-3}$  m/s relative to the strand. All other settings for the two cases are the same as before. The calculated  $f_e$  values at two moments (9000 s and 9400 s) for Cases I and II are shown in **Figure 10 (b.1)** and **(b.2)**. The isoline for  $f_e^{env} = 0.637$  is overlaid on the contours to mark the equiaxed region. At 9400 s, the height of the equiaxed zone is 1.63 m for Case I, which is 0.14 m higher than that of Case II. It appears that the upward movement scheme of S-EMS (Case I) is more beneficial for the accumulation of equiaxed grains at the casting center compared to

Case II. The calculated  $c_{\text{mix}}^{\text{index}}$  values for the two cases are shown in **Figure 10 (c.1) and (c.2)**.

Case I seems to exhibit a more uniform solute distribution in the casting than Case II.

It is known that the moving scheme of the S-EMS is only one factor among several others which can influence the casting quality, such as the stirring intensity S-EMS, the timing of the S-EMS, even the type of S-EMS (travelling vs. rotational), with or without combination with the M-EMS, casting temperature/speed, dimension (diameter) and maximum length of the strand, hot topping and shielding parameters, and alloy composition. Without a model that can quantitatively predict the solidification process, it would be extremely exhausting to design and optimize a new SCC process. Therefore, as an outlook, experimental evaluations of the numerical model are suggested, and on this basis, uncertain modeling parameters can be determined. Finally, the model can be used to perform systematic parameter studies, instead of costly pilot/field-casting trials, towards the optimization of the SCC process.

## 5. Conclusion

A three-phase mixed-columnar-equiaxed solidification model was used to investigate the solidification principle (formation of the as-cast structure and macrosegregation) of large vertical steel casting under the effect of EMS. For this purpose, the model was extended by considering crystal fragmentation as the only origin of equiaxed grains and the remelting/destruction of equiaxed grains. As an example, a semi-continuous casting (SCC) of steel with a format of  $\phi 1.0 \text{ m} \times 10.0 \text{ m}$  was simulated. It was shown that the following critical solidification phenomena can be captured by the model.

- 1) With the application of EMS, crystal fragments, serving as the origin of equiaxed grains, are generated in the mushy zone near the columnar tip front of the stirred area. They can grow and be brought by the EMS-induced primary/secondary flow and gravity-induced sedimentation to the lower part of the casting, forming the central equiaxed zone.
- 2) During the withdrawing stage (Stage I) of the SCC, some equiaxed grains were transported to the upper mold region owing to the effect of M-EMS, where the liquid melt was still superheated. Equiaxed grains can be re-melted or destroyed in the superheated region. The simultaneous solidification/remelting phenomenon represents an important energy/species transport mechanism in such large castings.

- 3) During the late withdrawing process, when M-EMS is stopped and S-EMS is activated, the superheated region is enlarged under the effect of S-EMS, and the remelting process can occur even in the lower part of the casting.
- 4) During the solidification process (Stage II), the entire superheat was dissipated from the casting. Thus, no remelting/destruction of equiaxed grains occurred. The equiaxed grains survived and accumulated in the central and lower parts of the casting.

Although the solidification principle of the SCC process has been successfully addressed, the current model is still subject to further experimental evaluation. Some uncertain modeling parameters must be determined and confirmed experimentally before the model can be applied to design and optimize the actual SCC process. Finally, the capability of the model for process optimization was demonstrated. A numerical parameter study on the moving scheme of S-EMS and its effect on the as-cast structure and macrosegregation was performed. According to the current settings of the SCC, the upward movement of S-EMS seems favorable for the formation of central equiaxed grains and is beneficial for a relatively uniform solute distribution in comparison to the downward movement of S-EMS.

## 6. Acknowledgements

The authors acknowledge the financial support from the Austria Research Promotion Agency (FFG) through the Bridge 1 project (No. 868070) as well as the technical support of the industrial partner Primetals Technologies Austria GmbH.

## 7. Conflict of Interest

On behalf of all authors, the corresponding author states that there is no conflict of interest.

## 8. Reference

- [1] H. Wu, C. Xu, C. Lei, T. Wang, Y. Gao, X. Zhang and H. Jin: *JOM*, 2022, pp. 1–11.
- [2] L. Zhang, Z. Wang, C. Xu, S. Li, X. Ai and J. Li: *Ironmaking Steelmaking*, 2019, vol. 46, pp. 742–46.
- [3] H. Wu, C. Xu, H. Jin, Y. Gao, X. Zhang and Y. Jin: *Appl. Phys. A*, 2022, vol. 128, pp. 1–9.
- [4] J. Penn, P. Pennerstorfer and A. Jungbauer: *Berg Huettenmaenn. Monatsh.*, 2018, vol. 163, pp.11–

17.

- [5] S. Lee: *Berg Huettenmaenn. Monatsh.*, 2018, vol. 163, pp. 3–10.
- [6] A. Eichinger, H. Kogler, A. Puehringer, G. Hrazdera, S. Hahn and F. Wimmer: *9<sup>th</sup> Eur. Contin. Cast. Conf., Vienna, Austria*, 2017, pp. 267–76.
- [7] S. Michelic and M. Riedler: *Berg Huettenmaenn. Monatsh.*, 2016, vol. 161, pp. 39–44.
- [8] M. Knabl, K. von Eynatten, M. Kubin, A. Scheriau and H. Holzgruber: *Berg Huettenmaenn. Monatsh.*, 2018, vol. 163, pp. 355–60.
- [9] W. Zhang, S. Luo, Y. Chen, W. Wang and M. Zhu: *Metals*, 2019, vol. 9, pp. 66.
- [10] Q. Fang, H. Ni, B. Wang, H. Zhang and F. Ye: *2017: Metals*, 2017, vol. 7, pp. 72.
- [11] L. Trindade, J. Nadalon, A. Contini and R. Barroso: *Steel Res. Int.*, 2017, vol. 88, pp. 1600319.
- [12] B. Ren, D. Chen, H. Wang, M. Long and Z. Han: *Ironmaking Steelmaking*, 2015, vol. 42, pp. 401–08.
- [13] H. An, Y. Bao, M. Wang and L. Zhao: *Metall. Res. Technol.*, 2018, vol. 115, pp.12.
- [14] S. Kunstreich: *Metall. Res. Technol.*, 2003, vol. 100, pp. 1043–61.
- [15] H. Wu, N. Wei, Y. Bao, G. Wang, C. Xiao and J. Liu: *Int. J. Miner. Metall. Mater.*, 2011, vol. 18, pp. 159–64.
- [16] X. Li, X. Wang, Y. Bao, J. Gong, W. Pang and M. Wang: *JOM*, 2020, vol. 72, pp. 3628–33.
- [17] C. Yao, M. Wang, Y. Ni, J. Gong, L. Xing, H. Zhang and Y. Bao: *JOM*, 2022, vol. 74, pp. 4823–30.
- [18] T. Campanella, C. Charbon and M. Rappaz: *Metall. Mater. Trans. A*, 2004, vol. 35, pp. 3201–10.
- [19] H. Zhang, M. Wu, C.M.G. Rodrigues, A. Ludwig, A. Kharicha, A. Rónaföldi, A. Roósz, Z. Veres and M. Svéda: *Acta Mater.*, 2022, vol. 241, pp. 118391.
- [20] M. Bridge and G. Roger: *Metall. Mater. Trans. B*, 1984, vol. 15, pp. 581–89.
- [21] M. Wu, L. Könözy, A. Ludwig, W. Schützenhöfer and R. Tanzer: *Steel Res. Int.*, 2008, vol. 79, pp. 56–63.
- [22] J. Zhang, C. Xu, L. Zhang, Y. Jin and C. Lei: *Can. Metall. Q.*, 2021, vol. 60, pp. 350–58.
- [23] Y. Yao, Z. Liu, B. Li, L. Xiao and Y. Gan: *J. Mater. Res. Technol.*, 2022, vol. 20, pp. 1770–85.
- [24] M. Wu and A. Ludwig: *Metall. Mater. Trans. A*, 2006, vol. 37, pp. 1613–31.
- [25] Y. Zheng, M. Wu, A. Kharicha and A. Ludwig: *Modell. Simul. Mater. Sci. Eng.*, 2018, vol. 26, pp. 015004.
- [26] H. Zhang, M. Wu, P. Schumacher, C.M.G. Rodrigues, A. Ludwig and A. Kharicha: *Appl. Math. Modell.*, 2021, vol. 97, pp. 821–38.
- [27] Z. Zhang, M. Wu, H. Zhang, S. Hahn, F. Wimmer, A. Ludwig and A. Kharicha: *J. Mater. Process. Technol.*, 2022, vol. 301, pp. 117434.
- [28] M. Wu and A. Ludwig: *Metall. Mater. Trans. A*, 2007, vol. 38 A, pp. 1465–75.

- [29] J. Li, M. Wu, A. Ludwig and A. Kharicha: *Int. J. Heat Mass Transfer*, 2014, vol. 72, pp. 668–79.
- [30] M. Wu, A. Ludwig and A. Kharicha: *Metals*, 2019, vol. 9, pp. 229.
- [31] J. Lipton, M.E. Glicksman and W. Kurz: *Mater. Sci. Eng.*, 1984, vol. 65, pp. 57–63.
- [32] A. Ludwig and M. Wu: *Metall. Mater. Trans. A*, 2002, vol. 33, pp. 3673–83.
- [33] Y. Zheng, M. Wu, E. Karimi-Sibaki, A. Kharicha and A. Ludwig: *Int. J. Heat Mass Transfer*, 2018, vol. 122, pp. 939–53.
- [34] H. Zhang, M. Wu, Z. Zhang, A. Ludwig, A. Kharicha, A. Rónaföldi, A. Roósz, Z. Veres and M. Svéda: *Metall. Mater. Trans. B*, 2022, vol. 53, pp. 2166–81.
- [35] Z. Zhang, M. Wu, H. Zhang, A. Ludwig and A. Kharicha: *Steel Res. Int.*, 2022, vol. 93, pp. 2200065.
- [36] M. Wu, A. Ludwig and A. Kharicha: *Steel Res. Int.*, 2018, vol. 89, pp. 1700037.
- [37] L. Hachani, K. Zaidat and Y. Fautrelle: *Int. J. Heat Mass Transfer*, 2015, vol. 85, pp. 438–54.
- [38] Z. Zhang, M. Wu, H. Zhang, A. Ludwig and A. Kharicha: *Int. J. Heat Mass Transfer*, 2022, submitted, in review.





## **Paper 5**

# **Experimental evaluation of MHD modeling of EMS during continuous casting**

Haijie Zhang, Menghuai Wu, Zhao Zhang, Andreas Ludwig, Abdellah Kharicha,  
Arnold Rónaföldi, András Roósz, Zsolt Veres, Mária Svéda

Metallurgical and Materials Transactions B

Volume 53B, 2022, pp. 2166–2181.



# Experimental Evaluation of MHD Modeling of EMS During Continuous Casting



HAIJIE ZHANG, MENGHUAI WU, ZHAO ZHANG, ANDREAS LUDWIG, ABDELLAH KHARICHA, ARNOLD RÓNAFÖLDI, ANDRÁS ROÓSZ, ZSOLT VERES, and MÁRIA SVÉDA

Electromagnetic stirring (EMS) has been recognized as a mature technique in steel industry to control the as-cast structure of steel continuous casting (CC), and computational magnetohydrodynamic (MHD) methods have been applied to study the EMS efficiency. Most MHD methods de-coupled the calculations of electromagnetic and flow fields or simplifications were made for the flow–electromagnetic interactions. However, the experimental validations of the MHD modeling have been rarely reported or very limited. In this study, we present a benchmark, *i.e.*, a series of laboratory experiments, to evaluate the MHD methods, which have been typically applied for steel CC process. Specifically, a rotating magnetic field (RMF) with variable intensity and frequency is considered. First experiment is performed to measure the distribution of magnetic field without any loaded sample (casting); the second experiment is conducted to measure the RMF-induced torque on a cylindrical sample (different metals/alloys in solid state); the third experiment is (based on a special device) to measure the RMF-induced rotational velocity of the liquid metal (Ga75In25), which is enclosed in a cylindrical crucible. The MHD calculation is performed by coupling ANSYS Maxwell and ANSYS Fluent. The Lorentz force, as calculated by analytical equations, ANSYS Fluent add-on MHD module, and external electromagnetic solver, is added as the source term in Navier–Stokes equation. By comparing the simulation results with the benchmark experiments, the calculation accuracy with different coupling methods and modification strategies is evaluated. Based on this, a necessary simplification strategy of the MHD method for CC is established, and application of the simplified MHD method to a CC process is demonstrated.

<https://doi.org/10.1007/s11663-022-02516-3>  
© The Author(s) 2022

## I. INTRODUCTION

ELECTROMAGNETIC stirring (EMS) has been recognized as a mature technique and mandatorily implemented in the steel continuous casting (CC) process to control the melt flow and casting quality.<sup>[1–3]</sup>

It can extend the center equiaxed zone,<sup>[4,5]</sup> refine the grain size,<sup>[6]</sup> minimize the shrinkage porosity and macrosegregation,<sup>[1,7,8]</sup> and even improve the surface quality and lower the risk of entrapment of non-metallic inclusions in the CC product.<sup>[1,3]</sup> Both the rotating magnetic field (RMF) and traveling magnetic field (TMF) can be implemented. Based on the installed position in the CC, the EMS can be classified as mold electromagnetic stirring (M-EMS), secondary electromagnetic stirring (S-EMS), and final electromagnetic stirring (F-EMS).

To understand the principle of the EMS, in addition to the plant trials on real steel CC,<sup>[9,10]</sup> laboratory experiments were performed based on model alloys of low melting point.<sup>[11–15]</sup> When an RMF is applied on the melt sample, which is enclosed in a cylindrical crucible, the induced angular flow can drive a secondary poloidal flow.<sup>[14]</sup> Although the secondary poloidal flow is approximately an order of magnitude slower than the angular flow, it transports the angular momentum out of the stirred region. It is known that it is not possible to

---

HAIJIE ZHANG, MENGHUAI WU, ZHAO ZHANG, ANDREAS LUDWIG, and ABDELLAH KHARICHA are with Chair of Simulation and Modelling Metallurgical Processes, Metallurgy Department, Montanuniversität Leoben, Franz-Josef Street 18, 8700 Leoben, Austria. Contact e-mail: menghuai.wu@unileoben.ac.at ARNOLD RÓNAFÖLDI, ANDRÁS ROÓSZ, and MÁRIA SVÉDA are with the MTA-ME Materials Science Research Group, ELKH, Miskolc Egyetemváros 3515, Hungary. ZSOLT VERES is with the Institute of Physical Metallurgy, Metal Forming and Nanotechnology, University of Miskolc, Miskolc Egyetemváros 3515, Hungary.

Manuscript submitted January 6, 2022; accepted March 29, 2022.

Article published online April 19, 2022.

obtain the flow information inside the casting *via* plant trials. The laboratory experiments are also limited to the model alloys of low melting point. Hence, the multiphase nature of solidification process has to be neglected. Therefore, computational magnetohydrodynamic (MHD) methods were popularly applied to examine the EMS efficiency.<sup>[16,17]</sup> Many simulation studies have been conducted to calculate the EMS-driven flow and study its interaction with the solidification.<sup>[18–21]</sup>

It is challenging to numerically couple the flow and electromagnetic (EM) fields in the industry process of CC. When the melt flow is subjected to a static magnetic field, similar to the electromagnetic brakes (EMBr),<sup>[22,23]</sup> it is possible to couple the electromagnetic–flow interaction by programming it in the CFD solver. However, this coupling technique can hardly be applied for EMS where the implemented EM field is moving/changing. The ANSYS Fluent addon MHD module provides one coupled method for MHD calculations, but the external magnetic field ( $\vec{B}_0$ ) should be known in advance. Specifically, the  $\vec{B}_0$  field is imported into ANSYS Fluent, where the induced magnetic field ( $\vec{b}$ ), eddy current ( $\vec{J}$ ), and Lorentz forces ( $\vec{F}_L$ ) are calculated by solving *User-Defined Scalar* equations.<sup>[24,25]</sup> The drawbacks of this method are as follows: (1) the addon MHD module is incompatible with the Eulerian–Eulerian multiphase approach on which most advanced solidification models were developed; (2) the calculation time-step ( $\Delta t$ ) should be set extremely low to resolve the rotation of the imported  $\vec{B}_0$  field. Therefore, the most widely used method is still based on the de-coupled method. Generally, there are two de-coupled methods to calculate the EM field. The first method is to use an analytical solution of the time-averaged  $\vec{F}_L$ , which is derived based on an infinite solid conductive cylinder by assuming that the skin depth is significantly higher than the sample radius.<sup>[19,26–28]</sup> Then,  $\vec{F}_L$  is used to calculate the flow. This simplification is not in line with the case of high frequency, *i.e.*, high magnetic Reynolds number ( $R_m$ ), because the skin effect cannot be ignored.<sup>[29,30]</sup> The second method is to calculate the EM field with a commercial EM solver, and then transfer  $\vec{F}_L$  as a field function into the computational fluid dynamic (CFD) calculation.<sup>[31]</sup> In this case, the EM field was solved mostly based on an assumption that the liquid melt is stationary.<sup>[32–34]</sup> In addition to the de-coupled MHD calculations, further simplifications were often performed for CC. The ignorance of the existence of solid shell,<sup>[33,35,36]</sup> where the maximal  $\vec{F}_L$  applies, can overestimate the melt flow. Furthermore, Sun and Zhang<sup>[32]</sup> used this de-coupled method to study the solidification of a bloom CC. However, the effect of the solidified shell on  $\vec{F}_L$  was ignored by using the same electrical

conductivity for the liquid and solid steel. The main drawback of the de-coupled MHD method is that the influence of the melt flow on the EM field is ignored. Most recent studies appeared to ignore this effect.<sup>[18,32–34,37]</sup> It is known that ignoring the flow effect on the EM field is only valid when the rotating angular speed ( $\omega_\ell$ ) of the flow is not comparable to the applied EM angular speed ( $\omega_B$ ). As reported in the previous studies,<sup>[27–29]</sup> the effective  $\vec{F}_L$  decreases with the induced  $\omega_\ell$ . Hence,  $\vec{F}_L$  should be modified by multiplying  $(1 - \omega_\ell/\omega_B)$ . Nevertheless, most recent studies appear to ignore this effect.<sup>[18,32–34,37]</sup> Therefore, the aforementioned de-coupled methods along with other assumptions should be carefully validated.

The aim of this study is to present a benchmark, *i.e.*, a series of laboratory experiments, to validate the MHD methods that are typically employed for the steel CC process. An RMF field with variable intensity and frequency is considered. The MHD calculation is performed by coupling ANSYS Maxwell and ANSYS Fluent. An iteration scheme is proposed to consider the flow–electromagnetic interactions. Furthermore,  $\vec{F}_L$ , which is calculated with different methods and modification strategies, is termed as a source field in CFD calculations using coupled or de-coupled scheme. The calculation accuracy of different methods and modification strategies are compared. Based on this, the suitability of the MHD method with a necessary simplification strategy for CC is evaluated and discussed. Finally, application of the proposed MHD method to an industry process of CC is demonstrated.

## II. BENCHMARK EXPERIMENTS

The experiments were conducted on an upward Bridgman furnace equipped with an RMF. The RMF was generated by a two-pole inductor charged by a three-phase alternating current (AC). As shown in Figure 1(a), the diameter of the iron core of the inductor is 230 mm, and its height is equal to 300 mm. In the center of the inductor, the Bridgman-type furnace was assembled concentrically with the inductor, and the length of the measurement sample was 150 mm. Detailed information on the furnace is available in Reference 38. The application ranges of the facility are as follows: frequency  $f$  (30 to 400 Hz), magnetic induction  $|\vec{B}|$  (0 to 150 mT), a withdrawal speed of sample in the Bridgman furnace  $v$  (0 to 0.8 mm/s), and temperature gradient  $G$  (0 to 10 K/mm).

### A. Experiment 1: Magnetic Field ( $\vec{B}$ ) Measurement

Without loading any sample, the  $\vec{B}$  field along the axis and in the azimuthal directions was measured with GM08 Gaussmeter (Hirts Magnetics).

## B. Experiment 2: Torque ( $\tau$ ) Measurement

As schematically shown in Figure 1(b), the sample is suspended in the inductor and fixed by an insulated organic sample holder (PA6 polyamid). The sample holder is connected to a cylindrical steel bar through a bearing housing. With the RMF load, the induced Lorentz force on the sample is transported to a digital dynamometer *via* the sample holder. All these components are placed coaxially in the height direction. To eliminate the error due to friction of the facility, the measured force that can initiate the movement of the sample was 0.34 N, *i.e.*,  $Friction = 0.34$  N. The Force exerted on the sample under different values of  $|\vec{B}|$  were measured. Hence, the Pull is calculated as  $Pull = Friction + Force$ . The torque  $\tau = Pull * R$ , where  $R$  denotes the radius of the sample. During the experiment, the sample is cooled by circulating water to maintain the sample at room temperature (20 °C). As listed in Table I, three metal samples with  $H = 150$  mm and  $R = 10$  mm were measured.

## C. Experiment 3: Flow Velocity Measurement

A so-called pressure compensation method is applied to measure the RMF-induced rotating angular speed.<sup>[39]</sup> This experiment was performed at room temperature with cold alloy Ga75In25. As shown in Figure 1(c), the closed cylindrical tank (Teflon) with two opening vessels (inner diameter = 1.0 mm) is filled with Ga75In25 alloy. The inner diameter of the tank was changeable (Table II), and its height was 100 mm. One vessel was at the center of the top surface, and another vessel was placed 0.2 mm to the inner surface of the tank. The maximal pressure was measured at position  $r = R - 0.2$  mm, so one vessel was set here to minimize the relative error of the measurements. The zero level before RMF load is denoted by the blue dash line in Figure 1(c). With the RMF load, a level difference ( $\Delta H$ ) develops between two vessels, as schematically indicated by the red dash lines in Figure 1(c). A compensatory pressure of air ( $P_{comp}$ ) was applied on the peripheral vessel to set the melt back to zero level. In this manner, the pressure difference can be measured and used to calculate the liquid velocity. In this experiment, the penetration distance  $\delta$  (Table II) is significantly higher than the sample radius, and the aspect ratio  $H/R \geq 8$ . Therefore, the skin effect and end effect should be neglectable. As listed in Table II, the rotating velocities for eight cases with varying  $|\vec{B}|$  are measured.

## III. MHD MODELING AND SIMPLIFICATION

### A. Calculation Method 1: Analytical Solution

Instead of directly solving Maxwell's equations, the analytical equations,<sup>[27,29,40]</sup> as shown in Figure 2(a), are employed to calculate  $\vec{F}_L$  (composed of  $\vec{F}_\theta$  and  $\vec{F}_r$ ). Specifically,  $\vec{B}_0$  should be known in advance. Typically,

it is measured, and its distribution  $f(z)$  can be obtained by fitting the measurements. In this benchmark study, the inductor is significantly longer than the sample (Figure 1(a)). Hence,  $f(z)$  is assumed to be equal to 1.

According to References 29 and 40,  $\vec{F}_r$  has a minor effect on the fluid flow when compared to  $\vec{F}_\theta$ . Thus, we neglect it in this MHD simulation. As presented in Figure 2(a), the relative motion between the liquid and  $\vec{B}$  has been considered by a factor of  $(1 - \omega_\ell/\omega_B)$ .

### B. Calculation Method 2: Coupled Simulation via ANSYS Fluent Addon MHD Module

$\vec{B}_0$  was first calculated *via* ANSYS Maxwell, and then it was imported into ANSYS Fluent. It should be noted that ANSYS Maxwell is another software package, which is de-coupled from ANSYS Fluent. In a time-dependent transient simulation, the rotation of  $\vec{B}_0$  can be resolved with the given frequency  $f$ . As shown in Figure 2(b), given that  $\vec{B}_0$  is known, only  $\vec{b}$  should be solved. Specifically,  $\vec{B}$  is a sum of  $\vec{B}_0$  and  $\vec{b}$ , *i.e.*,  $\vec{B} = \vec{B}_0 + \vec{b}$ . The generated  $\vec{F}_L$  due to the interaction between  $\vec{B}$  and  $\vec{J}$  can drive the liquid to flow. In turn,  $\vec{b}$  can be updated by the forced flow ( $\vec{u}$ ) to further modify  $\vec{B}$ ,  $\vec{J}$ , and  $\vec{F}_L$ . When the conductive liquid is heated due to the generated  $Q_J$ , the electrical conductivity can be updated according to local temperature, which in turn affects  $\vec{b}$  and  $\vec{u}$ . The coupling between  $\vec{B}$ ,  $\vec{u}$ , and  $T$  is automatically solved in ANSYS Fluent.

### C. Calculation Method 3: Iteration Scheme Between EM and CFD Solvers

The MHD calculation is performed by combining ANSYS Maxwell and ANSYS Fluent. An iteration scheme, as shown in Figure 2(c), is proposed to consider the flow–electromagnetic interaction. Specifically,  $\vec{F}_L$  was calculated *via* the EM solver, which was used to solve Maxwell equations. The extracted  $\vec{F}_L$  was transported to the CFD solver. According to Roplekar and Dantzig,<sup>[28]</sup>  $\vec{F}_L$  was modified by multiplying  $(1 - \omega_\ell/\omega_B)$  before applying it as a source term for the Navier–Stokes equation. Then, the calculated averaged liquid rotating angular velocity,  $\bar{\omega}_\ell = \left( \int_0^R |\vec{u}_\theta| dr \right) / R^2$ , was used to modify the effective frequency of the magnetic field,  $f_{eff} = (\omega_B - \bar{\omega}_\ell) / 2\pi$ . The effect of the liquid flow on the generated  $Q_J$  can also be considered with this method.

A two-way coupling between EM and CFD solvers (*Calculation method 3*) is possible, but the iteration scheme should be established manually. Before the activation of RMF, the liquid is assumed stationary, *i.e.*,  $\bar{\omega}_{\ell,0} = 0$ ,  $f_{eff} = f$ , and  $\omega_B = 2\pi f$ . These are the initial

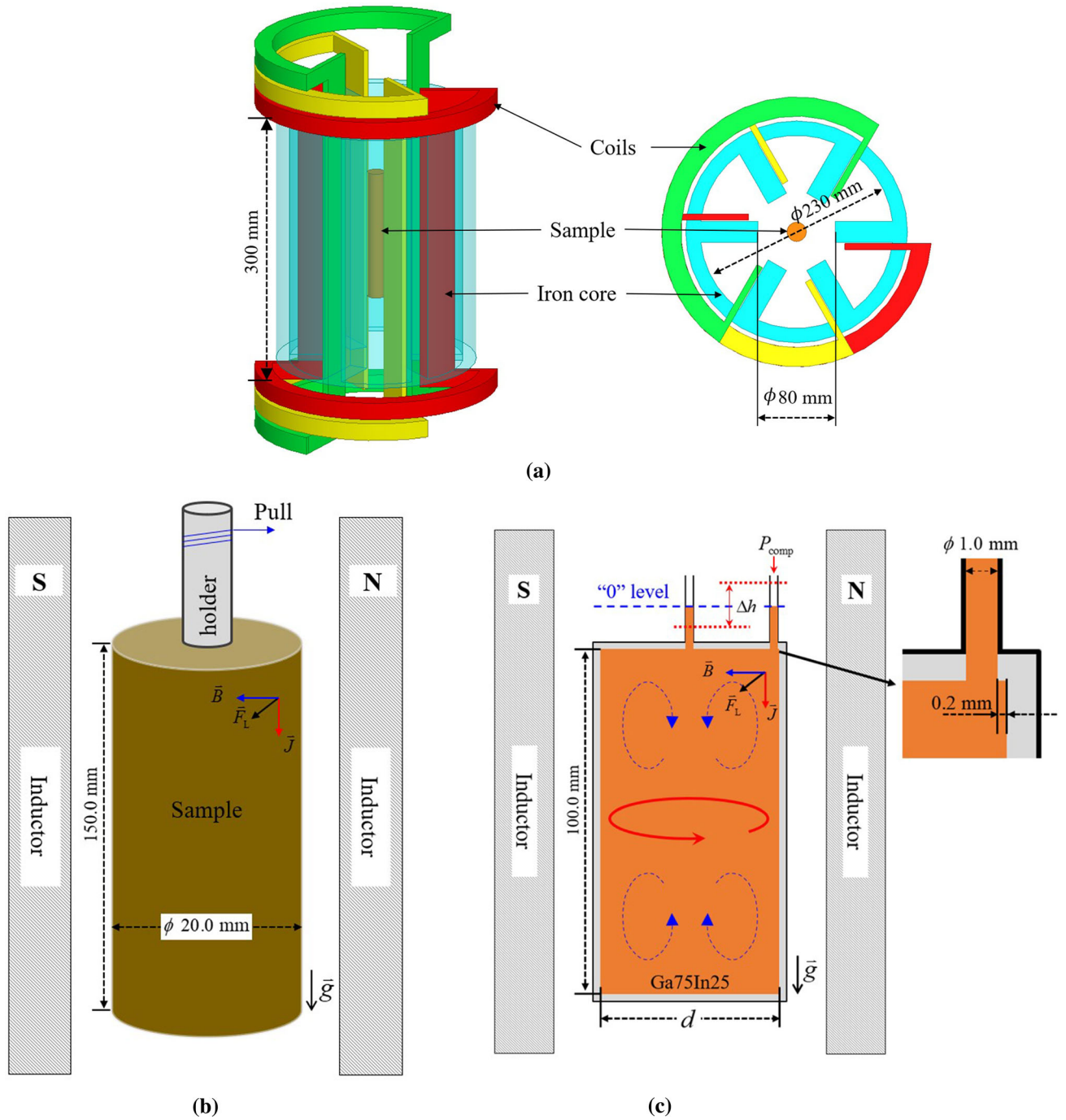


Fig. 1—Schematic of experiment design. (a) Layout of the inductor and sample position; (b) sketch of torque measurement; (c) sketch of liquid velocity measurement.

**Table I. Different Cylindrical Solid Samples Used for Torque Measurement**

Materials	$R$ (mm)	$H$ (mm)	$ \vec{B} $ (mT)	$f$ (Hz)
Cu	10	150	0–160	50
Al				
AlSi7				

conditions for the first EM calculation between the EM–CFD iteration. Then, the calculated  $\vec{F}_L$ , with the  $(1 - \omega_\ell/\omega_B)$  modification, is used for the first CFD calculation. Typically, the calculated angular velocity of the liquid ( $\omega_\ell = |\vec{u}_\theta|/r$ ) is not uniform because  $u_\theta$  is not linearly distributed along the radius. Hence, the averaged angular velocity  $\overline{\omega}_\ell$  was used to characterize the angular flow. Based on this, the effective rotation frequency of  $\vec{B}$  field is obtained,  $f_{\text{eff}} = \frac{\omega_B - \overline{\omega}_\ell}{2\pi}$ . Hence,

$\vec{F}_L$  can be updated in the next EM–CFD iteration based on the obtained  $f_{\text{eff}}$ . As shown in Figure 2(c), further iterations are made until  $|\Delta\bar{\omega}_\ell/\bar{\omega}_\ell| < 5$  pct, and then the iteration is terminated, where  $|\Delta\bar{\omega}_\ell|$  denotes the difference of the averaged angular velocity  $\bar{\omega}_\ell$  between two sequent iterations. It should be noted that the criterion of 5 pct is arbitrarily set, but it can be modified for other simulations when higher accuracy is demanded.

As shown in Figure 1(a), a full-scale inductor was developed to perform EM calculation. The sample is placed at the middle height of the inductor. Eddy current ( $\vec{J}$ ) was considered only in the conductive sample. When a three-phase AC is excited on the three

windings, a primary rotating magnetic field can be induced. Given that the current inductor has one pair of poles, the frequency of the magnetic field is the same as the frequency of the applied current. Based on Faraday's law, the  $\vec{J}$ -induced magnetic field opposes the change in the primary rotating magnetic field. The interaction between the total  $\vec{B}$  and  $\vec{J}$  produces the Lorentz force ( $\vec{F}_L$ ). The strength of electric field ( $\vec{E}$ ) can be calculated as follows:

$$\nabla \times \vec{E} = -\frac{\partial \vec{B}}{\partial t}. \quad [1]$$

The strength of the induced  $\vec{J}$  can be calculated as follows:

$$\vec{J} = \sigma(\vec{E} + \vec{u} \times \vec{B}), \quad [2]$$

where  $\vec{u}$  denotes the liquid velocity of the sample. Specifically,  $\vec{u}$  is set as zero for the case of solid sample (torque measurement) or it is calculated according to the averaged  $\bar{\omega}_\ell$  for the case of liquid sample. The Lorentz force exerted on the sample can be calculated as follows:

$$\vec{F}_L = \frac{1}{2} R_e(\vec{J} \times \vec{B}), \quad [3]$$

**Table II. Cases Performed for Flow Measurement Based on Ga75In25 Alloy**

Case No.	$f$ (Hz)	$R$ (mm)	$H$ (mm)	$ \vec{B} $ (mT)	$\delta^*$ (mm)
1	50	5	100	0 to 90	36
2		7.5		0 to 90	
3		12.5		0 to 90	
4	100	5		0 to 70	26
5	150	5		0 to 65	21
6		7.5		0 to 65	
7		12.5		0 to 65	
8	200	5		0 to 60	18

\*Penetration distance  $\delta = \sqrt{\frac{1}{4\pi^2 \sigma_{\text{Ga75In25}} f \cdot 10^{-7}}}$ .

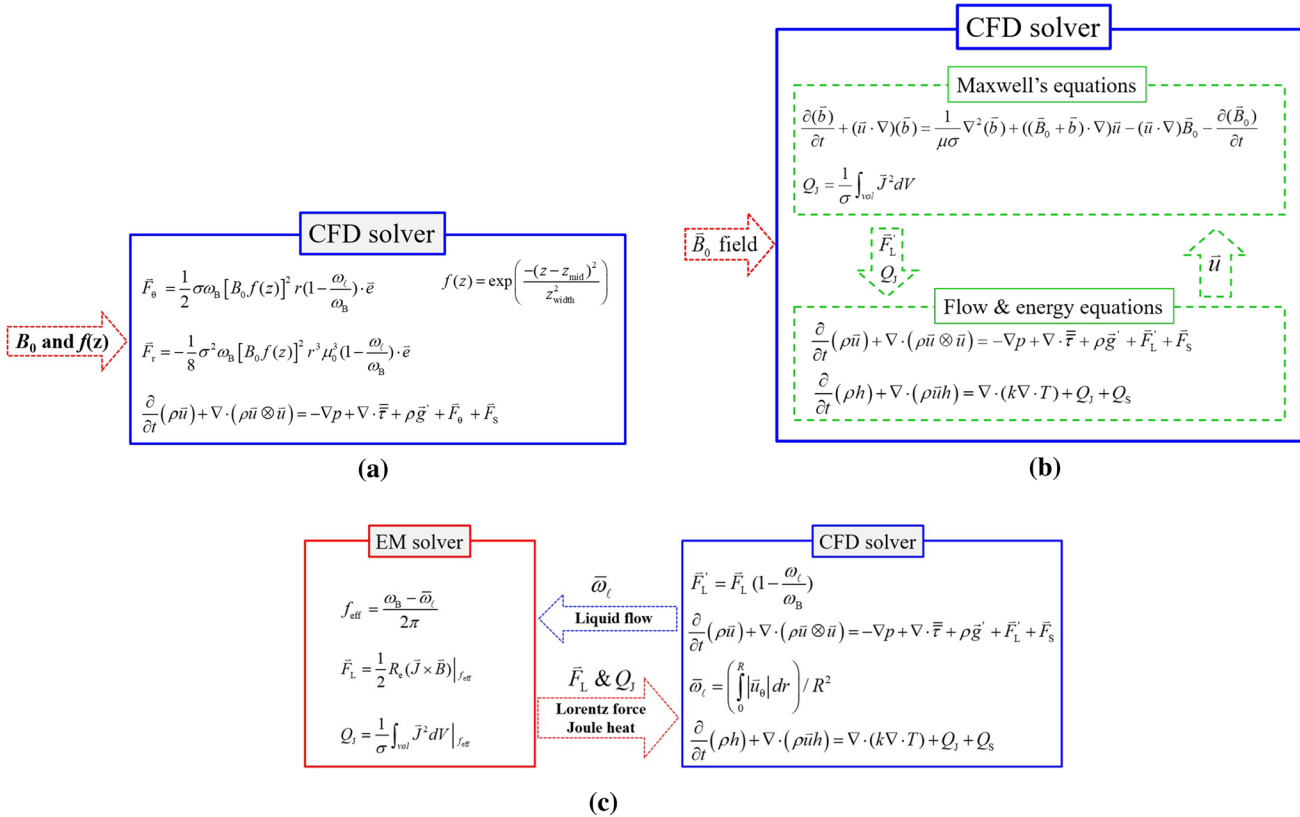


Fig. 2—Sketch of different MHD calculation methods and coupling schemes: (a) Analytical solution; (b) Coupled simulation via ANSYS Fluent add-on MHD module; and (c) Iteration scheme between EM and CFD solvers.

where  $R_e$  denotes the real part of a complex number. The torque on the solid sample is given by

$$\vec{\tau} = \frac{1}{2\pi} \int_0^{2\pi} \left\{ \int_{Vol} \vec{r} \times (\vec{J} \times \vec{B}) dV \right\} d\theta. \quad [4]$$

In the current study, the transient 3D flow was calculated. Further assumptions were made as follows:

- (1) The Joule heat is neglected during the CFD calculation.
- (2) The secondary (and higher order of) eddy current in the EM calculation is not considered.
- (3) The liquid alloy is incompressible and isothermal with constant density and viscosity.
- (4) In the CFD calculation, a so-called course-grid direct numerical simulation is conducted, *i.e.*, no turbulence model is used.
- (5) All walls of the crucible are assumed to be no-slip.

Among all eight experiment cases in Table II, only Case (3) ( $f = 50$  Hz,  $R = 12.5$  mm) is analyzed numerically in detail. The alloy (Ga75In25) is confined in a cylindrical crucible with  $H = 100.0$  and  $R = 12.5$  mm. The sample is emeshed into  $8.5 \times 10^5$  hexahedral elements with maximum mesh size of  $400 \mu\text{m}$ .  $\Delta t$  for the first and third calculation method is  $1 \times 10^{-3}$  s, and a smaller  $\Delta t$  of  $5 \times 10^{-5}$  s is used for the second calculation method due to the spatial and temporal interpolation of the rotating  $\vec{B}_0$ . As listed in Table III, four simulations are conducted with different RMF intensities. The material properties and other parameters are summarized in Table IV.

#### IV. EXPERIMENTAL RESULTS AND MODEL EVALUATIONS

##### A. Magnetic Induction

The magnetic induction is calculated *via* the EM solver ANSYS Maxwell, Figure 2(c). With the three-phase AC ( $I = 5700$  A,  $f = 50$  Hz), a rotating  $\vec{B}$  is induced. The calculated  $\vec{B}$  on the plane of middle height of the inductor at a phase of  $300^\circ$  is shown in Figure 3(a). The maximal  $|\vec{B}|$  (1650 mT) is realized in the iron core, while  $|\vec{B}|$  at the inductor center is an order of magnitude smaller. The calculated  $|\vec{B}|$  along the axis of the inductor (the red vertical line in Figure 3(a)) for the case without sample loading matches the experimental measurements quite well, Figure 3(b). In this paper, the calculated  $\vec{B}$  field without sample loading is served as the input  $\vec{B}_0$  field in calculation method 2, Figure 2(b). When a copper sample ( $H = 150$  mm,  $R = 10$  mm) is loaded, the  $\vec{B}$  field in the sample is subject to the skin effect. As displayed by the black dash line in Figure 3(b), the calculated  $|\vec{B}|$  along the axis of the sample should be

reduced by approximately 13 mT. However, there is no measurement data for this case. Furthermore,  $|\vec{B}|$  along the blue circle ( $R = 10$  mm) for the case without sample loading, as denoted in Figure 3(a), is measured and compared with the calculation results in Figure 3(c). The experiment and calculation results are in excellent agreement, and a constant/uniform  $|\vec{B}|$  (160 mT) is obtained.

##### B. Torque

The magnetic torque ( $\tau$ ) is also calculated *via* the EM solver ANSYS Maxwell, Figure 2(c). The calculated  $\tau$  for solid samples of three metal/alloys (Table I) as a function of  $\vec{B}$  is compared with those obtained *via* experiments as shown in Figure 4. For all samples,  $\tau$  increases exponentially with  $|\vec{B}|$ . The simulation results are in excellent agreement with the measurements. Given the difference in electronic conductivities, as listed in Table IV, the torque of Cu is the highest, followed by Al and AlSi7.

##### C. RMF-Driven Liquid Flow

Different simulation cases (Table III) exhibit similar flow pattern when they are calculated with different calculation methods (Figure 2). Only the results of Simulation C, which are calculated using calculation method 3 (Figure 2(c)) after 3 EM-CFD iterations, are presented in Figure 5. According to Figure 6, the calculation gets converged after 3 EM-CFD iterations. The liquid flow is dominated by the rotating toroidal flow ( $\vec{u}_\theta$ ), which exhibits the same magnitude with  $\vec{u}_\ell$  ( $|\vec{u}_\ell| = \sqrt{\vec{u}_\theta^2 + \vec{u}_\psi^2}$ ). As shown in Figures 5(a) and (b), a strong rotating flow up to the magnitude of 1.2 m/s was induced in the sample, while the induced secondary poloidal flow ( $\vec{u}_\psi$ ) is approximately one magnitude lower. Furthermore, as shown in Figure 5(c),  $\vec{u}_\theta$  is characterized by those intermittent tubes, but  $\vec{u}_\psi$  is chaotic and is characterized by the prevailing of multiple Taylor-Görtler (T-G) vortices.<sup>[11,41]</sup> Most of the T-G vortices are observed near the sample surface. They originate randomly around those tubes, and then increase in size, coalesce with neighboring ones, or even split into sub-vortex. Simultaneously, they move up and downward. Finally, they dissipate near the top and bottom wall (the so-called Bödewadt/Ekman layer<sup>[2,41]</sup>). The vertical motion of these T-G vortices transports the angular momentum. According to Figure 5(c), a few of the vortices can also be observed in the central area. Although they exhibit similar features to the vortex near the sample surface, their nucleation frequency and survival number density are much lower. These vortices are responsible for the slow velocity oscillation along the axis, Figure 5(a). The total pressure  $P_{\text{Total}}$ , excluding the hydrostatic pressure ( $P' = \rho gh$ ), is demonstrated in Figure 5(d). The maximum of  $P_{\text{Total}}$  is located in the



range of 0.5 to 1.0 mm to the surface. This result is consistent with our previous experimental observation.<sup>[39]</sup>

To analyze the convergence behavior of EM-CFD coupling scheme, the evolution of  $|\vec{u}_\ell|$  at a reference point (mid-height of the sample and 2.5 mm to the sample surface as denoted by the black spot in Figure 5(a)) during different EM-CFD iterations is plotted in Figure 6(a). According to the EM-CFD coupling scheme in Figure 2(c), the first EM simulation is conducted by assuming that the liquid melt in the sample is stationary ( $\overline{\omega}_\ell = 0$ , *i.e.*,  $f_{\text{eff}} = 50$  Hz) such that maximum  $\vec{F}_L$  is generated. As a consequence, the maximum of  $|\vec{u}_\ell|$  (or the maximum  $\overline{\omega}_\ell$ , *i.e.*, the black line in Figure 6(a)), is obtained. It should be noted that the high-frequency oscillation of  $|\vec{u}_\ell|$  is not due to numerical iterations, but due to the prevailing T-G vortices, which are observed in Figure 5(c). For the

second iteration of the EM simulation,  $f_{\text{eff}}$  is updated as  $((\omega_B - \overline{\omega}_\ell)/2\pi)$ . Hence, a reduced  $\vec{F}_L$  is obtained, and in turn a reduced  $|\vec{u}_\ell|$ , *i.e.*, the red line in Figure 6(a), is obtained. Following the further EM-CFD coupling scheme,  $f_{\text{eff}}$  is updated again, and a new  $|\vec{u}_\ell|$  is obtained with further EM-CFD iterations. The iteration is terminated when the convergence criterion  $|\Delta\overline{\omega}_\ell/\overline{\omega}_\ell| < 5$  pct is satisfied. The calculated  $\overline{\omega}_\ell$  of different simulation cases (Table III) following the iteration scheme is displayed in Figure 6(b). As mentioned previously, only Case 3 ( $R = 12.5$  mm,  $f = 50$  Hz) of Table II is analyzed in detail. The simulations are in good agreement with the experimental results, but more iterations between the EM and CFD calculations are required with an increase in  $|\vec{B}|$ . Figure 6(c) shows the necessary EM-CFD iteration numbers as a function of the RMF intensity ( $|\vec{B}|$ ). When  $|\vec{B}|$  is low, *e.g.*, Simulation A and B, no iteration is required to obtain results close to the experiment, while 2 and 4 iterations are required for simulations C and D to converge to the experimental results, respectively. For the current experiment configuration, when  $|\vec{B}| < 28$  mT, the accuracy of the simulation results can be accepted without any iteration, while iterations are required when  $|\vec{B}| \geq 28$  mT. Therefore, we divide Figure 6(c) into two regions (green vs. red) with critical  $|\vec{B}| = 28$  mT.

**Table III. Simulations Performed for the Model Alloy (Ga75In25)**

	$ \vec{B} $ (mT)	$f$ (Hz)	$R$ (mm)	$I$ (A)
Simulation A	5.6	50.0	12.5	200.0
Simulation B	14.0			500.0
Simulation C	28.0			1000.0
Simulation D	42.0			1500.0

**Table IV. Summary of Material Properties and Other Parameters\***

Parameters	Symbols	Unit	Values
Density	$\rho_{\text{Cu}}(\text{s})$	$\text{kg m}^{-3}$	8933.0
	$\rho_{\text{Al}}(\text{s})$		2689.0
	$\rho_{\text{Al7Si}}(\text{s})$		2535.0
	$\rho_{\text{Ga75In25}}(15.7\text{ }^\circ\text{C})$		6517.5
Relative Permeability	$\mu_{\text{Cu}}$	—	1
	$\mu_{\text{Al}}$		
	$\mu_{\text{Al7Si}}$		
	$\mu_{\text{Ga75In25}}$		
Electrical Conductivity	$\sigma_{\text{Cu}}(\text{s})$	$\text{S m}^{-1}$	$5.8 \times 10^7$
	$\sigma_{\text{Al}}(\text{s})$		$3.8 \times 10^7$
	$\sigma_{\text{Al7Si}}(\text{s})$		$2.4 \times 10^7$
	$\sigma_{\text{Ga75In25}}(15.7\text{ }^\circ\text{C})$		$3.6 \times 10^6$
	$\nu_{\text{Ga75In25}}(15.7\text{ }^\circ\text{C})$		$3.4 \times 10^{-7}$
Kinematical Viscosity	$\nu_{\text{Ga75In25}}(15.7\text{ }^\circ\text{C})$	$\text{m}^2 \text{s}^{-1}$	$3.4 \times 10^{-7}$
Electric Current Frequency	$f$	Hz	50.0
Pair of Poles	$q_\perp$	—	1.0
Magnetic Induction	$ \vec{B} $	mT	0–160.0
Total source Current	$I$	A	0–5700.0
Sample Height	Solid: Torque	$H$	150.0
	Liquid: Velocity		100.0
Sample Diameter	Solid: Torque	$R$	10.0
	Liquid: Velocity		12.5

\*The temperature of the material properties in the solid state, as indicated by 's' in the table, is 25 °C. For experiments, which are performed at temperatures other than 25 °C are labeled in the table.

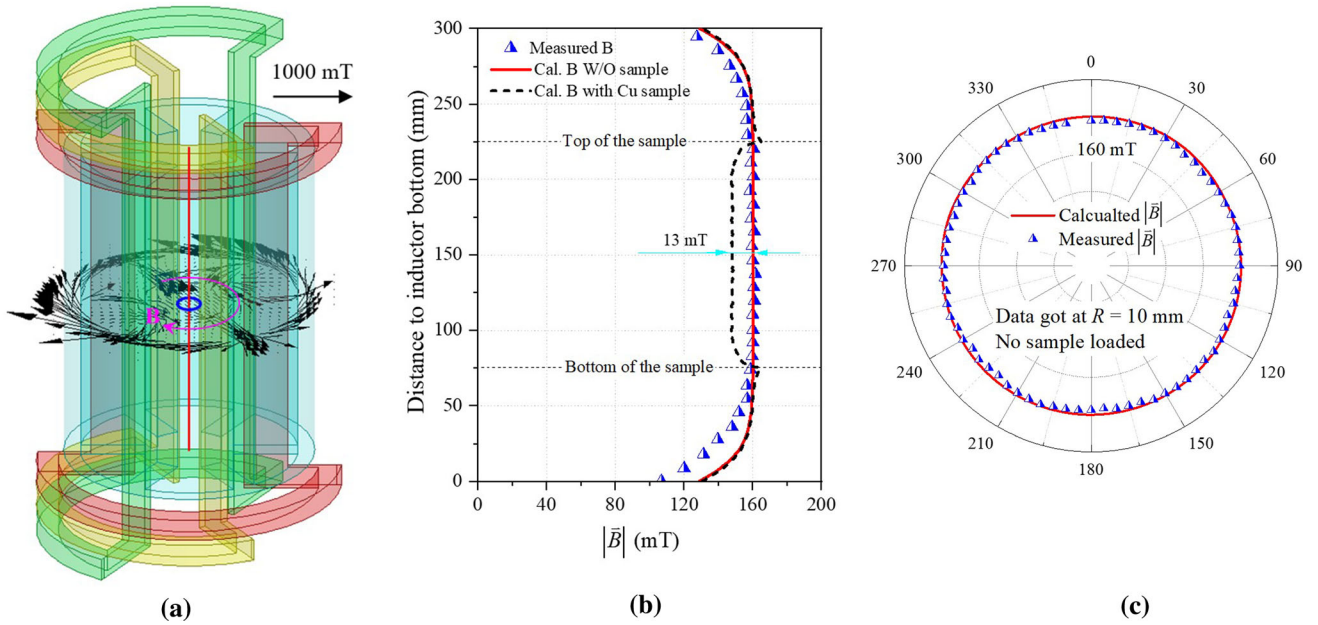


Fig. 3—Experiment–simulation comparison of  $|\vec{B}|$  for the case with  $f = 50$  Hz,  $I = 5700$  A. (a) Calculated  $\vec{B}$  on the plane of middle height of the inductor at a phase of  $300^\circ$ . (b)  $|\vec{B}|$  along the axis of the inductor. (c)  $|\vec{B}|$  along the blue circle as marked in (a).

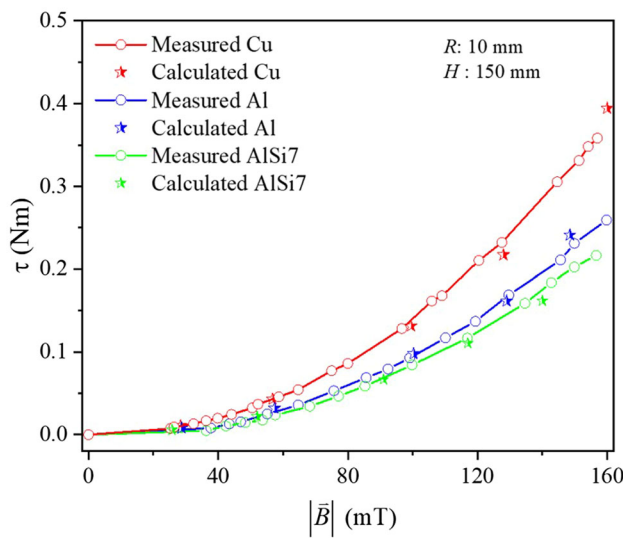


Fig. 4—Comparison of  $\tau$  on different samples.

The experimentally measured RMF-driven rotating angular velocity  $\bar{\omega}_\ell$  in the liquid sample as a function of  $|\vec{B}|$  is shown in Figure 7(a). Within the measured range of  $|\vec{B}|$ ,  $\bar{\omega}_\ell$  of all experimental cases show almost a linear function of  $|\vec{B}|$ . It should be noted that with an increase in  $|\vec{B}|$ ,  $\bar{\omega}_\ell$  approaches closer and closer to  $\omega_B$ , but it can

never reach  $\omega_B$ . The calculated  $\bar{\omega}_\ell$  as a function of  $|\vec{B}|$  with different methods and modification strategies is shown in Figure 7(b). Specifically,  $\bar{\omega}_\ell$  is calculated via  $\bar{\omega}_\ell = \left( \int_0^R u_\theta dr \right) / R$ . With the first calculation method (Figure 2(a)), as shown by the green line in Figure 7(b),  $\bar{\omega}_\ell$  is considerably overestimated. By referring to simulation C ( $|\vec{B}| = 28.0$  mT), the calculated  $\bar{\omega}_\ell$  is overestimated by ca. 34.4 pct. With the second calculation method (Figure 2(b)), as demonstrated by the black line and squares in Figure 7(b),  $\bar{\omega}_\ell$  shows good agreement with the experimental measurements. With the third calculation method (Figure 2(c)), different modification strategies were performed to check their effect on the calculation accuracy. In Figure 7(b), the blue line indicates the calculated  $\bar{\omega}_\ell$  using the EM–CFD iteration scheme without any modification and iteration, red line indicates the calculated  $\bar{\omega}_\ell$  by solely using the EM–CFD iteration scheme with the modification  $(1 - \omega_\ell / \omega_B)$  but without any iteration, and pink line indicates the calculated  $\bar{\omega}_\ell$  using the EM–CFD iteration scheme with the modification by  $(1 - \omega_\ell / \omega_B)$  and iteration. Evidently,  $\bar{\omega}_\ell$  differs significantly if modification strategies of  $\vec{F}_L$  are varied. The calculated  $\bar{\omega}_\ell$  is overestimated by ca. 66.2 pct without any modification and iteration. If  $\vec{F}_L$  is solely modified by a factor of  $(1 - \omega_\ell / \omega_B)$ ,  $\bar{\omega}_\ell$  is overestimated by ca. 29.6 pct. Hence, only when the modification and iteration are conducted,  $\bar{\omega}_\ell$  can reproduce the experimental results.

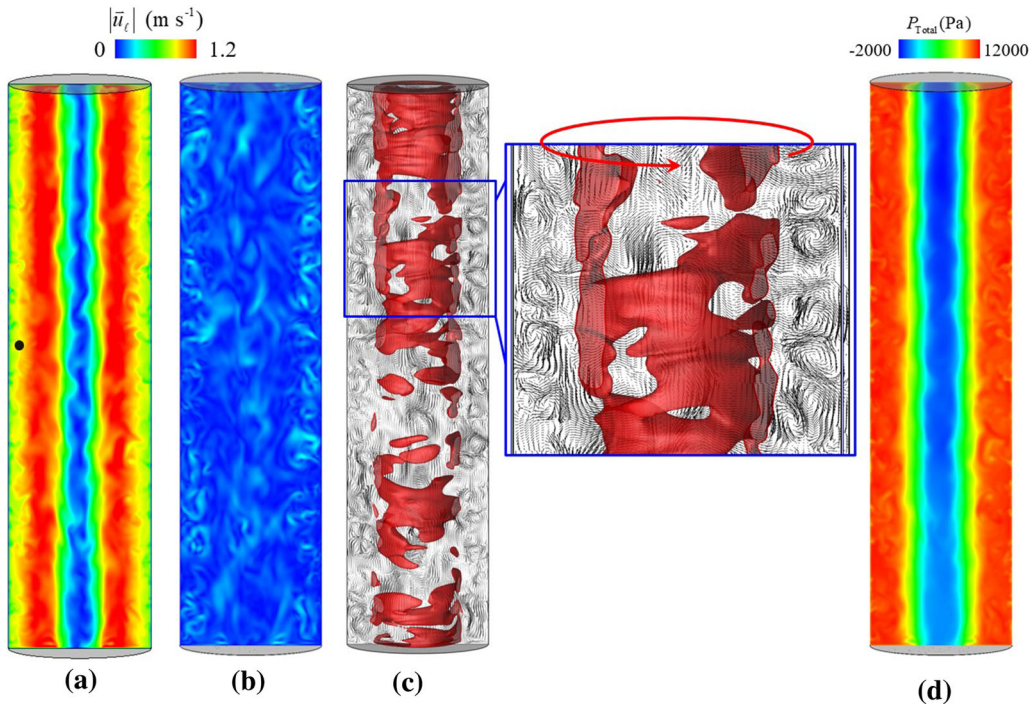


Fig. 5—Calculated results of Simulation C of Table III at  $t = 20$  s. (a)  $|\vec{u}_\theta|$  on a symmetry plane; (b)  $|\vec{u}_\psi|$  on a symmetry plane; (c) vectors of  $\vec{u}_\psi$  on a symmetry plane together with one 3D iso-surface of  $|\vec{u}_\theta| = 1.2$  m/s, and the thick red vector (zoomed section) indicates the flow direction of azimuthal flow; (d) Counter of total pressure  $P_{\text{Total}}$  excluding the hydrostatic pressure (Color figure online).

## V. APPLICATION IN CONTINUOUS CASTING PROCESS

The methodology, as introduced in this study, was used to study the effect of M-EMS on the superheat dissipation and the formation of as-cast structure in a billet CC casting ( $195 \times 195 \text{ mm}^2$ ) via a three-phase mixed columnar-equiaxed solidification model.<sup>[42,43]</sup> The three phases correspond to the steel melt, columnar dendrites from which the steel shell is fabricated, and equiaxed crystals, which are treated as an additional disperse continuum solid phase as schematically shown in Figure 8(a). Their volume fractions correspond to  $f_\ell, f_c, f_e$ . The growth kinetics for the columnar dendrites and movable equiaxed crystals are considered. The origins of the equiaxed crystals by the mechanisms of crystal fragmentation and heterogeneous nucleation are included. Furthermore, remelting and destruction of the equiaxed crystals in the superheated and/or oversaturated liquid are also considered. The details of the model and implementation of model can be referred to in References 42 and 43. Only the simulation results related to M-EMS near the mold region are analyzed in this study.

The M-EMS is created by a two-pole inductor with a three-phase AC, Figure 8(b).  $|\vec{F}_L|$  is shown on a symmetry section of the strand, Figure 8(c). The maximum  $|\vec{F}_L|$  of  $6000 \text{ N/m}^{-3}$  appears at the strand surface. It should be stressed that during the

solidification and flow simulation,  $\vec{F}_L$  is modified by multiplying  $(1 - \omega_\ell/\omega_B)$  to consider the relative motion between the melt and  $\vec{B}$ , i.e.,  $\vec{F}'_L = \vec{F}_L(1 - \omega_\ell/\omega_B)$ . Additionally, due to the multiphase nature of the solidification, the total effective  $\vec{F}'_L$  must be partitioned among three phases according to their volume fractions, i.e.,  $f_\ell \vec{F}'_L, f_c \vec{F}'_L,$  and  $f_e \vec{F}'_L$ . They are the corresponding source terms for the momentum equations. A relatively strong rotating liquid flow is induced in the mold region by M-EMS, as depicted in Figure 8(d). The strongest liquid flow is obtained at the position several centimeters above the middle height of the stirrer (inductor). This is attributed to the thickening of the shell along the casting direction. This liquid flow  $\vec{u}_\ell$  is composed of the azimuthal flow  $\vec{u}_\theta$  and secondary (radial and axial) flow  $\vec{u}_\psi$ , which can be observed on the cross section and vertical section of the strand, respectively, in Figure 8(e). According to References 14 and 29,  $\vec{u}_\psi$  is due to the imbalance in the radial pressure gradient owing to the centrifugal force. This differs from the laboratory case, Figure 5, wherein  $\vec{u}_\psi$  is characterized by the two pairs of recirculation loops above and below the stirrer center. The upper recirculation loop inhibits the downward flow of the melt coming from the side ports of the submerged entry nozzle (SEN), and a small part of the melt is blocked near the SEN, Figure 8(e). The interaction between  $\vec{u}_\psi$  with the jet flow coming from the downward

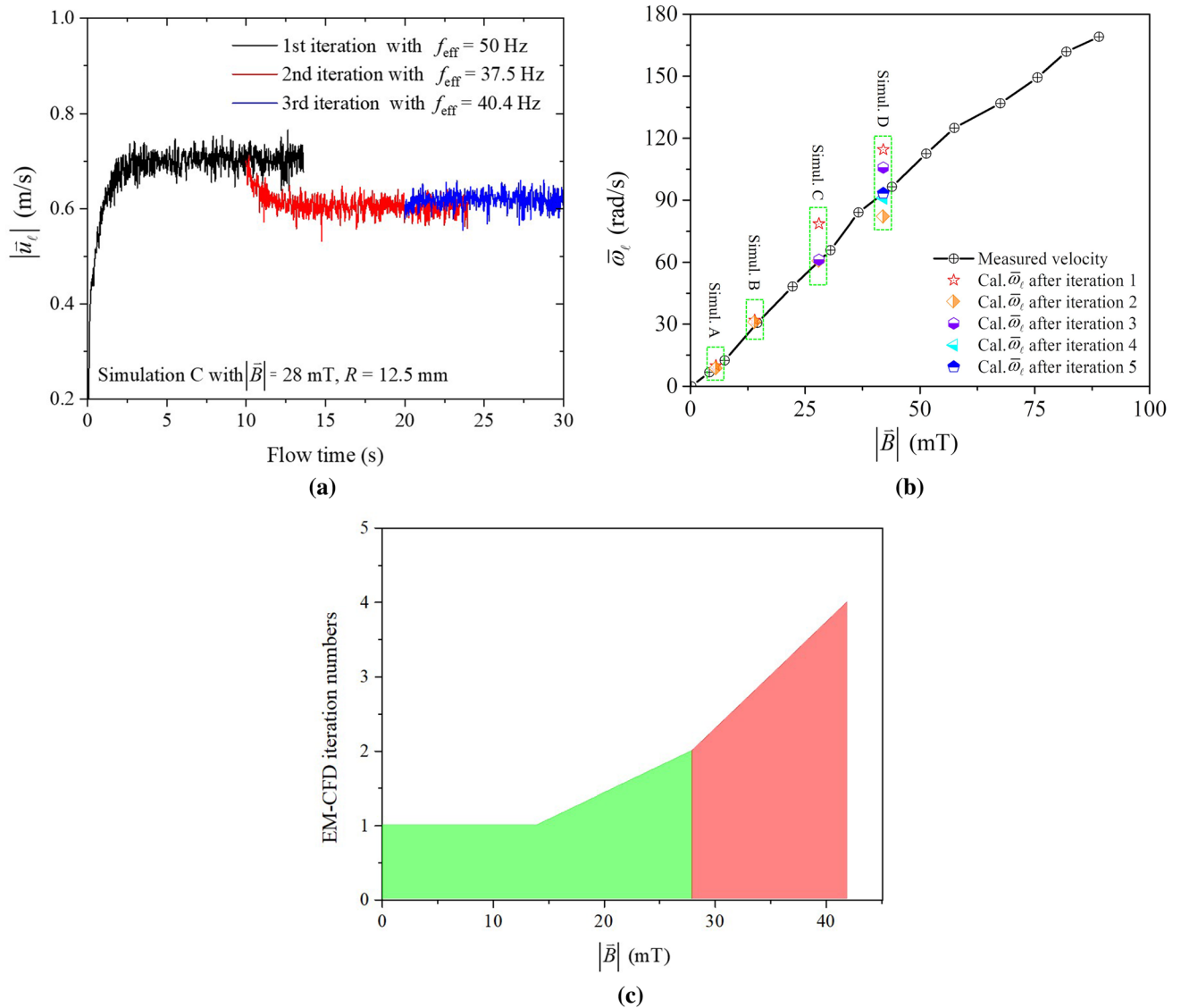


Fig. 6—Convergence analysis of EM–CFD coupling scheme. (a) Evolution of  $|\bar{u}_z|$  at a reference point (as denoted in Fig. 5(a)) for Simulation C ( $|\bar{B}| = 28$  mT,  $R = 12.5$  mm), and the curves with different colors (black, red, and blue) indicate the calculated velocities corresponding to three sequent iterations; (b) Calculated  $\bar{\omega}_\ell$  of different simulation cases during the iteration scheme; (c) Necessary EM–CFD iteration numbers, required to satisfy the criterion  $|\Delta\bar{\omega}_\ell/\bar{\omega}_\ell| < 5$  pct, as a function of  $|\bar{B}|$  (Color figure online).

port of the SEN strengthens the upper pair of recirculation loop. However, this downward flow is still weaker than  $\bar{u}_\theta$ . Despite its low intensity, a consensus is that the transport of heat and mass in the casting is dominated by  $\bar{u}_\psi$ .<sup>[14,19,29,44]</sup> Figure 8(f) shows that the motion of equiaxed crystals exhibits the same pattern as the melt flow. If the crystals are transported to the superheated region, then they can be remelted and even destroyed. The ratio between the rotating angular velocity of the liquid to  $\bar{B}$  ( $\omega_\ell/\omega_B$ ) is shown in Figure 8(g). Given that  $\omega_\ell$  is not uniform along the axis direction of the strand, the suggested EM–CFD iteration scheme cannot be directly applied to this CC case. This implies that the flow in the center mold region can be slightly overestimated.

To demonstrate the feasibility of the proposed method for M-EMS in CC billet, the calculated temperature distribution on the surface of the strand, the calculated phase distribution on a cross section of as-solidified strand, and a macrograph of the as-cast structure (field experiment) are shown in Figure 9. It is verified that the numerical model can reproduce the experimental results successfully. Based on our previous study,<sup>[42]</sup> the main functionalities of the M-EMS are (1) to promote the fragmentation of crystal fragments *via* the mechanism of fragmentation; (2) to disperse the superheat in the mold region, leaving the lower region beneath the mold undercooled; and (3) to allow the crystal fragments to survive and continue to grow in the undercooled region, and thereby, to form the equiaxed structure in the core region of the strand.

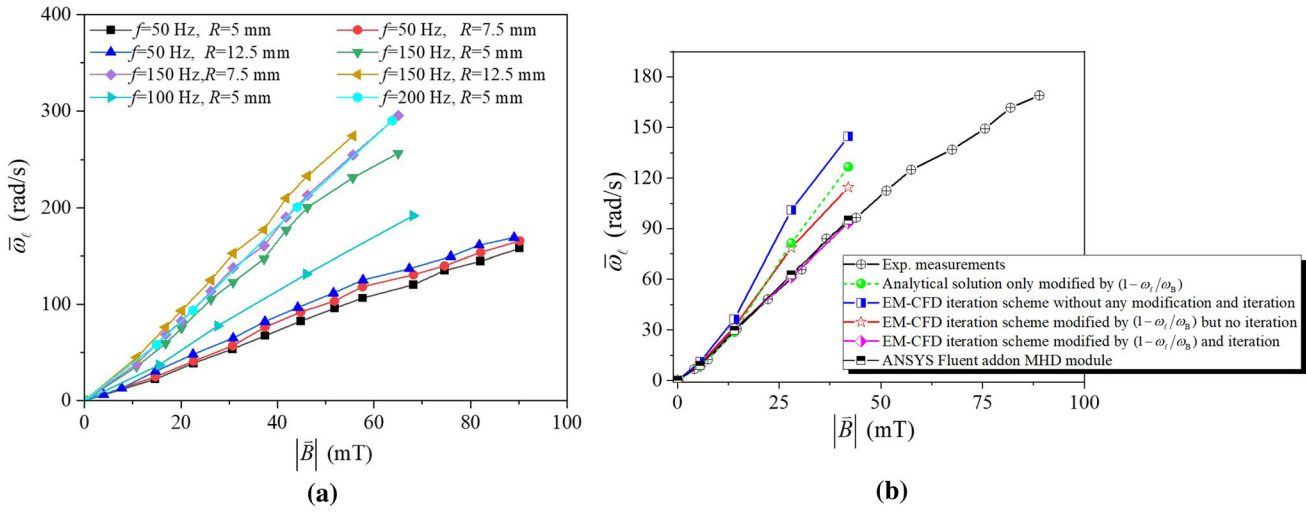


Fig. 7—(a) Measured angular velocities as a function of  $|\bar{B}|$  for all eight experiment cases as defined in Table II; (b) Comparison between simulations and experiments for Case 3 ( $R = 12.5$  mm,  $f = 50$  Hz). The experimental results are reprinted from Ref. [39], under the terms of the Creative Commons CC BY license.

## VI. DISCUSSION

### A. Evaluation of Different Iteration/Simplification Schemes

During the MHD calculation, there are two main points that should be carefully treated, *i.e.*, the eddy current effect and relative motion between the liquid and  $\bar{B}$ . As shown in Figure 3(b), once a conductive sample is loaded,  $\bar{B}$  is updated by the eddy current. The slip motion between the liquid and  $\bar{B}$  field modifies the effective frequency  $f_{\text{eff}}$ . As mentioned in § 3,  $f_{\text{eff}}$  decreases with  $\bar{\omega}_\ell$  following  $f_{\text{eff}} = (\omega_B - \bar{\omega}_\ell)/2\pi$ . The analytical solution, Figure 2(a), cannot account for the eddy effect and end effect. The effect of liquid rotating on  $f_{\text{eff}}$  can only be considered one-way by a factor of  $(1 - \omega_\ell/\omega_B)$ . Given these simplifications, as demonstrated in Figure 7(b), the calculated  $\bar{\omega}_\ell$  is considerably overestimated. The eddy effect and slip motion can be iteratively solved by using the coupled simulation *via* ANSYS Fluent add-on MHD module, Figure 2(b), which ensures high calculation accuracy at the expense of excessive computation time. Given the demanded small  $\Delta t$ , this method is limited to simple cases as opposed to the multiphase solidification simulations of CC process. If the MHD calculation is performed with the third calculation method, Figure 2(c), then the calculation accuracy is highly dependent on the modification strategies. From Figure 7(b), it can be observed that if the coupling between  $\bar{\omega}_\ell$  and  $\bar{F}_L$  is neglected, *i.e.*, the blue line, then it leads to unacceptable simulation results. Nevertheless, this de-coupled method was adopted in many simulations.<sup>[9,18,21,31–34,37,45]</sup>

Different solutions exhibit different computational costs. For the case with  $B = 28$  mT and  $f = 50$  Hz, which were run on a high-performance cluster (2.6 GHz, 12 cores), to reach a quasi-steady state, the analytical solution (Figure 2(a)) took four days ( $\Delta t = 1 \times 10^{-3}$  s);

the second method, Figure 2(b), took about ten days ( $\Delta t = 5 \times 10^{-5}$  s); depending on the modification strategies of the third method, Figure 2(c), one to two weeks was needed ( $\Delta t = 1 \times 10^{-3}$  s). For the third solution, if  $\bar{F}_L$  was only modified by multiplying  $(1 - \omega_\ell/\omega_B)$  but without any iteration, *i.e.*, the red line in Figure 7(b), it took about one week.

Although the simulations are in good agreement with the experimental measurements after several EM-CFD iterations (pink line in Figure 7(b)), it should be noted that  $\bar{\omega}_\ell$  was used to approximate  $\omega_\ell$  during each EM-CFD iteration. With the increase in  $\bar{F}_L$ , the flow becomes more chaotic, and  $\bar{u}_\theta$  becomes more non-linear along the radius of the sample. In this case,  $\bar{\omega}_\ell$  can potentially not characterize the overall flow correctly. This decreases the accuracy of this approach. Given that  $\omega_\ell$  is not uniform along the axis direction of the strand during the CC process, Figure 8(g), the suggested EM-CFD iteration scheme cannot be fully applied.

However, the following was realized. (1)  $\bar{F}_L$  was modified by multiplying  $(1 - \omega_\ell/\omega_B)$  to consider the relative motion between the melt and  $\bar{B}$ , and (2)  $\bar{F}_L'$  was partitioned among three phases according to their volume fractions. Based on Figure 8(g), the overestimated melt flow is enclosed in a short and narrow core of the casting. This implies that this slight overestimation should not significantly impact the as-cast structure.

### B. Analytical Solution for EMS

The analytical formulae were derived based on an infinite cylinder to approximate the time-averaged  $\bar{F}_L$ .<sup>[27,29,40]</sup> In a cylindrical coordinate system,  $\bar{F}_L$  is composed of  $\bar{F}_\theta$ ,  $\bar{F}_r$ , and  $\bar{F}_z$ . In the case of a uniform magnetic field rotating about a long cylinder,  $\bar{F}_z$  is

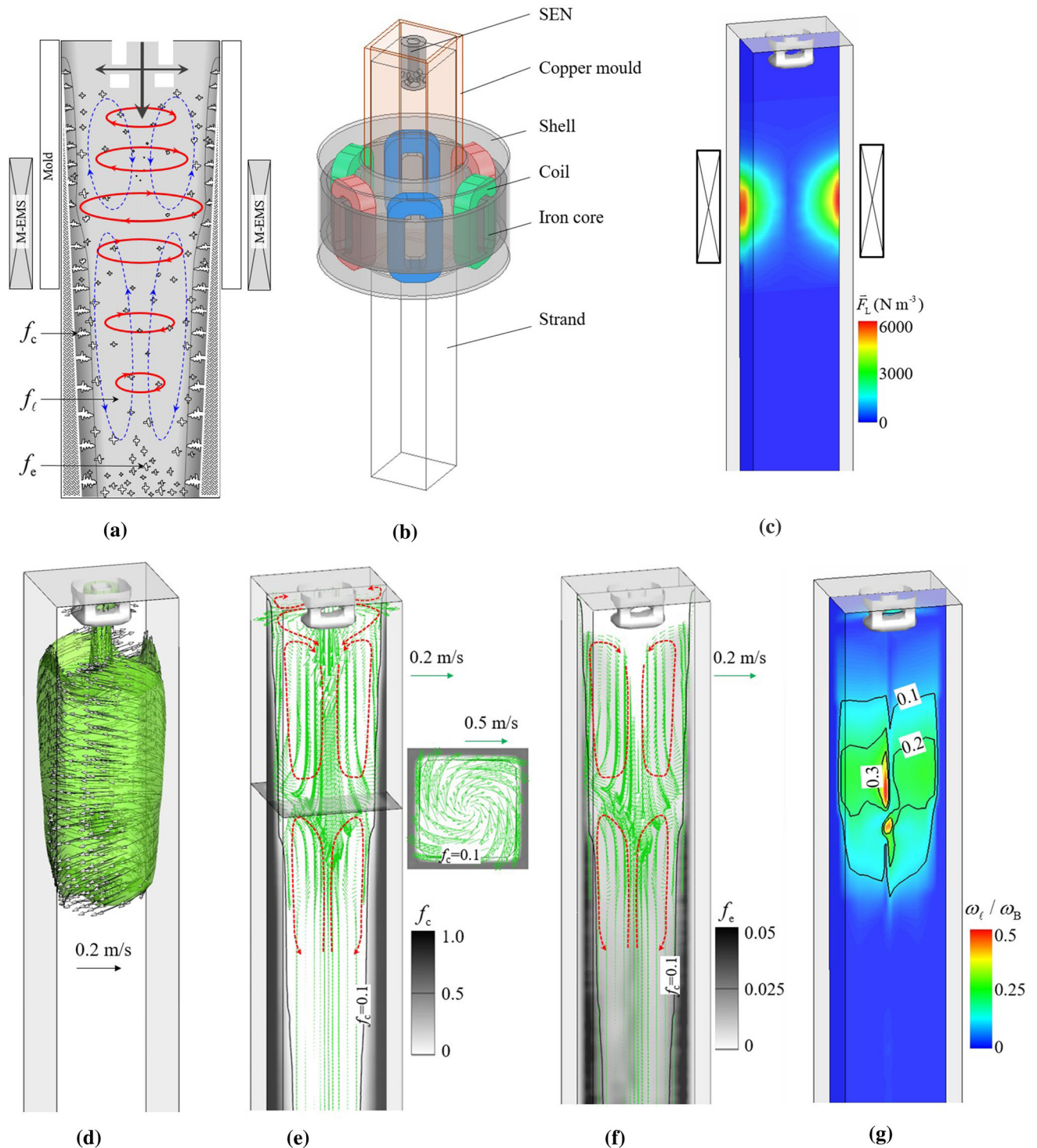


Fig. 8—A mixed columnar–equiaxed solidification model is used to simulate the as-cast structure formation in a CC billet casting under the effect of M-EMS. (a) Schematic of mixed columnar–equiaxed solidification model; (b) Layout of the M-EMS stirrer (inductor); (c) Contour of  $|\overline{F}_L|$  on the vertical section of the strand; (d) Vector of  $\vec{u}_t$  on a 3D iso-surface of  $|\vec{u}_t| = 0.08$  m/s; (e) Contour of volume fraction of columnar phase ( $f_c$ ) overlaid by the vectors of  $\vec{u}_\theta$  (vertical section) and  $\vec{u}_\psi$  (cross section) of the liquid; (f) Contour of volume fraction of equiaxed phase ( $f_e$ ) overlaid by the vectors of  $\vec{u}_\psi$  of the equiaxed crystals on the vertical section; (g) Contour of  $\omega_t/\omega_B$  on the vertical section.

shown to be zero.<sup>[29,40]</sup> The expressions for  $\vec{F}_\theta$  and  $\vec{F}_r$  can be observed in Figure 2(a) wherein  $\mu_0$  ( $=4\pi \times 10^{-7}$  H/m) denotes the electrical permeability

of free space, and  $f(z)$  denotes a distribution function of  $|\vec{B}|$  along the axial direction of the inductor. If the inductor height is infinite relative to the casting,  $\vec{B}$  can

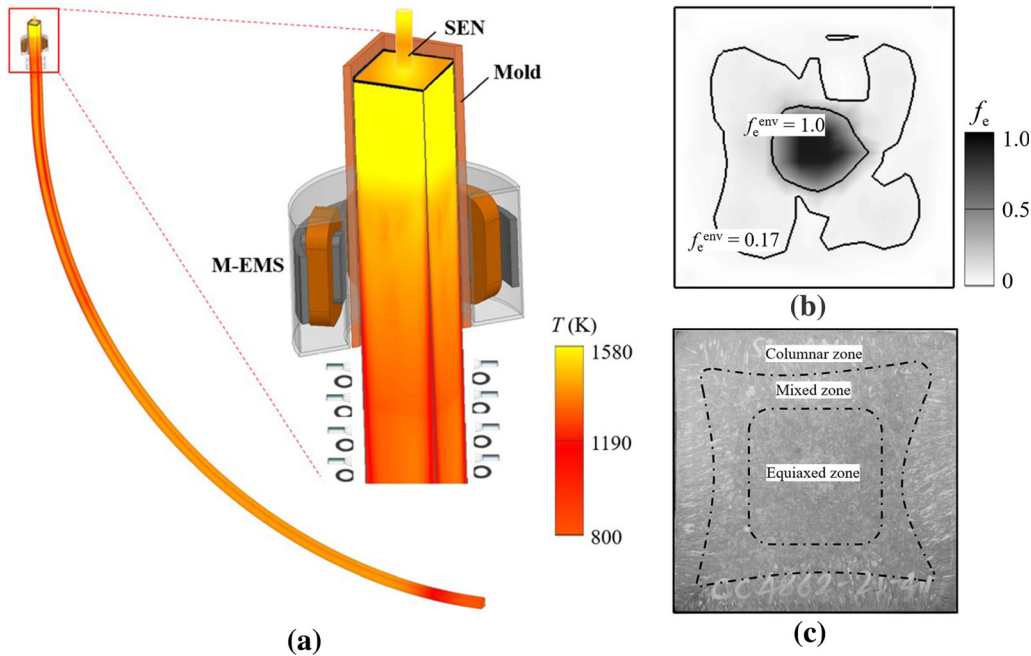


Fig. 9—(a) Calculated temperature distribution on the surface of the strand; (b) Calculated distribution of  $f_e$  overlaid by two isolines to indicate different macrostructures. (c) Macrograph of the as-cast structure of the strand (field experiment). (b) and (c) are reprinted from Ref. 42, under the terms of the Creative Commons CC BY license (<https://creativecommons.org/licenses/by/4.0/>).

be presumed as uniformly distributed along the height direction, *i.e.*,  $f(z) = 1$ .<sup>[19,26,46]</sup> Regarding the CC process, the stirrer is significantly shorter than the casting. Generally,  $f(z)$  is obtained by fitting the measured  $|\vec{B}|$ .<sup>[27,30,40]</sup> An example for  $f(z)$  is also shown in Figure 2(a) wherein  $z_{\text{mid}}$  denotes the middle position of the stirrer, and  $z_{\text{width}}$  denotes the effective width of the  $\vec{B}$  field. This analytical solution can also be applied to the CC process of billet and bloom by reverting the length ( $a$ ) and width ( $b$ ) of the casting cross section to an equivalent radius *via*  $R_e = 2\sqrt{\frac{ab}{\pi}}$ .<sup>[27]</sup> As discussed in § 6.1, the liquid flow can be overestimated with this method. The Joule heat ( $Q_J$ ) can also be analytically approximated, and the formula for  $Q_J$  is obtained from a previous study.<sup>[27]</sup>

### C. Other Issues for EMS and Outlook

One of the main objectives of this study was to quantify the accuracy of different modification strategies and emphasize certain necessary modifications on  $\vec{F}_L$ , which are summarized as below:

- (1) The analytical solution (Figure 2(a)), relying on its calculation efficiency and easy implementation, is an alternative option to obtain acceptable simulation results. An extra EM solver is not required, but  $\vec{B}$  field should be known in advance *via* other measurement or calculation method. With this one-way coupling method, the main drawback involves neglecting the eddy effect. As pronounced by Spitzer *et al.*,<sup>[29]</sup> this analytical solution is accurate for  $R_m \leq$

3 ( $R_m = \omega_B \sigma \mu_0 R^2$ ). Furthermore, the influence of the solidified shell,<sup>[42]</sup> mold temperature,<sup>[42]</sup> liquid flow, and the formation of air gap between the casting the mold<sup>[47]</sup> on  $\vec{B}$  field cannot be considered. When this method is applied to continuous castings (billet, bloom, or slab), the converted equivalent radius *via*  $R_e = 2\sqrt{\frac{ab}{\pi}}$  can also lead to significant discrepancy.

- (2) The ANSYS Fluent add-on MHD module (Figure 2(b)) provides a coupled calculation scheme, but  $\vec{B}_0$  must be provided either by EM calculation or physical measurement. Because of the explicit temporal resolution of  $\vec{B}_0$ ,  $\Delta t$  should be very small.<sup>[24]</sup>

Based on the frequency of  $\vec{B}_0$  (3–50 Hz),  $\Delta t$  can be varied in the range of  $10^{-4}$  to  $10^{-5}$  s. The additional solving of  $\vec{b}$  equations and their interaction with the momentum equations and energy equations significantly decrease the speed of the calculation, and this in turn poses challenges for the simulation to converge. According to the simulation results,  $|\vec{b}|$  is about 10 pct of  $|\vec{B}_0|$  for the currently studied laboratory scale casting, *e.g.*,  $|\vec{b}| = 0.53$  mT for  $|\vec{B}_0| = 5.6$  mT, and  $|\vec{b}| = 2.1$  mT for  $|\vec{B}_0| = 28$  mT. It should be noted that this additional MHD module is not compatible with the Eulerian–Eulerian multiphase approach in ANSYS Fluent on which

most advanced solidification models have been developed.

- (3) If  $\vec{F}_L$  is calculated by an external EM solver, then it is possible to consider all the aforementioned effects, including the eddy effect, formation of air gap between casting and mold,<sup>[47]</sup> insulating/conducting wall boundary conditions,<sup>[42]</sup> temperature-dependent electrical conductivities,<sup>[42]</sup> and different mold temperatures.<sup>[32]</sup> There are even more possibilities to perform parameter study on  $\vec{B}$ . As demonstrated in Figure 7(b), terming the calculated  $\vec{F}_L$  directly as the source force without any modifications leads to the unacceptable calculated flow field.<sup>[24]</sup> We do not recommend using the currently proposed EM–CFD iterative scheme in the simulations of CC process, but the modification of  $\vec{F}_L$  by a factor of  $(1 - \omega_\ell/\omega_B)$  is necessary and can improve the calculation accuracy considerably. It should be stated that the currently proposed EM–CFD iteration scheme provides one option for Eulerian–Eulerian multiphase simulation to improve the calculation accuracy.

It is known that the casting size/geometry can also affect the EMS-driven flow. However, performing velocity measurements on the engineering continuous casting is not possible. In addition to the current benchmark, there is a middle-scale facility which was built in Dresden.<sup>[15]</sup> The sample size is 800 mm in length and 80 mm in diameter. The cold liquid metal ( $\text{Ga}_{68}\text{In}_{20}\text{Sn}_{12}$ ) in the casting mold was stirred by a rotary electromagnetic field. The melt, as injected from the SEN into the mold, interacts with the RMF-driven flow. The fluid rotating velocities under different  $|\vec{B}|$  (4.1 to 18.3 mT) were measured *via* ultrasound doppler velocimetry technique. As an additional step, the scaling effect should be investigated based on the current laboratory benchmark and middle-scale physical model.

## VII. SUMMARY

An experiment benchmark was presented to verify the MHD methods that were typically used for investigation of the flow and solidification during continuous casting (CC) process. A two-pole inductor charged by a three-phase AC was developed to generate a rotating magnetic field (RMF) with variable  $|\vec{B}|$  and  $f$ . Systematic data, including the magnetic field, torque, and RMF-driven liquid flow, were provided.

Three typically used MHD methods for CC process were evaluated *via* comparison with the experiment data set. The analytical solution for the  $\vec{F}_L$  corresponded to easy-to-implement method with highest computation efficiency, but it was limited to the low-frequency cases, and the liquid velocity can be considerably overestimated because the eddy effect was ignored. The ANSYS Fluent addon MHD module provided the highest calculation accuracy, but there were drawbacks of

excessively high computation cost, incompatibility for multiphase solidification problem, and the external magnetic field should be measured or calculated elsewhere. The third method involves combining the EM and CFD calculations between ANSYS Maxwell and ANSYS Fluent. To ensure the calculation accuracy by considering the eddy current and flow effect on the EM field, an iteration scheme was proposed. As the iteration was conducted manually, it was not feasible for industry CC.

Although the EM–CFD iteration is not recommended for the CC process, necessary calculation accuracy can still be realized by this scheme without iteration.

However, additional modifications to  $\vec{F}_L$  must be carefully considered in the CFD and solidification calculation. The relative motion between the melt and  $\vec{B}$  field should be considered by  $\vec{F}_L' = \vec{F}_L(1 - \omega_\ell/\omega_B)$ . Finally, due to the multiphase nature of solidification during CC, the  $\vec{F}_L'$  must be further partitioned among different phases (liquid, equiaxed, and columnar) according to their volume fractions, *i.e.*,  $f_\ell \vec{F}_L'$ ,  $f_e \vec{F}_L'$ , and  $f_c \vec{F}_L'$ .

## ACKNOWLEDGMENTS

This work was financially supported by the FWF Austrian Science Fund and the Hungarian National Research Development, and Investigation Office (No. 130946) in the framework of the FWF-NKFIN joint project (FWF, I4278-N36) and the Austria Research Promotion Agency (FFG) through the Bridge 1 project (No. 868070)

## CONFLICT OF INTEREST

On behalf of all authors, the corresponding author states that there is no conflict of interest.

## FUNDING

Open access funding provided by Montanuniversität Leoben.

## OPEN ACCESS

This article is licensed under a Creative Commons Attribution 4.0 International License, which permits use, sharing, adaptation, distribution and reproduction in any medium or format, as long as you give appropriate credit to the original author(s) and the source, provide a link to the Creative Commons licence, and indicate if changes were made. The images or other third party material in this article are included in the article's Creative Commons licence, unless indicated



otherwise in a credit line to the material. If material is not included in the article's Creative Commons licence and your intended use is not permitted by statutory regulation or exceeds the permitted use, you will need to obtain permission directly from the copyright holder. To view a copy of this licence, visit <http://creativecommons.org/licenses/by/4.0/>.

## NOMENCLATURE

$\vec{b}$ (mT)	Induced magnetic field
$\vec{B}_0$ (mT)	External magnetic field
$\vec{B}$ (mT)	Combined magnetic field
$\vec{e}$ (-)	Unit vector of the Lorentz force
$\vec{E}$ (V m <sup>-1</sup> )	The strength of electric field
$f$ (Hz)	Frequency of the magnetic field
$f_{\text{eff}}$ (Hz)	Effective frequency of the magnetic field
$f_l, f_c, f_e$ (-)	Volume fraction of liquid, equiaxed, and columnar phases
$\vec{F}_L, \vec{F}_\theta, \vec{F}_r$ (N m <sup>-3</sup> )	Lorentz forces
$\vec{F}_L$ (N m <sup>-3</sup> )	Modified Lorentz forces
$\vec{F}_s$ (N m <sup>-3</sup> )	Other source terms for momentum equation
$\vec{g}'$ (m s <sup>-2</sup> )	Deduced gravity acceleration
$\vec{g}$ (m s <sup>-2</sup> )	Gravity acceleration
$G$ (K mm <sup>-1</sup> )	Temperature gradient
$h$ (J kg <sup>-1</sup> )	Enthalpy
$H$ (mm)	Sample height
$\Delta H$ (mm)	Height difference
$I$ (A)	Source electric current
$\vec{J}$ (A m <sup>-2</sup> )	Eddy current
$k$ (W m <sup>-1</sup> K <sup>-1</sup> )	Thermal conductivity
$P$ (Pa)	Pressure
$Q_J$ (J m <sup>-3</sup> s <sup>-1</sup> )	Joule heat
$Q_s$ (J m <sup>-3</sup> s <sup>-1</sup> )	Other source terms for energy conservation equation
$R_m$ (-)	Magnetic Reynolds number
$R$ (mm)	Sample radius

$R_e$ (-)	The real part of a complex number
$r$ (mm)	Radial coordinate
$\tau, \bar{\tau}$ (N m)	Torque
$T$ (K)	Temperature
$t$ (s)	Time
$\Delta t$ (s)	Time step for the simulation
$\vec{u}, \vec{u}_\theta, \vec{u}_\psi$ (m s <sup>-1</sup> )	Liquid velocity and its components
$v$ (mm s <sup>-1</sup> )	Withdrawal speed of sample
$v_{\text{Ga75In25}}$ (m <sub>2</sub> s <sup>-1</sup> )	Kinematical viscosity
$z$ (mm)	Coordinate in $z$ direction
$z_{\text{width}}$ (mm)	Effective width of the magnetic field
$z_{\text{mid}}$ (mm)	Middle position of the magnetic field
$\omega_l, \omega_{l,0}, \omega_B$ (Rad s <sup>-1</sup> )	Rotating angular speed
$\bar{\omega}_l$ (Rad s <sup>-1</sup> )	Volume-averaged rotating angular speed
$\delta$ (mm)	Eddy current penetration distance
$\sigma, \sigma_{\text{Cu}}, \sigma_{\text{Al}}, \sigma_{\text{AlSi7}}, \sigma_{\text{Ga75In25}}$ (S m <sup>-1</sup> )	Electrical conductivity
$\rho, \rho_{\text{Cu}}, \rho_{\text{Al}}, \rho_{\text{AlSi7}}, \rho_{\text{Ga75In25}}$ (kg m <sup>-3</sup> )	Density
$\mu_0$ (H·m <sup>-1</sup> )	Vacuum magnetic permeability
$\mu, \mu_{\text{Cu}}, \mu_{\text{Al}}, \mu_{\text{AlSi7}}, \mu_{\text{Ga75In25}}$ (H·m <sup>-1</sup> )	Real magnetic permeability
$\bar{\tau}$ (kg m <sup>-1</sup> s <sup>-1</sup> )	Stress-strain tensors
$\theta$ (deg)	Angle

## REFERENCES

1. S. Kunstreich: *Metall. Res. Technol.*, 2003, vol. 100, pp. 1043–61.
2. J. Stiller, K. Koal, W.E. Nagel, J. Pal, and A. Cramer: *Eur. Phys. J. Spec. Top.*, 2013, vol. 220, pp. 111–22.
3. A.A. Tzavaras and H.D. Brody: *J. Met.*, 1984, vol. 36, pp. 31–37.
4. J. Kovács, A. Rónaföldi, Á. Kovács, and A. Roósz: *Trans. Indian Inst. Met.*, 2009, vol. 62, pp. 461–64.
5. P.P. Sahoo, A. Kumar, J. Halder, and M. Raj: *ISIJ Int.*, 2009, vol. 49, pp. 521–28.
6. B. Willers, S. Eckert, P.A. Nikrityuk, D. Rábiger, J. Dong, K. Eckert, and G. Gerbeth: *Metall. Mater. Trans. B*, 2008, vol. 39, pp. 304–16.
7. S. Kunstreich: *Metall. Res. Technol.*, 2003, vol. 100, pp. 395–408.
8. A. Scholes: *Ironmak. Steelmak.*, 2005, vol. 32, pp. 101–08.
9. H. An, Y. Bao, M. Wang, and L. Zhao: *Metall. Res. Technol.*, 2018, vol. 115, p. 103.

10. M.R. Bridge and G.D. Rogers: *Metall. Trans. B.*, 1984, vol. 15, pp. 581–89.
11. S. Eckert, P.A. Nikrityuk, D. Rübiger, K. Eckert, and G. Gerbeth: *Metall. Mater. Trans. B*, 2008, vol. 39, pp. 374–86.
12. I. Grants and G. Gerbeth: *Phys. Fluids.*, 2003, vol. 15, pp. 2803–09.
13. D. Rübiger, S. Eckert, and G. Gerbeth: *Exp. Fluids.*, 2010, vol. 48, pp. 233–44.
14. P. Dold and K.W. Benz: *Cryst. Res. Technol.*, 1997, vol. 32, pp. 51–60.
15. B. Willers, M. Barna, J. Reiter, and S. Eckert: *ISIJ Int.*, 2017, vol. 57, pp. 468–77.
16. Z. Liu, A. Vakhrushev, M. Wu, A. Kharicha, A. Ludwig, and B. Li: *Metall. Mater. Trans. B*, 2019, vol. 50, pp. 543–54.
17. R. Chaudhary, C. Ji, B.G. Thomas, and S.P. Vanka: *Metall. Mater. Trans. B*, 2011, vol. 42, pp. 987–1007.
18. Y. Wang, L. Zhang, W. Chen, and Y. Ren: *Metall. Mater. Trans. B*, 2021, vol. 52, pp. 2796–2805.
19. H. Zhang, M. Wu, C.M.G. Rodrigues, A. Ludwig, and A. Kharicha: *Metall. Mater. Trans. A*, 2021, vol. 52, pp. 3007–22.
20. P.A. Nikrityuk, K. Eckert, and R. Grundmann: *Int. J. Heat Mass Transf.*, 2006, vol. 49, pp. 1501–15.
21. D. Jiang and M. Zhu: *Metall. Mater. Trans. B*, 2016, vol. 47, pp. 3446–58.
22. A. Vakhrushev, A. Kharicha, E. Karimi-Sibaki, M. Wu, A. Ludwig, G. Nitzl, Y. Tang, G. Hackl, J. Watzinger, and S. Eckert: *Metall. Mater. Trans. B*, 2021, vol. 52, pp. 3193–3207.
23. R. Chaudhary, B.G. Thomas, and S.P. Vanka: *Metall. Mater. Trans. B*, 2012, vol. 43, pp. 532–53.
24. M. Javurek, M. Barna, P. Gittler, K. Rockenschaub, and M. Lechner: *Steel Res. Int.*, 2008, vol. 79, pp. 617–26.
25. P. Galdiz, J. Palacios, J.L. Arana, and B.G. Thomas: *Eur. Contin. Cast. Conf. Graz, Austria*, 2014, pp. 1–10.
26. H. Zhang, M. Wu, Y. Zheng, A. Ludwig, and A. Kharicha: *Mater. Today Commun.*, 2020, vol. 22, p. 100842.
27. S. Wang, G. Alvarez De Toledo, K. Välimaa, and S. Louhenkilpi: *ISIJ Int.*, 2014, vol. 54, pp. 2273–82.
28. J.K. Roplekar and J.A. Dantzig: *Int. J. Cast Met. Res.*, 2001, vol. 14, pp. 79–95.
29. K.H. Spitzer, M. Dubke, and K. Schwerdtfeger: *Metall. Trans. B.*, 1986, vol. 17, pp. 119–31.
30. A. Noepfel, A. Ciobanas, X.D. Wang, K. Zaidat, N. Mangelinck, O. Budenkova, A. Weiss, G. Zimmermann, and Y. Fautrelle: *Metall. Mater. Trans. B*, 2010, vol. 41, pp. 193–208.
31. K. Fujisaki, K. Wajima, and T. Ohki: *IEEE Trans. Magn.*, 2000, vol. 36, pp. 1319–24.
32. H. Sun and J. Zhang: *Metall. Mater. Trans. B*, 2014, vol. 45, pp. 1133–49.
33. H.Q. Yu and M.Y. Zhu: *Ironmak. Steelmak.*, 2012, vol. 39, pp. 574–84.
34. R. Guan, C. Ji, and M. Zhu: *Metall. Mater. Trans. B*, 2020, vol. 51, pp. 1137–53.
35. H. Liu, M. Xu, S. Qiu, and H. Zhang: *Metall. Mater. Trans. B*, 2012, vol. 43, pp. 1657–75.
36. B.Z. Ren, D.F. Chen, H.D. Wang, M.J. Long, and Z.W. Han: *Ironmak. Steelmak.*, 2015, vol. 42, pp. 401–8.
37. Q. Fang, H. Zhang, J. Wang, C. Liu, and H. Ni: *Metall. Mater. Trans. B*, 2020, vol. 51, pp. 1705–17.
38. A. Rónaföldi: Hungary University of Miskolc, Hungary, doctoral dissertation, 2008.
39. A. Rónaföldi, A. Roósz, and Z. Veres: *J. Cryst. Growth*, 2021, vol. 564, p. 126078.
40. P.A. Davidson and J.C.R. Hunt: *J. Fluid Mech.*, 1987, vol. 185, pp. 67–106.
41. J. Stiller, K. Fraña, and A. Cramer: *Phys. Fluids.*, 2006, vol. 18, pp. 1–10.
42. Z. Zhang, M. Wu, H. Zhang, S. Hahn, F. Wimmer, A. Ludwig, and A. Kharicha: *J. Mater. Process. Technol.*, 2021, vol. 301, p. 117434.
43. M. Wu, A. Ludwig, and A. Kharicha: *Metals (Basel)*, 2019, vol. 9, p. 229.
44. G. Zimmermann, A. Weiss, and Z. Mbaya: *Mater. Sci. Eng. A.*, 2005, vol. 413–414, pp. 236–42.
45. R. Vertnik, K. Mramor, and B. Šarler: *Eng. Anal. Bound. Elem.*, 2019, vol. 104, pp. 347–63.
46. P.A. Nikrityuk, K. Eckert, and R. Grundmann: *Metall. Mater. Trans. B*, 2006, vol. 37, pp. 349–59.
47. Y. Wang, W. Chen, D. Jiang, and L. Zhang: *Steel Res. Int.*, 2020, vol. 91, pp. 1–11.

**Publisher's Note** Springer Nature remains neutral with regard to jurisdictional claims in published maps and institutional affiliations.